FINAL REPORT

Submitted to the Florida Department of Transportation

Project: Long-Term Behavior of Geosynthetic Reinforced Mechanically Stabilized Earth (MSE) Wall System – Numerical /Analytical Studies, Full Scale Field Testing, and Design Software Development

Authors: D.V Reddy, F. Navarrete, C. Rosay, A. Cira, A.K. Ashmawy, and M. Gunaratne

Contract No.: BC-129

Dr. D.V. Reddy
Department of Civil Engineering
Florida Atlantic University
Boca Raton, FL 33431
Tel: 561-297-3443
January, 2003

Project Manager: Peter Lai

ABSTRACT

This report summarizes the methods, results and findings of a comprehensive research study on geogrid-reinforced MSE walls. Small and full scale experiments are supplemented with numerical and analytical methods to provide the Department (FDOT) with the necessary knowledge and tools to design and analyze geogrid-reinforced MSE walls under long-term conditions. Specifics regarding the creep behavior of the geogrids, and a new model for geogrid creep are included in the study. Scale effects are addressed by comparing the experimental and numerical results from small and full scale tests, and by conducting an analytical study using dimensional analysis. Based on the research findings, a software package is developed to aid in the design and analysis of geogrid-reinforced MSE walls under long-term conditions.

TABLE OF CONTENTS

1 INTRODUCTION

Utilization of geosynthetic reinforced soil technology has grown dramatically in the past ten years due to enhanced durability, simplicity and rapidity of construction, less site preparation, less space requirement for construction operations, reduced right-of-way acquisition, elimination of the need for rigid or unyielding formations, and cost-effectiveness. A significant advantage of mechanically stabilized earth (MSE) walls is their flexibility and capability to absorb deformations due to poor subsoil conditions in the foundations. MSE walls with geogrid reinforcement have thus gained substantial approval, both state- and nation-wide, as an alternative to conventional reinforced concrete retaining structures for bridge abutments and wing walls, and roadway/underpass widening with right-of-way restrictions, and embankments and excavations necessitating steeper slopes. The cost savings are of the order of 25 to 50% in comparison with conventional reinforced concrete retaining structures, especially when supported by deep foundations.

Despite their widespread usage, the long-term behavior of geogrid-reinforced MSE walls remains uncertain. In particular, the tendency of polymeric geogrids to creep under sustained loading at high temperature poses a potential risk to the performance of MSE walls in warm climates such as in Florida. In this report, an experimental and analytical investigation addresses these issues through an integrated set of small- and large-scale tests and numerical model studies. In addition, the project includes the development of a Windows-based computer program to assist design engineers and Department (FDOT) personnel with the selection, design, and analysis of MSE walls subjected to long-term degradation.

1.1 OBJECTIVES AND METHODS

The specific objectives of this study are:

1. To evaluate the influence of system properties, such as soil, geogrid and interface stress-strain parameters and loading conditions on the overall wall response as indicated by performance parameters such as the maximum settlement of the wall and maximum tension in the geogrid.

2. To account for scale effects that would occur when predicting the response of large-scale reinforced systems based on small-scale test data.

3. To evaluate the effect of different types of geogrid reinforcement and/or backfill soils.

4. To explore appropriate means of analytically modeling creep and geogrid degradation effects.

5. To evaluate and verify the long-term performance of MSE walls through experiments, supplemented with analysis methods.

6. To incorporate the above findings in the current design guidelines and to develop a computer program for designing and analyzing MSE walls under creep conditions.

1.2 ORGANIZATION OF THE REPORT

This report is organized in eleven Chapters, in addition to a References section. The Chapters mostly follow the developmental progress of the research, although some

rearrangement was at times necessary in favor of a more logical sequence of concepts and ideas. The following is a breakdown of the specific topics covered in each of the Chapters.

Chapter 2 covers a comprehensive literature review on the research subject, and provides reference to relevant earlier studies by the Department and the authors.

Chapter 3 deals with the evaluation of important system components (parameters) and their influence on the overall behavior of the wall. These parameters include soil strength and stiffness, geogrid load-deformation behavior, and interface properties.

Chapter 4 presents a new model for creep of geosynthetics, based on data from an earlier related study.

Chapter 5 addresses design considerations, which include a preliminary design of the full-scale MSE wall and an assessment of scale effects. Scale effects are analyzed through dimensional equivalence of the small- and large-scale systems. Preliminary numerical studies are also presented.

Chapter 6 covers the experimental setup, materials, and construction details of the small scale walls.

Chapter 7 presents experimental test results and comparison with numerical analysis data for the small scale walls.

Chapter 8 outlines the construction methods of the full scale wall. Details on the instrumentation, geometry, loading conditions, and monitoring program are included.

Chapter 9 includes the experimental test results of the full scale wall. Results are compared with the numerical modeling predictions, and corrections are made accordingly to the design procedure.

Chapter 10 contains a detailed description of the software program for design of geogrid-reinforced MSE walls, which was developed as part of this study. Sample inputs and an example problem are presented.

Chapter 11 concludes this report by providing a summary of the findings and recommendations.

A list of References cited and bibliographical material follows the last Chapter.

2 LITERATURE REVIEW

An extensive literature review was carried out on a number of relevant topics. This review covers research in the following areas: 1) Mechanically-Stabilized Earth (MSE) Walls, 2) design methodology for MSE walls, 3) analytical prediction of performance for MSE walls, 4) field evaluation (case studies); and factors that influence the long term performance–based design of MSE walls 5) pullout strength, 6) durability and degradation, 7) environmental stress cracking resistance, 8) creep, and 9) connections and junctions between facings and geogrids.

2.1 MECHANICALLY-STABILIZED EARTH (MSE) WALLS

2.1.1 INTRODUCTION

The use of inclusions for soil reinforcement can be traced to prehistoric times. Some examples of man-made soil reinforcement include dikes constructed of earth and tree branches, which have been used in China for at least 1,000 years and were used along the Mississippi River in the 1880's. French settlers along the Bay of Fundy in Canada used sticks to reinforce mud dikes during the 17th and 18th Centuries. In England wooden pegs have been used for erosion and land slide control, and bamboo or wire mesh has been used universally for revetment erosion control (Elias *et al.*, 1997).

The French architect Henry Vidal's research led to the development of the *Terre Armée* or Reinforced Earth®, patented in 1966, which used steel strips for reinforcement. In 1972, the first such wall was constructed in the United States as a 55 ft high wall in the San Gabriel Mountains of Southern California (Munfakh, 1995). Currently, most process patents

covering soil-reinforced systems have expired, leading to the proliferation of different reinforced earth systems (Elias *et al.*, 1997).

The use of geotextiles in soil reinforcement started in 1971 in France after their beneficial effect was noticed in the construction of embankments over weak subgrades. The use of geogrids for soil reinforcement was developed around 1980 (Elias *et al.*, 1997). By placing tensile reinforcing elements (inclusions) in the backfill soil of an MSE wall, the strength of the soil is improved. With the addition of a facing system, very steep slopes and vertical walls can be constructed safely (Elias *et al.*, 1997). Geogrid reinforced walls can be used where conventional reinforced-concrete walls, or steel segmental walls are used.

As of 1997, polymer-reinforced permanent walls have been approved by AASHTO in the U.S. (Koerner, 1998). The US Department of Transportation in its technical report FHWA-SA-96-038, published in 1997, describes a Segmental, Precast Facing MSE wall as follows:

> *[The system] employs metallic (strip or barmat) or geosynthetic (geogrid or geotextile) reinforcement that is connected to a precast concrete or prefabricated metal facing panel to create a reinforced soil mass. The reinforcement is placed in horizontal layers between successive layers of granular soil backfill. Each layer of backfill consists of one or more compacted fills.*

A detailed description of each component of an MSE wall is presented in the following sections. Figure 2.1 shows the principal components of an MSE wall.

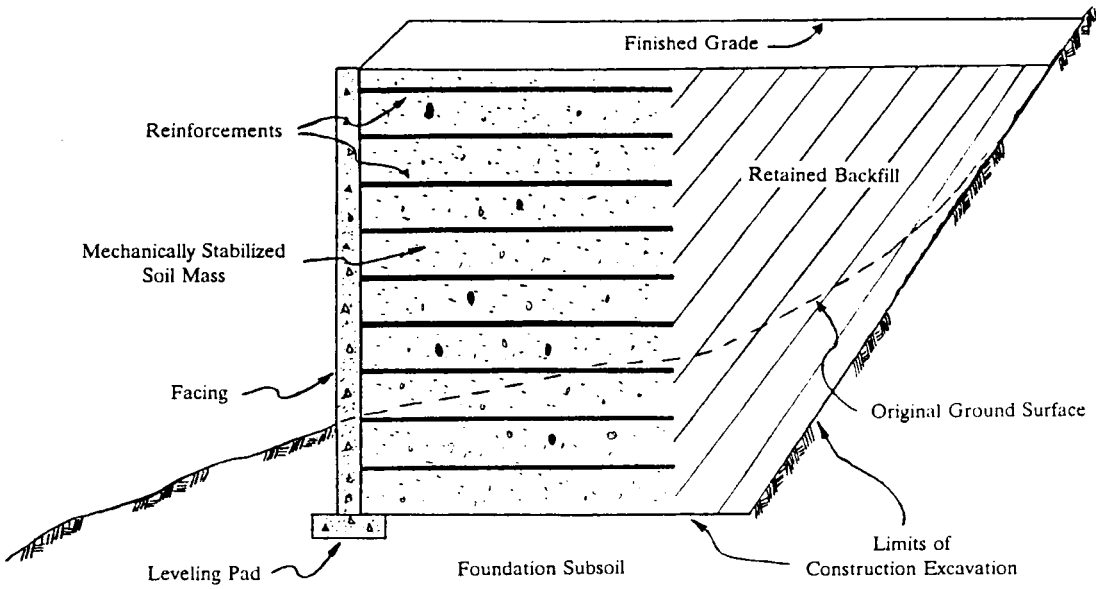

Figure 2.1 Principal components of an MSE wall. (Long, 1995).

2.1.2 REINFORCING ELEMENTS

The reinforcing materials most commonly used in MSE walls can be divided into the following categories:

1) Metallic reinforcements: typically made of mild steel, usually galvanized or epoxy coated.

2) Nonmetallic reinforcements: geotextiles of polymeric materials consisting of polypropylene, polyethylene, or polyester (Elias, 1997).

These reinforcements come in different shapes, such as strips, grids, sheets, rods, and fibers (Munfakh, 1995).

For walls reinforced with geogrids, the anchorage strength, or pullout resistance, is a result of three different mechanisms. The first is the shear strength along the top and bottom interfaces between the geogrid and soil along the longitudinal ribs. The second is the shear strength along the top and bottom interfaces between the geogrid and soil along the transverse ribs. The third is the passive resistance against the front of the transverse ribs. In this last mechanism, the soil goes into a passive state and resists pullout by means of bearing capacity (Koerner, 1998).

2.1.3 BACKFILL MATERIAL

High quality backfill is required for durability, good drainage, constructability, and good soil reinforcement interaction, which can be obtained from well graded, granular materials. Most MSE systems require material with high friction characteristics, since they rely on the friction between the soil and reinforcing for anchoring strength or pullout. Some systems rely on passive pressure on the reinforcing elements; in those cases, the quality of backfill material is critical. This performance requirement generally eliminates soils with high clay contents. From a reinforcement capacity point of view, lower quality soils could be used. However, a high quality granular backfill has the advantages of being free draining, thus providing better durability for metallic reinforcement and requiring less reinforcement. Granular soils also have significant handling, placement and compaction advantages. These contribute to an increase rate of wall erection and improved maintenance of wall alignment tolerances.

2.1.4 FACING ELEMENTS

In front of the backfill, the facing units control the aesthetics of the MSE wall since they are the only visible part of the completed structure. Facings also protect the soil and reinforcing elements from weathering effects. The facings currently used include precast concrete elements, metal sheets and plates, welded wire mesh, concrete blocks, timber, rubber tires, and shotcrete (Munfakh, 1995). Koerner (1998) listed the following types of permanent geogrid-reinforced walls facings:

Articulated precast concrete panels: Discrete precast concrete panels, which contain inserts for attaching the geogrid.

Full height precast panels: Concrete panels made for the total height of the wall and temporarily supported until backfilling is complete.

Cast-in-place concrete panels: These are often used for wrap-around walls that are allowed to settle and, after a year or two, are covered with cast-in-place facing panels.

Masonry block facing walls: These walls have the geogrid embedded between the blocks and are held in place by pins, nubs, and/or friction.

Timber facings: These facing are made of railroad ties or of other large treated timber elements, with the geogrid attached by batten strips and/or held by friction when placed between the timber elements.

Gabion facings: These polymer or steel-wire baskets are filled with stone, with a geogrid held between the baskets and fixed with rings and/or friction.

Welded wire-mesh facings: These facings are similar to gabion facings, but are often used for small temporary walls. The geogrids are attached to the mesh facings with metal rings.

Wrap-around facings: The geogrid wrapped around the backfill. The geogrids need protection against ultraviolet light and vandalism; therefore, an asphalt or concrete coating is usually applied.

2.2 DESIGN METHODOLOGY FOR MSE WALLS

Various design methodologies have been established for MSE walls. The most comprehensive write-up on design guidelines for MSE walls is that of the Committee on Transportation Earthworks #A2K02, of the Transportation Research Board (Long, 1995). The sections addressed in this reference include Mechanics of Soil Reinforcement (Internal and External Stability), Construction Methods and Control (Materials Handling, Erection Procedures, Alignment Control, and Earthwork Control), and Applications (Limitations and Advantages, Evaluation Including Development of Design Data, Review of Structure Designs, and Construction Inspection). The design procedures for a hybrid gabion-facing geogrid retaining wall in Canada were presented by Simac *et al.* (1997).

The analysis of anchored woven geotextiles for in-situ slope stabilization of fine-grained soils was presented by Vitton *et al.* (1998). Chang *et al.* (1991) designed a geotextile-reinforced retaining wall for stabilizing a weathered mudstone slope in Southwest Taiwan. The development of a computer-aided Limit State design method for geosynthetic reinforced soil structures has been developed by McGown *et al.* (1998). A method for the

preliminary design of geosynthetics reinforced soil structures for the case of localized surface loads was developed by Haza *et al.* (1998).

The current design practice for geogrid-reinforced retaining walls, widely implemented by the FHWA (Christopher *et al.*, 1990), is essentially based on the analysis methods introduced in the sixties for reinforced soil walls. In the current practice, seven potential failure mechanisms are investigated, and the corresponding factors of safety are determined and compared to acceptable values.

Since the procedure for investigation of the external stability of conventional (gravity and cantilever) walls has been well established for decades, the same procedure is typically used for MSE walls. The first four failure mechanisms illustrated in Figure 2.2, pertain to the external stability of the wall: a) sliding, b) overturning, c) bearing capacity, and d) global stability (slope stability).

The three internal failure mechanisms specific to geogrid-reinforced walls illustrated in Figure 2.3, are a) breakage of the geogrid due to under-designed vertical spacing, b) pullout, due to insufficient anchorage length and c) failure at the geogrid/facing connection.

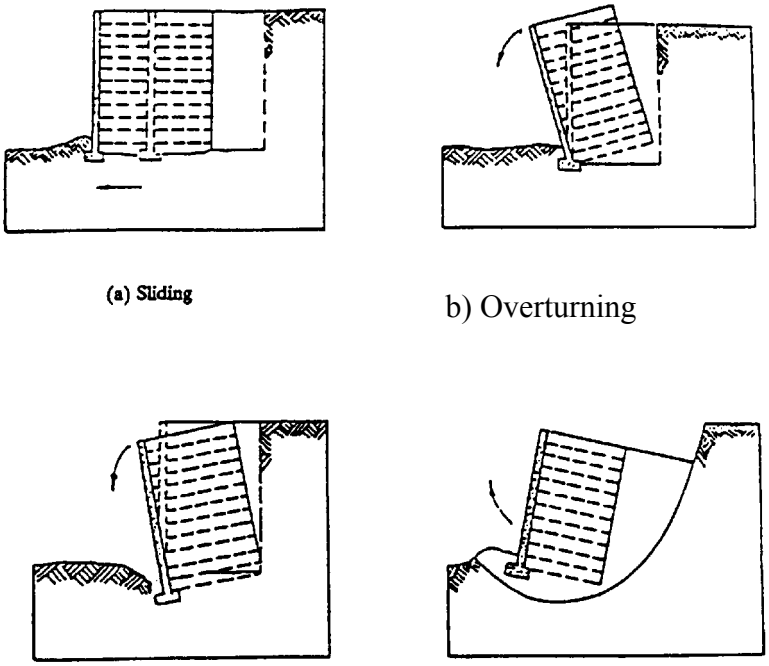

Figure 2.2 External stability design characterizations. (Elias and Christopher, 1997).

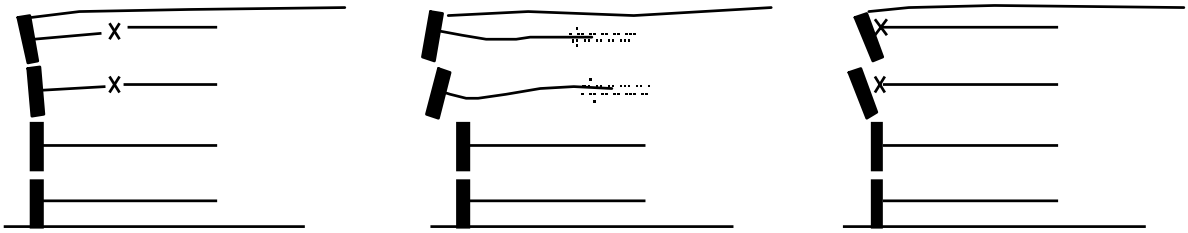

Figure 2.3 Potential failure mechanisms of MSE walls. (a) geogrid breakage; (b) geogrid pullout; and (c) facing connection failure.

Despite its widespread acceptance, the current design practice suffers from several limitations that can be summarized as follows:

1. Most currently-available models do not account for long-term effects in polymers such as creep and degradation. Previous research (Koerner *et al.*, 1992; Leshchinsky *et al.*, 1997) has demonstrated the significance of creep and stress relaxation in geosynthetic. In addition, degradation due to environmental factors such as temperature variation, oxidation, ultraviolet light, and exposure to contaminants can cause a significant reduction in the strength of the geogrid because of an increase in its brittleness.

2. Limit equilibrium methods can describe failure or near-failure conditions, but they do not account for deformations associated with pre-failure conditions, such as wall settlement and creep in the geogrid.

3. Limit equilibrium methods do not account for strain-compatibility of various model components, which is an essential consideration for deformation behavior of the geosynthetic-soil (composite) systems.

4. The interface is inadequately modeled in most current analyses because they do not include the latest findings on pullout and geogrid mechanical properties. In geosynthetic-soil systems, the interface itself plays a pivotal role in the response mainly due to the large difference between the mechanical properties of the soil and the geosynthetic. Therefore, accurate modeling of the interface constitutive behavior becomes as important as that of the soil and the geosynthetic.

Since the procedure for investigation of the external stability of conventional (gravity and cantilever) walls has been well established for decades, the same procedure is typically used for MSE walls. Recently, there has been a strong thrust toward the use of Load and Resistance Factor Design (LRFD) rather than Allowable Stress Design (ASD), in which all the loads are assumed to have the same reliability or variability. For this reason, the factors of safety are not applied to the load combinations considered for either the strength or service limit states (Withiam *et al.*, 1998). In ASD, the factor of safety (FS) is greater than unity. It provides reserve strength in the event that an unusually high load occurs or the resistance is less than expected. For the Service Limit State, the deformations are calculated based on unfactored loads, and these deformations are compared to the maximum tolerable values (Withiam *et al.*, 1998).

Equation 2.1 is the basic equation for LRFD and involves both load factors and resistance factors; for this reason, the design is called Load and Resistance Factor Design (LRFD).

$$\Sigma \phi R_n \geq \Sigma \eta_i \gamma_i Q_i \qquad (2.1)$$

where:

R_n = Nominal Resistance

ϕ = Statistically-based resistance factor

η_i = Load modifier to account for effects of ductility, redundancy and operational importance

γ_i = Statistically-based load factor

Q_i = Load effect

The resistance side (left side) of Eq. 2.1 is multiplied by ϕ, a statistically-based resistance factor, whose value is usually less than one and accounts for factors such as weaker foundation soils than expected, foundation construction materials, i.e., concrete, steel, geosynthetic, or wood, which may not completely meet the specifications; or poor foundation construction (Withiam *et al.*, 1998).

A particular limit state involves a combination of different load types Qi, each with a different degree of predictability. In Eq. 2.1 the different loads, Qi, are multiplied by their respective statistically based load factors, γ_i, whose values are usually greater than one, and will differ in magnitude for different load types.

Uncertainty of material resistance represented by a resistance factor was first investigated by AASHTO in 1989, and LRFD was later approved in 1994. Due to the differences between ASD and LRFD, a workbook on "Load and Resistance Factor Design (LRFD) for Highway Bridge Substructures" was developed by the U.S. Department of Transportation (Withiam *et al.* 1998). A generalized Flow Chart for MSE Wall Design by LRFD (Withiam et al. 1998) is shown in Figure 2.4 .

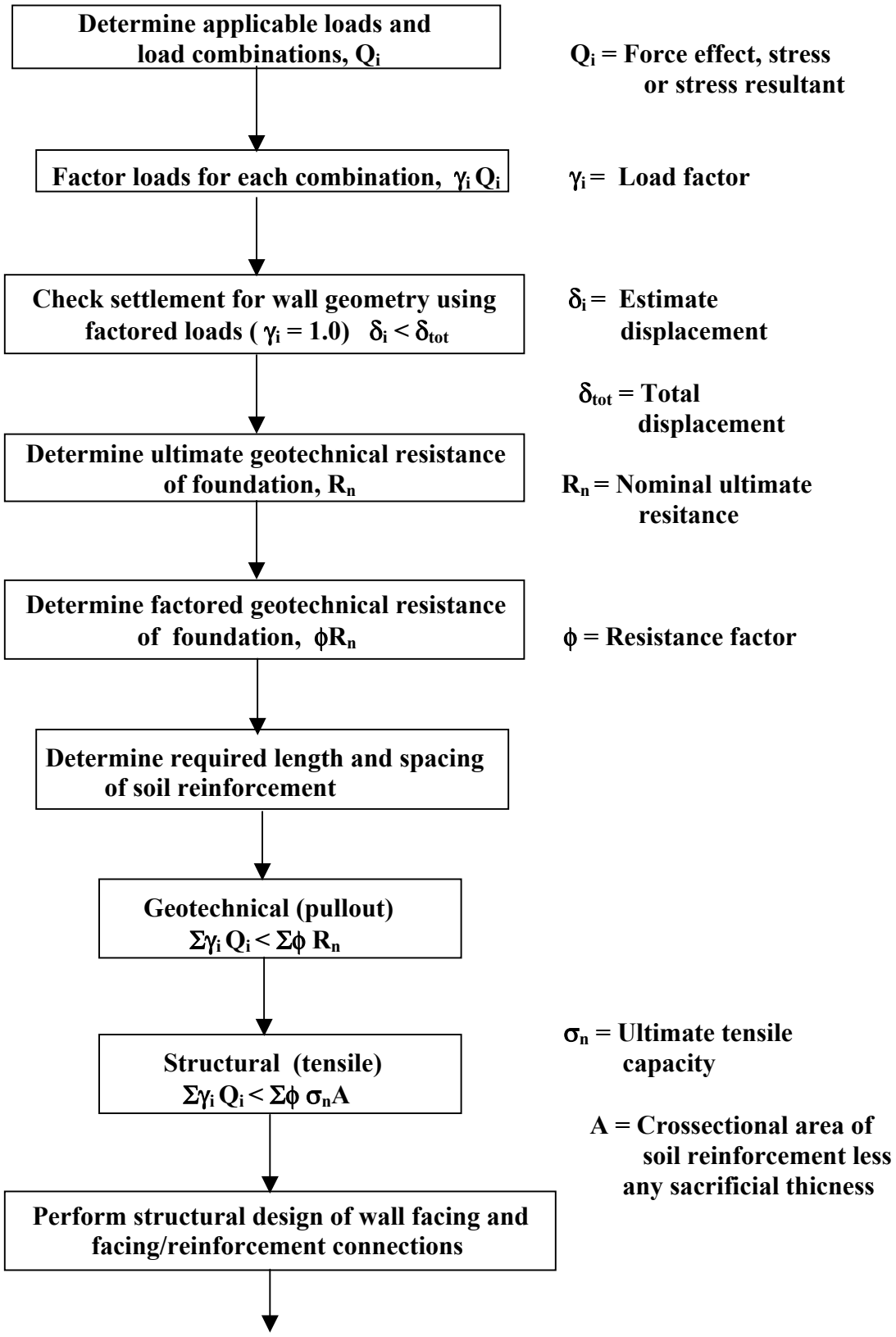
Determine applicable loads and load combinations, Q_i
Q_i = Force effect, stress or stress resultant
Factor loads for each combination, $\gamma_i Q_i$
γ_i = Load factor
Check settlement for wall geometry using factored loads ($\gamma_i = 1.0$) $\delta_i < \delta_{tot}$
δ_i = Estimate displacement
δ_{tot} = Total displacement
Determine ultimate geotechnical resistance of foundation, R_n
R_n = Nominal ultimate resitance
Determine factored geotechnical resistance of foundation, ϕR_n
ϕ = Resistance factor
Determine required length and spacing of soil reinforcement
Geotechnical (pullout)
$\Sigma\gamma_i Q_i < \Sigma\phi R_n$
Structural (tensile)
$\Sigma\gamma_i Q_i < \Sigma\phi \sigma_n A$
σ_n = Ultimate tensile capacity
A = Crossectional area of soil reinforcement less any sacrificial thicness
Perform structural design of wall facing and facing/reinforcement connections

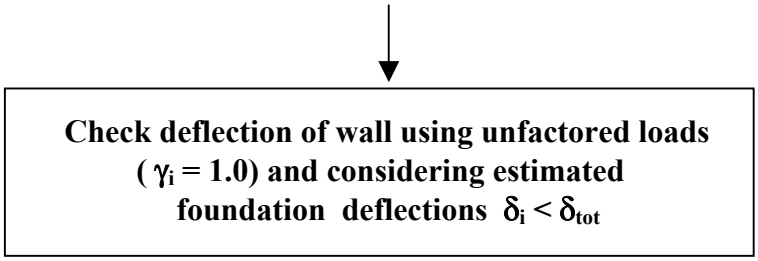

Figure 2.4. Generalized Flow Chart for MSE Wall Design by LRFD, Withiam et al. (1998).

2.3 ANALYTICAL PREDICTION OF MSE WALL PERFORMANCE

Although experimental data are essential for understanding the behavior of engineering systems, due to time and economic limitations, it is often impractical to devise comprehensive analysis and design methodologies based on testing alone. Numerical modeling offers an economical and time-effective alternative to extensive testing. When used in conjunction with experimental studies, numerical analysis leads to the development of a comprehensive design methodology for MSE walls subjected to long-term degradation and creep.

A finite element analysis was developed by Desai and Lightner (1979) to compare model results with field test data from a geogrid earth retaining wall with a precast concrete panel. The computed geogrid strains were smaller than the measured values; therefore, it was concluded that the finite element analysis should be further refined to improve the accuracy. Desai and Lightner (1979) also outlined the areas in which the refinement is needed, i.e. simultaneous construction sequence and nonlinear soil behavior, and interfaces between the soil used for the wall fill and geogrids.

Chua *et al.* (1993) used a program called GEO 2D, which is an updated Lagrangian code that allows large deformations in the soil-fabric system, for predicting the deformation pattern due to pullout forces. Both unsaturated and saturated sand/clay media were addressed, but only with continuum (not poroelastic) elements.

Ho and Rowe (1993) used the finite element program, AFENA, and modified it to allow the modeling of a reinforced soil wall. They concluded that the finite element method is suitable for the analysis of geosynthetic reinforced walls. The results demonstrated that the role of reinforcement in reinforced soils walls is to suppress the horizontal soil strain. Finite element analysis using two-dimensional plain strain formulation has been used to predict the performance of geogrid reinforced backfills by Karpurapu and Bathurst (1995) using a program called GEOFEM.

Soni *et al.* (1996) incorporated a constitutive model developed by Desai *et al.* (1986) in finite element analysis to characterize the stress-strain and volume change behavior of reinforced soils. The results were satisfactory and supported the validity of the model. Arab *et al.* (1998) used the finite element method GOLIATH to model two experimental walls reinforced with a geotextile. This software is appropriate for modeling large deformations of MSE structures. The results were satisfactory until large deformations developed, and some physical phenomena like the "breakpoint" of the surcharge-settlement were observed in the testing. The authors recognized the necessity of taking into account the compaction effect and construction stages.

Biondi *et al.* (2000) built a 4m high vertical retaining wall for testing and analyzed its static behavior with the finite difference program Fast Lagrangian Analysis of Continua

(FLAC); the numerical analysis and the collected data showed good agreement. For the embankment without surcharge, the best fit was obtained using an interface between the reinforcements and the soil with an angle of friction lower than the soil friction angle. On the other hand, in the presence of surcharge , *i.e*. for stress conditions close to failure, the best fit was obtained with an angle of friction greater than the soil's angle of friction. The envelope of maximum tensile strains in the geogrids showed good agreement between the empirical data and the numerical model for an interface angle of friction greater than the soils angle of friction.

Simonini *et al.* (2000) conducted experiments on a small-scale physical model of a retaining wall of medium-fine quartz sand reinforced with polypropylene geogrids and full height metal facings. The experimental study was used to check the capabilities and effectiveness of two numerical codes, i.e. PLAXIS and FLAC, to describe the response of this complex system. PLAXIS is based on the finite element method and FLAC on the finite difference method; both are used widely to solve boundary problems in geotechnical engineering. The authors concluded that the experimental load-vertical displacement curve of the loading plate is affected by an initial bedding error and, once the peak load is reached, a brittle failure develops due to breaking of the reinforcements. On the other hand, for the numerical model, the curves showed more rigidity. This is attributed to the small cohesion introduced to reduce the numerical instabilities. Except for these two aspects, both numerical codes showed remarkably good agreement. For the wall deformation, neither numerical code could reproduce the top reinforcement layer slippage, shown in the physical model. Therefore, it was concluded that the numerical walls were more restrained and moved less than the real wall.

Hatami *et al.* (2000) used the program FLAC to model wrapped-face type walls with two types of reinforcement (non-uniform reinforcement). The reinforcement types and mechanical properties were selected to match alternating polyester geogrids and a woven wire mesh. The results showed that the displacement shape of the wall with alternating reinforcement was similar to one with an average reinforcement stiffness. The results of the analysis also showed that the reinforcement loads and equivalent lateral earth pressure coefficient values for uniform or near-uniform reinforcement schemes were independent of reinforcement stiffness for the same reinforcement spacing.

The numerical modeling program FLAC was also used by Fadzilah *et al.* (2001) to study the response of a 7.1m (22 ft) high modular block faced MSE wall subjected to increasing surcharge loading. The conclusions of their study are very interesting and directly relevant to the experiments discussed in this report. Fadzilah *et al.* (2001) essentially concluded that *"at failure, the maximum tension in the reinforcement was well below its capacity and failures were due to localized instability of the facing"*. This indicates that failure for this wall configuration is not due to pullout or rupture of the reinforcement but due to excessive deflection of the modular block facing. In addition, the design capacity of the reinforcement is not fully mobilized even with high surcharges. It was also found that the tensile modulus of the reinforcement has a significant effect on the amount of load that the wall can carry.

2.4 FIELD EVALUATION (CASE STUDIES)

A comprehensive review of the relevant literature revealed a very large number of available field studies. Case studies published since 1990 are summarized as follows:

i) Construction and testing of a large-scale reinforced soil wall with four layers of relatively weak grids to ensure the failure mode, Bathurst and Benjamin (1990).

ii) Instrumentation of a geogrid-reinforced soil wall, Bathurst (1991).

iii) A review of three instrumented geogrid reinforced soil retaining walls, Simac *et al.* (1991).

iv) Testing of a geogrid reinforced earth retaining wall in Tucson, Arizona with precast concrete wall facing, Fishman and Desai (1991).

v) Stabilization of a bridge embankment in Oregon, and construction of an 18 foot high concrete block wall in Seminole County, Florida, Barrows and Machan (1991).

vi) Stabilizing weathered mudstone slopes in Taiwan, Chang, Chen, and Su (1991).

vii) Load test of a large-scale geotextile-reinforced retaining wall, Billiard and Wu (1991).

viii) Steepened embankment design in Montana Yagen and Barnes. (1991).

ix) Reinforcement of a granular fill to create a large distribution mat for a refinery processing unit in Port Arthur, Texas, Wharton *et al.* (1993).

x) Foundation stabilization of a mechanically stabilized earth wall constructed on an uncontrolled backfilled borrow pit adjacent to the sloping shoreline of a lake in Miami, Florida, Ramos *et al.* (1993).

xi) Retaining walls at the Port Authority's Wando terminal in South Carolina, Kemp *et al.* (1993).

xii) Installation damage testing of four PET geogrids in Venezuela, Sandri *et al.* (1993).

xiii) Construction of a bored modular concrete block mall in Fiesta, TX, Moreno, *et al.* (1993).

xiv) Database of results from an incrementally geogrid-reinforced soil wall test, Bathurst *et al.* (1993).

xv) Case history of a geogrid reinforced retaining wall, constructed with cohesive backfill, that failed, Leonards *et al.* (1994).

xvi) Nationwide experiences with mechanically stabilized structures and native soil backfill, Keller (1995).

xvii) Value engineering replacement of high-strength geotextile with geogrid system for embankment stabilization in New Jersey, Bailey II (1995).

xviii) Behavior of a reinforced earth retaining wall during construction and during static and dynamic surcharge loading with an instrumented test section of 7.30m height, Floss and Thamm (1995).

xix) Full scale experimental study of geotextile reinforced structures as bridge abutments, Gourc *et al.* (1995).

xx) Forensic analysis of the collapse of a 6.7m high geogrid reinforced, Berg and Meyers (1997).

xxi) Field performance testing of a 8m high geosynthetic reinforced wall on soft ground with concrete block facing, Tsukada *et al.* (1998).

xxii) Mechanical performance testing, comprising both static and cyclic loading of two full scale embankments, 3-6m height and 5 x 5m base, reinforced by geotextiles (non-woven and woven), Kharchafi and Dysli (1998).

xxiii) Study of the seismic stability against high seismic loads of geosynthetic-reinforced soil retaining structures, Tatsuoka *et al.* (1998).

xxiv) Experimental and FEM analysis study of large deformations of a reinforced earth structure, Arab *et al.* (1998).

xxv) Experimental and numerical analysis of Small-scale physical model wall reinforced with polypropylene geogrids, Simonini *et al.* (2000).

xxvi) Study of a 4 meter height geogrid reinforced wall and numerical modeling with the software FLAC, Biondi *et al.* (2000).

xxvii) Numerical study of retaining walls with non-uniform reinforcement, Hatami *et al.* (2000).

xxviii) Study of a 7.1m high modular block faced Geosynthetic-reinforced soil (GRS) wall and modeling with the software FLAC, Fadzilah *et al.* (2001).

The FHWA demonstration project for design and construction guidelines for mechanically stabilized earth walls and soil slopes (Elias et al., 1997) is a valuable reference source and is the FHWA's primary guideline. It is comprised of project evaluation,

applications, advantages and disadvantages, relative costs, description of systems, construction sequence, and proprietary aspects.

Since the conditions, materials, and parameters varied significantly among these case studies, it is unreasonable to draw a single conclusion. However, the general lessons learned from these case studies are as follows:

1. The use of cohesive backfill is the main cause of failure and can be detrimental to MSE walls. Well-draining granular material is almost a necessity.

2. No catastrophic failure has been observed in an MSE wall, with the exception of walls subjected to construction errors, such as shorter embedment depth than what the design called for.

3. The use of weak reinforcement layers at small spacing is more beneficial than the use of stronger reinforcement at large spacing.

2.5 PULLOUT STRENGTH

A very important mechanical property of geogrids is the anchorage strength against pullout from the soil, or simply *pullout resistance*. The excellent behavior of geogrids is a result of their large apertures, allowing for soil to strike-through from one side of the geogrid to the other. Eq. 2.2 represents the relationship between the recommended 50 percentile particle size (d_{50}) for a particular geogrid with an aperture B_{gg} (Koerner, 1998).

$$B_{gg} > 3.5\ d_{50} \tag{2.2}$$

Pullout resistance is the result of the following three mechanisms 1) friction or shear strength along the top and bottom of the longitudinal ribs, 2) friction or shear strength along the top and bottom of the transverse ribs, and 3) passive soil resistance against the front of the transverse ribs by means of bearing capacity. It has been analytically shown that this bearing capacity is a major contributor to the pullout resistance of geogrids (Koerner *et al.* 1998). To maintain equilibrium, the bond must resist the maximum tensile load carried by the reinforcing element.

The anchorage strength between soil and geogrid can be determined from a pullout test or direct shear test; the limit shear resistances obtained differ between the two. The pullout resistance can far exceed the direct shear strength obtained by a shear strength test performed between a geogrid and soil (Koerner, 1998). The factors affecting the evaluation of pullout resistance in the laboratory are the type of soil, the geosynthetic material properties, the geometry, and the configuration of the test apparatus (Fannin and Raju, 1991).

Fannin and Raju (1993) performed large scale pullout testing of geogrids and geomembranes embedded in sand. The principal finding was that the interface bond, is dependent on relative displacement between the geosynthetic and the soil, the stiffness of the geosynthetic, and the normal stress acting on it. Raju and Fannin (1995) continued the work using five types of geosynthetics: three geogrids, a smooth geomembrane, and a textured geomembrane. The pullout response of these polymeric materials was compared to that of an inextensible fully rough sheet. The mobilization of pullout resistance was described from measurements of pullout force, displacement of the clamped and embedded ends, strain along the embedded length of the specimen, and lateral stress at the interface of soil and the

retaining plate. Cyclic loading of the test specimen in most cases revealed that the interaction factor mobilized was equal to or slightly exceeded the value mobilized in a corresponding constant loading test.

Chua *et al.* (1993) performed pullout tests on an HDPE geogrid in both sand and clay samples, under both dry and saturated conditions. The results of the tests for sand samples showed a decrease in the pullout strength of the geogrid due to wetting, achieving 0.57 times the strength in dry conditions. Clay samples showed a relatively lesser decrease in the pullout strength of the geogrid under saturated conditions, *i.e.* 81 % of the dry pullout strength.

Farrag *et al.* (1993), conducted a pullout testing program on HDPE geogrids to develop reliable testing procedures and interpretation schemes for the evaluation of the short-term and long-term pullout performance of geosynthetic reinforcements. The important conclusions drawn were: 1) increased thickness of the soil cushioning the geosynthetic decreases the effects of top and bottom boundaries; a thickness of at least 0.3m above and below the geogrid is recommended to eliminate the influence of these boundaries; 2) the displacement rate effects are minimized if a rate less than 6mm/min is used.

Pullout testing of HDPE geogrids aimed to evaluate the functional relationship between soil water content and the interface frictional parameters depending on soil type, density, and the confining pressure was carried out by Farrag *et al.* (1995). Pullout tests were performed on HDPE geogrid specimens in two different types of cohesive soils at optimum moisture content and higher levels of moisture content for the Modified Proctor test, (AASHTO T-180). Pullout tests were performed immediately after applying the confining pressure, and the results represented essentially unconsolidated-undrained test conditions.

The pullout rate was 2 mm/min and the confining stress was 48.2 kN/m^2. The pore water pressure at the interface of the geogrid and the soil was measured during pullout by a vibrating wire piezometer. The results indicated that an increase in the soil water content causes a decrease in the pullout resistance. Such an effect is due to soil slippage along the geogrid interface in wet soils and the development of pore water pressure at the interface when the soil is saturated. In addition, the results showed an increase in the effective stress due to the dissipation of water pressure when shear strains were fully mobilized.

Bolt and Duszynska (2000) carried out thirty pullout experiments on biaxial polypropylene geogrid embedded in coarse sand. The findings were as follows: a) an increase in the normal pressure causes a significant increase in the pullout resistance; b) an increase in soil density leads to larger soil and soil-geogrid shear resistance, reducing the geogrid displacement and increasing the interface stiffness modulus and the pullout resistance; c) the displacement rate has a negligible effect, however, the higher the displacement rate, the larger the pullout resistance; d) a decrease in specimen width causes a small increase in pullout resistance. Additionally the pullout was achieved at relatively larger values of displacement; and e) the larger the anchoring length, the better the soil-reinforcement interaction. It was also found that an important factor influencing the soil-reinforcement interaction is the deformability of the geogrid.

Floss *et al.* (2000) conducted pullout tests for different geogrids and a full scale model test of a two layer miniature steep slope (MSS). The results showed clear differences depending on the soil and type of geogrid. The woven geogrids had approximately half the maximum pullout resistance of the extruded and the laid geogrids, even though the three

geogrids have the same tensile strength. Also the overall comparison with an unreinforced slope showed the high reserves of bearing capacity of geosynthetic reinforced systems which also has the advantage of undergoing failure by partial breakage of the geosynthetic instead of brittle catastrophic failures encountered in conventional retaining wall systems. Finally, the high levels of loading (up to 1500 kPa) in the MSS test are in agreement with the field loading tests performed by Brau and Floss (2000).

Pullout testing was also carried out by Gao (1999) under the supervision of this report's author, Dr. D.V. Reddy of Florida Atlantic University (FAU). It was found that under the same pullout load, soil, and testing conditions, the HDPE geogrid experienced a smaller strain than the PET geogrid at all four gage locations. This was attributed to the fact that the HDPE geogrid is made of stiff low-creep-sensitivity polymers and has a relatively higher modulus of elasticity compared to the PET geogrid. The PET geogrid, on the other hand, displayed a very uniform deformation capacity. The pullout transferred evenly all the way to the back end of the geogrid. During the pullout process, the movement of the test specimen was very smooth while the pullout characteristic pattern of the HDPE geogrid demonstrated some degree of discontinuity. Gao (1999) attributed this result to the high stiffness and specific profile of the HDPE geogrid.

The geometric differences in the HDPE and PET geogrids resulted in a difference in performance based on the surrounding soil. For the PET geogrid, the open area was relatively small without much protruding contour. Therefore, the pullout resistance derived from interface friction takes most of the pullout load. On the other hand, for the HDPE geogrid, the bearing resistance component is the main component resisting pullout. The HDPE geogrid,

under unsaturated working conditions, had sliding coefficients of 1.05 and 1.02 for limerock and sand, respectively. In contrast, , the sliding coefficients for the PET geogrid against limerock and sand were 1.08 and 1.12, respectively.

Based on the tests and theoretical analysis, Gao (1999) concluded that under unsaturated working conditions, the PET geogrid has better pullout resistance performance than the HDPE geogrid, when used in sand. Because fine sand can provide more contact surface, a larger friction resistance is mobilized. On the other hand, in limerock which is a coarser material with good gradation, the HDPE geogrid is the better choice.

For a PET geogrid in limerock, the sliding coefficient was 1.08 under the unsaturated testing condition and 0.669 under the saturated condition. This difference corresponds to a 38.1% reduction due to the wetting effect. Similarly, the sliding coefficient for test specimen PET in sand was 1.12 in the unsaturated condition and 0.688 under saturated condition. From the test results it can be inferred that the wetting condition causes a 38.6% decrease in the resistance. For HDPE in limerock, the sliding coefficient was 1.05 in the unsaturated condition and 0.758 under the saturated condition. The decrease was only 27.8%. In sand, the sliding coefficient was 1.02 under the unsaturated condition, and 0.729 under the saturated condition, corresponding to a 28.5% reduction. It was concluded that saturation had more impact on fine sand than coarse sand. The reduction in sliding coefficient was larger for the PET geogrid than the HDPE geogrid. This is because the friction resistance was subjected to a greater loss due to saturation, and the bearing resistance was marginal.

3 CONSTITUTIVE PROPERTIES OF MSE SYSTEM

All mechanically stabilized earth systems consist of two materials, namely the soil and the reinforcement (geosynthetic). From a design and analysis standpoint, three components affect the mechanical behavior of the system: the soil, the reinforcement, and the interface. It is, therefore, essential to characterize all the relevant properties or design parameters of such components through laboratory or field testing in order to provide reliable designs.

Because of the large number of properties needed to be determined, it is more reasonable to first evaluate the relative influence of individual system components (soil, geosynthetic, and interface) on the overall response of the MSE system. In this Chapter, parametric studies will be carried out through analytical and numerical simulations to examine the contributions of the various system components. Properties deemed to have an insignificant effect on the response need not be tested, while more effort could be diverted toward accurate quantification of important system properties. The analyses are based on data and results available from earlier studies on pullout of geosynthetics.

3.1 NUMERICAL SIMULATION OF PULLOUT EXPERIMENTS

A series of geogrid pullout experiments were performed by Gao (1999) as part of an earlier study. Because of the similarity in soil and geogrid materials to the present study, it was decided to perform numerical simulations of the pullout experiments, with the goal in mind to calibrate the properties of the materials and interface. Once a match is established between experimental and numerical results, the model parameters can be used in numerical simulations of the wall. Details of the materials and test conditions can be found in Gao

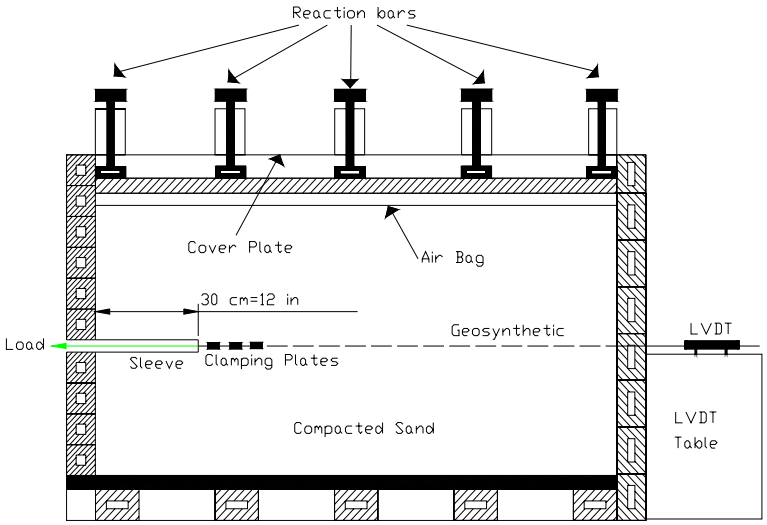

Figure 3.1. Schematic of the pullout box.

(1999). Two geogrid types were used: Tensar 1600 High Density Polyethylene (HDPE) and Matrex 60 Polyester (PET), and were tested against both limerock and sand. Since the MSE walls in the present study are constructed of sand, only the sand pullout data is used in the analysis. Figure 3.1 represents a schematic of the pullout apparatus.

The numerical simulations were carried out using the software package FLAC (Fast Lagrangian Analysis of Continua) Version 3.3. The software provides a finite difference based solution to continuum problems, and has the advantage of simulating transient and dynamic conditions such as large deformations leading to collapse and failure. The analysis sequence consisted of a preliminary analysis, first conducted with the HDPE-1600 geogrid in the unsaturated soil conditions. The properties used in the analysis were obtained from Gao (1999) and from the geosynthetics manufacturers. The output from this analysis was compared with the experimental results obtained from FAU. The main purpose of the

preliminary study was to calibrate the system properties and to examine the influence of the geogrid modulus and the angle of friction between the soil and the geogrid. From the study, it was possible to define: a) the accurate value of the geogrid modulus used in the research done by FAU, and b) the accurate value of the angle of friction between the soil and the geogrid. This last parameter is considered very important because the values back calculated from the pullout analysis are used later (Chapter 4) in the analysis of the MSE wall. A similar analysis was conducted on the PET (Matrex 60) geogrid.

Once the results obtained in FLAC were matched to those obtained by FAU, the HDPE-1600 geogrid was taken again as the baseline case with the new (calibrated) values for the angle of friction (soil-geogrid) and the geogrid modulus. This "new" baseline case was studied further by varying certain properties of the model such as boundary conditions, size of the pullout box, modulus of elasticity of the geogrid, angle of friction soil-geogrid, soil modulus, and normal/shear stiffness. The results of this parametric analysis are used to establish the level of relevance or importance of the various system parameters.

3.1.1 DESCRIPTION OF THE PROGRAM INPUT

An initial grid (mesh) of 40×17 elements was generated with the Mohr-Coulomb Model assigned to all the elements (zones). The *null* model was used to remove one row in the mid-height of the mesh, thus obtaining two different regions. The purpose of this was to create an open space for placing the geogrid, and to define the interface between the soil and the geogrid on both sides (top and bottom). The geometry of the boundaries was then defined to assign the actual coordinates to the box, and to close the gap at the interface (Fig 3.2).

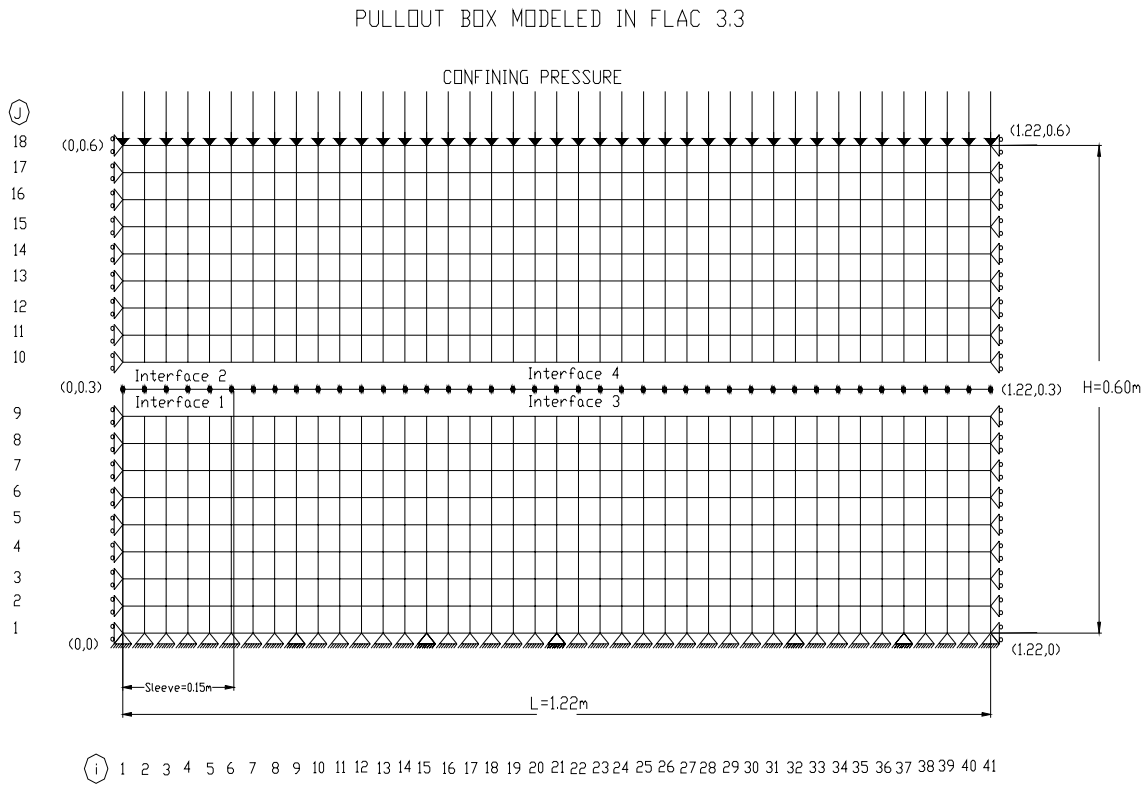

Figure 3.2. Schematic of the FLAC mesh used to model the pullout experiments.

A flexible beam structure was considered to simulate the geogrid. To this end, the nodes of the geogrid were defined along the entire width of the original model. Then, the interfaces between soil and geogrid on both faces of the geogrid were generated (refer to Fig. 3.2). The first two interfaces (Interfaces one and two) represent the zone where the metal sleeve of the pullout box is located. This sleeve is used to minimize the passive pressure that develops at the front boundary of the box and thus reduces its influence on the pullout resistance. The angle of friction for this zone is zero, because the geogrid and the soil are not in contact.

Interfaces three and four represent the region where the geogrid and the soil are in contact along the top and bottom faces of the geogrid. An interface friction angle value was initially assumed in the preliminary analysis, as will be discussed later. Then, once the model parameters were calibrated, the accurate value of the interface friction was used in the analysis of the MSE wall. Initial values of normal stiffness (k_n) and shear stiffness (k_s) were also calculated and assigned to the four interfaces.

The boundary conditions for the vertical sides were assumed to be fixed in the horizontal (x) direction, and the bottom boundary was fixed on both (x) and (y) directions. The effects of the boundary conditions will also be studied later. Before applying the constant normal pressure at the top and the pullout load on to the geogrid, the system was brought to equilibrium under gravity in order to obtain the initial stresses in the system. This equilibrium condition was saved and retrieved later in subsequent analyses. The displacements in both (x) and (y) directions were then set to zero.

After establishing equilibrium of the system, the normal pressure was applied to the top, and the model was solved again. Then, increments for the pullout load were applied subsequently, and the corresponding stresses and strains were calculated for each increment of load.

3.1.2 PROPERTIES USED IN THE NUMERICAL MODEL

The initial parameters chosen to simulate the pullout tests were obtained from Gao (1999). Two types of geogrids and two types of soil under saturated and unsaturated conditions were used. However, because the full scale and small scale walls were to be

constructed using unsaturated sand, only this material was simulated in the numerical study. The parameters used in the numerical model are listed next.

Soil properties (Unsaturated Florida Sand)

1. Density	1560 kg/m^3	97.3 pcf
2. Modulus of elasticity	30000 kN/m^2	4350 psi
3. Poisson's ratio (ν)	0.3	
4. Friction angle	36°	
5. Shear modulus (G)	1.15×10^4 kN/m^2	1670 psi
6. Bulk modulus (B)	5×10^4 kN/m^2	7240 psi

The values of Poisson's ratio and modulus of elasticity were obtained from Das (1994) for sands with the corresponding density. The shear and bulk moduli were computed from the following equations:

$$G = \frac{E}{2(1+\nu)} \tag{3.1}$$

$$B = \frac{E}{3(1-2\nu)} \tag{3.2}$$

Geogrid properties. The types of geogrids used are UX-1600 SB (HDPE) and PET (Matex-60) with the following properties, corresponding to manufacturers' data:

HDPE geogrid

1. Modulus of elasticity (E)	1.05×10^6 kN/m^2	150,000 psi

2. Area(A)	0.0018 m^2	2.8 in^2
3. Moment of inertia (I)	4.9×10^{-10} m^4	1.2×10^{-3} in^4

PET geogrid

1. Modulus of elasticity (E)	5.8×10^{6} kN/m^2	900,000 psi
2. Area (A)	0.0018 m^2	2.8 in^2
3. Moment of inertia (I)	4.9×10^{-10} m^4	1.2×10^{-3} in^4

The area is calculated as the equivalent area per unit width of the geogrid, and the modulus of elasticity is equal to the tensile modulus of the geogrid (kN/m) divided by the thickness.

Angle of interface friction of soil/geogrid (δ). This value was calculated from the following equations to obtain an approximate value for preliminary analysis:

$$T_{max} = 2\,\tau_{max} \times A \tag{3.3}$$

$$\tau_{max} = \sigma_v \tan(\delta) \tag{3.4}$$

where:

T_{max}= maximum pullout load applied in the geogrid

τ_{max}= maximum shear stress applied in the geogrid

A= area of the geogrid along top and bottom faces (length of the pullout box × unit length)

σ_v= Confining pressure

δ= Angle of friction between soil and geogrid

Based on the experimental pullout data, the angle of friction (δ) was found to be 28.4 degrees for both types of geogrids.

Normal stiffness and shear stiffness. These values (k_n and k_s) were calculated based on the procedure outlined in the FLAC manual, whereby k_n and k_s are set to ten times the equivalent stiffness of the stiffest neighboring zone. The equivalent stiffness of a zone in the normal direction is:

$$Equivalent\ stiffness = \max\left[\left(\frac{K+\frac{4}{3}G}{\Delta_{z\min}}\right)\right] \tag{3.5}$$

where:

K= bulk modulus

G= Shear modulus

Δ_{zmin}= Smallest width of an adjoining zone in the normal direction

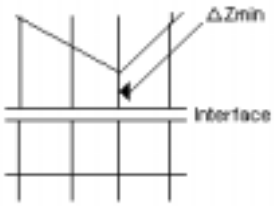

The value for the normal and shear stiffness obtained from this equation is 1.4×10^{10} N/m.

Confining pressure and pullout load values. The confining pressure value is 41 KPa, and the increments of pullout load are: 5.7 KN/m, 15.7 KN/m, 31.3 KN/m, 45.6 KN/m and 54 KN/m. These values conform to the experimental procedure used by FAU.

Dimensions of the model. The dimensions of the pullout box are 1.22 m length by 0.6 m width. Later in this Chapter, the effect of box dimensions on the results is presented.

3.2 PRELIMINARY ANALYSIS FOR THE HDPE 1600 GEOGRID

Detailed calculations related to the preliminary analysis of the HDPE 1600 Geogrid are given in Appendix A. Figure 3.3 shows the comparison between the results obtained by FAU, and FLAC modeling. As can be observed in the experimental results, the strain is constant up to 0.15 m from the front wall. This is because the first 0.15 m represents the sleeve, where no contact exists between the geogrid and the soil. The difference between experiment and simulation in the maximum strain value is a result of the error in the preliminary value assigned to the geogrid modulus. On the other hand, the angle of friction between soil and geogrid affects the slope of the curve.

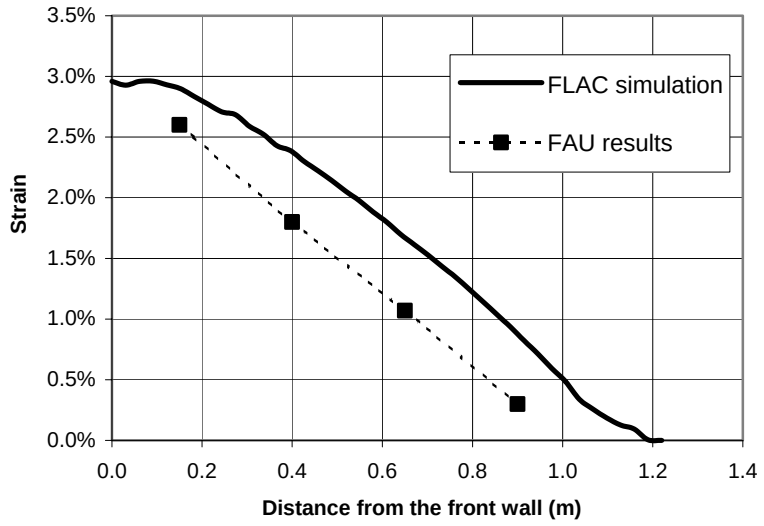

Figure 3.3. Comparison of HDPE geogrid strains: FAU testing vs FLAC modeling

In order to match the maximum strain value, the geogrid modulus was varied until the maximum strain value values in the FLAC model and the FAU analysis were equal (Fig. 3.4). Following this, the angle of friction between the soil and geogrid was varied until a match was obtained with the FAU data (Fig 3.5). As can be seen in Figs. 3.4 and 3.5, a modulus of elasticity of 1.13×10^{9} Pa and a friction angle of 35° gave the closest match.

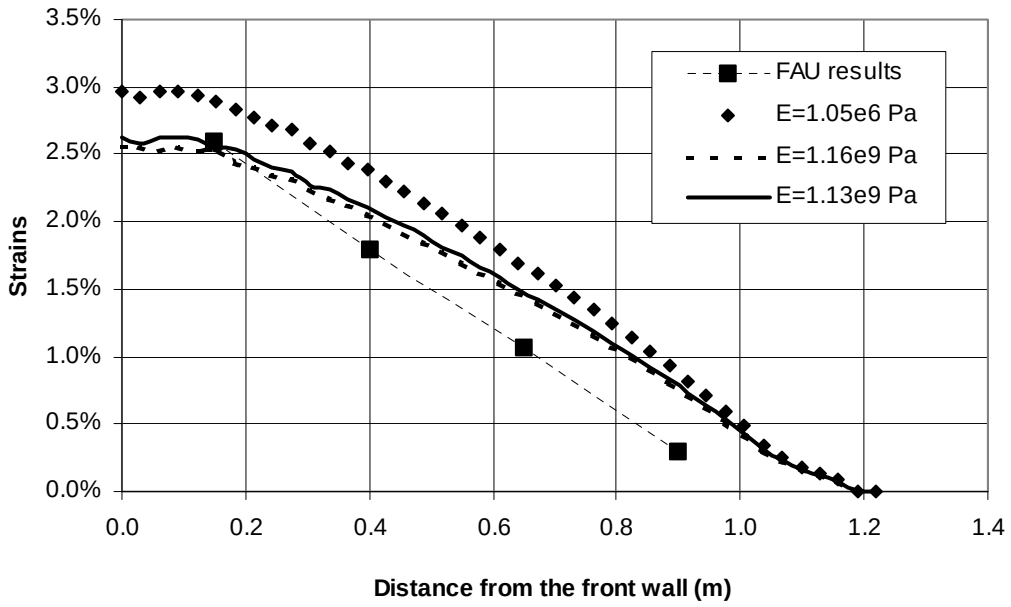

Figure 3.4. Influence of geogrid modulus on the geogrid strains.

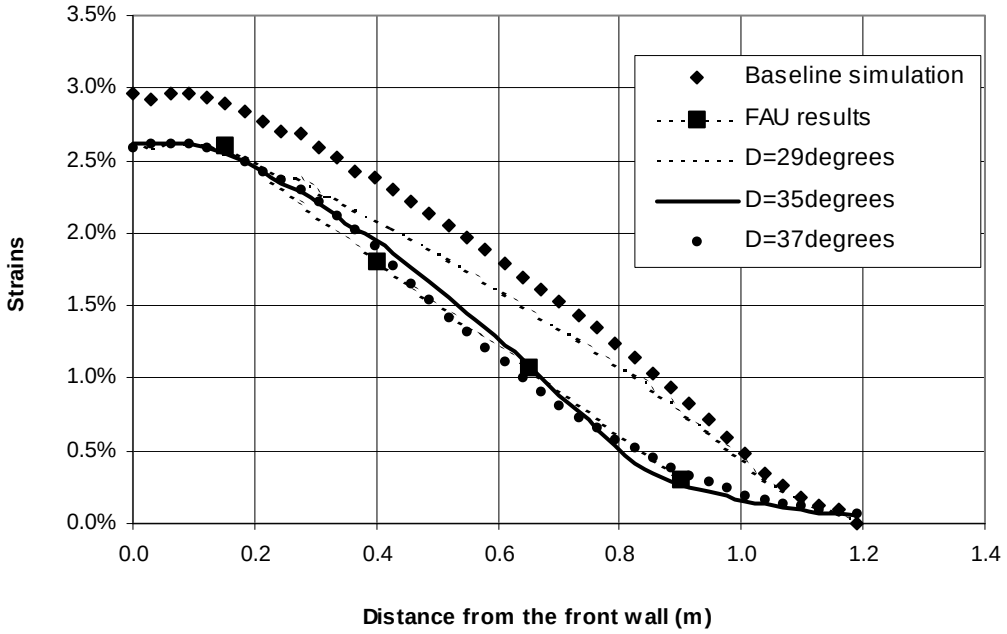

Figure 3.5. Influence of interface friction angle on the strain along the geogrid.

Taking into consideration the above analysis, a new baseline case was established according to the best matching parameters. This new baseline will be used from this point forward, with an angle of interface friction of 35° and a modulus of elasticity of the geogrid of 1.13×10^{9} Pa. Figure 3.6 shows a comparison between the new baseline simulation and the experimental data.

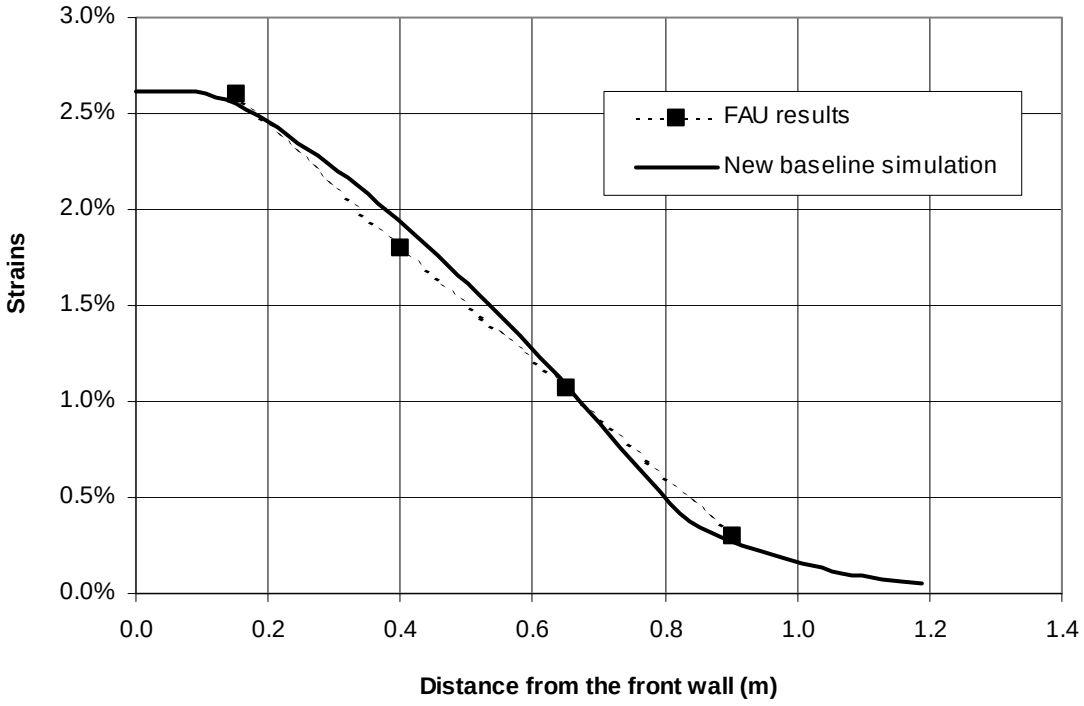

Figure 3.6. Comparison between FAU results and baseline simulation used the modified geogrid and interface parameters.

3.2.1 DISPLACEMENTS AND STRESSES

Figures 3.7 through 3.12 show the displacement and stress fields corresponding to the new baseline simulation.

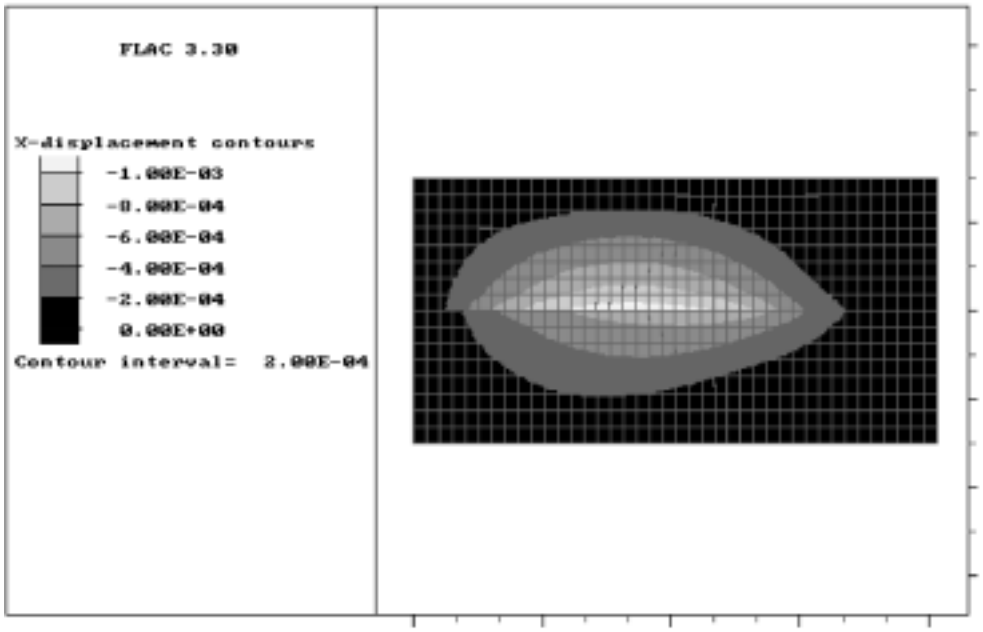

Figure 3.7. Horizontal (x) displacements in the soil in meters

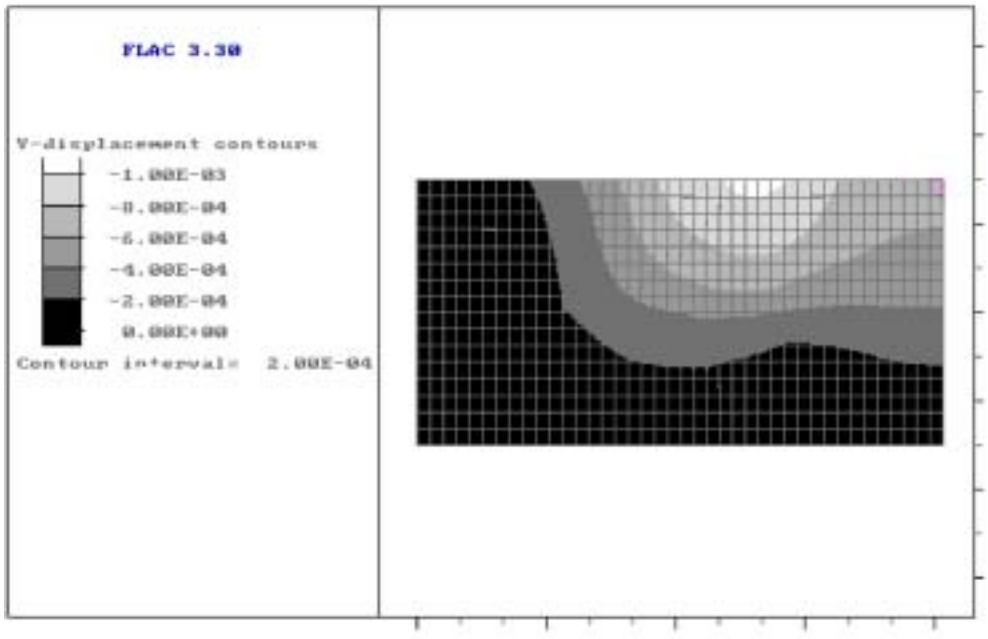

Figure 3.8. Vertical (y) displacements in the soil in meters

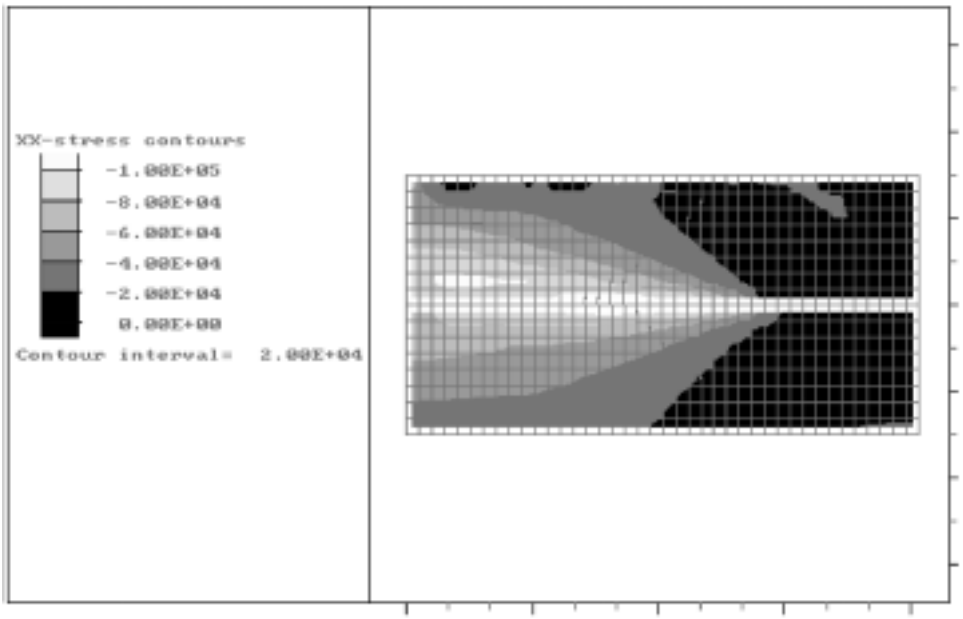

Figure 3.9. Horizontal (x) stresses in the soil in Pascals.

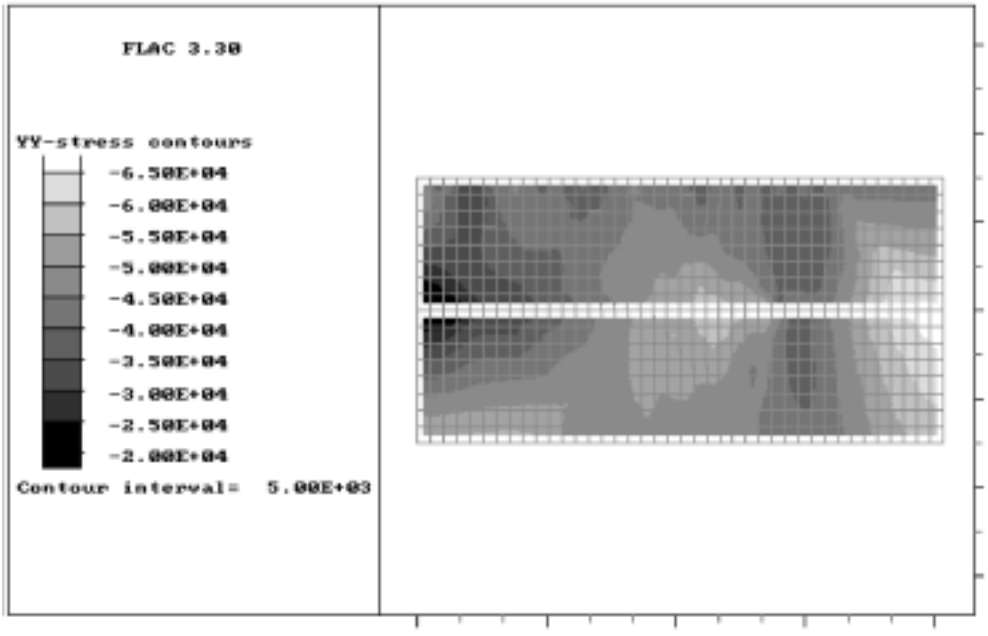

Figure 3.10. Vertical (y) stresses in the soil in Pascals.

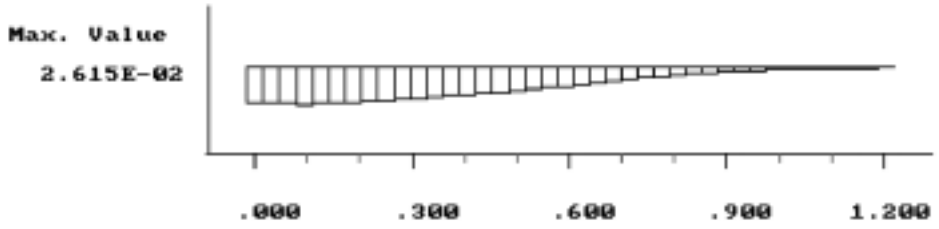

Figure 3.11. Strains along the geogrid at the onset of pullout

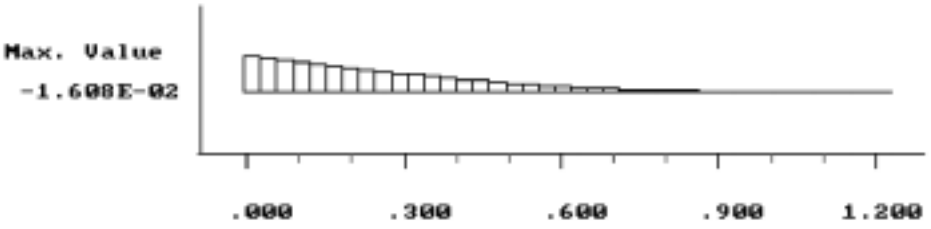

Figure 3.12. Horizontal (x) displacements in the geogrid in meters.

Based on Figs. 3.7 through 3.12, it can be concluded that the maximum x-displacements in the soil occurs in the zones that are nearest to the geogrid. The x-displacements decrease with increasing distance from the geogrid. These results are rational, as the maximum displacements must occur in those zones which are displaced by the pullout load. The y-displacements are large in the top right region and decrease with depth. The large y-displacements to the right side increase as the pullout load increases.

The maximum x-stresses occur in the zones that are near the sleeve and decrease with distance away from the sleeve, while the maximum y-stresses occur at the end of the geogrid, in the zones that are farther from the pullout load. Smaller y-stresses occur in the zones where the pullout load is applied. These results are consistent with the y-displacement pattern. The strains and x-displacement in the geogrid are largest near the sleeve and decrease as a function

of distance. The numerical analysis patterns of strains along the geogrid are in agreement with the experimental results.

3.3 PRELIMINARY ANALYSIS FOR THE PET (MATREX 60) GEOGRID

This analysis was conducted in the same manner as for the HDPE geogrid. The plots, shown in Figs. 3.13 and 3.14 are very similar in trend to the HDPE geogrid case. The most important conclusion from the PET geogrid analysis is that the angle of friction that best matches the results obtained by FAU is 35°. This value of angle of friction will be used as a new baseline in the analysis of PET MSE walls.

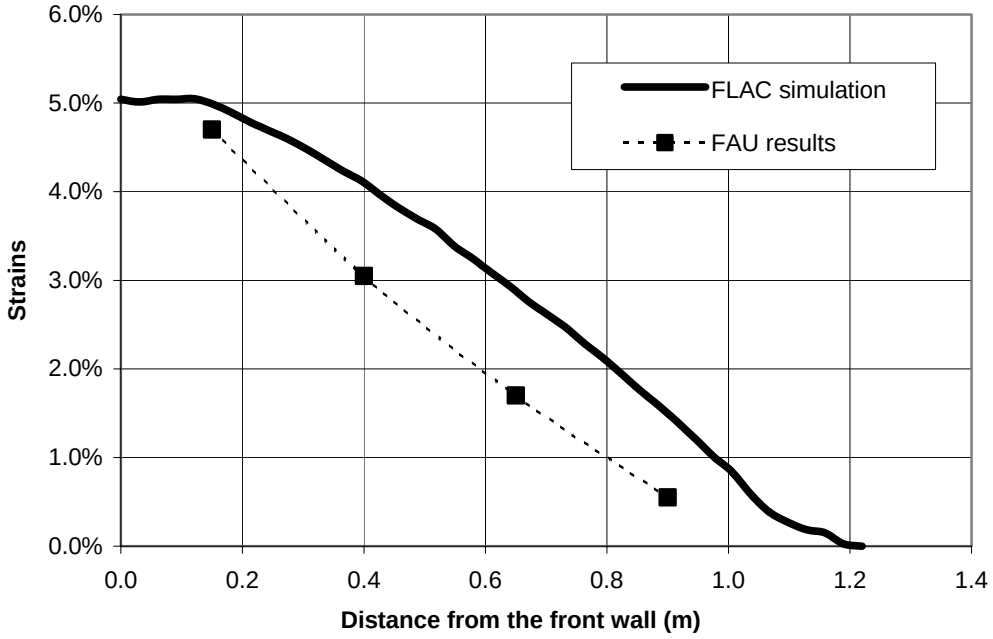

Figure 3.13. Comparison of PET geogrid strains: FAU testing vs FLAC modeling

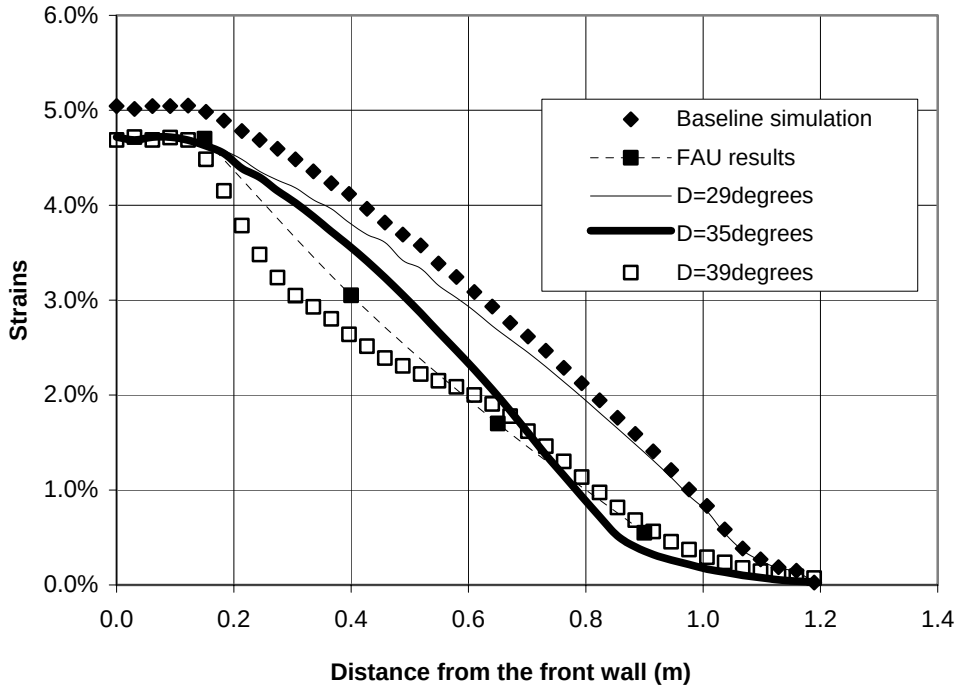

Figure 3.14. Influence of interface friction angle on the strain along the geogrid.

3.4 PARAMETRIC ANALYSIS OF THE PULLOUT EXPERIMENTS

Parametric studies were performed with the new baseline parameters to examine how the various system parameters affect the strain distribution along the geogrid. Since the baseline parameters were similar for both geogrid types, the parameters were varied around the new baseline values for both HDPE and PET geogrids. The conditions varied in the model were: geogrid modulus, angle of friction at interface, boundary conditions, size of the pullout box, soil modulus, and shear/normal stiffness. Figures 3.15 through 3.20 show the results for these different analyses.

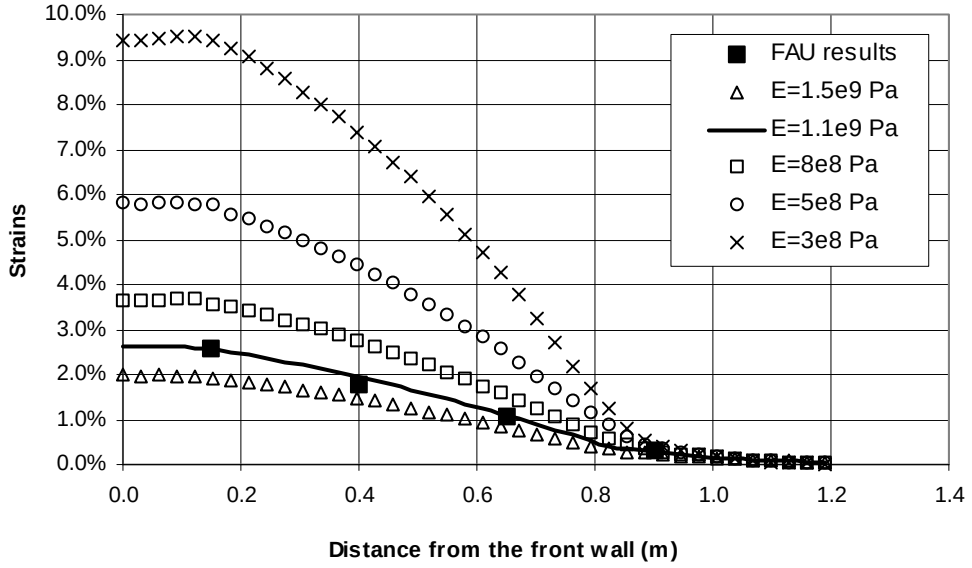

Figure 3.15. Influence of geogrid modulus on the strains along the geogrid

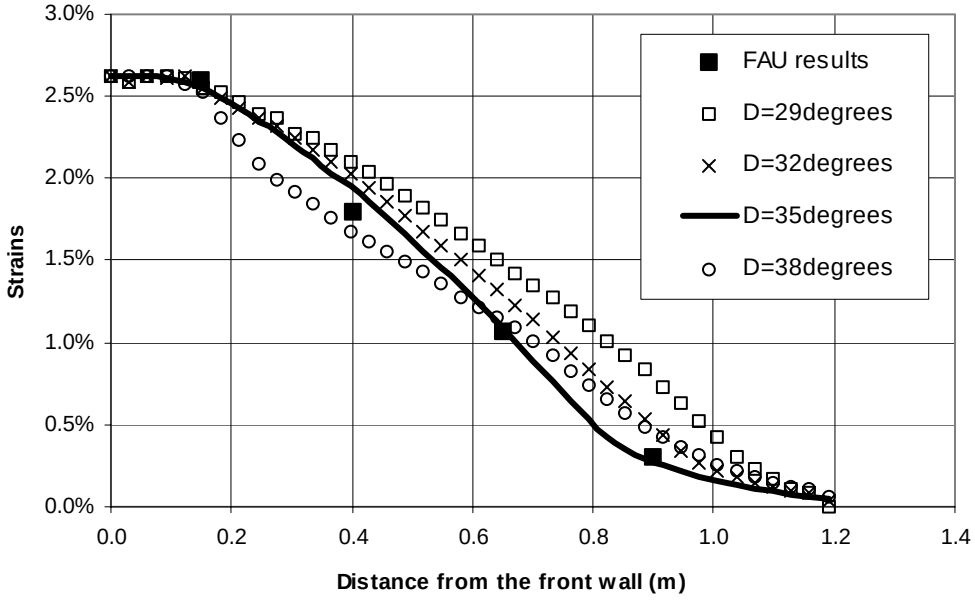

Figure 3.16. Effect of angle of friction at the interface on the geogrid strain

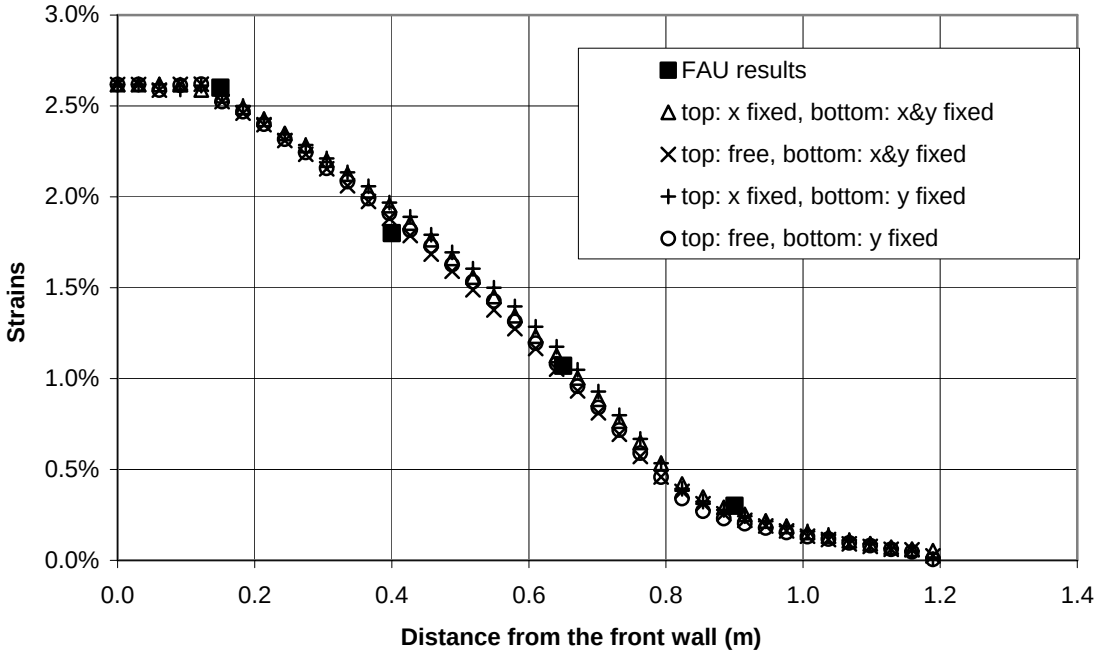

Figure 3.17. Effect of boundary conditions on the geogrid strain

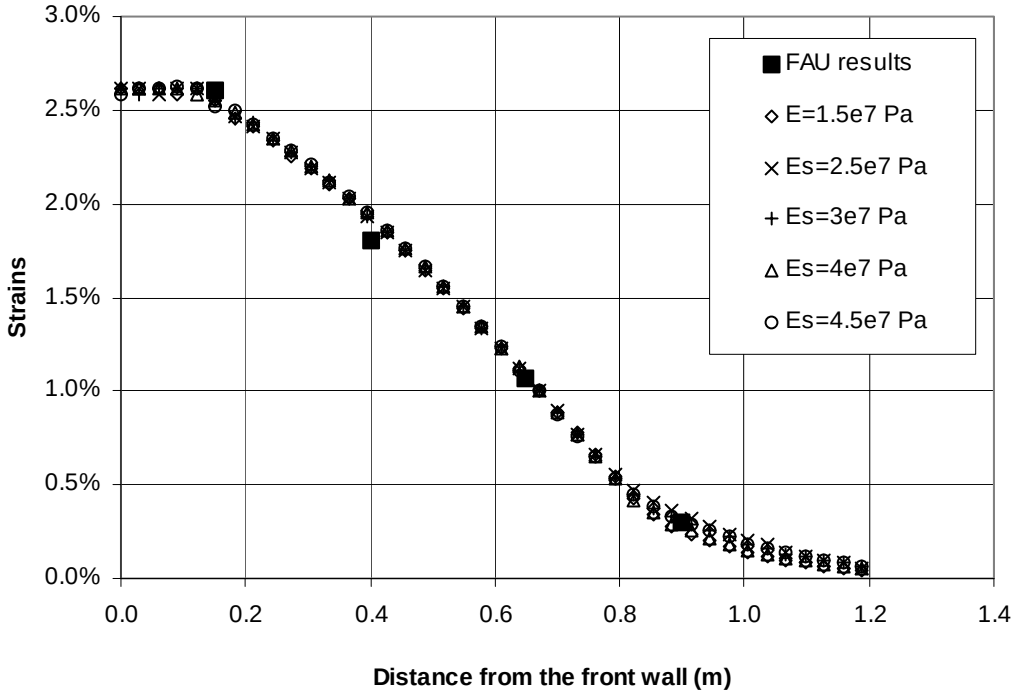

Figure 3.18. Effect of the soil modulus on the geogrid strain

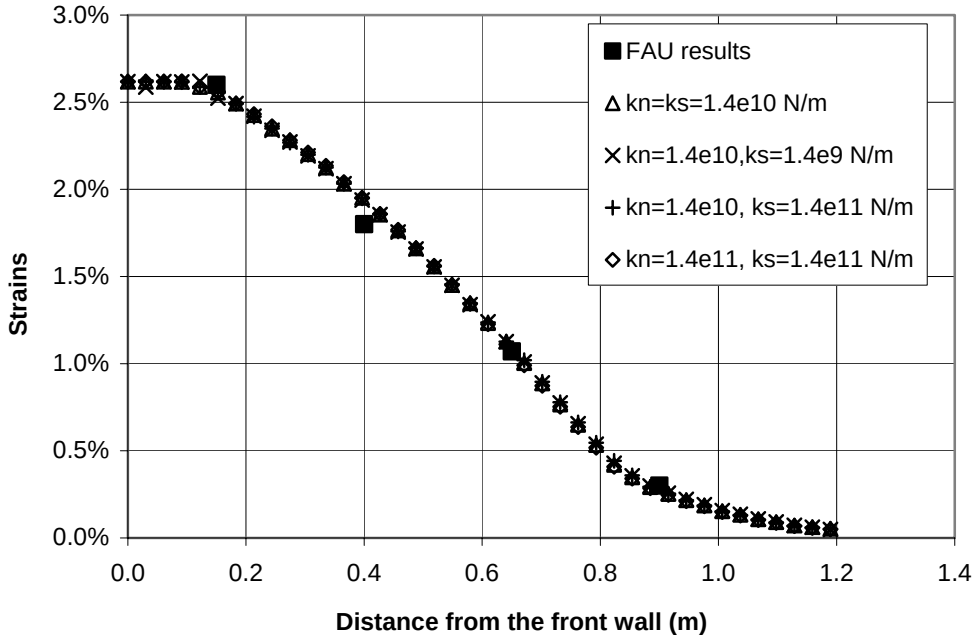

Figure 3.19. Effect of the normal and shear interface stiffness on the geogrid strain

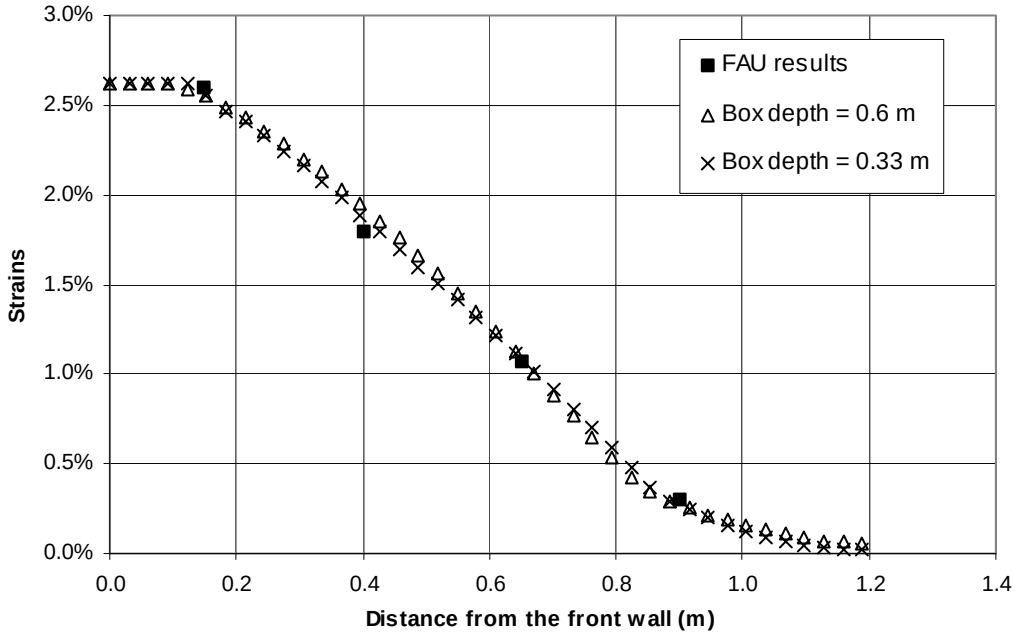

Figure 3.20. Effect of the size of the pullout box on geogrid strain

From the results presented in Figures 3.15 through 3.20, it can be concluded that the geogrid modulus has a profound influence on the strains along the geogrid, even at the far end of the box, where small deformations are anticipated. However, the location most affected by changes in the geogrid modulus is close to the front (loaded end) of the geogrid. On the other hand, the angle of friction at the interface affects the distribution of strains along the geogrid. The higher the interface friction angle, the sharper the difference in strains along the geogrid. At lower interface friction angles, the far end of the geogrid undergoes higher strains compared to high interface friction angles.

It is important to notice in Fig. 3.16 (and earlier from Fig. 3.5 and 3.14) that the interface friction angle that most closely replicates the experimental data for both geogrids is 35 or 36 degrees, which is equal to the internal friction angle of the soil (φ). This is a clear indication that full interaction occurs along the interface due to the high interlocking between the soil and the geogrid. In other words, because of this strong interaction, large passive forces develop along the transverse geogrid ribs and failure occurs in the soil near the interface zone, with no distinct slippage along the soil-geogrid interface.

Other findings from Figs. 3.15 through 3.20 confirm that changes in boundary conditions of the model do not considerably affect the results. The same applies to the soil modulus, when changed within an acceptable range of values. The normal and shear stiffness along the interface has virtually no effect on the geogrid strains, even when varied by an order of magnitude. Similarly, the size of the pullout box doesn't have a significant impact on the results.

3.5 SUMMARY OF PULLOUT ANALYSIS

A preliminary analysis was performed for the HDPE and PET geogrids to determine the accurate values for the angle of friction between the soil and the geogrids. These values will be use for the MSE wall analysis. The interface friction angle that gave the best match with the experimental results was almost equal to the internal friction angle of the soil, which indicates an intimate contact and strong interlocking between the soil and the geogrids. The analyses concluded that the main properties that affect the results in the model are the geogrid modulus and the angle of friction at the interface. Changes in the boundary conditions, normal/shear interface stiffness, soil modulus and size of the pullout box, within a typical (reasonable) range of values, were all deemed to have insignificant effects on the results.

4 CREEP MODELING

4.1 INTRODUCTION

Creep, a physical phenomenon occurring in most materials and particularly in polymers, is the deformation of the material as a function of time under constant load. Creep is a material, load, temperature, and time-dependent phenomenon. Although creep occurs under tensile, compression, torsion, and flexure conditions, tensile creep is the only deformation of interest in geogrids since they are subjected to mostly tension.

Creep is of primary importance in the design of geosynthetic reinforced structures (Allen 1991). The work performed by Leshchinsky et al. (2000) and cited in Chapter 2 (Literature Review) also highlights the importance of creep in MSE wall systems, and outlines relevant procedures for testing HDPE and PET geogrids. Their research work allowed the development of rheological models proposed by Sawicki et al. (1998) to predict creep behavior for HDPE and PET geogrids at low stress levels. The experimental results of Leshchinsky et al. (2000) and Cazzuffi et al. (1997) showed creep plots (strain vs log time) very similar in trend to the creep data analyzed later in this report.

The different models proposed in the majority of the papers found in the literature review showed the necessity to develop creep models that can define creep behavior of geosynthetics at high stress levels and after yielding. The scope of this report was to develop such a model to predict creep behavior for HDPE and PET geogrids, taking into account temperature and stress level conditions.

The data utilized in this analysis were provided through previous experimental work developed by the main author and his co-workers (Reddy et al., 1999; Reddy, 2000; Reddy et al., 2000). Creep tests were performed on HDPE (UX-1600 SB), and PET (Matrex-30) geogrids (see properties in Table 4.1) submerged in different chemical solutions. The purpose of this work was to model the mechanical characteristics of geogrids exposed to typical construction soils and environmental conditions in Florida. The solutions utilized in the experimental creep tests were: phosphate (pH 4.5), calcareous (pH 9.0), seawater, limerock and water (only for PET specimens).

Table 4.1 Properties of the geogrids utilized in creep tests

Property	**HDPE UX-1400**	**PET Matrex-30**
Tensile modulus	737.7 kN/m	780 kN/m
Thickness of geogrid	0.001 m	0.001 m
Area	0.001 m^2	0.001 m^2
Geogrid modulus	7.377×10^8 Pa	7.8×10^8 Pa
Ultimate strength	1.321 kN/rib	1.263 kN/rib

Two specimens were tested for each condition (solution, temperature and stress level). The conditions for temperature were 30°C, 45°C, 55°C and 65°C. The load levels utilized were 30%, 40% and 50% of the ultimate strength of each respective geogrid (HDPE and PET). The ultimate strength was obtained by monotonic tests, resulting in values of 1.321 kN/rib for HDPE and 1.263 kN/rib for PET.

From the experimental data, it was concluded that the effect of environmental exposure on creep for these geogrids was negligible. This conclusion is well supported in the literature that indicates that inorganic compounds, including acids and bases, do not attack or have any adverse influence on long-chain polymers such as HDPE and PET geogrids.

This chapter presents a new model for creep of HDPE (UX-1400 SB) and PET (Matrex-30) geogrids, which was developed as part of this research project. The purpose of the creep model is to calculate, with accuracy, the strain as a function of time and temperature under a given loading condition. The results can be utilized to compute an equivalent long term modulus that is a function of the structure's design life, which can be used for design.

4.2 EVALUATION OF EXISTING MODELS

A preliminary analysis was first performed to evaluate the existing creep models in the literature. To this end, the experimental data was fitted to the model proposed by Merry and Bray (1997). However, the model showed to be highly inaccurate, possibly due to the fact that it was adapted from a soil creep model. Other models that were found in the literature review were also considered (e.g., Sawicki, 1998; Poh, 1998). Due to the inability of all these models to predict tertiary creep, especially for HDPE geogrids, it was necessary to develop a new model to satisfy the needs of the current project.

Because of the extended duration of testing, creep data are typically plotted as semi-log plots of strain in percent versus the logarithm of time. Several shapes of time-deformation curves can be obtained depending on the rheological behavior of the material, but three distinct types are generally common (Fig. 4.1). Type I, or P curves represent the time-

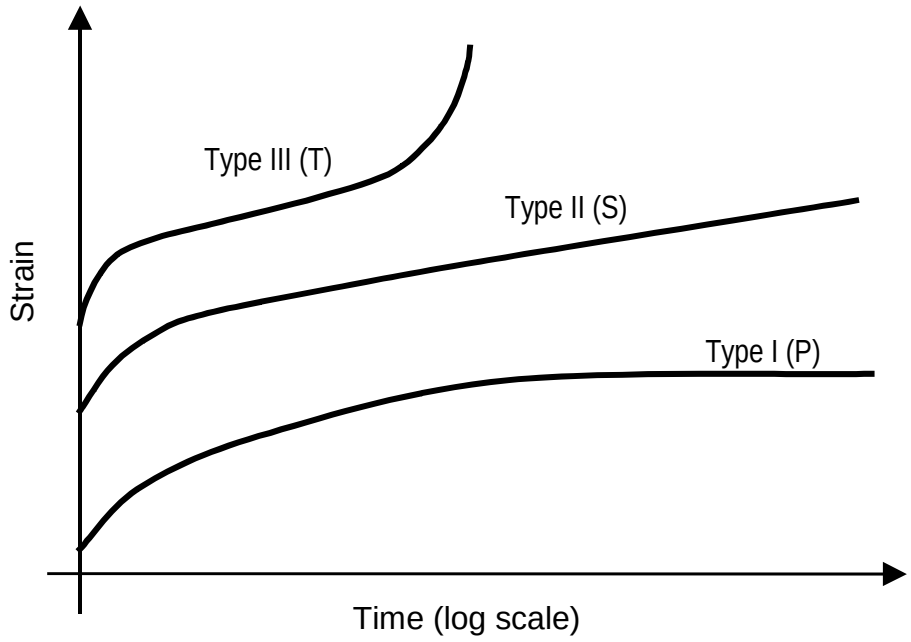

Figure 4.1. Typical time-deformation (creep) curves of engineering materials.

deformation behavior of materials that undergo only Primary creep, which is characterized by a increase in strain at a decreasing rate under constant load. Eventually, the strain approaches an asymptotic value at prolonged time periods and the material stabilizes. This is typical of highly elastic materials that are loaded at low stress levels. Secondary (Type II or S) curves initially undergo primary creep, but the strain continues to increase linearly as a function of log time. This type of behavior is common in medium plasticity materials that are loaded to intermediate stress levels. Type III (T) curves are common for plastic materials such as polymers, and undergo tertiary creep beyond the primary and secondary zones. tertiary creep is characterized by a more rapid increase in strain as a function of log time, eventually leading to substantial elongation and eventual failure of the material.

In this research project, HDPE and PET creep data obtained from the earlier study (Reddy, 2000) were plotted in a similar manner. The results are presented in Appendix B. From the creep data of HDPE and PET geogrids at different stress conditions and temperatures, several observations can be made. First, it was observed that for PET geogrid, creep behavior follows a linear pattern. The behavior of HDPE geogrid showed that at strains smaller than 12%, the creep curve also follows a linear pattern. However, at a strain of 12% strain, independent of temperature and stress level, the deformation-time curves become nonlinear. Therefore, a strain of 12% represented the initiation of tertiary creep. The tertiary zone can be represented by an exponential function.

4.3 MODEL FORMULATION

The data set considered for the analysis and model formulation herein (Reddy et al., 1999; Reddy, 2000; Reddy et al., 2000) demonstrates that primary creep for both materials (HDPE and PET) under all conditions lasted no more than one minute, which is much shorter than the duration of a typical monotonic test. For all practical purposes, primary creep can be ignored, as it is insignificant with respect to the long-term behavior of MSE walls. As such, creep data is plotted in Appendix B and throughout this report starting at a log (time) of zero, which corresponds to a time of one minute. In addition, tertiary creep was not observed with PET geogrids. Instead, the strains follows a secondary creep pattern before the termination of the test at 10^6 minutes (approximately 700 days). Similar data on PET materials has been reported throughout the literature by other researchers where the strain increased linearly with log time before the samples failed abruptly.

Statistical analysis was conducted using MathCad® to develop a general model for creep of geogrids as a function of temperature and loading level. Table 4.1 summarizes the conditions and parameters for the plots used in creep analysis for PET and HDPE geogrids. These correspond to the various plots presented in Appendix B.

Table 4.1 PET and HDPE geogrid creep test conditions

Condition No.	Temperature	% Ultimate stress level
1	30˚ C	30
2	30˚ C	40
3	30˚ C	50
4	45˚ C	30
5	45˚ C	40
6	45˚ C	50
7	55˚ C	30
8	55˚ C	40
9	55˚ C	50
10	65˚ C	30
11	65˚ C	40
12	65˚ C	50

Creep data for PET geogrids showed log time values from zero to six. The number of original readings for each interval was not uniform since the data is plotted on a log scale. Specifically, the concentration of data points is higher at higher values of log time because the readings were taken at constant time intervals. In order to obtain a representative unbiased creep function, it was necessary to use an equal number of data points for each log time

interval. This rearrangement of data points helped to avoid any bias in the regression analysis toward the higher data points.

Since the PET data followed a secondary creep trend, linear regression was used to find representative models for every combination of temperature and stress level. The linear equation form had the following form:

$$\varepsilon = mT_L + \varepsilon_o \tag{4.1}$$

where ε = strain (%)

T_L = log (time) in minutes

m = slope of the secondary creep segment

ε_o = initial strain at log (time) equal to zero

In the case of HDPE geogrids, creep data was resampled to model the linear behavior portion (up to 12% of strain). Similar to PET, linear regression was used to represent the linear secondary creep range for the HDPE geogrid (Eq. 4.1). All the data in the nonlinear portion (beyond 12% strain) was used separately to model tertiary creep. The reason for considering all the data points in the nonlinear portion (rather than resampling) is that the distribution of data points was almost uniform at the intervals corresponding to this portion of the curve. The statistical expression for tertiary creep relied on an exponential equation given by the following exponential function:

$$\varepsilon = C_1 + C_2 \exp^{C_3 T_1} \tag{4.2}$$

where ε = strain (%) > 12%

T_1 = log time from the onset of tertiary creep

C_1, C_2, and C_3 are statistical constants that are unit independent

In order to force continuity between the end of the linear curve and the beginning of the exponential curve, the slopes are equated at the intersection point. The slope of equation 4.2 is given by its derivative as follows:

$$\frac{d\varepsilon}{dx} = C_2 C_3 \, exp^{C_3 T_1} \tag{4.3}$$

In Eq. 4.3, the condition ($T_1 = 0$) represents the onset of tertiary creep. It is noted that at T_1=0, the exponential portion ($\exp^{C_3 T_1}$) is equal to one. Therefore the slope at T_1=0 is equal to C_2C_3. Consequently, C_3 is equal to:

$$C_3 = \frac{m}{C_2} \tag{4.4}$$

Where *m* is the slope corresponding to the slope of the secondary creep range. Therefore the original equation 4.2 can be rewritten in general terms as follows:

$$\varepsilon = C_1 + C_2 \, exp^{\frac{m}{C_2}(T_L - T_t)} \tag{4.5}$$

where T_t is the value of T_L (or log time) at the onset of tertiary creep.

In addition to forcing the slope at the onset of tertiary creep to be equal to the slope of the linear range (secondary creep), it is also necessary to force continuity of the strain function at a strain value of 12%. Otherwise, a jump in strain will occur in the model at the transition from secondary to tertiary creep. This restriction is guaranteed by the following condition:

$$At \;\; T_L = T_t \;\; , \quad \varepsilon = \varepsilon_t \tag{4.6}$$

where ε_t is the strain at the onset of tertiary creep, which is equal to 12% for HDPE geogrids.

From Eq. 4.2 and 4.6, it can be concluded that:

$$\varepsilon_t = C_1 + C_2 \exp^0 = C_1 + C_2 \tag{4.7}$$

Rearranging Eq. 4.7, we obtain:

$$C_1 = \varepsilon_t - C_2 \tag{4.8}$$

Substituting for the value of C_1 into Eq. 4.2 , the general creep function is written as:

$$\varepsilon = (\varepsilon_t - C_2) + C_2 \exp^{\frac{m}{C_2}(T_L - T_t)} \tag{4.9}$$

Or

$$\varepsilon = \varepsilon_t + C_2 \left[\exp^{\frac{m}{C_2}(T_L - T_t)} - 1 \right] \tag{4.10}$$

The above equation (Eq. 4.10) is used in the exponential regression analysis to formulate a model for tertiary creep for HDPE geogrids under the various test conditions.

4.4 CREEP MODEL PARAMETERS FOR PET GEOGRID

Linear regression equations were developed to express PET creep behavior in the form of Eq. 4.1. The results of these linear regressions at each given temperature and at different stress levels are plotted in Figs. 4.2 to 4.5. Table 4.2 summarizes the equation parameters for each condition of temperature and stress level. These results will be used later in this Chapter for developing the generalized creep equation.

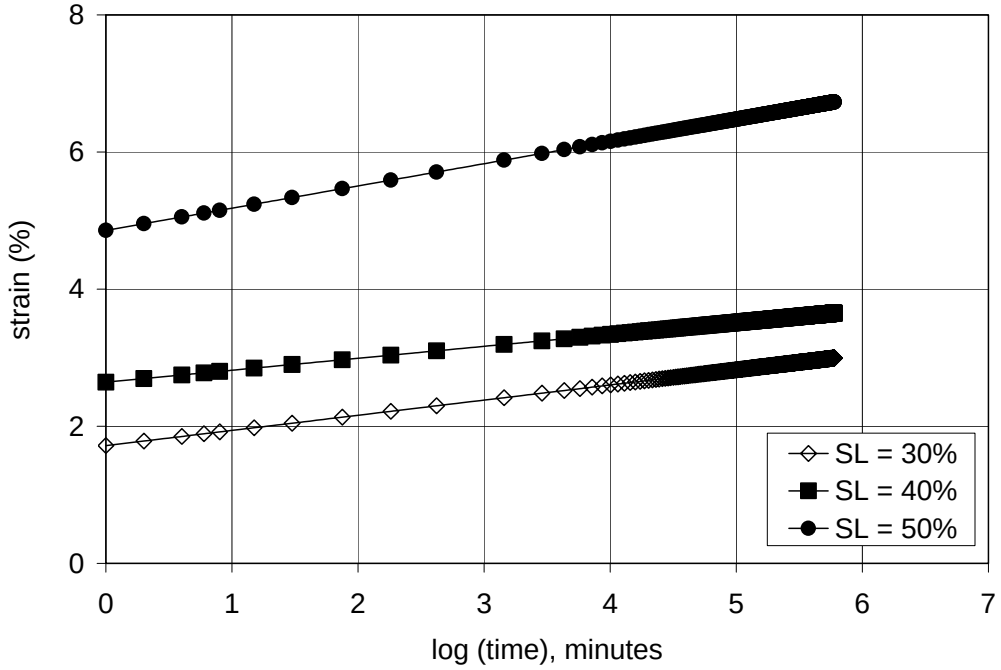

Figure 4.2. PET geogrid regressions at 30˚ C, for various stress levels (S_L).

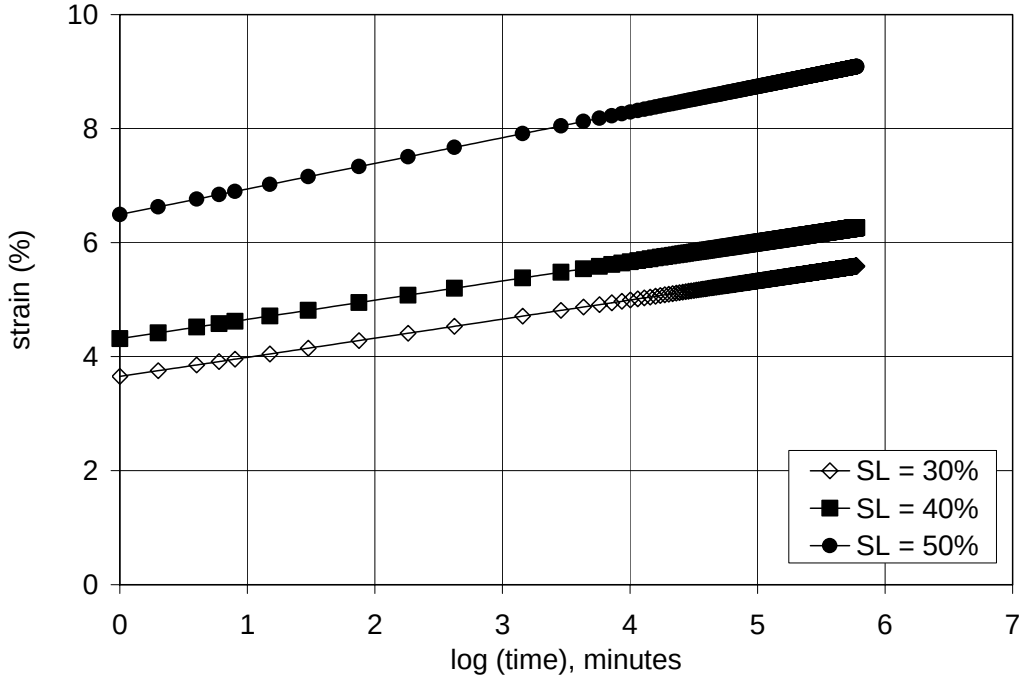

Figure 4.3. PET geogrid regressions at 45˚ C, for various stress levels (S_L).

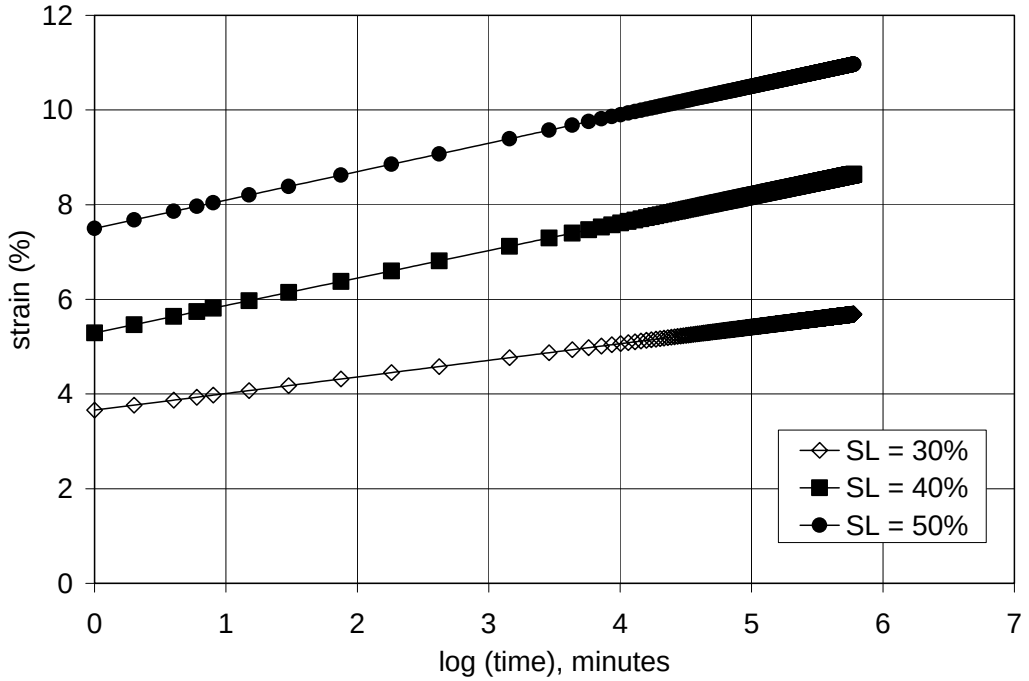

Figure 4.4. PET geogrid regressions at 55˚ C, for various stress levels (S_L).

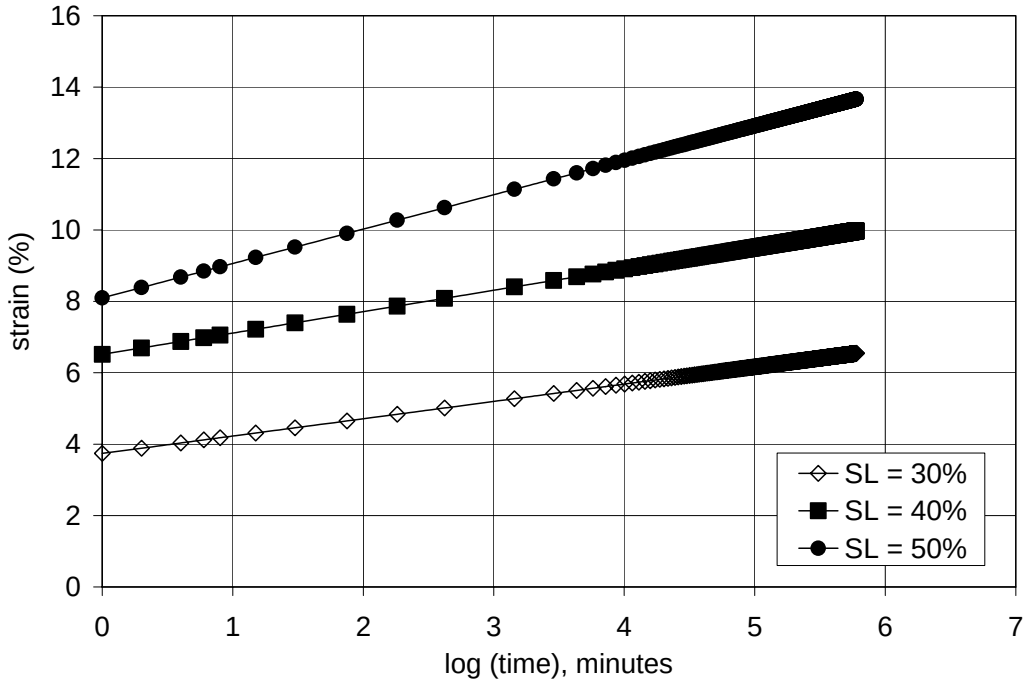

Figure 4.5. PET geogrid regressions at 65˚ C, for various stress levels (S_L).

Table 4.2. Summary of linear regression parameters for PET geogrid

$\varepsilon = mT_L + \varepsilon_o$					
Condition No.	**Temperature**	**Stress level %**	**Figure**	**m**	**ε_o**
1	30˚ C	30	4.2	0.221	1.718
2	30˚ C	40	4.2	0.174	2.643
3	30˚ C	50	4.2	0.324	4.857
4	45˚ C	30	4.3	0.335	3.653
5	45˚ C	40	4.3	0.337	4.316
6	45˚ C	50	4.3	0.449	6.493
7	55˚ C	30	4.4	0.351	3.659
8	55˚ C	40	4.4	0.580	5.290
9	55˚ C	50	4.4	0.600	7.498
10	65˚ C	30	4.5	0.485	3.741
11	65˚ C	40	4.5	0.598	6.515
12	65˚ C	50	4.5	0.963	8.097

4.5 CREEP MODEL PARAMETERS FOR HDPE GEOGRID

Linear and exponential regression equations were developed to express PET creep behavior in the form of Eqs. 4.1 and 4.10. The results of these linear regressions at each given temperature and at different stress levels are plotted in Figs. 4.6 to 4.9. Table 4.3 summarizes the equation parameters for each condition of temperature and stress level. These results will be used next in this Chapter for developing the generalized creep equations.

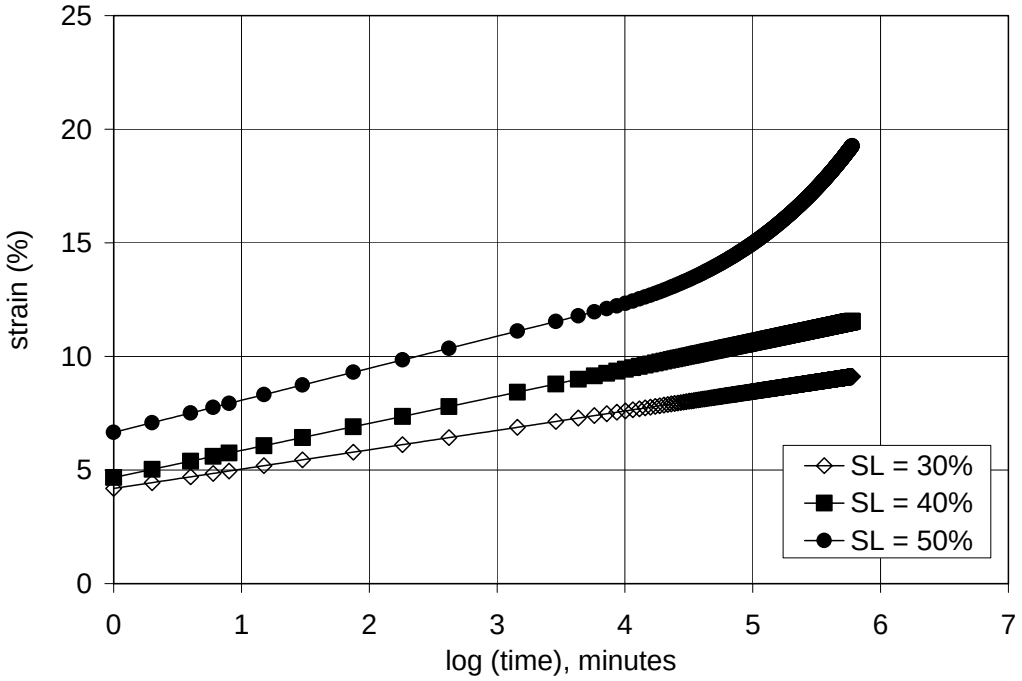

Figure 4.6. HDPE geogrid regressions at 30˚ C, for various stress levels (S_L).

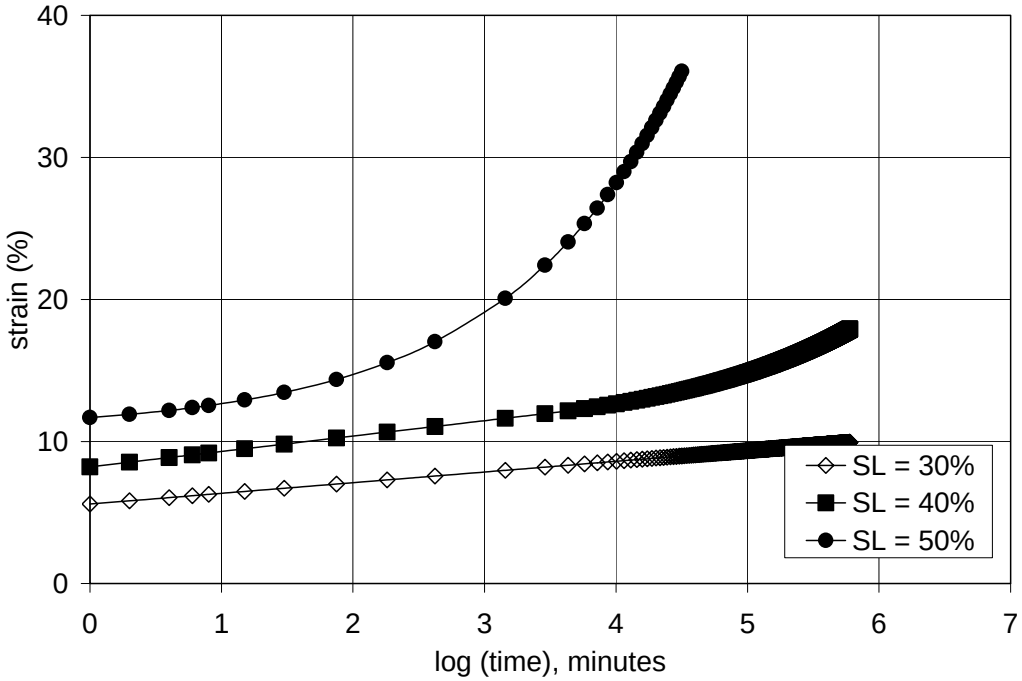

Figure 4.7. HDPE geogrid regressions at 45˚ C, for various stress levels (S_L).

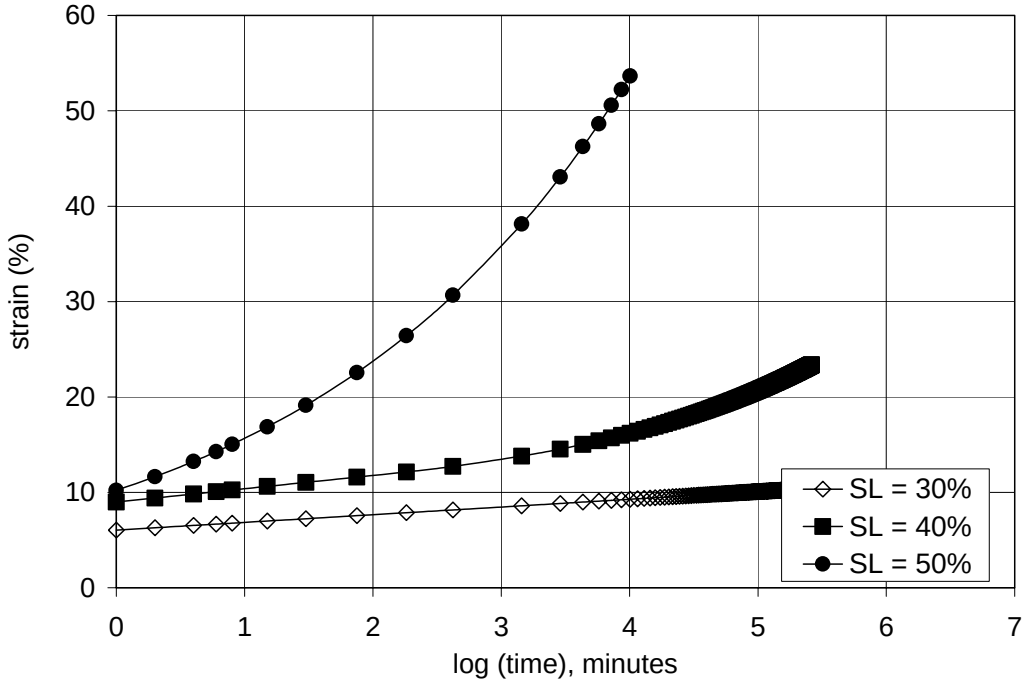

Figure 4.8. HDPE geogrid regressions at 55˚ C, for various stress levels (S_L).

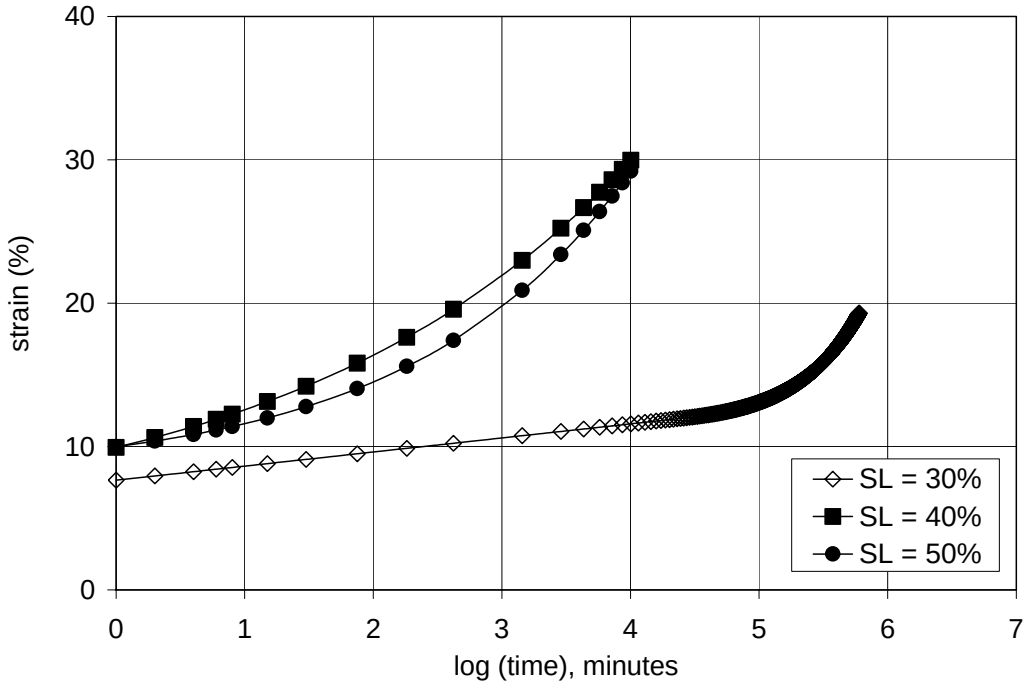

Figure 4.9. HDPE geogrid regressions at 65˚ C, for various stress levels (S_L).

Table 4.3 Summary of regression parameters for HDPE geogrid

Conditions				**Linear range (Eq. 4.1)**		**Exponential range (Eq. 4.10)**	
Condition No.	Temperature	Stress level %	Figure	m	ε_o	C_2	T_t
1	30˚ C	30	4.6	0.853	4.188	-	-
2	30˚ C	40	4.6	1.189	4.675	-	-
3	30˚ C	50	4.6	1.410	6.660	1.677	3.787
4	45˚ C	30	4.7	0.751	5.599	-	-
5	45˚ C	40	4.7	1.082	8.216	1.5905	3.497
6	45˚ C	50	4.7	1.075	10.644	1.086	1.261
7	55˚ C	30	4.8	0.807	6.049	-	-
8	55˚ C	40	4.8	1.391	8.996	2.789	2.160
9	55˚ C	50	4.8	2.240	11.030	2.752	0.433
10	65˚ C	30	4.9	0.981	7.659	0.475	4.425
11	65˚ C	40	4.9	1.881	10.217	2.829	0.948
12	65˚ C	50	4.9	2.197	9.543	3.349	1.119

4.6 DEVELOPMENT OF GENERALIZED CREEP MODEL

From the regression data presented in Tables 4.2 and 4.3, the values of the various parameters can be expressed in the form of equations. This may be done by statistically analyzing the regression parameters to express them in terms of stress level and temperature. For instance, the value of , ε_o, or the initial strain at (log time) of zero for PET is expressed as:

$$\varepsilon_o = S_L(0.002\theta + 0.0233) \tag{4.11}$$

where S_L is the stress level in percent, and θ is the temperature in degrees Celsius. Similarly, the slope of the secondary creep segment (m) in Eq. 4.1 is expressed as follows:

$$m = S_L(0.000313\theta - 0.00367) \tag{4.12}$$

By combining Eqs. 4.1, 4.11, and 4.12, we can thus obtain the general creep equation for PET geogrids, in which the strain (ε) is expressed solely as a function of log time (T_L), stress level (S_L), and temperature (θ).

$$\varepsilon = S_L\left[(0.000313\theta - 0.00367)T_L + 0.002\theta + 0.0233\right] \tag{4.13}$$

The general expression in Eq. 4.13 may be used, although it is more convenient to use only Eq. 4.1, where the terms ε_o and m are defined by 4.11 and 4.12, respectively.

Similarly, for HDPE geogrids, the initial strain, ε_o, and the slope of the secondary creep segment, m, are defined by Eqs. 4.14 and 4.15 as follows:

$$\varepsilon_o = S_L(0.0046\theta - 0.013) \tag{4.14}$$

$$m = S_L(0.000417\theta + 0.0146) \tag{4.15}$$

In addition, for the nonlinear (exponential) tertiary creep range, the corresponding parameters from Eq. 4.10 are defined as follows:

$$\varepsilon_t = 12\% \tag{4.16}$$

$$C_2 = 0.05\theta \tag{4.17}$$

$$T_t = (\varepsilon_t - \varepsilon_o)/m \tag{4.18}$$

4.7 SUMMARY

A general creep equation has been formulated to predict the strain of a geogrid subjected to prolonged constant loading. The strain is expressed as a function of stress level (percent of ultimate monotonic strength), time, and temperature. Material-specific parameters were developed for both HDPE and PET geogrids. In the case of PET, Eq. 4.1 is to be used, with the initial strain (ε_o) and secondary creep slope (m) defined by Eqs. 4.11 and 4.12, respectively. For HDPE geogrids, Eq. 4.1 is to be used for strains smaller than or equal to the tertiary strain ε_t (12%), with the initial strain (ε_o) and secondary creep slope (m) defined by Eqs. 4.14 and 4.15, respectively. Within the tertiary creep range (for $\varepsilon>\varepsilon_t$, i.e., $\varepsilon>12\%$), Eq. 4.10 is used to calculate the strain, with the parameters ε_t, C_2, and T_t defined through Eqs. 4.16, 4.17, and 4.18, respectively. The general creep equations will be used later in the analysis of MSE walls, by enabling the calculation of equivalent moduli for geogrids at various temperature and stress level conditions.

5 DESIGN CONSIDERATIONS

Among the main objectives of this research project is the development of improved design procedures for MSE walls. As a starting point, it was necessary to follow the conventional design methods, before they are modified to account for deformability and creep of geosynthetics. The standard design procedure is described in numerous documents, such as the FHWA Report No. H1-98-032, and is outlined in detail in Section 2.2 of this report. Therefore, a preliminary design was conducted, and is attached in Appendix C.

The proposed design calls for a 6 m (20 ft) high wall, reinforced with either HDPE or PET geogrids at a spacing of 0.8 m (2.5 ft). In this design, a factor of safety of 1.0 was adopted in order to emphasize the distress mechanisms and subsequently "fail" the wall while measuring the deformations and monitoring the failure mechanisms. However, as described later in the report, it has not been possible to actually fail the wall, even at high stress levels due to the substantial redundancies in the design of such walls.

5.1 SCALE EFFECTS

The construction of four small-scale walls, in addition to the full-scale wall, required special provisions in terms of design parameters. More specifically, it is necessary to scale the design parameters in order to account for scale effects, in a manner that ensures equivalence between small scale and full scale walls.

5.1.1 DIMENSIONAL ANALYSIS

Similitude can be secured through proper dimensional analysis of the model and prototype through the Buckingham Pi Theorem. To this end, a number of parameters were considered to be of specific importance were isolated, and are listed with their respective units [dimensions] as follows:

H	=	height of wall [L]
L	=	width of wall [L]
L_{max}	=	length of reinforcement [L]
g	=	gravitational acceleration [LT^{-2}]
J	=	modulus of geogrid [FL^{-1}]
S	=	strength of geogrid [FL^{-1}]
γ	=	unit weight [FL^{-3}]
q	=	surcharge [FL^{-2}]

The following conditions apply to the model and prototype, and constitute the physical, experimental, and design restrictions to scaled MSE walls:

$$H_m = nH_p \tag{5.1}$$

$$g_m = g_p \tag{5.2}$$

$$\gamma_m = \gamma_p \tag{5.3}$$

where subscripts *m* and *p* signify model and prototype, respectively. All lengths are therefore scaled down in the model by a factor (n) equal to 1/5, resulting in scaled walls 4 ft high. The corresponding Π values are:

$$\Pi_S = \Pi_J = \frac{J}{\gamma H^2} \tag{5.4}$$

$$\Pi_q = \frac{q}{\gamma H} \tag{5.5}$$

Note that the gravitational acceleration, g, does not appear anywhere, since the scaling factor for that parameter was set to one. In centrifuge testing, it is possible to scale gravity. However, since a centrifuge was not used in the present study, it was possible to avoid scaling of gravity by forcing a scaling factor of (1) while requiring the scaling of other factors. From Eqs. 5.4 and 5.5 it can be deduced that:

$$\frac{J_m}{\gamma_m H^2{}_m} = \frac{J_P}{\gamma_P H^2{}_P} \tag{5.6}$$

$$\frac{q_m}{\gamma_m H_m} = \frac{q_P}{\gamma_P H_P} \tag{5.7}$$

Therefore,

$$J_m = n^2 J_P \tag{5.8}$$

$$S_m = n^2 S_P \tag{5.9}$$

$$q_m = n\, q_P \tag{5.10}$$

Since this is a 1:5 model, the strength and stiffness of the geogrid must be scaled down by 25. The surcharge needs to be scaled down by 5.

5.1.2 GEOGRID SCALING

Following an extensive market survey, it became evident that no geogrid product is available in the market that satisfies the required scaling. Therefore, it became necessary to process the product in-house. Tests were carried out to find the right geometry to obtain the required scaling ratio for the pullout force of the geogrid. This was done by cutting some of the longitudinal ribs together with different combinations of cutting the transverse ribs.

To perform the pullout tests, a steel chamber was used. The chamber was 36" x 16" in plan and 16" high. A slot was made at a height of 6" to enable specimen pull out. The testing was performed by placing an initial 7" layer of soil, which was compacted to 95-100% AASHTO T-99 maximum relative compaction, giving a 6" layer of compacted soil. This was followed by the placement of the geogrid and a second layer of 7" also compacted down to 6". Finally, a load of 372 lb (normal stress of 93 psf) was applied.

After pullout testing of many "geometrically reduced" geogrids, it was determined that the most adequate geometry to simulate the pullout effect in small scale testing (1/5 scaling) for HDPE specimens was obtained by cutting 10 of the 12 longitudinal (Machine Direction) ribs, leaving only 2 ribs per 12, and cutting the transverse ribs to 5/8 in., as shown in Figs. 5.1 and 5.2. The results are presented in Table 5.1 for HDPE specimens, all reduced from 12 to 2 longitudinal ribs with the transverse ribs cut to the sizes shown in the Table.

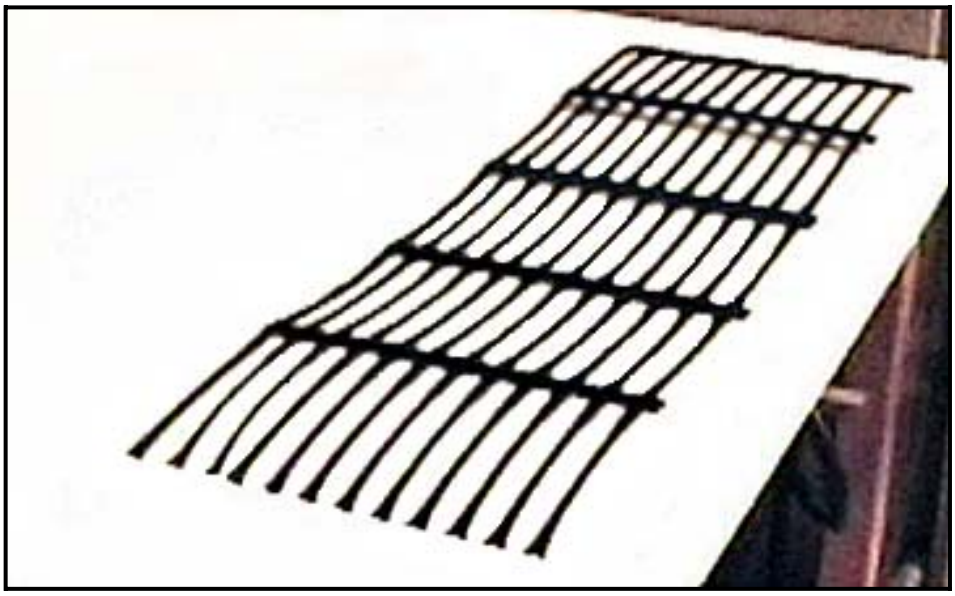

Figure 5.1. Prototype HDPE geogrid for full-scale testing

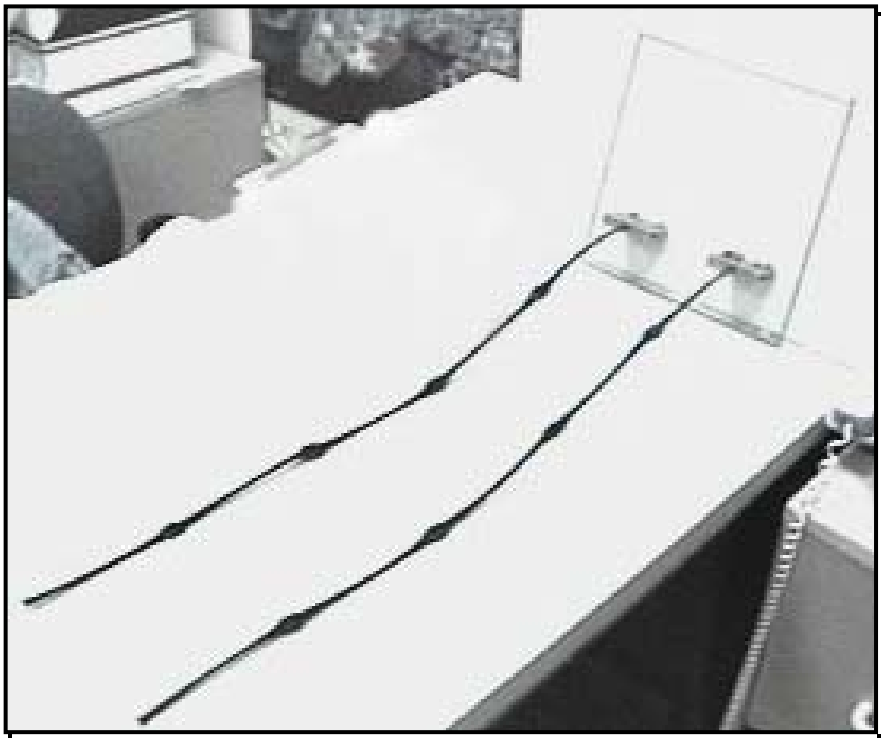

Figure 5.2. Modified HDPE geogrid for small-scale testing

Table 5.1. Pullout forces for HDPE grids

Geogrid Geometry	Number of specimens tested	Maximum Pullout Force (lb)
Complete geogrid	3	489
1-1/8" transverse rib	1	189
1" transverse rib	1	176
7/8" transverse rib	1	148
5/8" transverse rib	3	90
No transverse rib	1	74

For PET geogrids, the required scaling ratio was obtained by cutting six of the eight longitudinal ribs; additionally, all the transverse ribs were cut off and the effective length (L_e) of the two ribs was reduced 31%, as shown in Figures 5.3 and 5.4. The pullout test results are presented in Table 5.2.

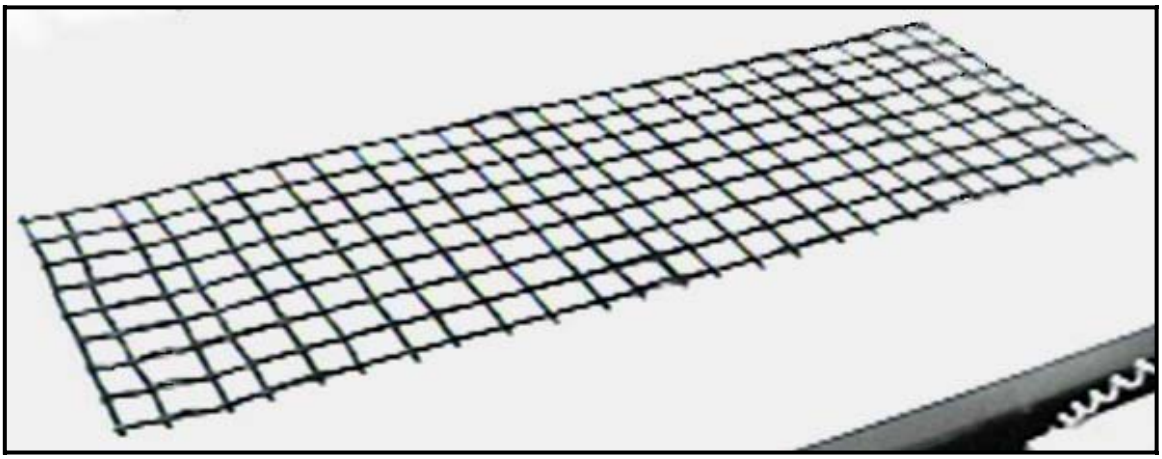

Figure 5.3. Prototype PET geogrid for full-scale testing

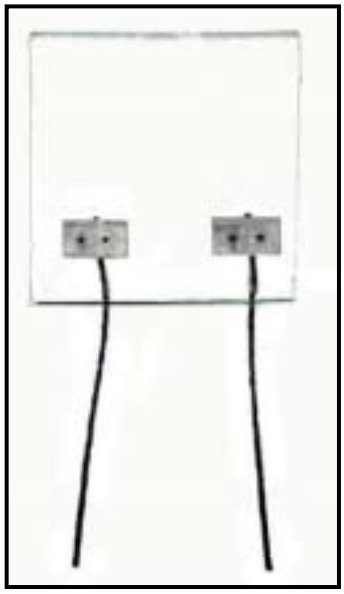

Figure 5.4. Modified PET geogrid for small-scale testing

Table 5.2. Pullout forces for PET grids

Geogrid Geometry	Number of specimens tested	Maximum Pullout Force (lb)
Complete geogrid	3	540
Complete transverse ribs	1	300
1" transverse ribs	1	246
No transverse ribs & 17.5 % length reduction	1	180
No transverse rib & 23 % length reduction	1	140
No transverse rib & 26 % length reduction	1	126
No transverse rib & 31 % length reduction	3	98

The scaled geogrids were utilized in subsequent testing of the small scale MSE walls. By placing the scaled geogrids in the MSE walls as reinforcement elements, compatibility between the model and the prototype was ensured. Thus, the resulting displacements and strains of the small scale walls could be converted into their full scale equivalents.

5.2 NUMERICAL MODELING

The objective of the numerical modeling of MSE walls is to simulate the full and scaled walls in order to study the influence of various parameters on their behavior. In these simulations the effect of single and multiple stage construction are studied, as well as the influence of material properties on the scaled wall. The multiple-stage construction was meant to simulate the sequential construction process in the field.

The numerical modeling was carried out using FLAC version 3.3. The properties and data were taken from Chapter 3 and the dimensions of the wall were taken from the initial design calculations of the MSE wall. Later in the report, adaptation of the final properties and dimensions as well as more detailed calibration and verification of the model parameters will be discussed. The sequence of this analysis follows a preliminary and a parametric study that are explained as follows:

1. The full-scale MSE wall was modeled with HDPE geogrid. Two cases of modeling were considered: multiple-stage construction, and single-stage construction.

2. A scaled MSE wall was modeled with the same type of geogrid in both single and multiple-stage constructions. All model parameters were scaled according to the scaling requirements outlined earlier in this Chapter (Section 5.1). The results for the full and

scaled wall were then compared to make sure that the results were identical. This was done to verify the accuracy of the numerical model and to validate the parameter scaling process.

3. In order to study the behavior of the scaled wall when the material properties are changed, the scaled MSE wall was taken as a base case for comparison. The geogrid and soil modulus were then varied in the model in order to study their effect on the results.

5.2.1 DESCRIPTION OF THE NUMERICAL MODELING INPUT

An initial grid consisting of 21×40 zones (elements) was generated with a Mohr-Coulomb Model assigned to all the zones. Because of geometric symmetry, only the left half of the MSE needed to be simulated with the objective to reduce computations (Fig. 5.5). A "null" model, simulating a very thin gap, was used to remove several rows of the initial grid, thereby creating space for eight layers of geogrid to be placed between the different soil layers. This allowed the generation of interfaces between the soil and the geogrid on both sides (top and bottom). The boundary conditions for the model were then defined as follows: i) restricted rotation at the middle of each facing unit to reduce numerical instability, ii) fixity in the horizontal direction at the right end of the geogrid to simulate symmetry, and iii) fixity in both horizontal and vertical directions long the bottom boundary.

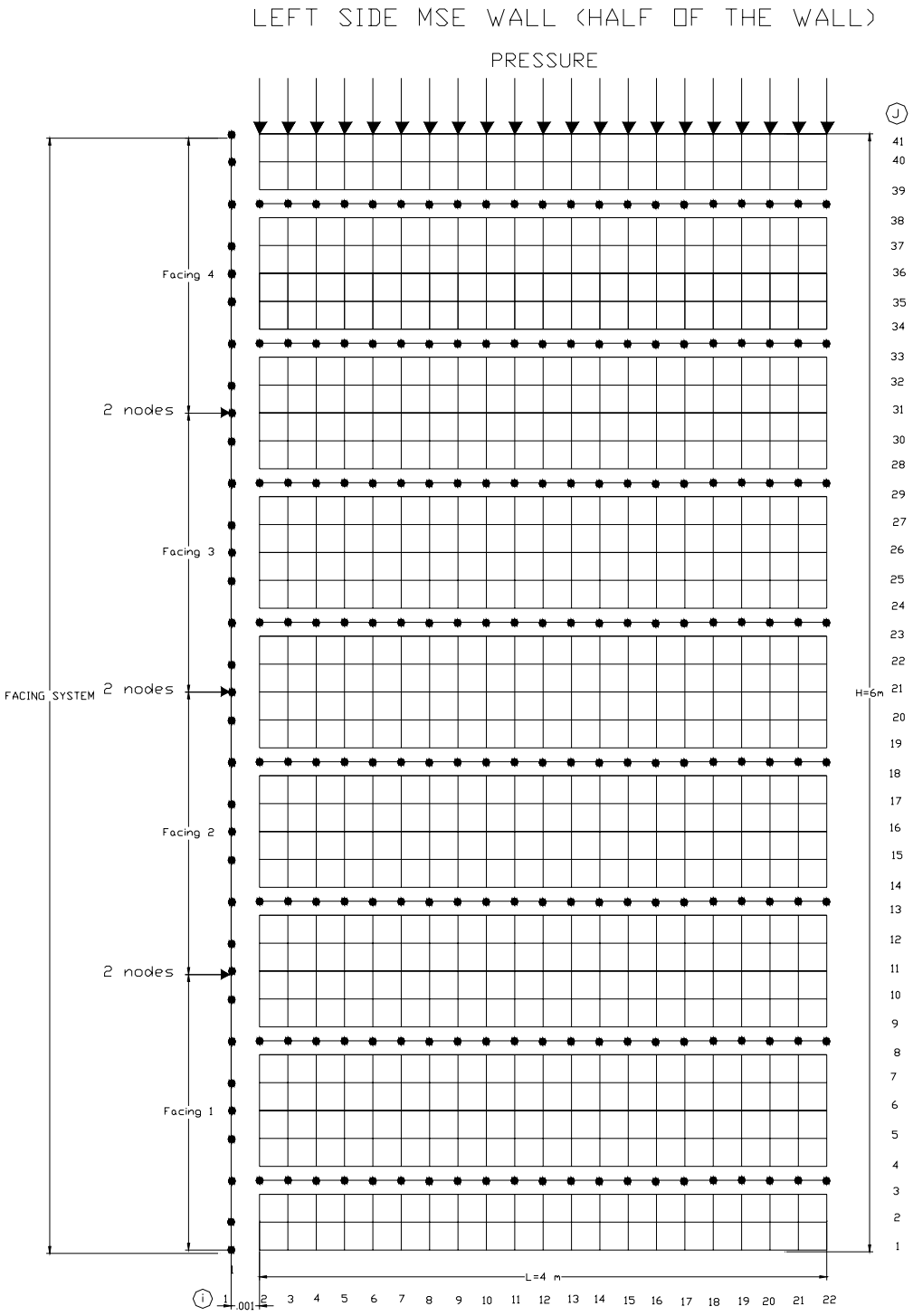

Figure 5.5. Schematic of the FLAC model, used to simulate the MSE wall

A flexible beam structure was considered to simulate the geogrid (as was done in the pullout analysis). The nodes and the structures of the elements of the geogrid were defined along the entire width of the model. Next, the interfaces between soil-geogrid and geogrid-soil were generated with Coulomb shear-strength interface properties. An automated process was used to create the facing system. In order to do that, a rigid beam was generated simulating four separated facing units in the wall. Two nodes were defined in the zones where the facings were joining (see Fig. 5.5). Next, the facing-soil interfaces were defined as elastic when in contact, with the capability of separating. The geogrid and the facing system were connected by attaching the first node of each layer (left side) with the respective facing node.

Before applying the normal pressure, the system was brought into initial equilibrium under its own weight in order to obtain the gravitational stresses in the system. In the case of the wall modeled in single stage construction, equilibrium was obtained with the surcharge (normal pressure) applied at the top. For the multiple-stage construction simulation, equilibrium was established sequentially for each soil layer under gravity, before the surcharge was applied after all layers were placed.

5.2.2 MATERIAL PROPERTIES IN THE NUMERICAL MODEL

The properties and the equations used in the MSE wall modeling are basically the same as those used in the pullout analysis (Chapter 3, Section 3.1.2). The scale factor considered in this analysis was 1:5. Following the investigation of scale effects using the Buckingham Pi Theorem (Section 5.1.1), the scaled MSE wall required that all dimensional properties be scaled by five. In addition, the confining pressure was scaled by a factor of five.

Following the Buckingham Pi theorem, the geogrid moduli were to be scaled by 25. However, since the modulus of elasticity in the numerical model is defined as the geogrid modulus divided by the geogrid thickness, the modulus of elasticity of the geogrid was to be scaled by a factor of five. Tables 5.3 through 5.14 show the properties used in the full and the scaled walls.

Table 5.3. Properties for the full-scale MSE wall

Parameter	**Basis**	**Value**	**Units**
Density (ρ)	measured	1560.0	kg/m^3
Modulus of elasticity (E_s)	assumed	4.0×10^7	N/m^2
Poisson's ratio (ν)	assumed	0.30	
Friction angle (ϕ)	measured	36.0	degrees
Cohesion (c)	assumed	1×10^3	Pa
Shear modulus (G)	calculated	1.54×10^7	Pa
Bulk modulus (B)	calculated	3.33×10^7	Pa

Table 5.4. Wall and facing dimensions for the full-scale MSE wall

Parameter	**Dimension (ft, in)**	**Dimensions (m)**
Height of facing unit	5.0 ft	1.52 m
Width of facing unit	4.8 ft	1.46 m
Thickness of facing unit	6.75 in	0.17 m

Table 5.5. Geogrid Properties for the full-scale MSE Wall

Parameter	**Basis**	**Value**	**Units**
Tensile modulus	measured	2,034,000	N/m^2
Thickness (t)	measured	0.0018	m^2
Area (A)	measured	0.0018	m^2
Modulus of elasticity (E)	calculated	1.13×10^{9}	Pa
Moment of inertia (I)	calculated	4.86×10^{-10}	m^4/m

Table 5.6. Facing Properties for the full-scale MSE Wall

Parameter	**Basis**	**Value**	**Units**
Modulus of elasticity (E_f)	measured	5×10^{9}	Pa
Thickness (t_f)	measured	0.17	m
Area (A_f)	calculated	0.17	m^2
Moment of inertia (I_f)	calculated	4.2×10^{-4}	m^4/m

Table 5.7. Interface properties (soil-geogrid) for the full-scale MSE wall

Parameter	**Basis**	**Value**	**Units**
Height of wall	given	6	m
Interface friction (δ)	FLAC analysis	35	degrees
Normal stiffness (K_n)	calculated	2.87×10^{9}	N/m
Shear stiffness (K_s)	calculated	2.87×10^{9}	N/m

Table 5.8. Interface Properties (soil-facing) for the full-scale MSE wall

Parameter	**Basis**	**Value**	**Units**
Length of the wall	given	4	m
Normal stiffness (K_n)	calculated	2.69×10^9	N/m
Shear stiffness (K_s)	calculated	2.69×10^9	N/m

Table 5.9. Soil properties for the scaled MSE wall

Parameter	**Basis**	**Value**	**Units**
Density (γ)	given	1560.0	kg/m^3
Modulus of elasticity (E)	assumed	1.6×10^6	N/m^2
Poisson's ratio (ν)	assumed	0.30	
Friction angle (ϕ)	given	36.0	degrees
Cohesion (c)	assumed	2×10^2	Pa
Shear modulus (G)	calculated	6.15×10^5	Pa
Bulk modulus (K)	calculated	1.33×10^6	Pa

Table 5.10. Geogrid properties for the scaled MSE wall

Parameter	**Basis**	**Value**	**Units**
Tensile modulus	given	1.26×10^{11}	N/ m^2
Thickness (t)	given	0.00036	m2
Area (A)	given	0.00036	m2
Modulus of elasticity (E)	calculated	4.52×10^{7}	Pa
Moment of inertia (I)	calculated	3.888×10^{-12}	m^4/m

Table 5.11. Facing properties for the scaled MSE wall

Parameter	**Basis**	**Value**	**Units**
Modulus of elasticity (E)	assumed	2×10^{8}	Pa
Thickness (t)	assumed	0.034	m
Area (A)	calculated	0.034	m^2
Moment of inertia (I)	calculated	3.36×10^{-6}	m^4/m

Table 5.12. Facing dimensions for the scaled MSE wall

Parameter	**Dimension (ft, in)**	**Dimensions (m)**
Height	5.0 ft	1.52 m
Width	4.8 ft	1.46 m
Thickness	6.75 in	0.17 m

Table 5.13. Interface properties in the geogrid for the scaled MSE wall

Parameter	**Basis**	**Value**	**Units**
Height of wall	given	1.2	m
Interface friction (δ)	FLAC anal.	35	degrees
Normal stiffness (K_n)	calculated	5.74×10^8	N/m
Shear stiffness (K_s)	calculated	5.74×10^8	N/m

Table 5.14. Interface Properties in the facing for the scaled MSE wall

Parameter	**Basis**	**Value**	**Units**
Length of the wall	given	0.8	m
Normal stiffness (K_n)	calculated	5.38×10^8	N/m
Shear stiffness (K_s)	calculated	5.38×10^8	N/m

5.2.3 PRELIMINARY ANALYSIS

In order to study the effect of single and staged constructions and to compare the results of full and small scale walls, both full and small scale walls were modeled under the assumption of single stage (rapid) and multiple stage (slow) construction. The results indicated discrepancies in terms of displacements, but not stresses, when single versus multiple stage assumptions were considered. For instance, the results presented in Figs. 5.6 and 5.7 suggest that both the total magnitude of vertical displacement as well as deformation patterns are dependent on the construction sequence. It is worth noting, however, that examination of the stresses throughout the wall showed that the stress distribution was

independent of construction sequence, with the stresses increasing almost linearly with depth, as would be expected.

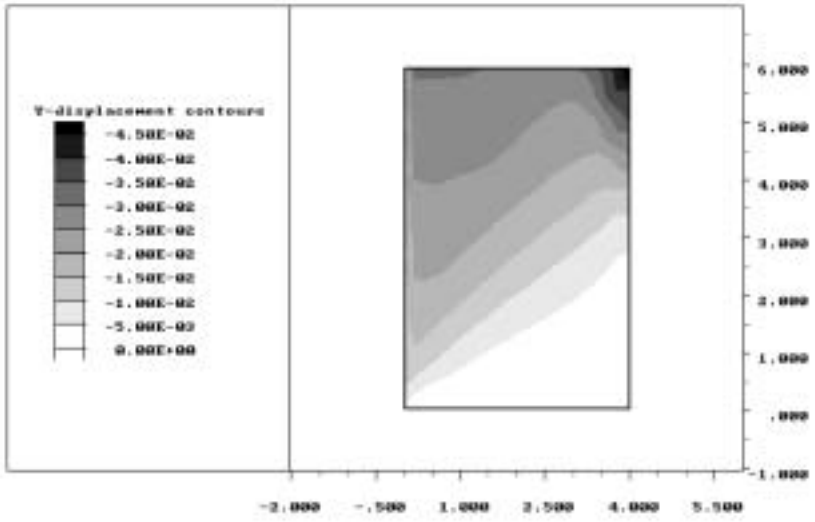

Figure 5.6. Vertical displacements in the soil (in meters) for the full scale wall under single stage construction conditions.

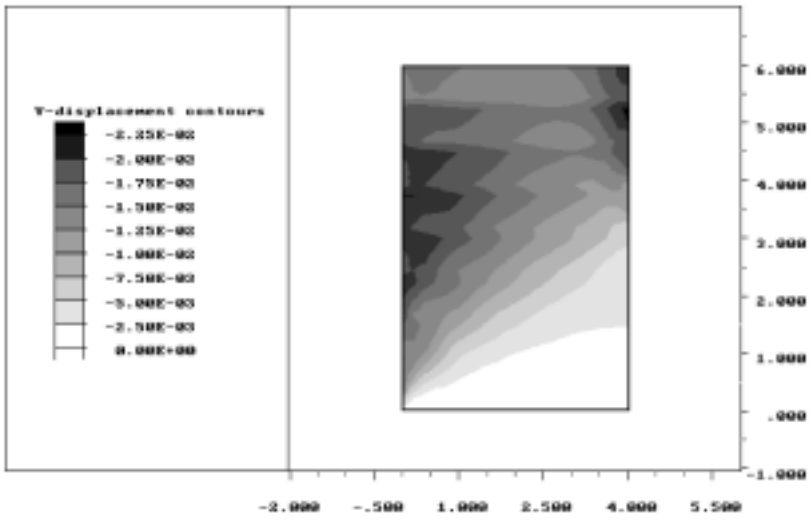

Figure 5.7. Vertical displacements in the soil (in meters) for the full scale wall under multiple stage construction conditions.

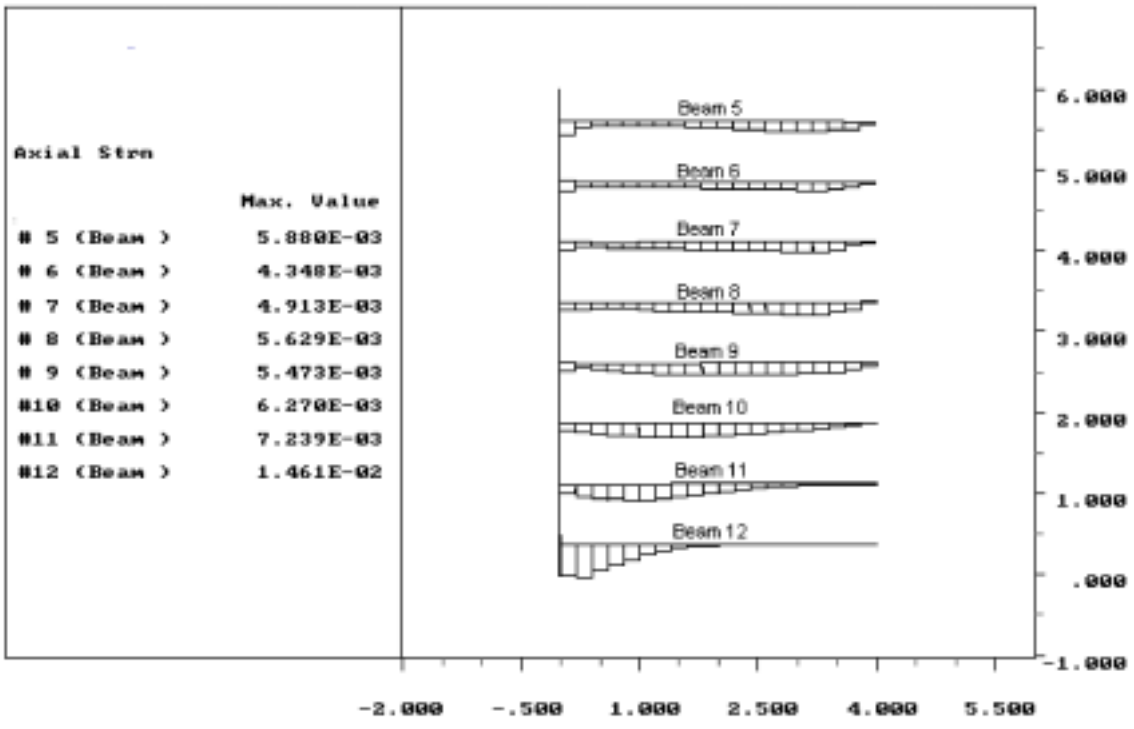

Figure 5.8. Axial strains in the geogrid layers in the full scale walls

The distribution of axial strains appeared to be independent of the construction sequence. For instance, the strain distribution shown in Fig. 5.8 is almost identical in the cases of single and multiple stage construction. This indicates that the stresses within the geogrid layers are solely a function of wall geometry. The locus of maximum strains also coincides with data published by earlier researchers in that it almost follows an active failure wedge. It is worth noting, however, that the stresses within the geogrid layers are well below the maximum strength of the geogrid, especially in the top layers. This is a clear indication of redundancy in design, even when a factor of safety of 1.0 is used. It is recalled here that the factor of safety used in this design does not include all the partial reduction factors. If these factors were included, the redundancy would increase even further.

5.2.4 PARAMETRIC ANALYSIS

In order to evaluate the influence of different parameters on the stress and strain distributions within the wall and geogrid layers, the scaled wall, under single-stage construction conditions, was taken as the base case. Various model parameters, namely soil modulus and geogrid modulus, were then changed and the results were compared. Figure 5.9 shows that the influence of geogrid modulus on the facing deformations is quite significant. The data suggests that the displacements are roughly inversely proportional to the geogrid modulus. In contrast, variations in soil modulus (Fig. 5.10) do not have any practical significance on the facing deformation. This is an interesting and important finding. This behavior is probably attributed to the substantial difference in stiffness between the soil and the geogrid. As a result, the majority of the system loads are carried by the geogrid layers, with minimal contribution from the soil.

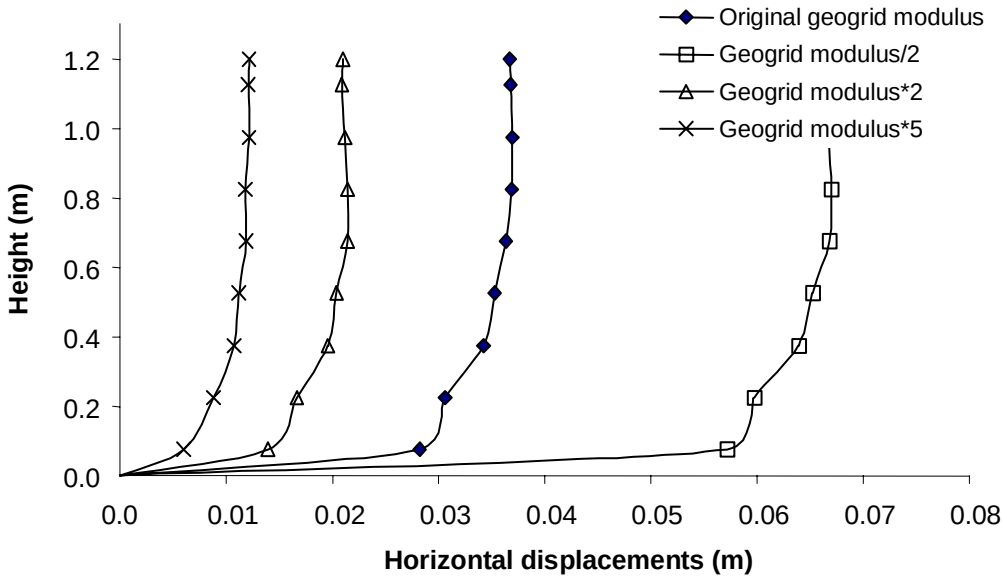

Figure 5.9. Influence of geogrid modulus on the horizontal displacement of the facing

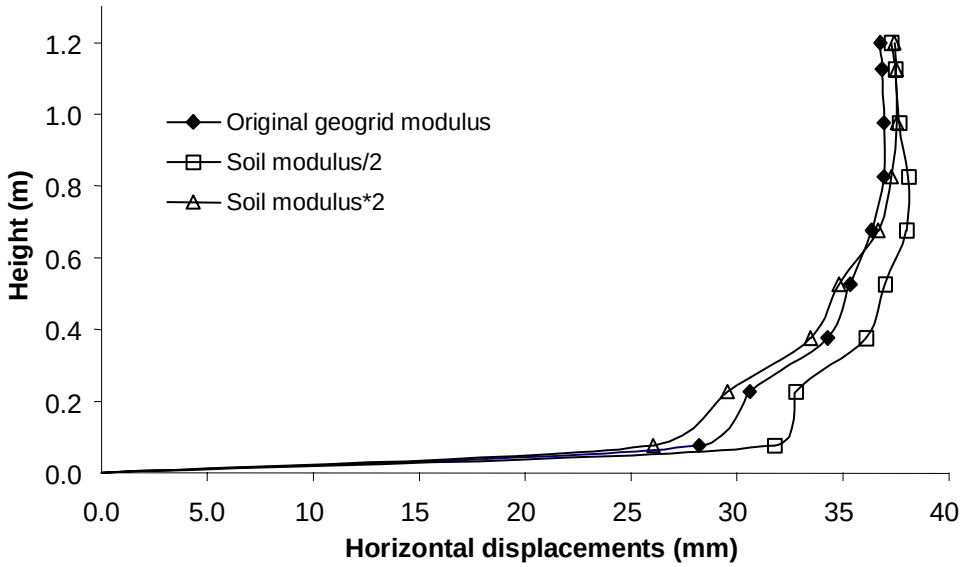

Figure 5.10. Influence of soil modulus on the horizontal displacement of the facing

Similar patterns were observed for the influence of soil and geogrid modulus on the vertical settlement and strains in the geogrid layers. Overall, the soil modulus had extremely minimal effect on the wall deformation patterns, whereas the behavior was very sensitive to the geogrid modulus. It is noted, however, that these results apply only to the as-built conditions, and not in service. For example, it is expected that when loads are applied on top of the wall during its service life, the effect of the soil modulus will indeed become much more significant, especially in terms of settlement.

6 TESTING OF SMALL SCALE MSE WALLS

6.1 INTRODUCTION

Four small scale MSE walls were tested to simulate the prototype with a scale of approximately 1 to 5. Two walls were reinforced with UX-1400 HDPE geogrids and two with Miragrid 3XT geogrids. The soil was an **SP Class II** [ASTM D2321 and D2487]. A load frame with dimensions established to accommodate the small-scale MSE wall was used for loading of the walls. The main objective of the small-scale testing was to evaluate the failure and distress mechanisms in MSE walls, in preparation for construction of the full-scale wall. For example, it is necessary to verify that the locations of instrumentation of the full scale wall captures the failure plane and records the important distress mechanisms. Construction of the small scale walls also allow the verification and calibration of the FLAC model and the constitutive properties, and will provide an assessment of the variability between two similar walls constructed using the same procedures.

6.2 MATERIAL PROPERTIES

6.2.1 HDPE GEOGRID PROPERTIES

The properties of UX-1400 HDPE geogrid are presented in table 6.1 Based on the information provided by the manufacturer, the life expectancy is 75 years.

6.2.2 PET GEOGRID PROPERTIES

The measured dimensions and properties of the Miragrid 3XT are shown in Table 2.2. Based on the information provided by the manufacturer, the life expectancy is 75 years.

Table 6.1. Properties of UX-1400 HDPE geogrid

Properties	Test methods	Units	Value
Apertures: MD	Calipered	mm	144.8 (nom.)
CDM	Calipered	mm	16.7 (nom.)
Open area	COE Method	%	60 (nom.)
Thickness: ribs	ASTM D1777-64	mm	0.76 (nom.)
junctions	ASTM D1777-64	mm	2.8 (nom.)
Creep Limited Strength	GRI GC3-87	kN/m	20.7 (min.)
Flexural Regidity	ASTM D1388-64	mg-cm	6600000 (min.)
Tensile Modulus MD	GRI GG1-87	kN/m	737.7 (min.)
Junctions: strength	GRI GG2-87	kN/m	49 (min.)

Table 6.2. Properties of the Miragrid 3XT geogrid

Properties	Test methods	Units	Value
Mass/Unit Area	ASTM D5261-92	g/m^2	203
Aperture size MD		mm	20
CDM		mm	27
Ultimate Tensile Strength	ASTM D-4595	kN/m	40.9
Creep Limited Strength	ASTM d 5262		24.5
Tensile strength at 5 % strain	ASTM D-4595	kN/m	39
at 5 % strain	GG3	kN/m	15.4
Long term allowable design load	GRI GG-4	kN/m	19.4

6.2.3 SOIL

The soil used is very common in South Florida and was classified as **SP** (poorly-graded sands and gravely sands, little or no fines) in **Class II** (coarse-grained one, clean) [ASTM D2321 and D2487].

6.2.3.1 Sieve analysis

The Grain Size Distribution curve, or percentages of the total weight of soil that passed through different sieves are plotted in Fig. 6.1

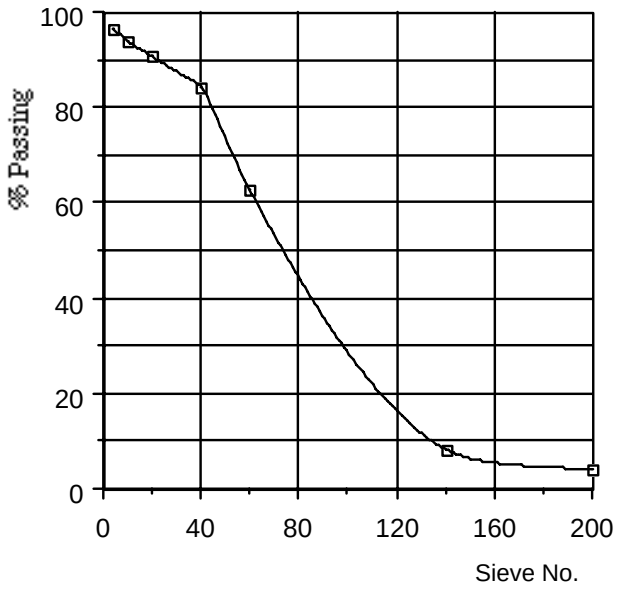

Figure 2.1 Sieve analysis of the South Florida soil sample

The coefficient of uniformity, C_u=3.75 < 6, and the coefficient of curvature, C_c=0.82 < 1, were calculated by Eqs. 6.1 and 6.2.

$$C_u = D_{60}/D_{10} \tag{6.1}$$

$$C_c = \frac{(D_{30})^2}{(D_{10} \times D_{60})} \tag{6.2}$$

D_{10}, D_{30}, and D_{60} are the particle size diameters corresponding to 10, 30, and 60%, respectively, in the cumulative particle size distribution curve.

6.2.3.2 Soil compaction

Laboratory Standard Proctor Tests (Standard Proctor Test, ASTM D698) were carried out prior to the in-situ compaction tests, and the relationship between the dry unit weight and moisture content of the soil was evaluated (Fig. 2.2). It was found that the maximum dry unit weight was 16.51 kN/m^3 (105 lb / ft^3) and the optimum moisture content was 10.5%.

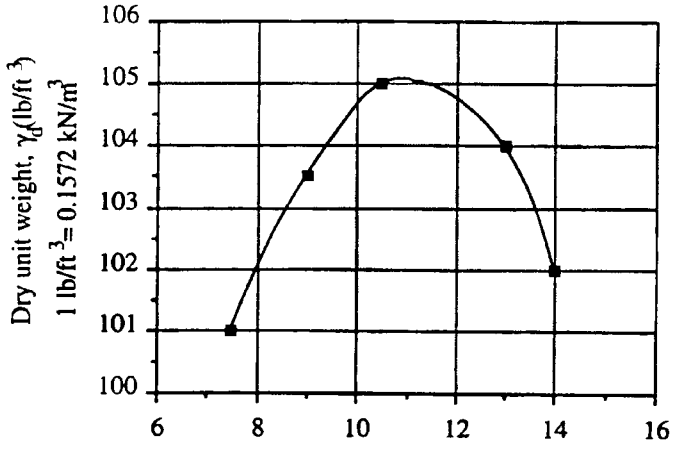

Figure 6.2 Plot of dry unit weight vs. moisture content

6.2.3.3 Angle of friction

A direct shear test was carried out to determine the angle of friction of the soil. The samples for the direct shear tests were prepared at 95-100% of the modified proctor compactor maximum dry density (AASHTO T-180). The shear strength for sand can be expressed by the following equation:

$$s = \sigma' \tan \phi \quad (6.3)$$

where

s = shear strength

σ'= effective normal stress

ϕ = angle of friction

The machine used for the direct shear test was an ELE D-300A Direct/Residual Shear Machine. The results are for a South Florida SP Class II soil, with area = 0.003117 m^2, weight = 0.094 kg, with the following normal loads: a) 98.5 kPa, b) 193.6 kPa, and c) 387.2 kPa. The results are shown in the following Tables (6.3 through 6.8).

Table 6.3. Shear Stress for Normal Stress = 96.8 kPa , Test-1A

Horizontal displacement	Vertical displacement	No of div. in proving ring dial gage	Shear force (N)	Shear stress (KPa)
0.1	-0.03	25	78	24.9
0.2	-0.04	36	112	35.9
0.3	-0.04	43	134	42.9
0.4	-0.04	47	146	46.9
0.5	-0.04	51	159	50.9
0.6	-0.04	56	174	55.9
0.7	-0.04	59	183	58.9
0.8	-0.03	61	190	60.9
0.9	-0.01	62	193	61.9
1	0	63	196	62.9

1.1	0.01	64	199	63.9
1.2	0.02	66	205	65.9
1.3	0.03	67	208	66.8
1.4	0.04	67	208	66.8
1.5	0.06	68	211	67.8
1.6	0.07	68	211	67.8
1.7	0.08	69	215	68.8
1.8	0.1	69	215	68.8
1.9	0.11	69	215	68.8

Table 6.4. Shear Stress for Normal Stress = 193.6 kPa, Test-1B

Horizontal displacement	Vertical displacement	No of div. in proving ring dial gage	Shear force (N)	Shear stress (KPa)
0.1	-0.01	56	174	55.9
0.2	-0.01	75	233	74.8
0.3	0.01	88	274	87.8
0.4	0.02	96	299	95.8
0.5	0.04	104	323	103.8
0.6	0.06	109	339	108.8
0.7	0.08	116	361	115.7
0.8	0.1	118	367	117.7
0.9	0.12	121	376	120.7
1	0.14	122	379	121.7

1.1	0.17	122	379	121.7
1.2	0.18	123	383	122.7
1.3	0.2	123	383	122.7
1.4	0.22	123	383	122.7
1.5	0.24	123	383	122.7
1.6	0.24	122	379	121.7

Table 6.5. Shear Stress for Normal Stress = 387.2 kPa, Test-1C

Horizontal displacement	Vertical displacement	No of div. in proving ring dial gage	Shear force (N)	Shear stress (KPa)
0.1	-0.04	142	442	141.7
0.2	-0.05	161	501	160.6
0.3	-0.045	195	606	194.6
0.4	-0.045	225	700	224.5
0.5	-0.045	234	728	233.5
0.6	-0.04	251	781	250.4
0.7	-0.03	258	802	257.4
0.8	-0.02	264	821	263.4
0.9	-0.01	267	830	266.4
1	-0.005	269	837	268.4
1.1	0.005	271	843	270.4
1.2	0.015	273	849	272.4
1.3	0.025	275	855	274.4

1.4	0.04	276	858	275.4
1.5	0.05	277	861	276.4
1.6	0.06	277	861	276.4
1.7	0.07	276	858	275.4

Table 6.6. Shear Stress for Normal Stress = 96.8 kPa , Test-2A

Horizontal displacement	Vertical displacement	No of div. in proving ring Dial gage	Shear force (N)	Shear stress (KPa)
0.1	-0.03	17	53	17.0
0.2	-0.04	21	65	21.0
0.3	-0.05	22	68	22.0
0.4	-0.055	24	75	23.9
0.5	-0.07	44	137	43.9
0.6	-0.075	51	159	50.9
0.7	-0.08	53	165	52.9
0.8	-0.075	60	187	59.9
0.9	-0.065	66	205	65.9
1	-0.055	70	218	69.8
1.1	-0.04	73	227	72.8
1.2	-0.03	75	233	74.8
1.3	-0.02	76	236	75.8
1.4	0	77	239	76.8
1.5	0.01	78	243	77.8

1.6	0.02	78	243	77.8
1.9	0.06	78	243	77.8

Table 6.7. Shear Stress for Normal Stress = 193.6 kPa, Test-2B

Horizontal displacement	Vertical displacement	No of div. in proving ring dial gage	Shear force (N)	Shear stress (KPa)
0.1	-0.02	44	137	43.9
0.2	-0.04	81	252	80.8
0.3	-0.05	101	314	100.8
0.4	-0.04	112	348	111.7
0.5	-0.03	120	373	119.7
0.6	-0.02	124	386	123.7
0.7	-0.01	127	395	126.7
0.8	0	128	398	127.7
0.9	0.01	131	407	130.7
1	0.03	132	411	131.7
1.1	0.04	132	411	131.7
1.2	0.06	133	414	132.7
1.3	0.08	133	414	132.7
1.4	0.09	133	414	132.7
1.5	0.1	132	411	131.7

Table 6.8. Shear Stress for Normal Stress = 387.2 KPa, Test-2C

Horizontal displacement	Vertical displacement	No of div. in proving ring dial gage	Shear force (N)	Shear stress (KPa)
0.1	-2	132	411	131.7
0.2	-4	170	529	169.6
0.3	-4	210	653	209.5
0.4	-3	233	725	232.5
0.5	-1	249	774	248.4
0.6	0	263	818	262.4
0.7	3	272	846	271.4
0.8	5	276	858	275.4
0.9	8	280	871	279.4
1	9	282	877	281.4
1.1	11	284	883	283.4
1.2	13	284	883	283.4
1.3	14	283	880	282.4
1.4	15	282	877	281.4
1.5	17	281	874	280.4
1.6	19	279	868	278.4

From these results the Shear Stress " s " vs. Normal Effective Stress " σ' " table (Table 6.9) and graph (Fig. 6.3) were obtained.

Table 6.9. Shear Stress " s " vs. Normal Effective Stress " σ ' "

Normal stress (kPa)	Shear stress Test 1 (kPa)	Shear stress Test 2 (kPa)
98.5	68.8	77.8
193.6	122.7	132.7
387.2	276.4	283.4

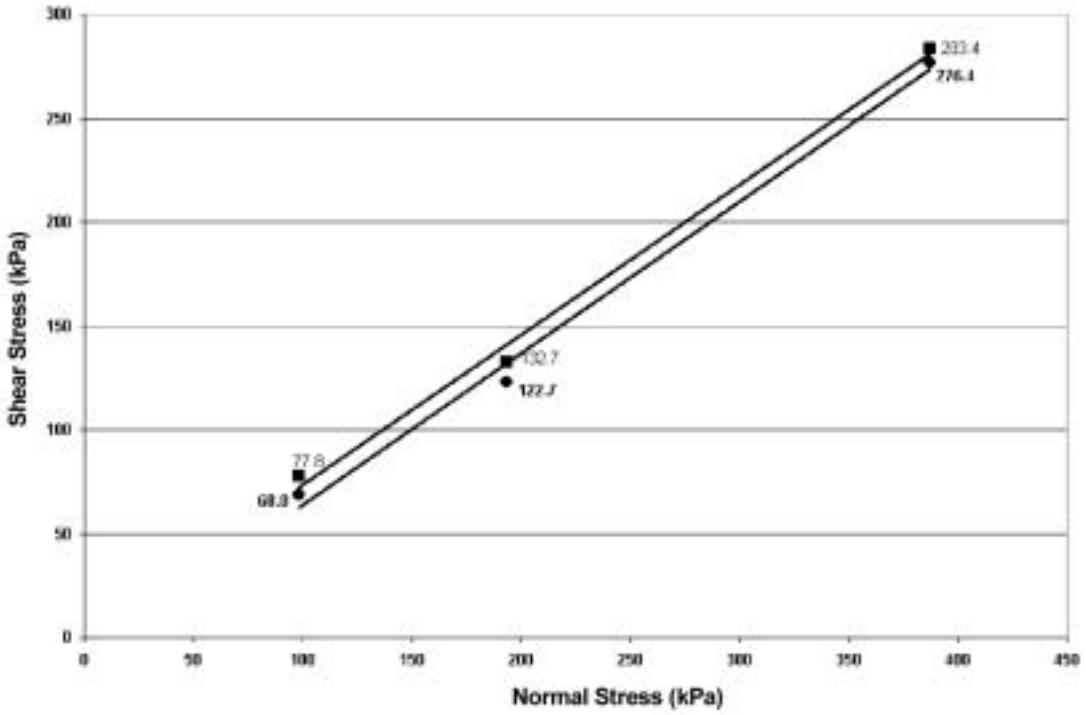

Figure 6.3. Shear Stress " s " vs. Normal Effective Stress " σ' "

From this graph the angle of friction was found by calculating the slope of the best fit lines. The corresponding calculations are shown in Table 6.10. From this, it was concluded that the angle of friction for the soil is 36 °.

Table 6.10. Angle of friction " ϕ " calculations

Normal stress kPa	Shear stress Test 1 (kPa)	Shear stress Test 2 (kPa)
100	63.7	73.4
400	282.8	290.4
	Angle of friction	Angle of friction
	36.1°	**35.8°**

6.2.4 FACING UNITS

The facing units were fabricated of 1/2" thick clear lexan with $E = 2.38 \times 10^9$ Pa. The dimensions were 11" high x 10.5" wide.

6.2.5 FACING SEPARATORS

To simulate the rubber separators used in MSE walls with concrete facings, pieces of the HDPE geogrid were cut to 1" length and sandwiched between the rows of facings.

6.2.6 PROTECTION AGAINST SAND EROSION

In the construction of MSE walls with concrete facings, geotextile is used to cover the gaps between facings to avoid sand erosion and to allow water drainage. Since the small-scale MSE wall experiment was covered to prevent any rain from getting onto the wall, clear plastic (1mm thick) covered the gaps between facings and was sufficient to prevent any sand migration.

6.3 TEST SETUP

6.3.1 LOADING FRAME

The dimensions of the loading frame were designed to accommodate a 1:5 scale experiment. However, due to practical limitations in the construction dimensions of the small scale wall and the full scale wall (to be discussed later in Chapter 8 of the report), the actual design dimensions were slightly different from the ideal design values. Therefore, the actual scale of the model walls was established at 1:5.5, with the height of the scaled walls being 1.11 m. Taking into consideration the maximum dimensions of the small-scale MSE wall, the frame was fabricated by modifying an available loading chamber for soil, which is shown in Figure 6.4.

Figure 6.4 Loading frame

A schematic of the small-scale loading frame is shown in Figs. 6.5 and 6.6. Plane Strain conditions were ensured with a stiffening grid on the steel crossing wall and a lubricated plastic placed in front of a sheet of clear lexan.

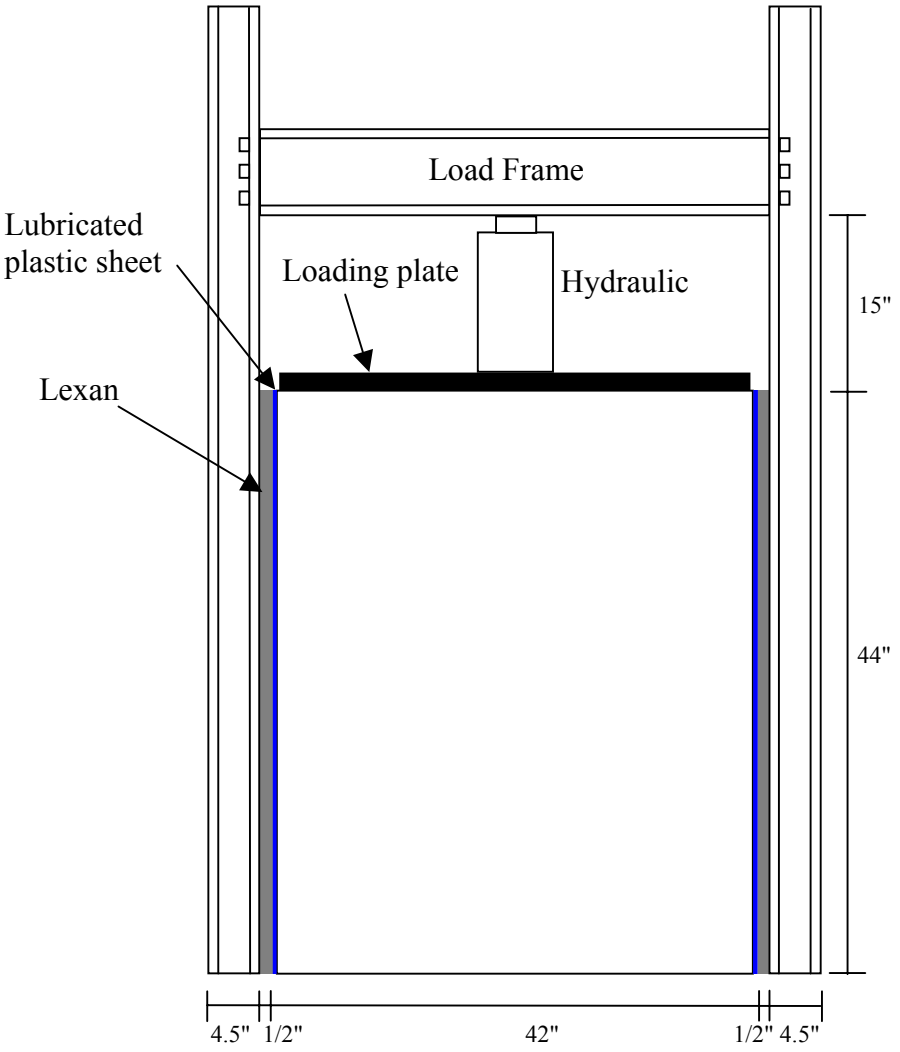

Figure 6.5 Front view of loading frame for small-scale MSE wall testing

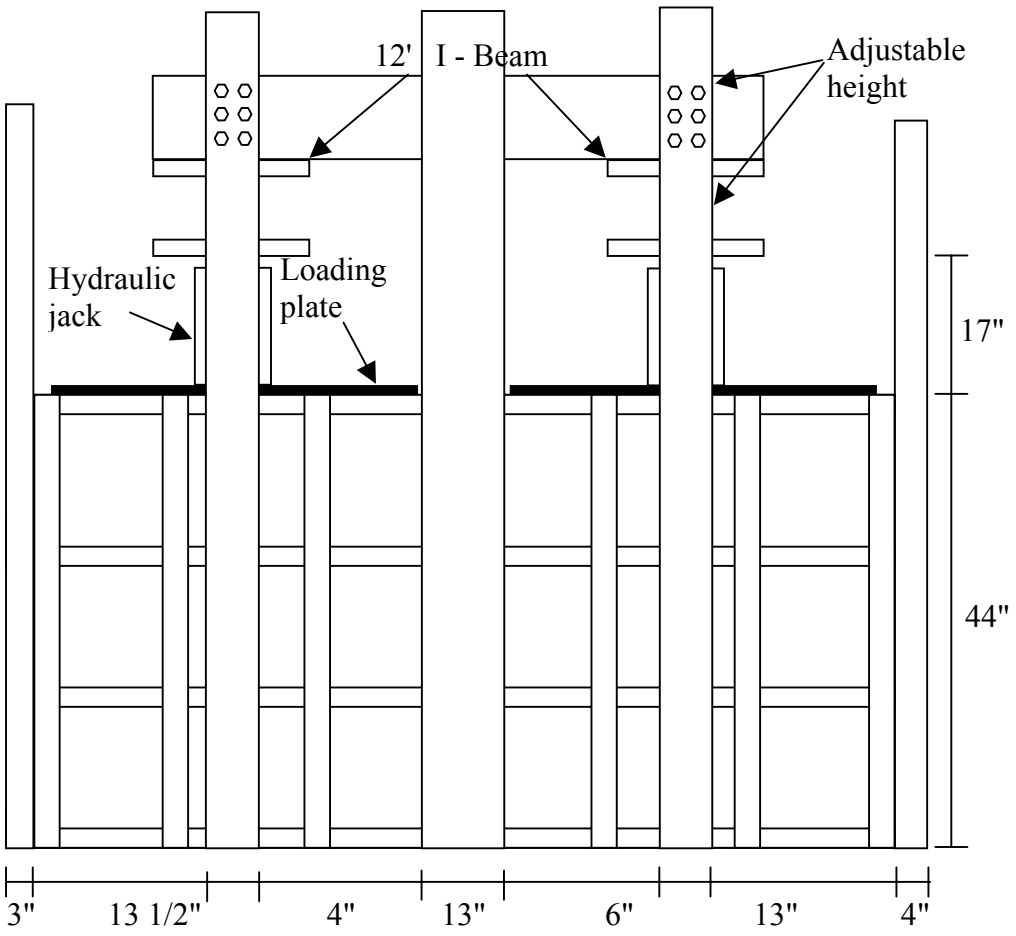

Figure 6.6 Side view of loading frame for small-scale MSE wall testing

6.3.2 INSTRUMENTATION

A schematic of the location of the instrumentation is presented in Figure 6.7.

6.3.2.1 Data acquisition system

After extensive evaluation on the measurement equipment, a Vishay System 5000 from Measurements Group, Inc., with 40 channels was acquired. Training for the operation of the system was carried out at Measurements Group, Inc., facilities in Raleigh, North Carolina.

In addition, two Digital Strain Indicators, Model P-3500, and a Switch and Balance Unit, Model SB-10 from Measures Group, Inc., were used. The Indicator is a portable, battery-powered instrument using strain-gage-based transducers. The Switch and Balance Unit has 10 channels with an open position to allow the use of additional SB-10's with a single P-3500 Strain Indicator.

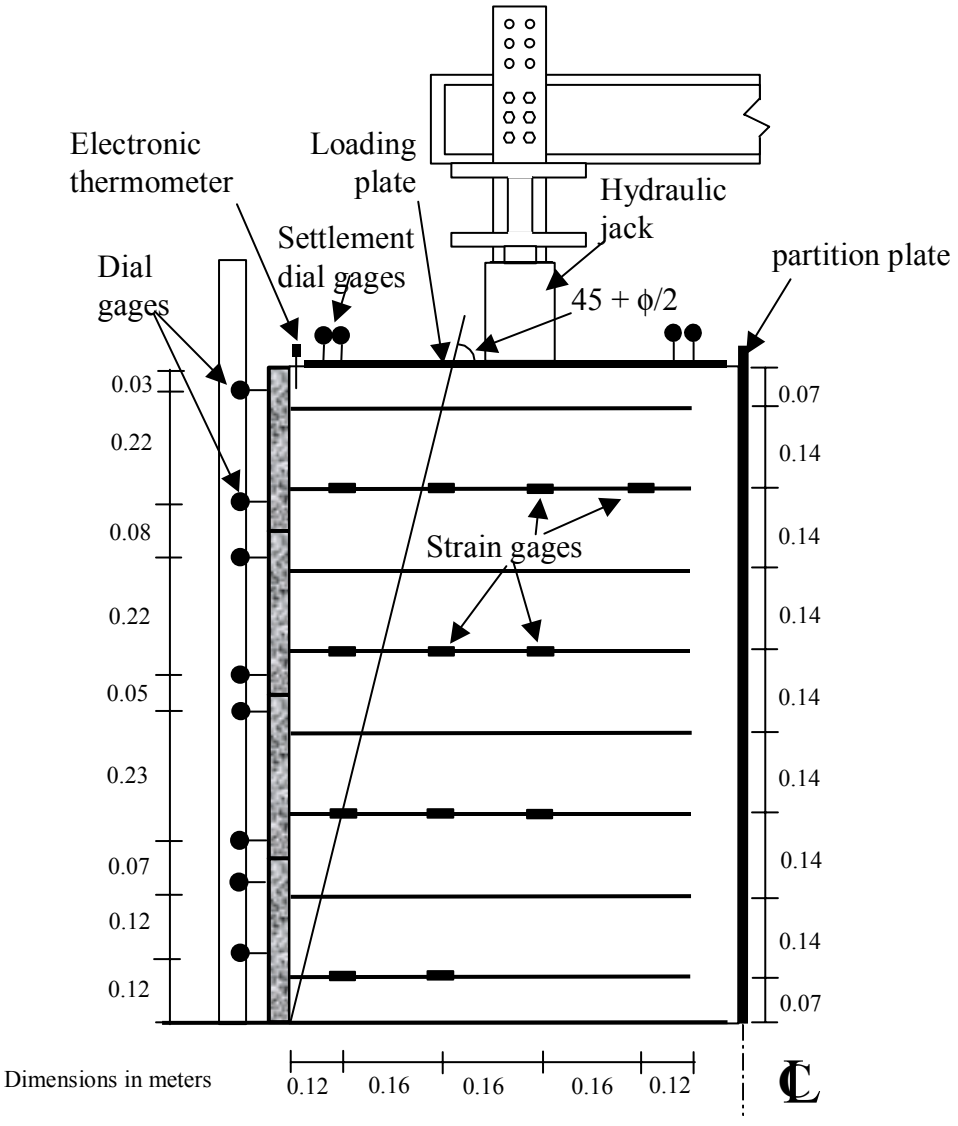

Figure 6.7. Small scale MSE wall instrumentation.

6.3.2.2 Strain gages

Strain Gages-YFLA-2-3L from Tokyo Sokki Kenkyujo were used for strain measurement. The gage utilizes a special plastic carrier base that is able to withstand extreme elongation without creeping or cracking, and is capable of measuring a strain of 10 to 20% with the needed accuracy. Extensive testing was carried out for the bonding and calibration of the strain gages.

6.3.2.3 Miscellaneous Agents for strain gages

Glue: Adhesive Type CN, Cyanoacrylate Base product from Yokyo Sokki Kenkyijo Co., Ltd, was used. The operating temperature ranges from –30°C to 100°C under curing pressure 980 kPa. It has a strain limit of 20 % and excellent electrical properties.

Degreaser: Type CSM-1A, a 1-1-1 Trichloro-ethylene solvent product of the Micro-Measurements Division of Measures Group, Inc, was used to degrease the surface of the test specimen because of its inertness to polyethylene. The degreaser prevents the embedding of contaminants on the surface of the geogrid specimen.

Neutralizer: Type MN5A-1, a mild ammonia solution that leaves the test specimen with a slightly alkaline pH value, a product of Micro-Measurements Division of Measures Group, Inc., was used.

ARON Polyprimer: Used only for the PET geogrid, this is a surface preparation agent that allows cyanoacrylate adhesives, such as TML type CN, to be used for strain gage bonding on polyethylene and polypropylene. It is a product of Yokyo Sokki Kenkyijo Co., Ltd.

Coating Material: A single-component microcrystaline wax was used to form a good moisture- and water-resistant coating.

Silicon cover: Marine glue 5200 was used to cover the coated strain gages for extra protection.

Plastic tubing: Clear plastic tubing (1/2" in diameter) was used for final protection of the strain gages.

6.3.2.4 Dial gages

Twenty-four Dial Gages (MSC 76450071) with a measuring range of 2” and a least count of 0.001” were used to measure panel displacements and loading plate settlement.

6.4 TEST PROCEDURES

6.4.1 GEOGRID PREPARATION

6.4.1.1 Trimming the Geogrid Specimens

The HDPE geogrid specimens were cut to a single rib, and the transverse ribs cut to 5/8 inches. For PET geogrids, the specimens were also cut to a single rib; additionally, the effective length (L_e) of the two ribs was reduced 31 %, and the transverse ribs were cut off In both cases these values gave the desired scaling of 1 to 5.5 of the pullout force.

6.4.1.2 Specimen Surface Preparation

The procedure below was followed to prepare the surface of the specimen:

1) Remove grease, scale, dust, paint, *etc*., from the bonding area.

2) Spray the gage location with degreaser and wipe clean with a gage sponge.

3) Grind an area somewhat larger than the bonding area uniformly and finely with No. 400 abrasive paper. Sand the surface first at 45° angle to the direction of testing, and then at right angles to get a pattern of cross hatches.

4) Clean the gage area with compressed air to remove any particles left by sanding operation.

5) Wipe the ground area with neutralizer. Wiping should be done untill the cleaning tissue is contaminant-free.

6) After surface preparation, attach the strain gage before the prepared surface is oxidized or is contaminated.

6.4.1.3 Bonding Procedures

1) Apply the required amount of the adhesive on the back of the gage base. The amount of adhesive is two drops (increased as needed).

2) Spread the adhesive on the back of the gage thinly and uniformly using an adhesive nozzle.

3) Use a polyethylene sheet and press down the gage constantly with the thumb. The work has to be done quickly as curing is completed very fast.

4) The curing time depends on the test specimen, temperature, humidity, and pressing force. In this test, the curing time was set to be 48 hours.

6.4.1.4 Gage Waxing Operation

A coating material, type W-1, produced by Yokyo Sokki Kenkyijo Co., Ltd., was used for moisture and water-proofing of the strain gages bonded on the test specimen surface. W-1 wax is light-yellow-colored micro-crystalline wax that can be used immediately after heat-melting.

1) Put W-1 wax in an oil bath with temperature adjustment and melt it completely at 100°C ~ 120°C. The melted W-1 is a light yellow transparent liquid.

2) Dip the tip of a brush in the melted W-1 for warming.

3) Soak the brush tip in the melted W-1 and apply it at once over the strain gage and extruded adhesive. W-1 hardens as soon as it cools and turns cloudy yellow.

4) As the once-used brush cools due to heat absorption of the test specimen, repeat steps (2) and (4) until application is complete.

6.4.1.5 Gage Protection

A plastic tube with a diameter slightly larger than the width of the gage was used to cover the gage. As the gage was embedded in the soil under both the confining pressure and the pullout force, proper coverage was needed to prevent damage of the strain gage.

6.4.1.6 Clamps (Models A and B)

Two kinds of clamps were used to fasten the test specimens. All clamps were stiff enough to assure a uniform pullout displacement across the width of the test specimens. Clamp A was used for geogrid HDPE (Fig. 6.8). It had two identical jaws with unique

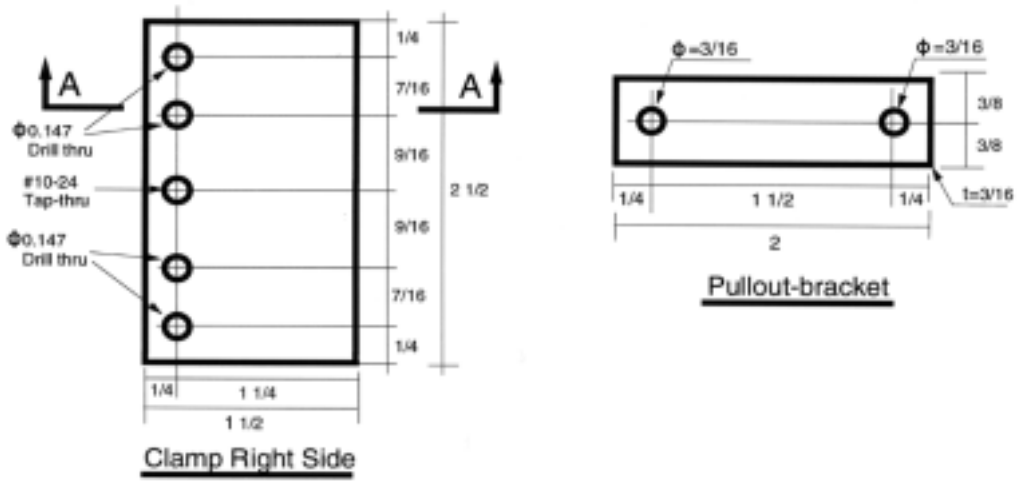

Note:

1. Materials: stainless steel. #304
2. Dimension unit: in. (1in. = 25.4mm)
3. The surface should be smooth but frosted.
4. There are two pullout- brackets in all.

Figure 6. 8 Clamp "A" for HDPE specimens

contours that fit the specimen very well. The inner corner of the front lip was rounded well to assure that the specimen would not be split. The space between the upper and lower lips was big enough to let the specimen to be pushed in transversely, but small enough to prevent it from sliding out.

Clamp B (Fig. 6.9), used for geogrid PET, was comprised of three identical plates. All the surfaces were well frosted to provide good fastening ability. The test specimen was wrapped around the plates. All plate edges were filleted to give a smooth surface. A design change was made from a circular clamp, which was producing stress concentration in the geogrid.

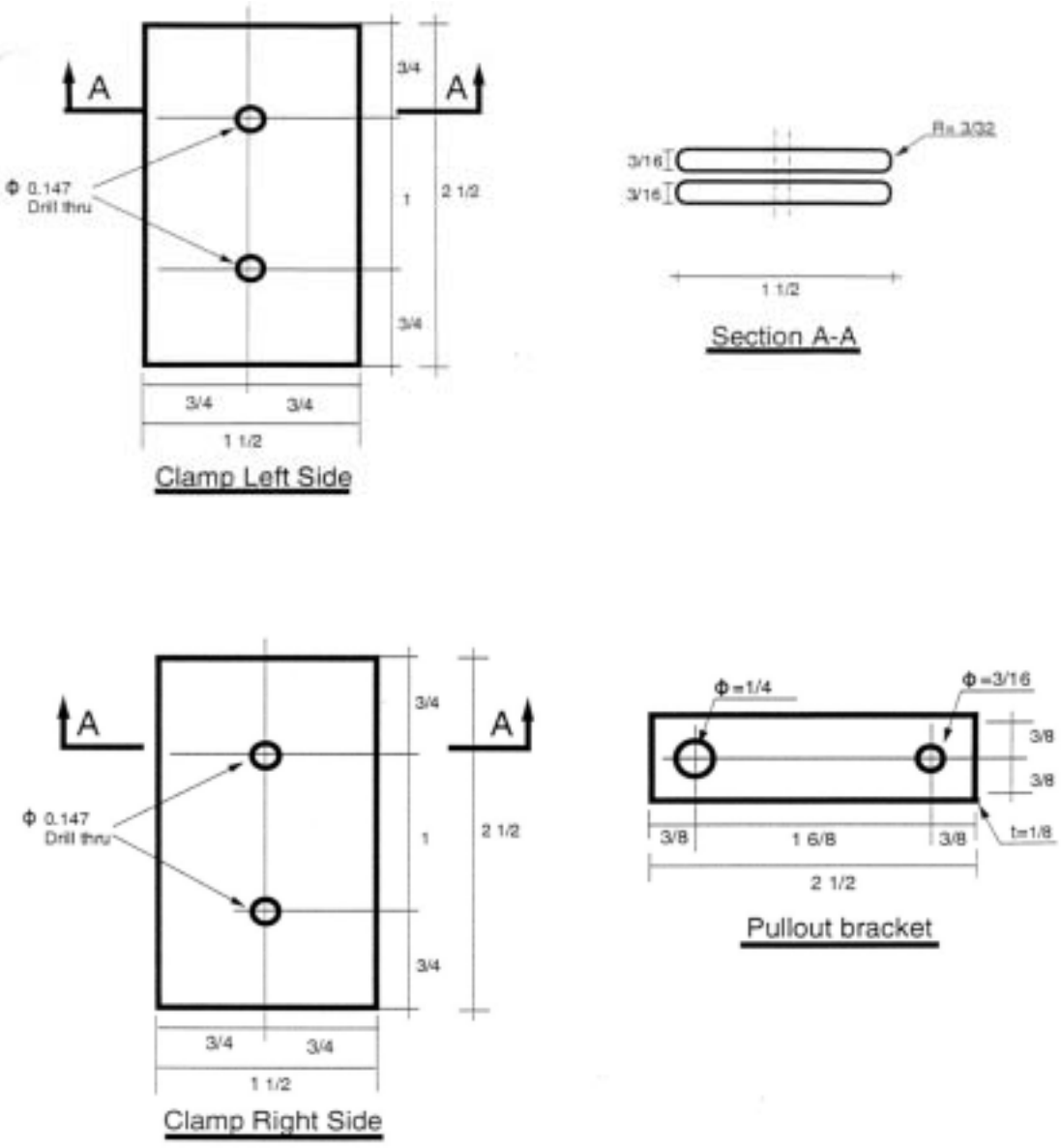

Note:

1. Materials: stainless steel. #304
2. Dimension unit: in. (1in. = 25.4mm)
3. The surface should be smooth but frosted.
4. There are four pullout brackets in all.

Figure 6.9. Clamp "B" for PET specimens

6.4.1.7 Clamping the Test Specimen

After clamping and bolting, four brackets were connected. Figure 6.10 shows the HDPE and PET clamping.

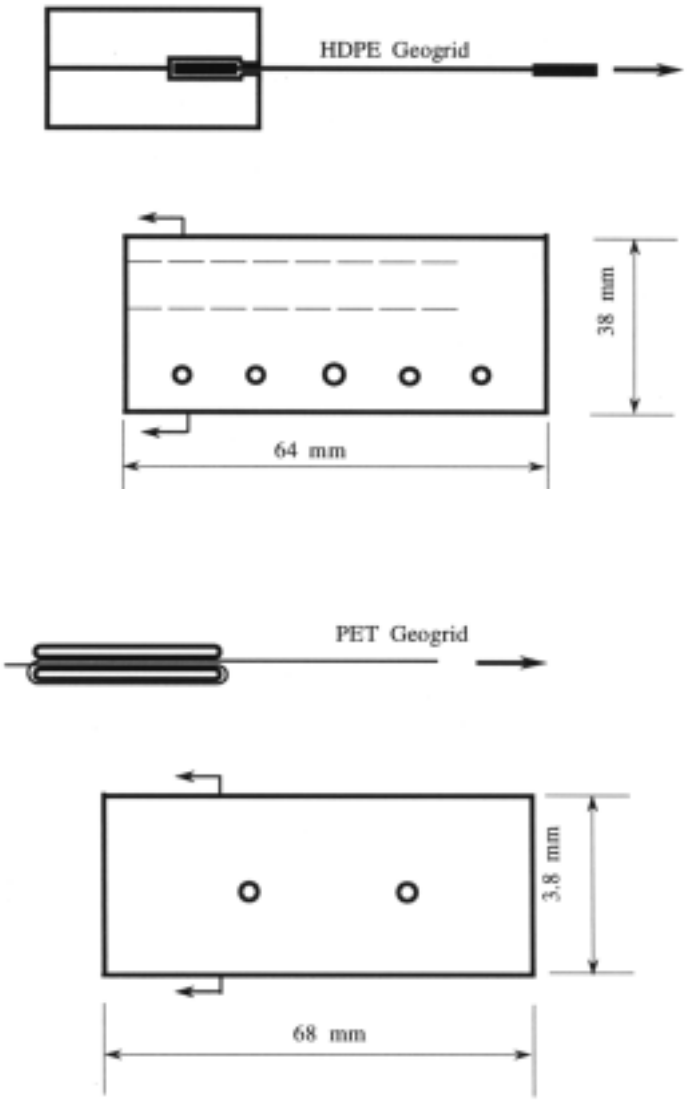

Figure 6.10. HDPE and PET clamping

6.4.1.8 Clamp/facing connection

The HDPE clamps were attached to the facing with two screws running through the facing and into two tap holes in the upper face of the clamps. For the PET clamps, the same screws used to tighten the clamps went through the facing to tie them together.

6.4.2 CONSTRUCTION PROCESS

The tank was cleaned thoroughly. Particular attention was paid to the lexan sheet. The next step was to spray WD-40 on the lexan sheets followed by placing a 3mm plastic sheet to avoid any friction between the soil and the side of the test frame. Next, vertical supports and the first two rows of horizontal supports were placed. This was followed by the placement of the first row of facings, which were aligned and secured to avoid horizontal movement resulting from the placement of the sand.

The next step was to place an 8.9 cm (3.5") layer of sand, which was compacted with a hand compactor to 95-100% maximum relative compaction (Modified Proctor AASHTO T−180) within the range of optimum moisture content. Once the compaction was obtained, the sand was leveled to the height of the first layer of geogrid. The HDPE geogrid was placed in the clamp which had previously been fixed to the facing panel. The PET geogrid was placed in the clamp and then attached to the facing.

The geogrids were pulled away from the facings to eliminate any slack, and some soil was placed on top of the geogrid to keep it tensioned. Next, a soil layer 17.8 cm (7") thick was placed, compacted, and leveled to the height of the next layer of geogrid. Again the geogrid was placed, tensioned and covered with a 7.6 cm (3") layer of soil that was compacted and

leveled to the upper edge of the first row of facings. Next, the third and fourth rows of supports were placed, and the second layer of facings put in place. After this, the process was repeated until the full height of four facings (1.11 m) was reached.

Figures 6.11 and 6.12 show the finished HDPE and PET walls. At the end of construction, the strain gages were read. Once the supports had been removed, the dial gages were installed, and readings of both the strain and dial gages were taken; the wall was left unloaded for 24 hours. Next, the loading plate and an additional load of 133 N were placed on top of the wall for a total surcharge of 0.8 kPa. This is equivalent to 1/5.5 the loading used in the prototype wall, which is 4.4 kPa, equivalent to twice the AASHTO HS-20 Highway Truck Loading (40 tons). This loading was kept for 48 hours, after which a loading jack was placed on each wall with an additional 2113 N to obtain a total surcharge of 3.64 kPa, which is 1/5.5 of the design surcharge of 20 kPa. This surcharge was kept for 72 hours.

The next surcharge level was 6.4 kPa; after 72 hours the wall surcharge was increased with the hydraulic jacks in increments of 5.13 kPa. Each surcharge level was kept for 72 hrs, and readings were taken every day except on a couple of occasions due to rain. Once a surcharge of 21.8 kPa had been reached, the surcharge was increased with increments of 10.26 kPa up to 83.4 kPa, at which stage the experiment was stopped due to the large deformation.

Figure 6.11. Finished small-scale MSE wall for HDPE geogrids

Figure 6.12. Finished small-scale MSE wall for PET geogrids

7 SMALL SCALE TESTING RESULTS AND ANALYSIS

7.1 TEST RESULTS

7.1.1 INTRODUCTION

The results are presented for strains in the first, third, fifth and seventh geogrid layers connected to the second facing from left to right to avoid any influence of the boundary with the test side walls. The distance between strain gages was 0.16 m as shown in Fig. 6.7. Panel displacements are given for the same second facing having for the two dial gages as shown in Fig. 6.7. The settlement was measured with four dial gages supported on the sides of the test frame monitoring the movements of the four corners of the loading plate. These measurements were averaged to obtain the overall settlement of the plate.

7.1.2 STRAIN IN REINFORCEMENT

The strains were the average of those measured in the two strain gages, located one in the upper face and one in the lower face of the geogrid. This prevents possible distortion of the readings due bending of the geogrid. As seen in Figure 6.7, the location of strain gages was selected to follow roughly the Rankine plane of failure. The results presented in Figs. 7.1 and 7.2 are for the two walls tested for each geogrid type and for a surcharge of up to 83.4 kPa with the loading schedule described in section 6.3.2. The data for wall number one is presented with solid lines and wall number two with dotted lines.

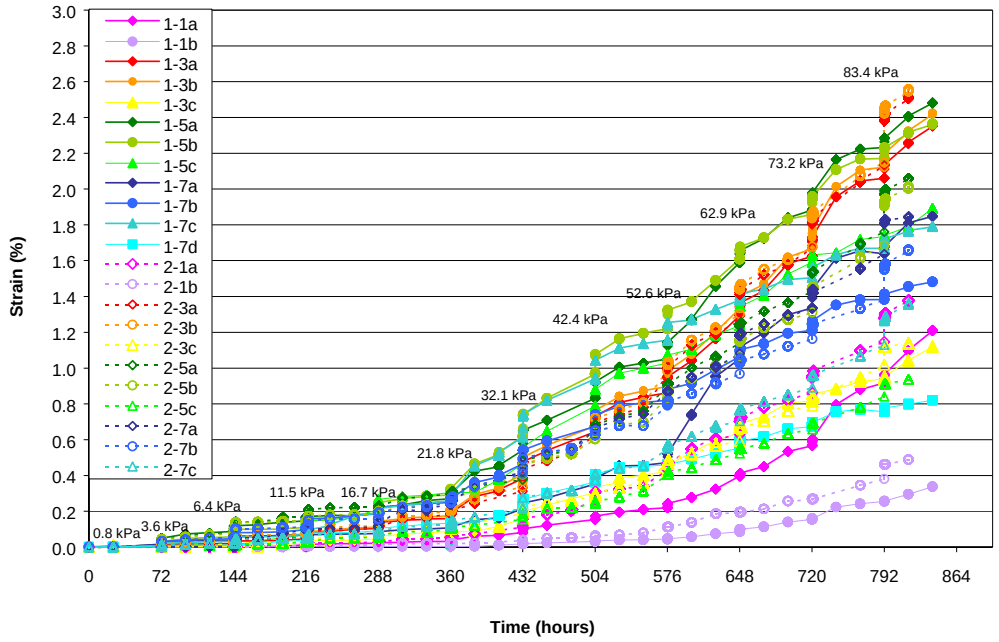

Figure 7.1. Strains in reinforcement for HDPE small-scale MSE wall

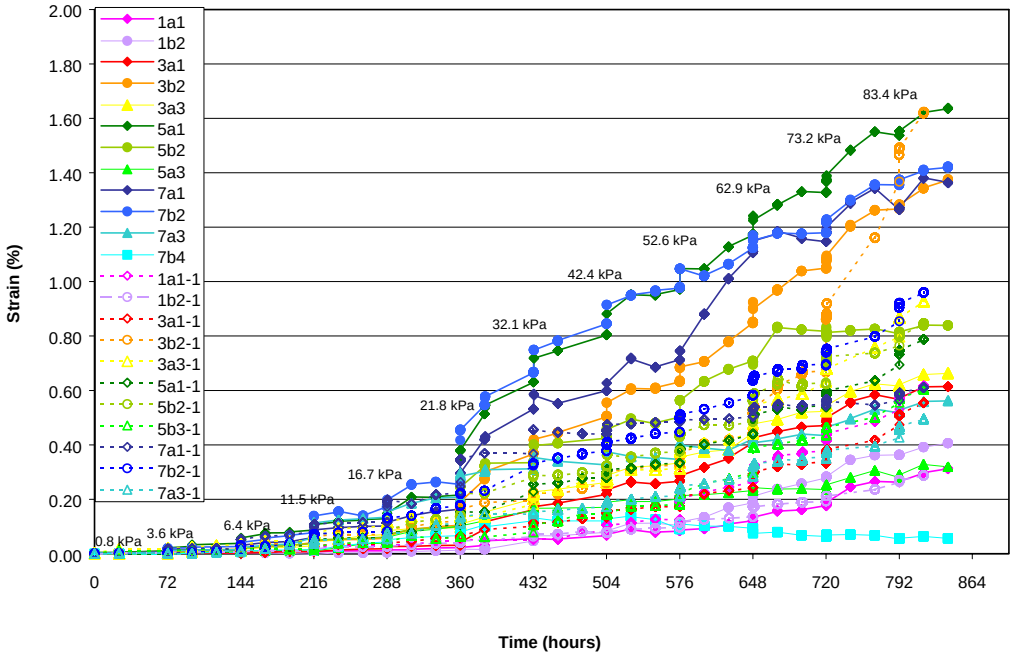

Figure 7.2. Strains in reinforcement for PET small-scale MSE wall

It can be observed from Figures 7.1 and 7.2 that for a surcharge of up to 16.7kPa, most of the strain due to creep was obtained during the first 24 hours of each load increment. For larger surcharge levels, most of the strain was obtained in the first 72 hours of each load increment, so the intervals chosen for increasing the surcharging seem to be adequate. This is evident in that the strain rate is sharper at the beginning of each new load addition, then decreases with time. At the same time, after the surcharge of 21.8 kPa, nonlinear behavior was observed. For this reason it was decided to take the surcharges up to 16.7 kPa for comparison with the computer modeling.

It can be seen that the strains are similar in the HDPE geogrids and in the PET geogrids for surcharges up to 16.7 kPa. For surcharges higher than 16.7 kPa, there was more strain in the HDPE geogrids than in the PET when specimens were subjected to critical conditions above normal usage. The maximum strain in the HDPE geogrids was 3.5% while for the PET geogrids it was 1.9%.

Comparing the first and second walls tested, it can be observed that there is very good agreement in the deformation behavior of both the HDPE and PET MSE walls. The maximum strains were obtained in first two strain gages in layer 3 and the three strain gages in layer 5. The locus of maximum tension or "plane of failure" obtained taking the 83.4 kPa surcharge, for example, is presented for the HDPE and PET geogrid MSE walls in Figures 7.3 and 7.4. From these figures, it can be observed that the curved surface of failure differs slightly from the Rankine plane of failure. The "failure planes" for the HDPE and PET MSE walls were very similar. These observations are based on the distribution of strain measured at the gage locations. Figure 7.3 shows the strains at the gage location for a surcharge of 83.4 kPa for the

walls reinforced with HDPE geogrids. The strains are reported for both Wall 1 and Wall 2. It can be observed that the strain measurement for both walls were very similar. Specifically, the locus of maximum strains agrees well for both walls.

For the walls reinforced with PET geogrids, Fig. 7.4 shows the same tendency. The plain of failure was drawn considering the location of the maximum strains with both walls each geogrids reinforcement type and trying to keep a consistent line between the points in both figures. An exception is evident for one of the gages in layer 5, where the maximum strain occurred near the facing. However, the overall trend suggests that the "failure" plane differs from the Rankine failure plane.

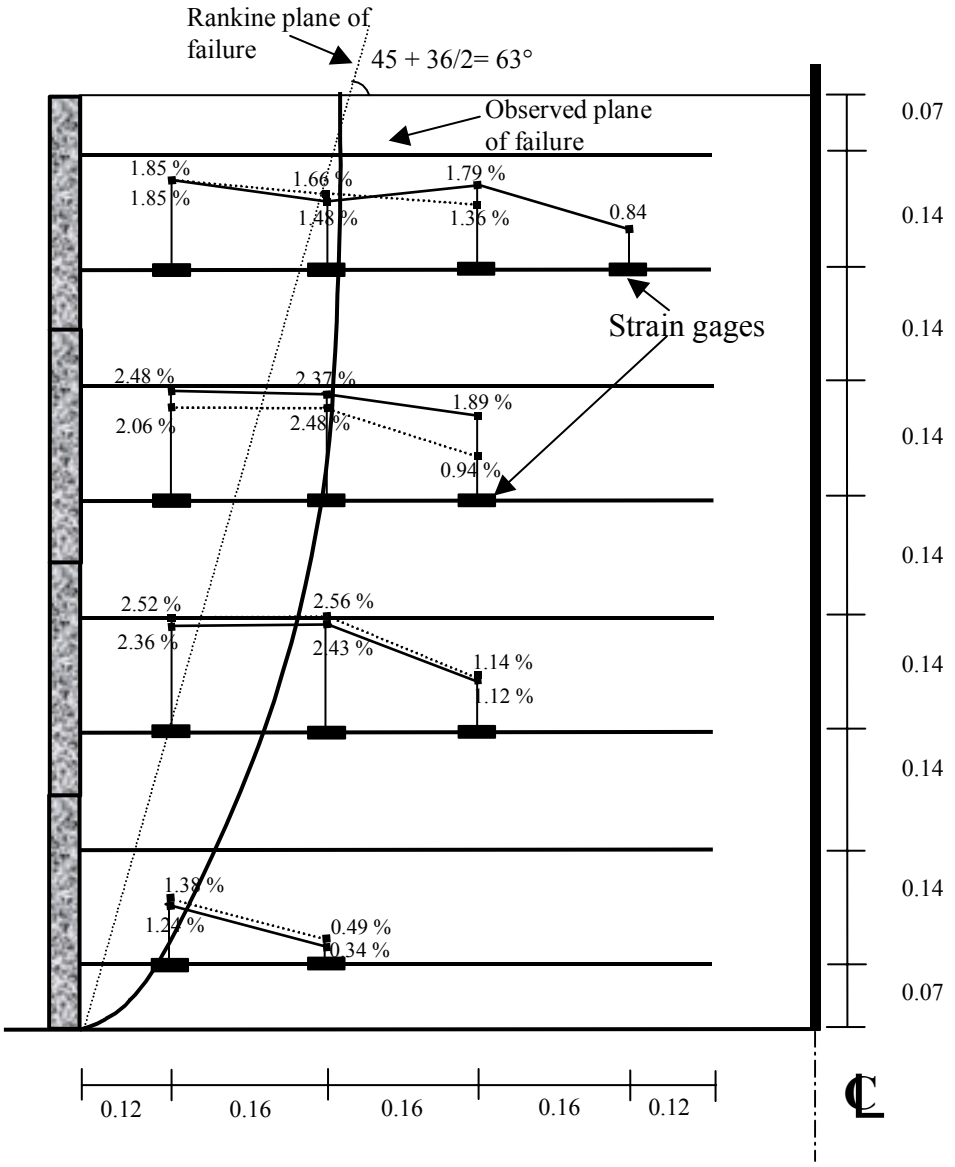

Figure 7.3. Observed vs Rankine planes of "failure" for HDPE geogrid for 83.4 kPa surcharge load

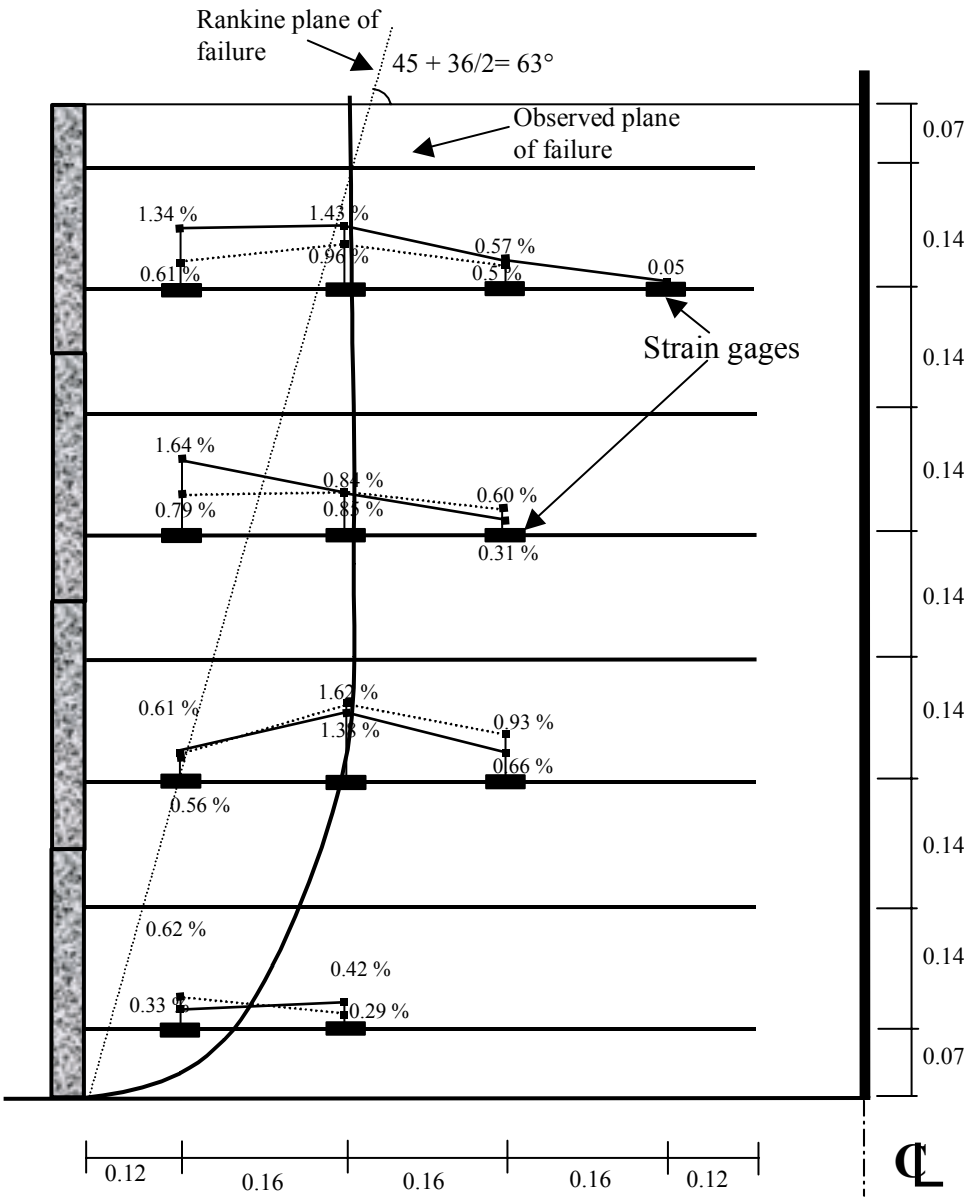

Figure 7.4. Observed vs Rankine planes of failure for PET geogrid for 83.4 kPa surcharge load.

7.1.3 PANEL DISPLACEMENTS

The panel displacements for the MSE walls reinforced with HDPE and PET geogrid are shown in Figs. 7.5 and 7.6. They are presented for all the surcharge loads in the same manner as for Figures 7.1 and 7.2. For the HDPE MSE walls, the maximum displacement was found in the second and third panels and the bottom of the fourth panel; this agrees with the strain results. There was good agreement between the two walls tested up to a surcharge of 21.8 kPa. After this point, Wall 1 had larger deformations than Wall 2 (Fig 7.7).

For the PET MSE walls, there was also good agreement for surcharges up to the 21.8 kPa. As in the HDPE wall, the maximum displacements were in the second and third panels and the bottom of the fourth panel. For both walls it can be observed that there was a large displacement in the bottom of panel four with a small displacement on the top of the same panel. This indicates that panel four rotated more than it displaced, Figure 7.8.

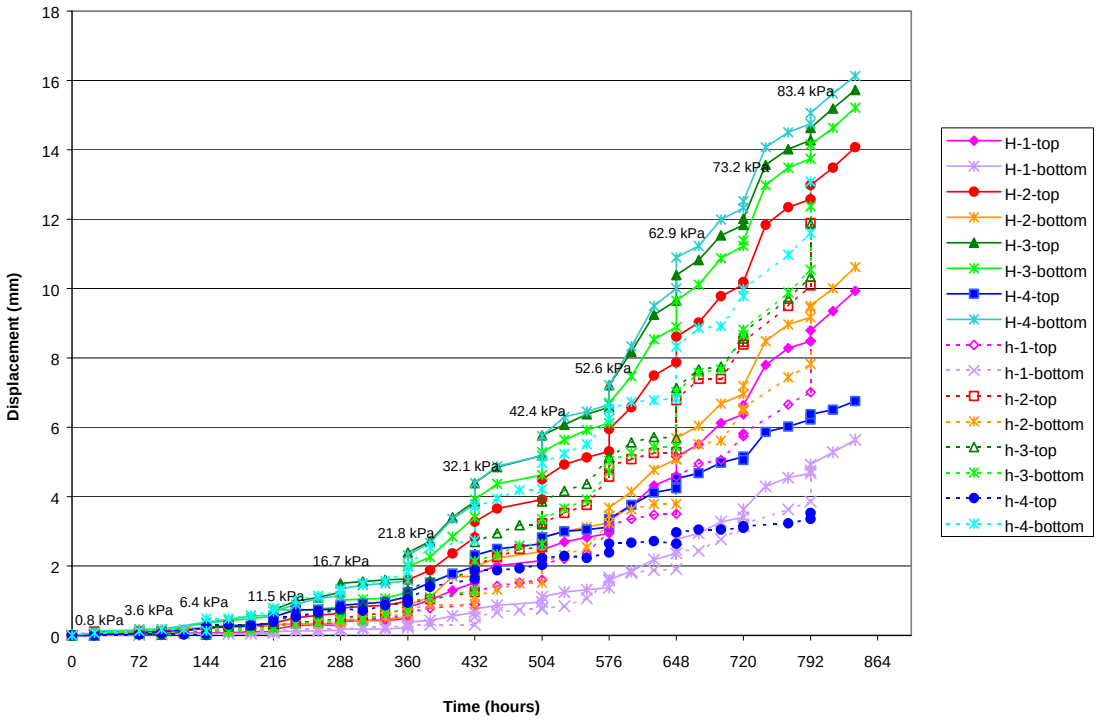

Figure 7.5. Panel displacement (time) for HDPE small-scale MSE wall

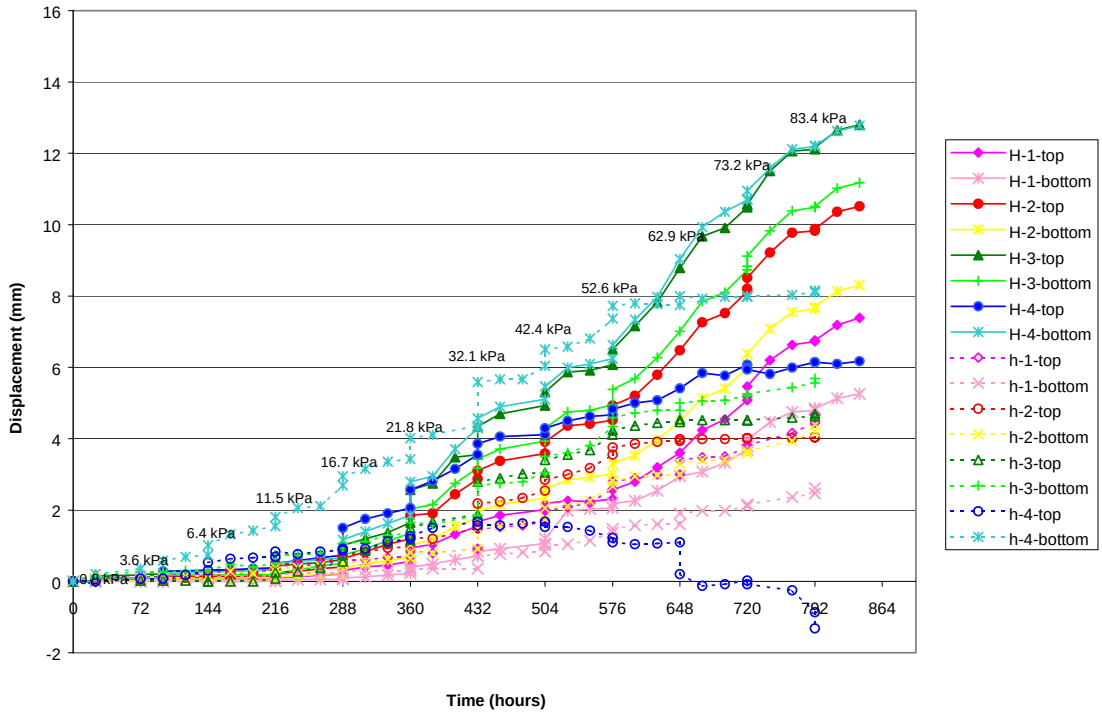

Figure 7.6. Panel displacement (time) for PET small-scale MSE wall

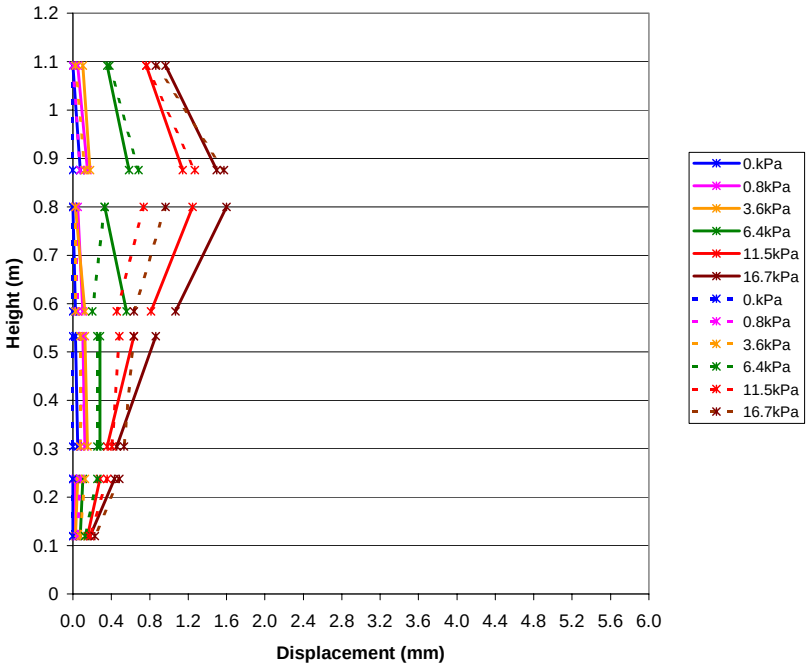

Figure 7.7. Panel displacements for HDPE small-scale MSE walls

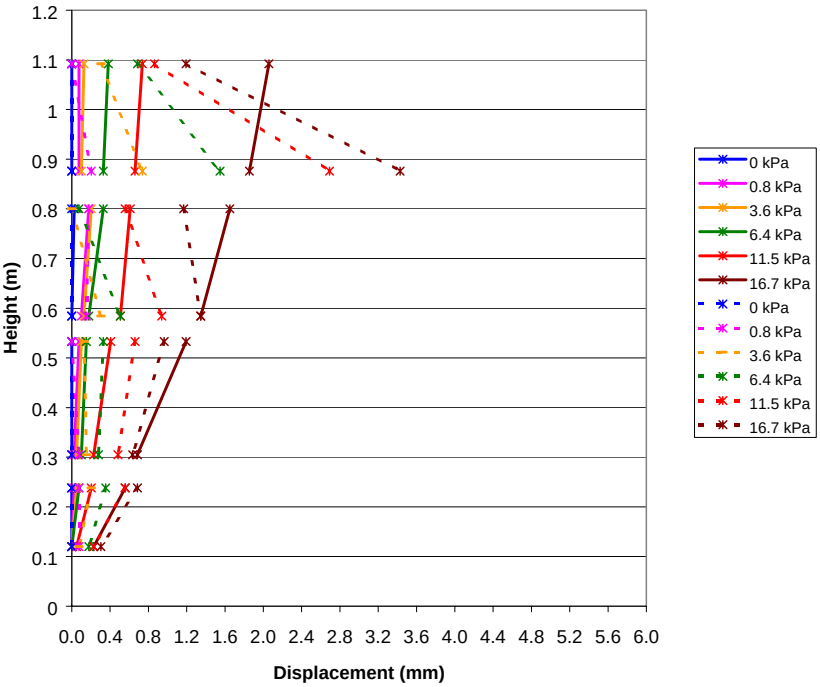

Figure 7.8. Panel displacements for PET small-scale MSE walls

7.1.4 PLATE SETTLEMENT

The settlements were measured with four dial gages, one in each corner of the loading plate. The results are presented in Figures 7.9 and 7.10 The HDPE MSE wall shows good agreement for the two walls tested for surcharges up to 21.7 kPa, similar to the results for the panel displacements. For the PET MSE wall there is also good agreement up to the 21.7 kPa surcharge. For both the HDPE and PET MSE walls, the first wall shows more deformation after the 21.7 kPa surcharge, which is consistent with the strain and panel movement results.

Figures 7.11 and 7.12 show the loading plate settlement movement for surcharges up to 21.7 kPa. The solid lines show the results for the first walls, and the dotted lines the results for the second walls. The settlements were very similar for both the HDPE and the PET MSE walls, although the PET MSE walls show less settlement than the HDPE at the back of the wall. There was a very good agreement between the HDPE MSE Walls 1 and 2. For the PET MSE walls, there is good initial agreement between the settlement of both walls, up to a surcharge level of 21.7 kPa. For the higher loads, it can be seen from Figure 7.11 that there is a change with Wall 1 settling more for surcharges over 52.6 kPa. For the HDPE walls, Wall 1 also has more settlement for surcharges higher than 32.1 kPa.

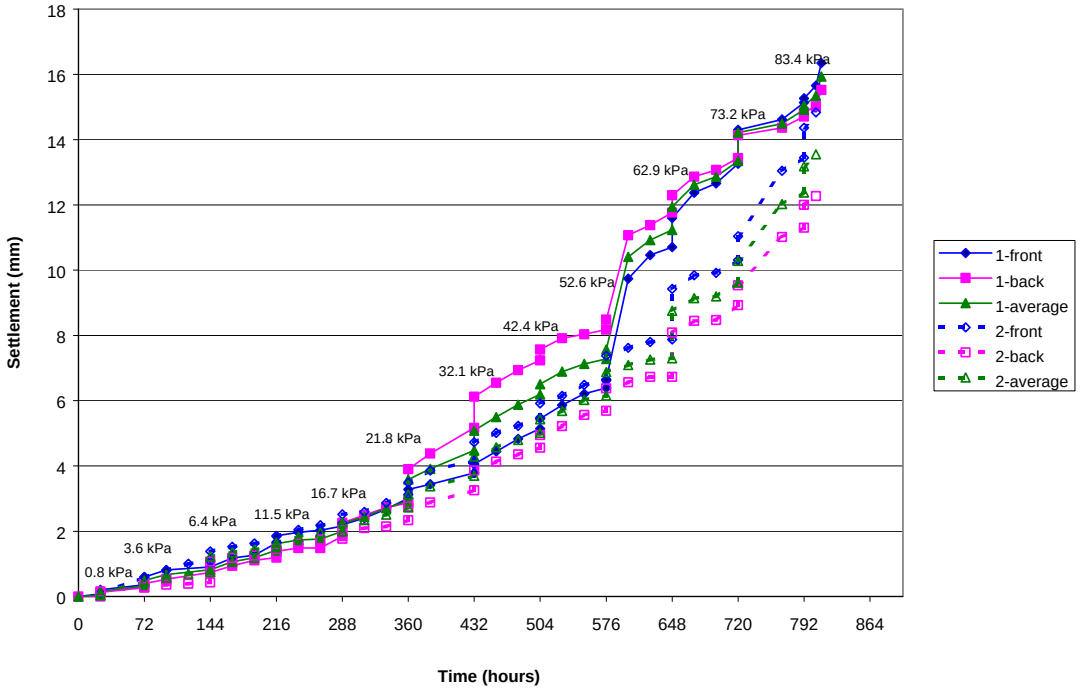

Figure 7.9. Loading plate settlement (time) for HDPE small-scale MSE wall

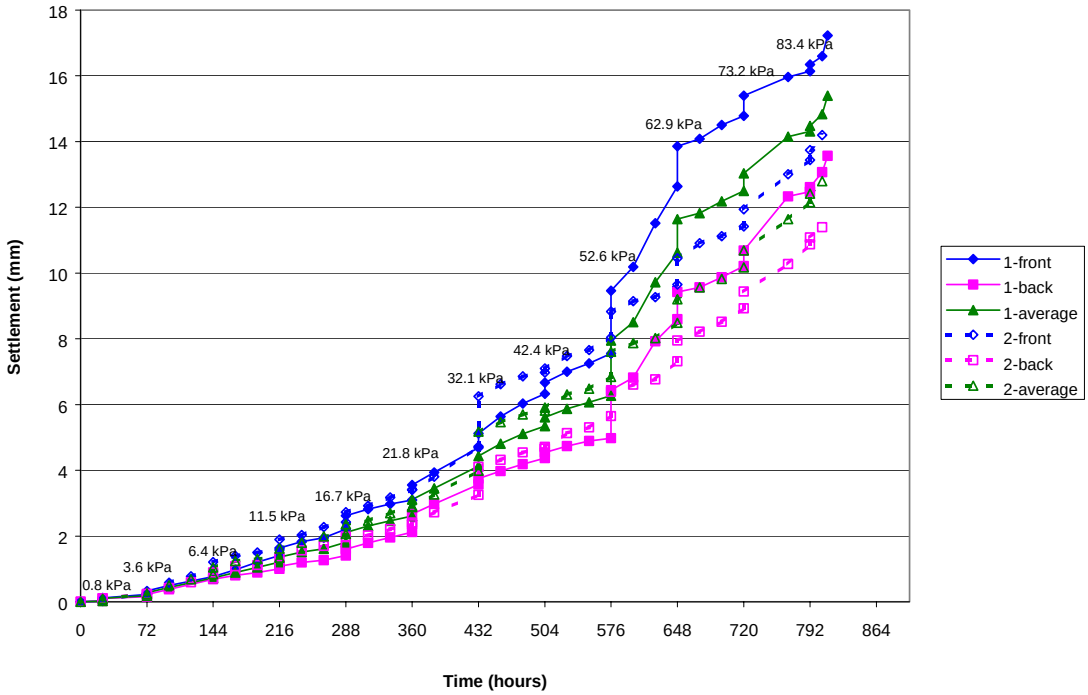

Figure 7.10. Loading plate settlement (time) for PET small-scale MSE wall

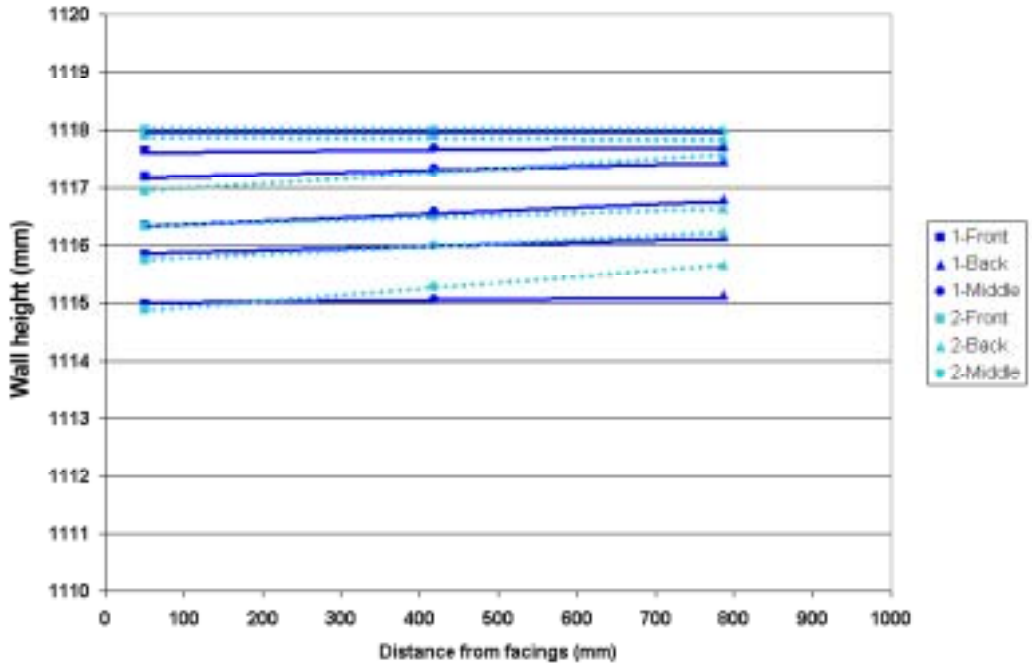

Figure 7.11. Plate settlement for HDPE small-scale MSE walls

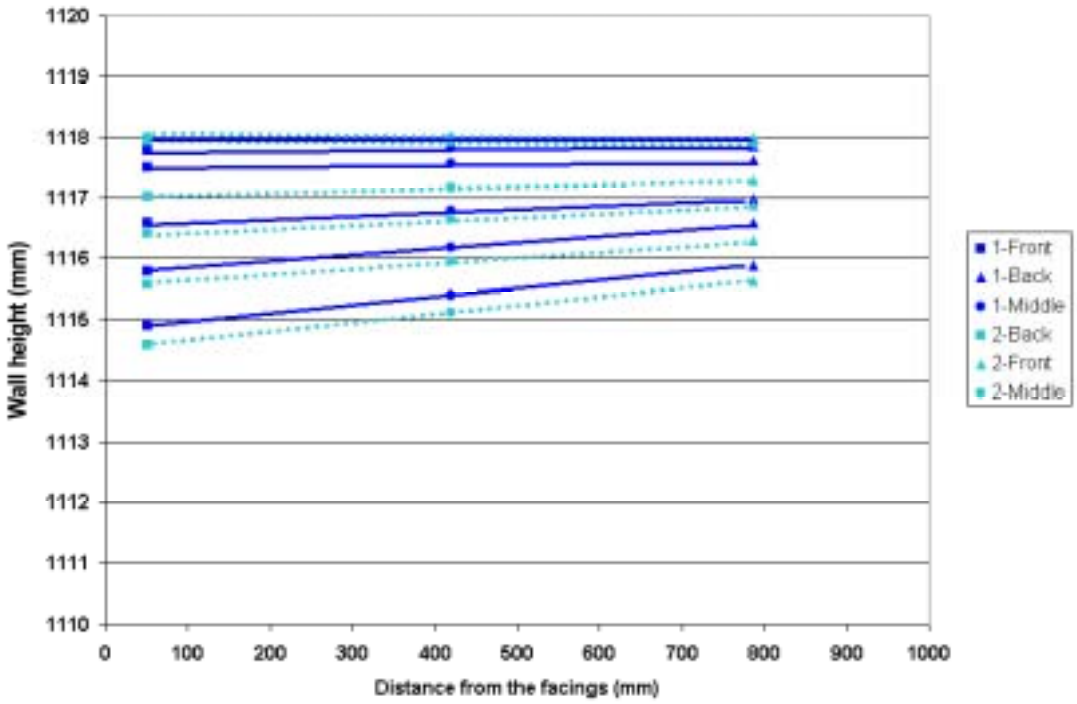

Figure 7.12. Plate settlement for PET small-scale MSE walls

7.2 NUMERICAL ANALYSIS OF SMALL SCALE MSE WALLS

The small-scale MSE walls were simulated using FLAC, following the procedures outlined earlier in Section 5.2. However, multiple-stage construction procedures were followed here in order to simulate the sequential construction process in the field. The soil properties were the same as those for the materials used in the small-scale MSE walls testing. The geogrid properties used in this analysis were as follows:

HDPE Geogrid (UX-1400 SB)

1. Modulus of elasticity (E)	7.38×10^{5}	Pa
2. Area(A)	0.001	m^2
3. Moment of inertia (I)	8.33×10^{-11}	m^4

PET Geogrid Miragrid 3XT

1. Modulus of elasticity (E)	3.08×10^{5}	Pa
2. Area(A)	0.001	m^2
3. Moment of inertia (I)	8.33×10^{-11}	m^4

The area is defined as the thickness of the geogrid multiplied by a unit width in the cross direction, and the modulus of elasticity is calculated by dividing the geogrid modulus by its thickness

The scale factor considered for the small-scale MSE walls was 1 to 5.5. Figures 7.13 through 7.18 show the results of the FLAC modeling for the HDPE and PET small-scale MSE walls with a 16.7 kPa surcharge.

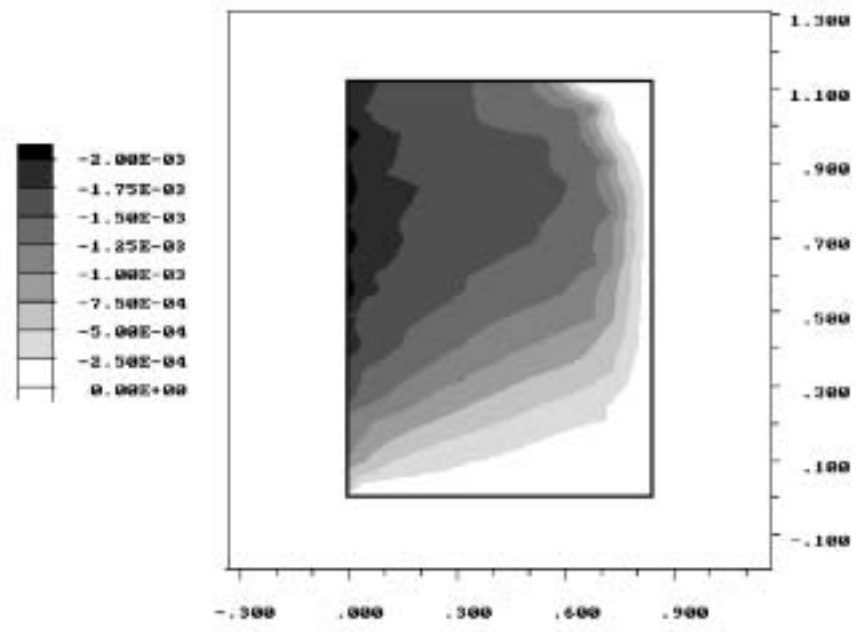

Figure 7.13. Horizontal displacements (in meters) in the soil, HDPE Wall, 16.7 kPa surcharge

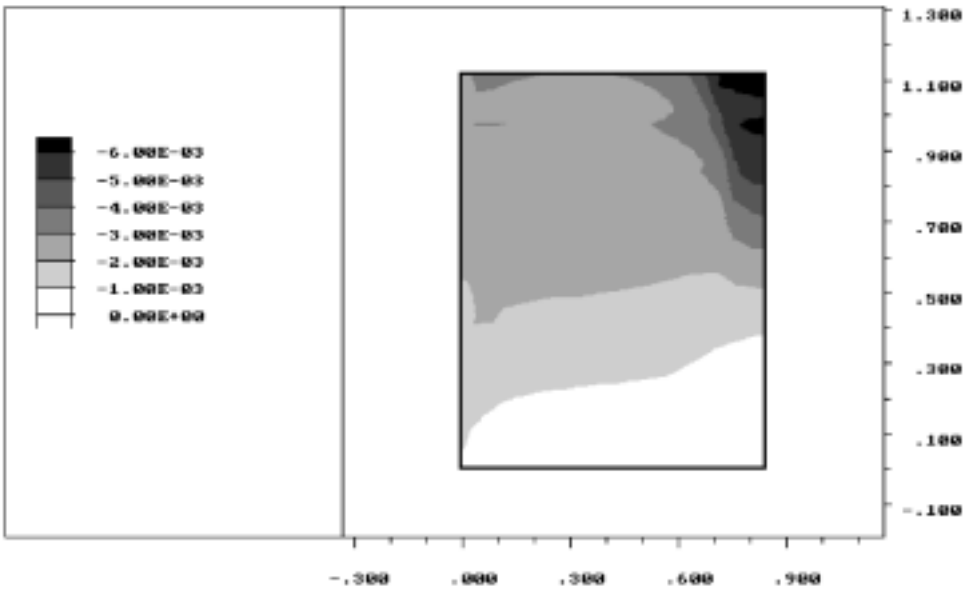

Figure 7.14. Vertical displacements (in meters) in the soil, HDPE Wall, 16.7 kPa surcharge

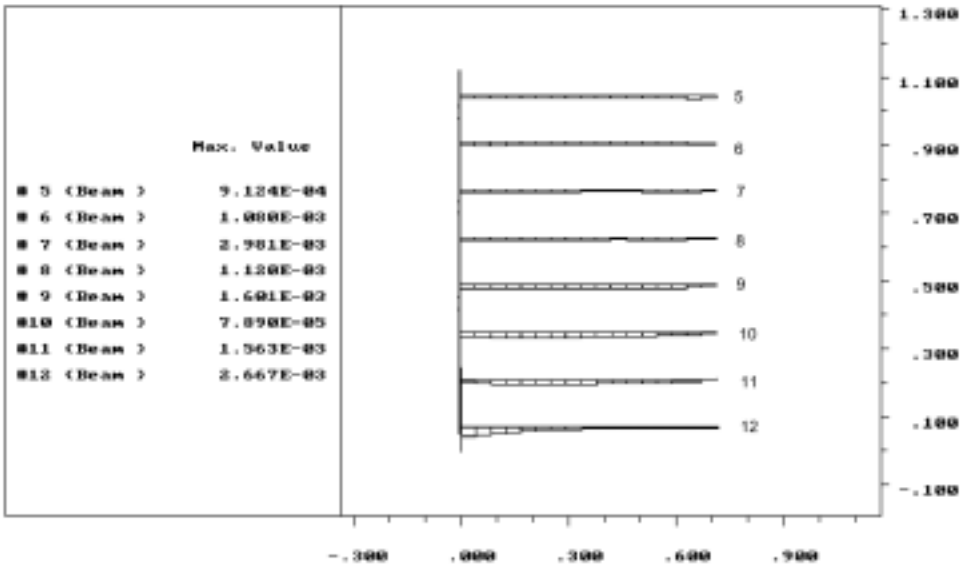

Figure 7.15. Strains in the geogrid, HDPE Wall, 16.7 kPa surcharge

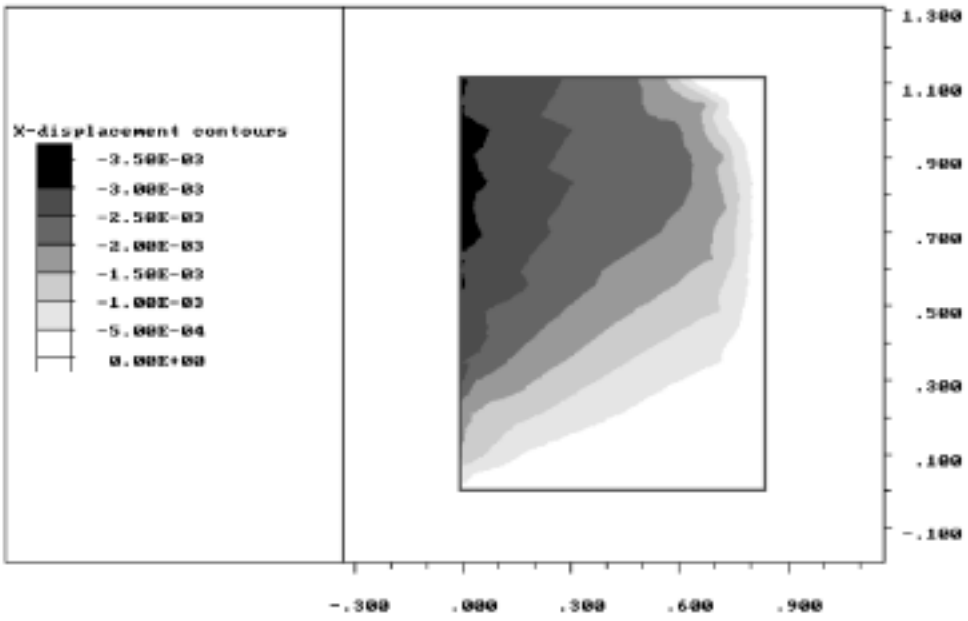

Figure 7.16. Horizontal displacements (in meters) in the soil, PET Wall, 16.7 kPa surcharge

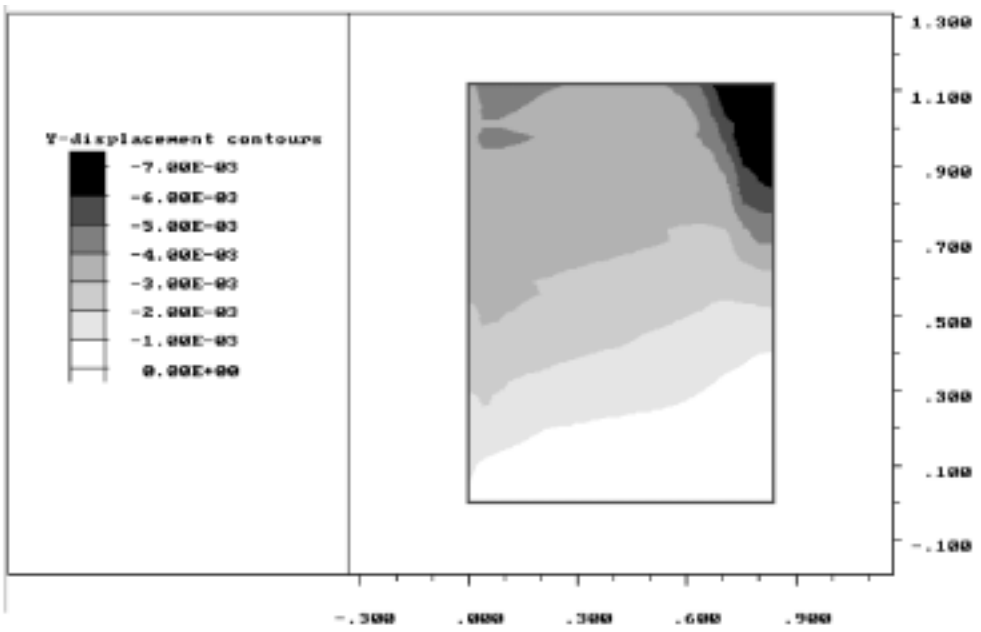

Figure 7.17. Vertical displacements (in meters) in the soil, PET Wall, 16.7 kPa surcharge

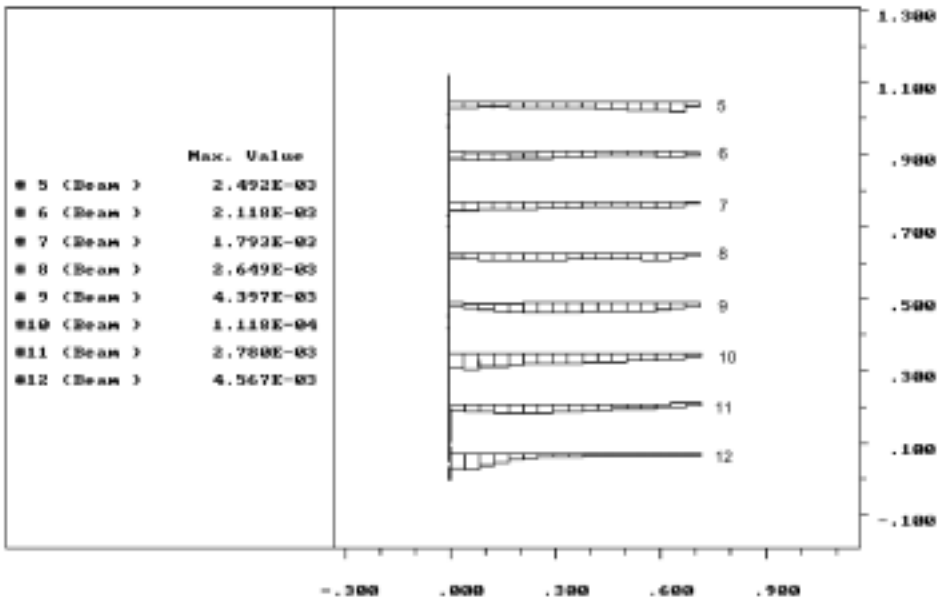

Figure 7.18. Strains in the geogrid, PET Wall, 16.7 kPa surcharge

It is important to note that the parameters used in the numerical model are "equivalent" parameters, not exactly identical to those of the physical model. For instance, the cross sectional area of the geogrid is not constant, but varies depending on proximity to the transverse ribs. The soil is a highly nonlinear material that could not be possibly modeled accurately except with very sophisticated numerical models that account for dilation and volume change. Therefore, it is important to keep in mind that the purpose of this study is to compare the results and behavior of the small-scale MSE wall and the FLAC model.

Close examination and comparison between the results of the FLAC model and the small-scale testing showed qualitative agreement between numerical model and experiments in terms of deformation trends, relative displacement between the panels, and location of maximum displacement. However, disparities were observed in terms of actual magnitude of deformation. This is not uncommon for numerical models, which are mainly intended to capture trends and identify distress mechanisms. The inability of numerical models to exactly match the deformation of the physical system is particularly evident in soils, which are highly nonlinear elastoplastic materials. Because the deformation of a system is heavily sensitive to changes in modulus, and since the "equivalent elastic" modulus of a soil is difficult to define or measure, corrections to the numerical model results must be applied using model calibration factors "a" and "b" to account for distortions due to scaling and modeling. The following sections present a comparison between the test data and the FLAC model, followed by an analysis and implementation of the model calibration factors.

7.3 COMPARISON OF EXPERIMENTAL AND NUMERICAL RESULTS

Comparison between the test and computer model were carried out for the parameters of interest in design, namely the horizontal displacements of the facings, the strains in the reinforcement, and the settlements. The results presented next show good agreement in terms of relative strain and deformation trends, but differences exist in terms of magnitudes of deformation and strains.

7.3.1 FACINGS HORIZONTAL DISPLACEMENTS

The comparison between the facing deformation of the small scale MSE wall tests and the corresponding FLAC modeling results is presented in Figs. 7.19 to 7.30. Data are presented for different reinforcement materials (HDPE and PET) and for various loading stages. It is noted that, due to the rigidity of the actual facing panels, and because they were connected to the geogrid at their midpoint, the facing panels in certain instances rotated around the point of fixity. This is, for instance, evident in the top two panels of Figs. 7.23 and 7.24, and is particularly pronounced in the top two panels of PET Wall 2 (see Figs. 7.26 through 7.30). It is important to keep in mind that the displacement of these particular panels may have been influenced by such rotation, and that only the displacement at the mid point of the panel is representative of the panel displacement. To this end, the numerical model deformation patterns are believed to be more representative of realistic conditions where the facing panel is fixed at more than one point to prevent rotation.

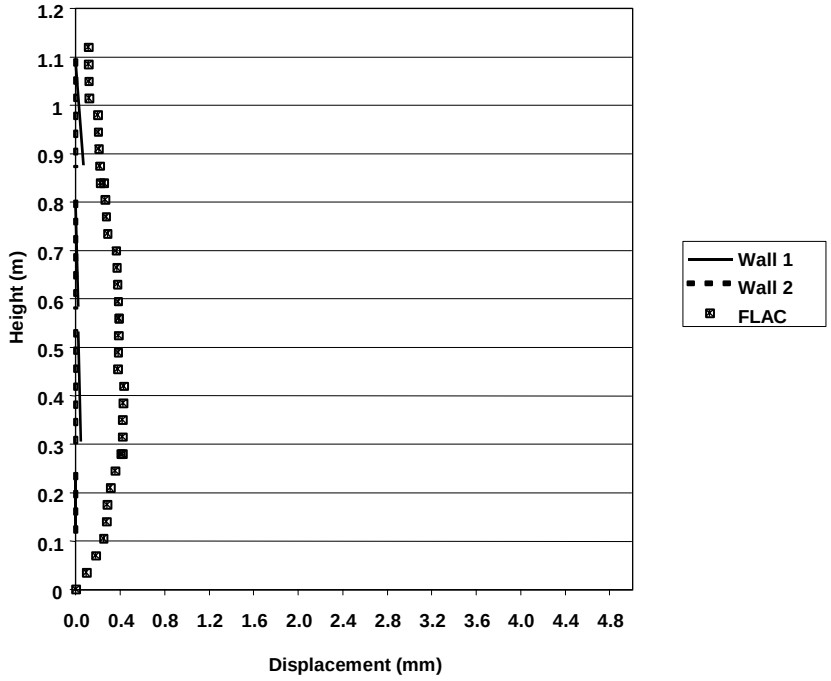

Figure 7.19. HDPE facing deformations at end of construction

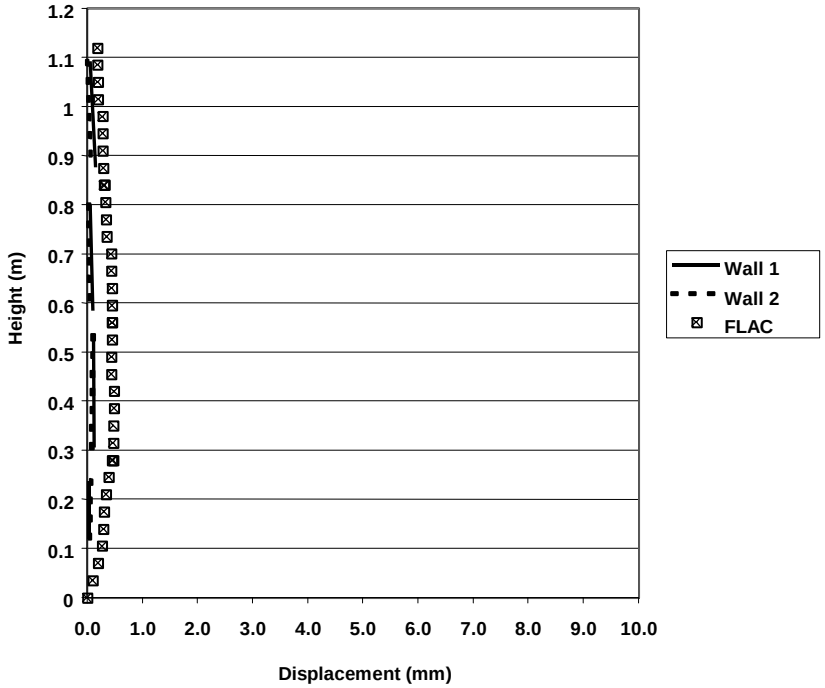

Figure 7.20. HDPE facing deformations at 0.8 kPa surcharge

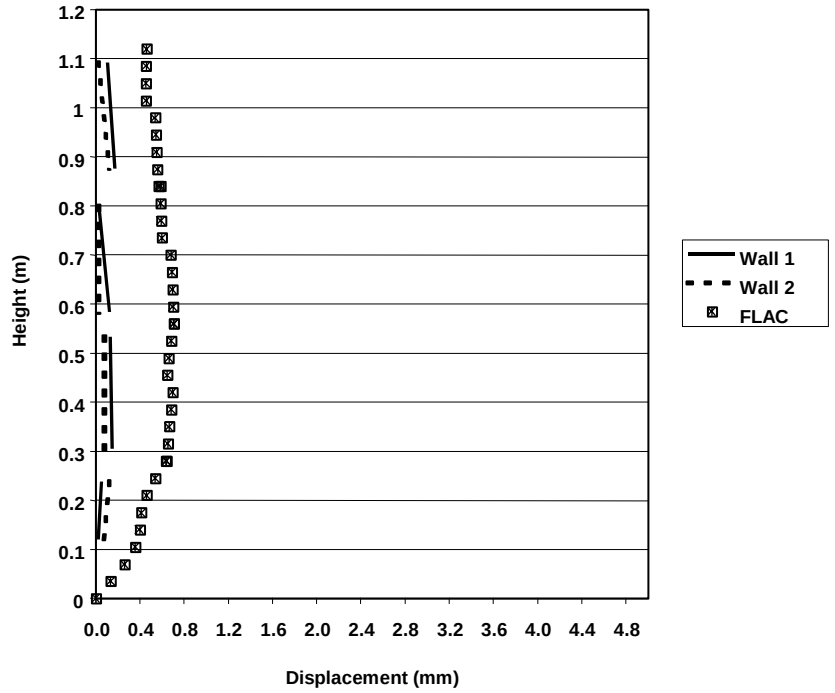

Figure 7.21. HDPE facing deformations at 3.6 kPa surcharge

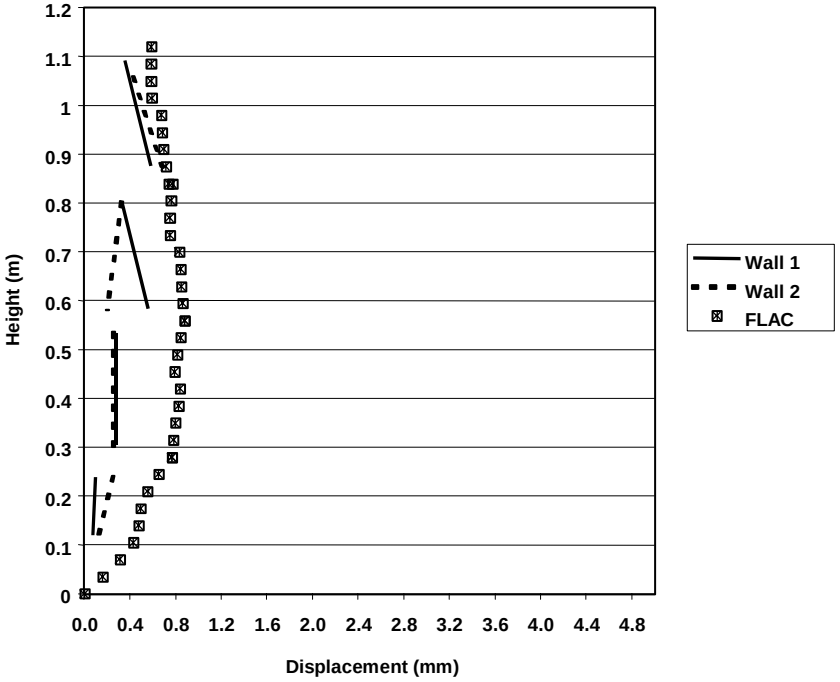

Figure 7.22. HDPE facing deformations at 6.4 kPa surcharge

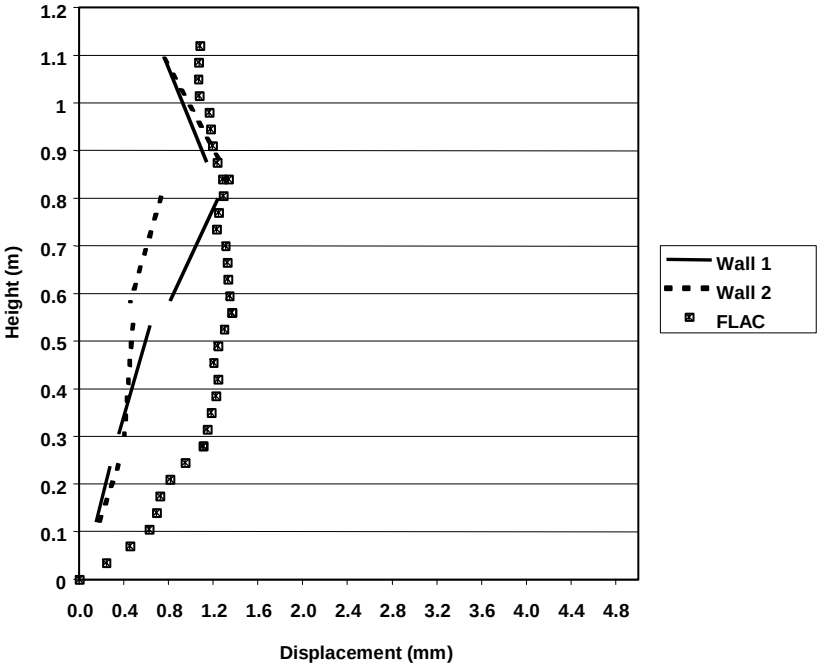

Figure 7.23. HDPE facing deformations at 11.5 kPa surcharge

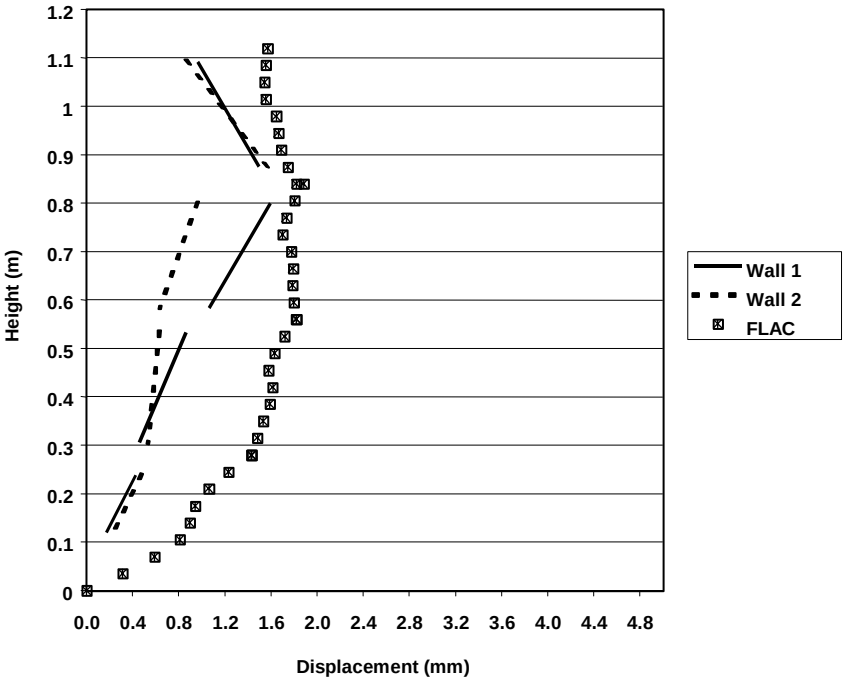

Figure 7.24. HDPE facing deformations at 16.7 kPa surcharge

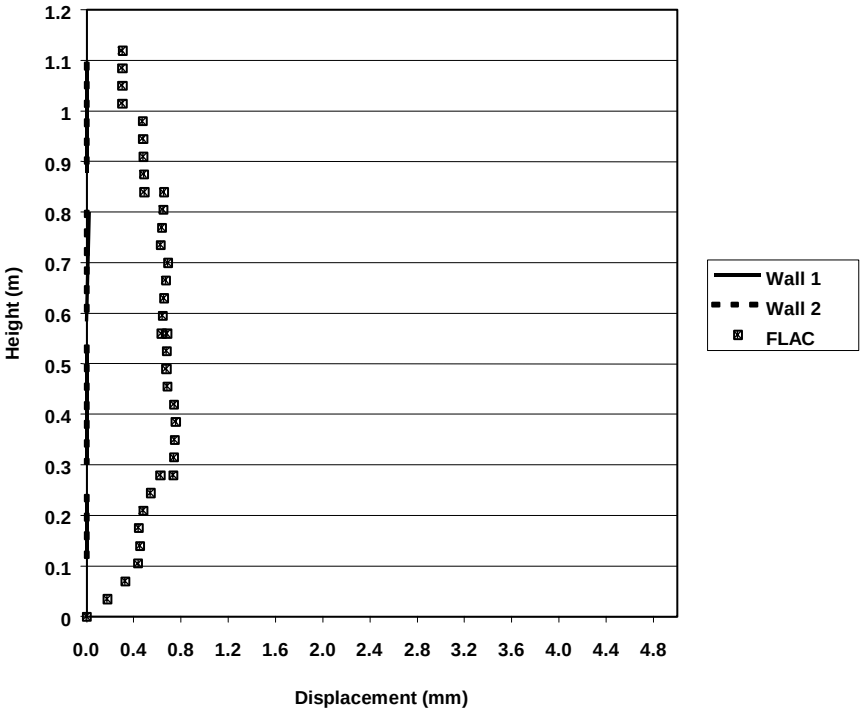

Figure 7.25. PET facing deformations at end of construction

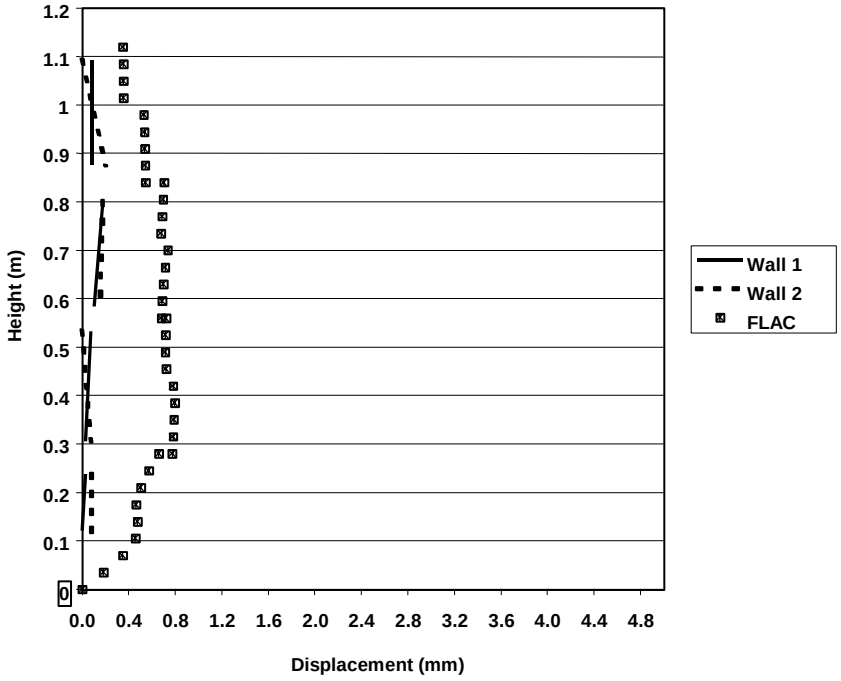

Figure 7.26. PET facing deformations at 0.8 kPa surcharge

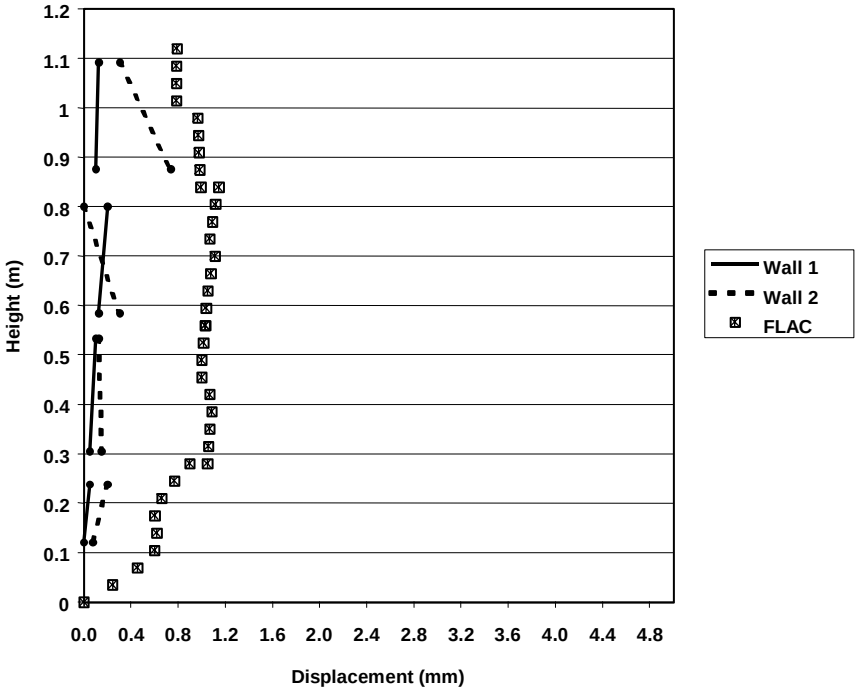

Figure 7.27. PET facing deformations at 3.6 kPa surcharge

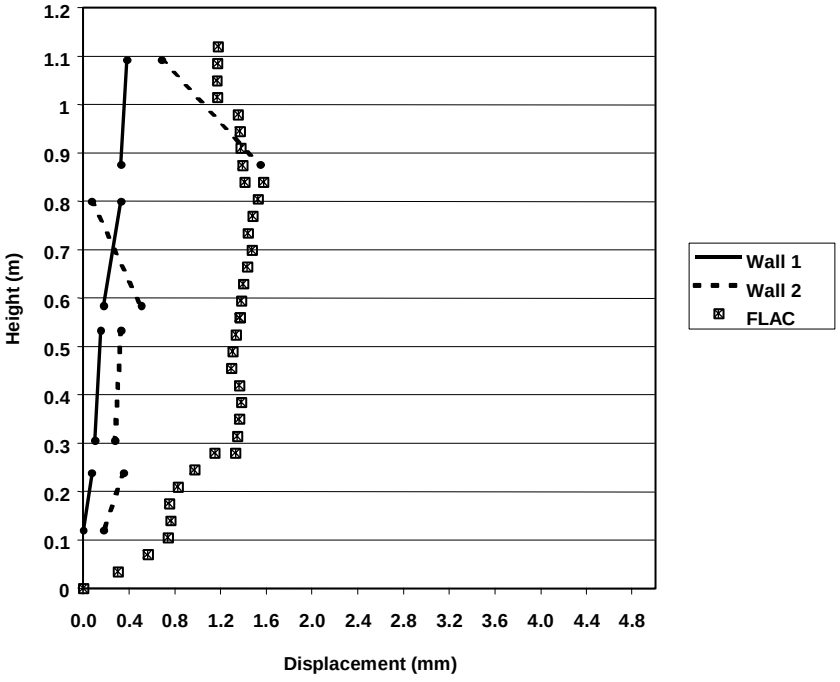

Figure 7.28. PET facing deformations at 6.4 kPa surcharge

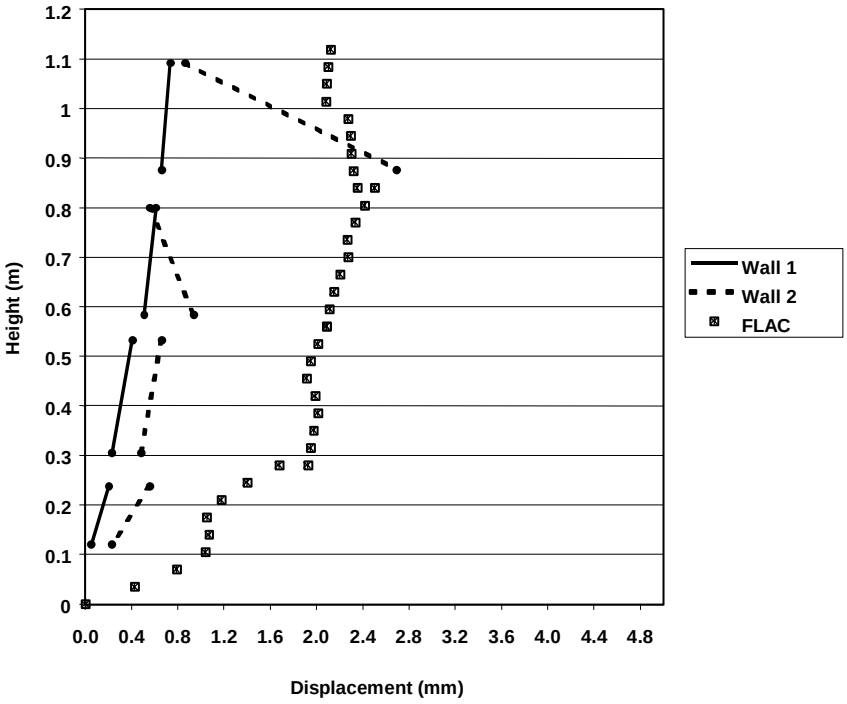

Figure 7.29. PET facing deformations at 11.5 kPa surcharge

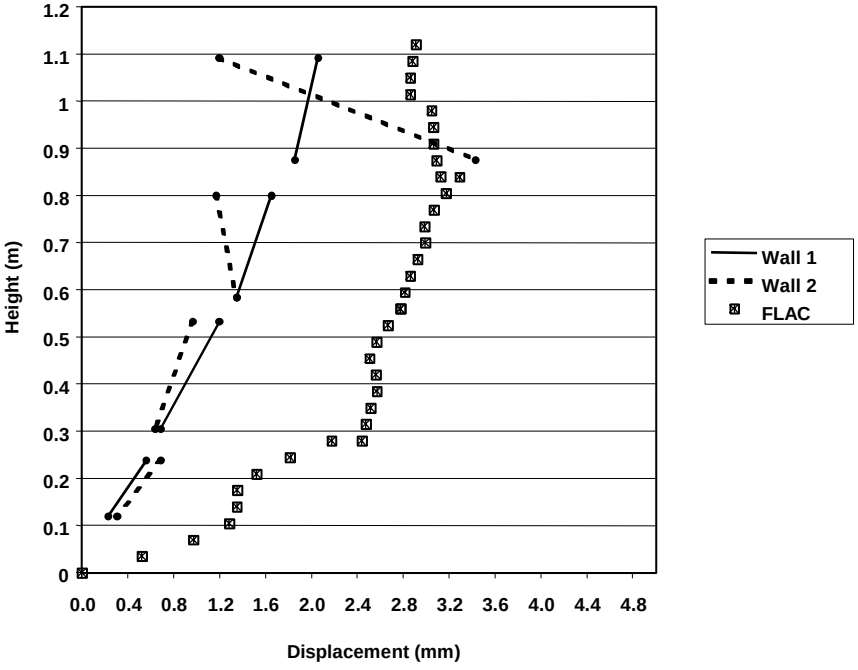

Figure 7.30. PET facing deformations at 16.7 kPa surcharge

7.3.2 STRAINS IN THE REINFORCEMENT

Figures 7.31 to 7.42 show the comparison between the strains in the first, third, fifth, and seventh layers of the reinforcement obtained from the small scale MSE wall testing and the FLAC modeling. FLAC modeling results are represented with the solid light lines, characterized by seventeen data points along the reinforcement within each layer, while the test data has a limited number of points in each layer. Wall 1 results are plotted with the solid darker lines, and Wall 2 with the dotted lines. The results are presented for various surcharge conditions.

The values of the FLAC modeling are, in general, larger, but the trends are similar for both tests and FLAC model. The difference is attributed to the fact that FLAC modeling allows for the calculation of strain from the beginning of construction, whereas the readings were only taken at the end of construction in the case of the actual walls. Therefore, any "locked-in" stresses during construction may not have been accounted for in the strain gage measurements. The values obtained from the FLAC model are, therefore, a better predictor of the stresses within the geogrid than the strain gage measurement. On the other hand, the strain gage measurements are directly related to the displacement of the facing panels due to post-construction loading.

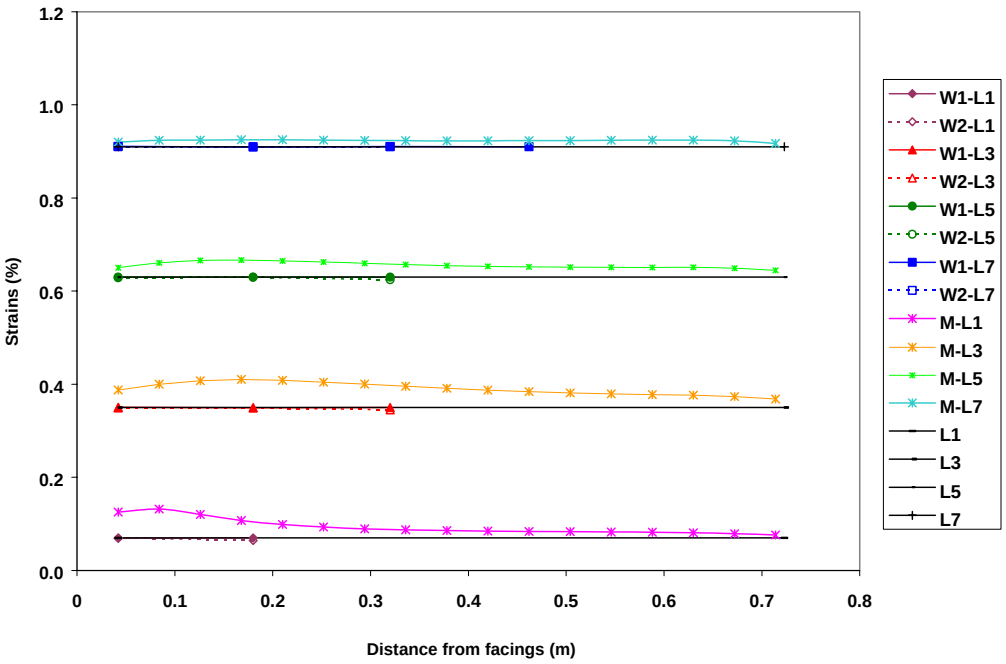

Figure 7.31. HDPE geogrid strains before loading

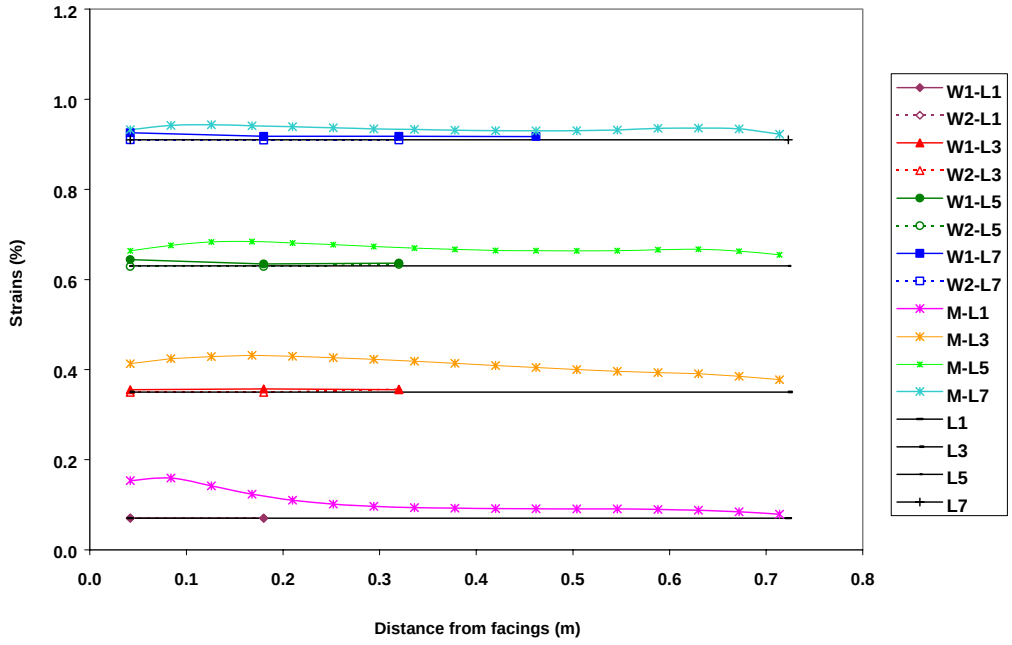

Figure 7.32. HDPE geogrid strains at 0.8 kPa surcharge

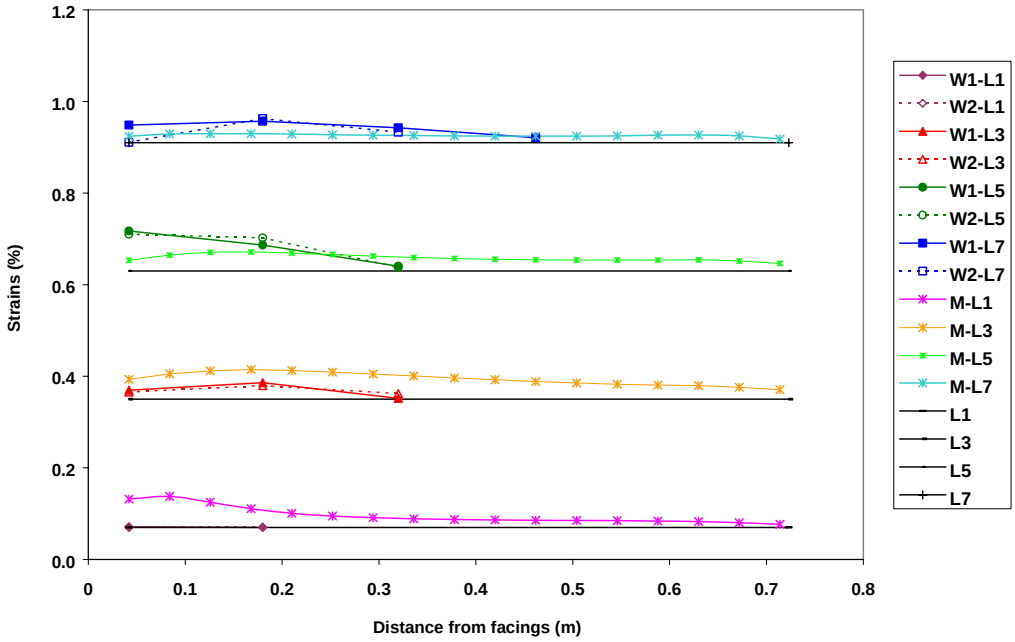

Figure 7.33. HDPE geogrid strains at 3.6 kPa surcharge

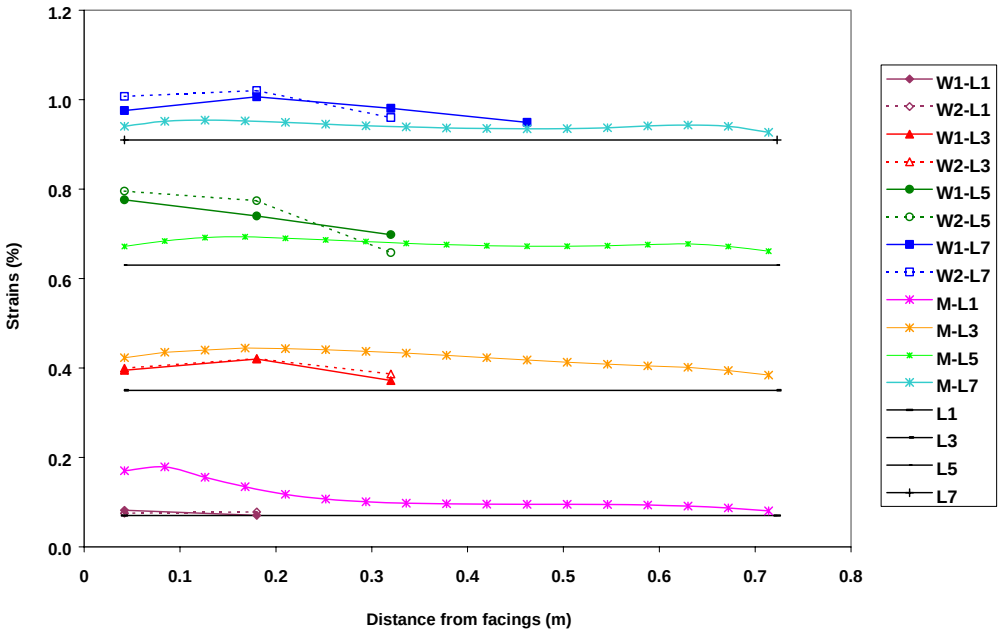

Figure 7.34. HDPE geogrid strains at 6.4 kPa surcharge

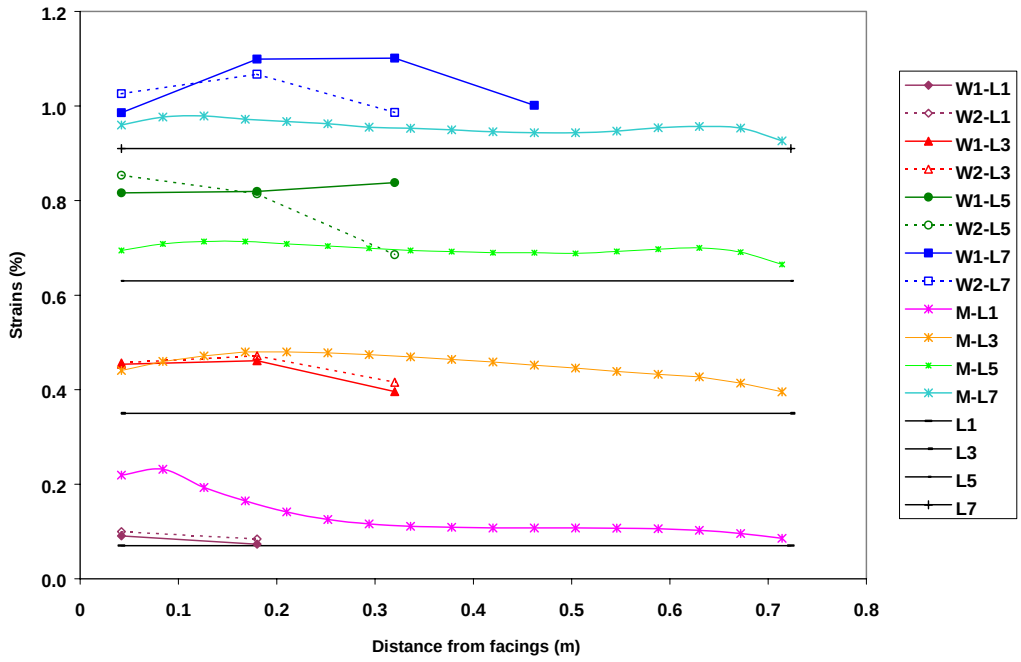

Figure 7.35. HDPE geogrid strains at 11.5 kPa surcharge

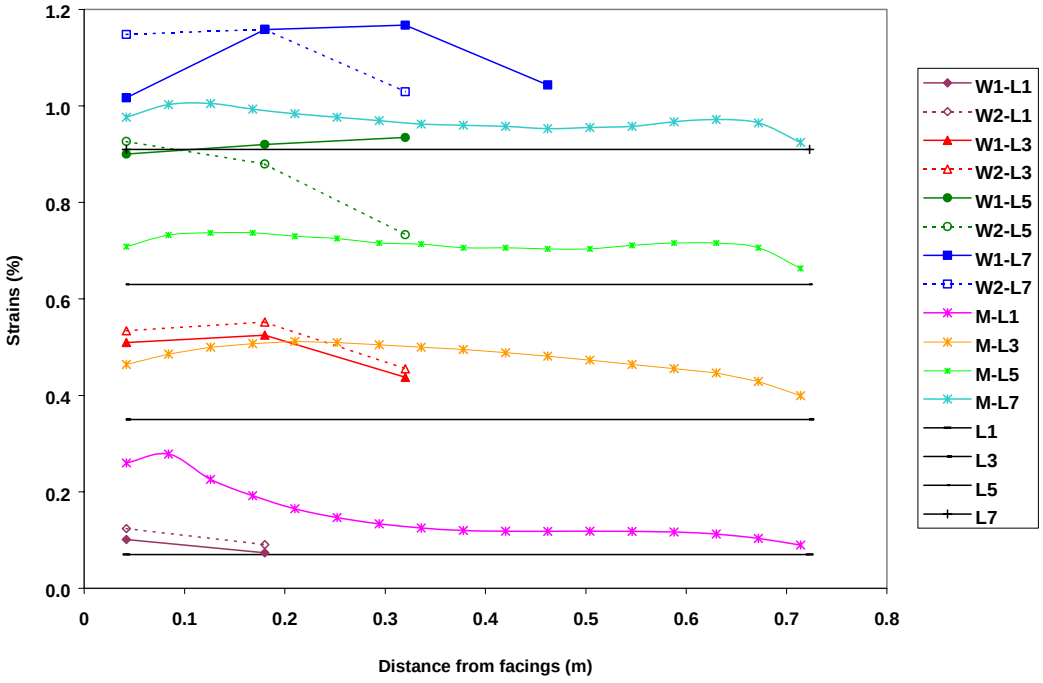

Figure 7.36. HDPE geogrid strains at 16.7 kPa surcharge

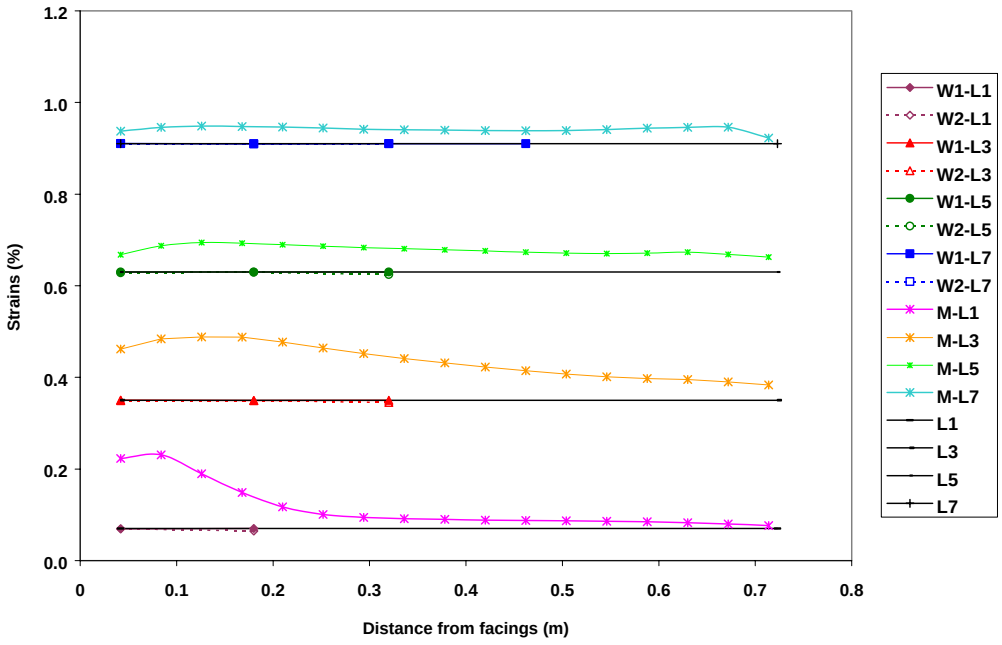

Figure 7.37. PET geogrid strains before loading

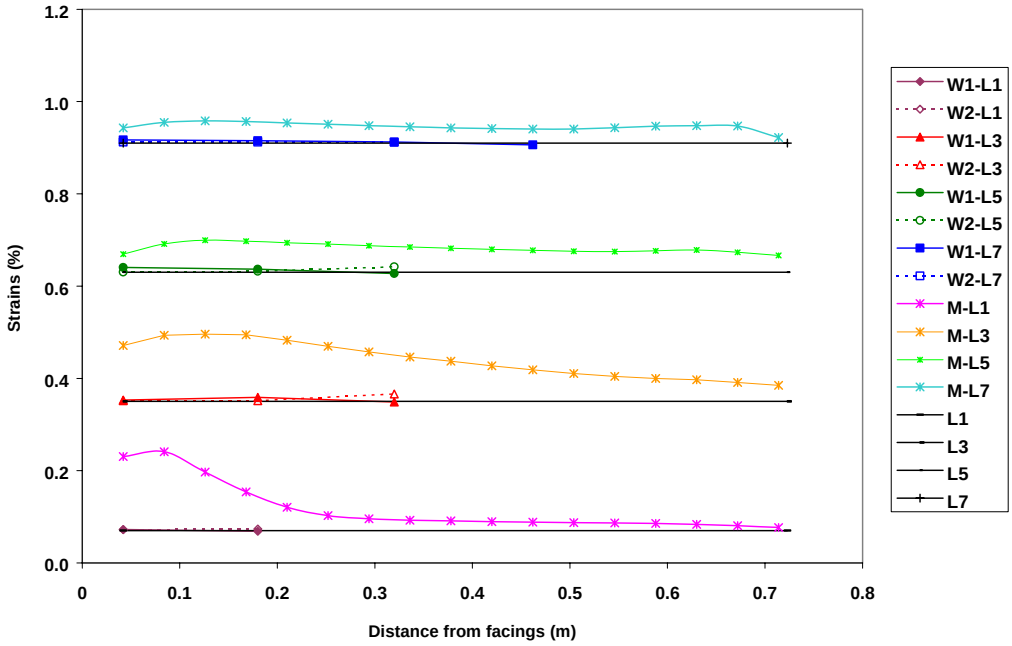

Figure 7.38. PET geogrid strains at 0.8 kPa surcharge

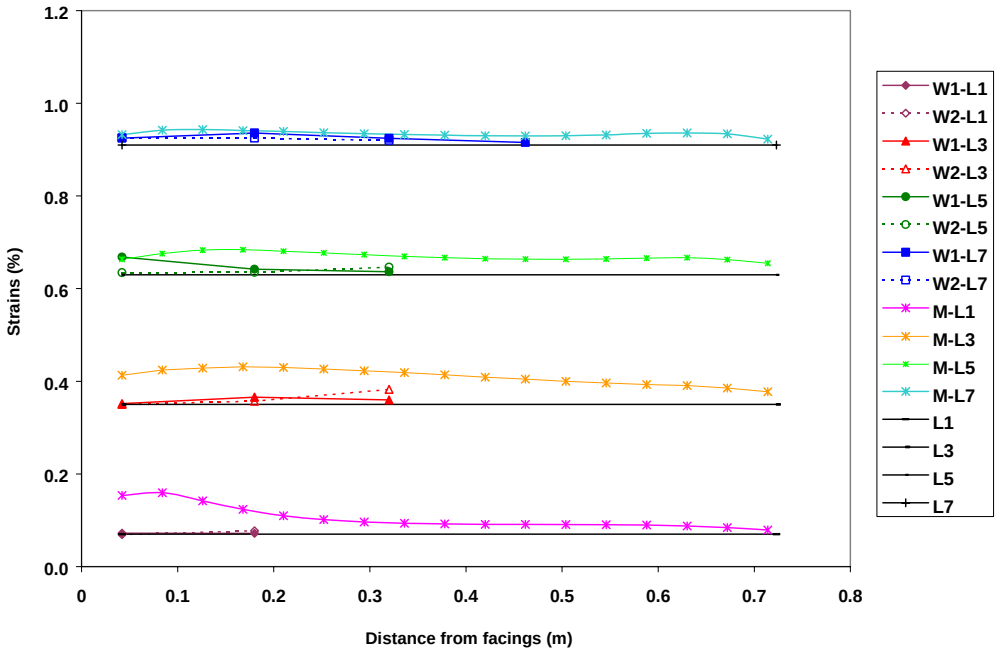

Figure 7.39. PET geogrid strains at 3.6 kPa surcharge

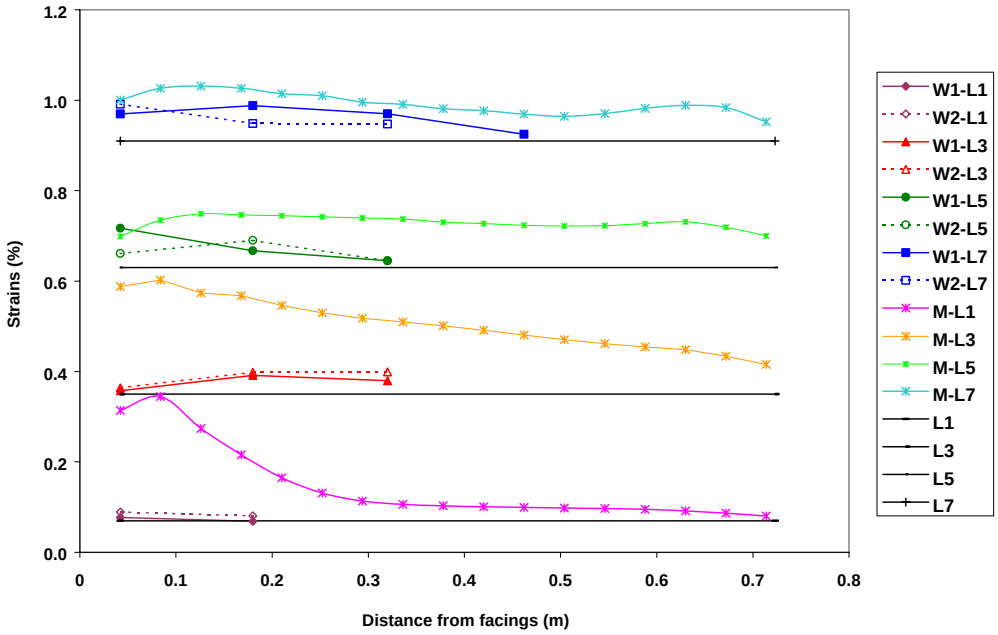

Figure 7.40. PET geogrid strains at 6.4 kPa surcharge

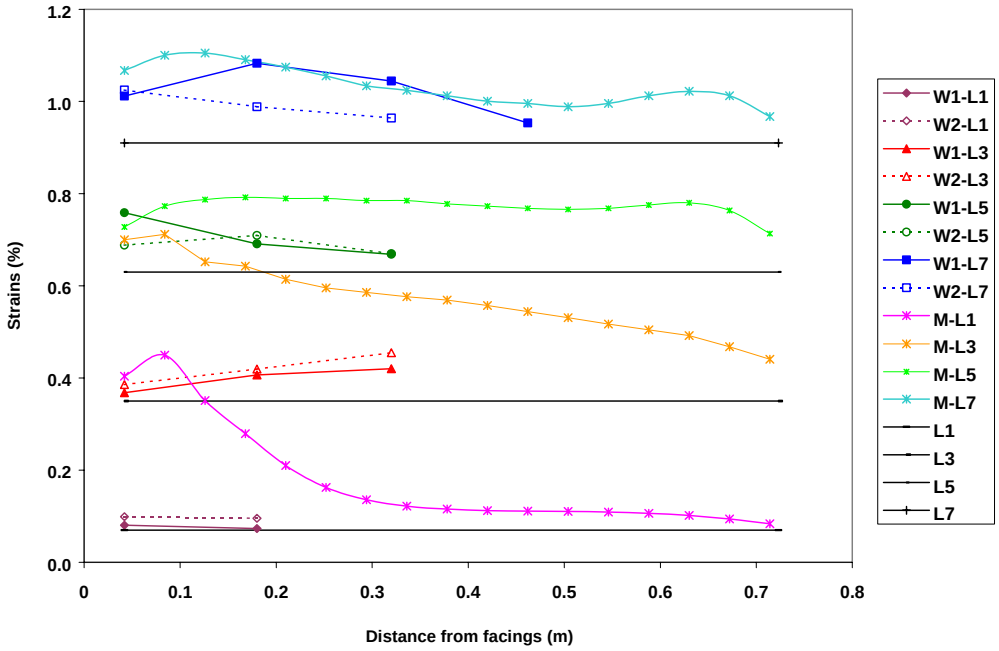

Figure 7.41. PET geogrid strains at 11.5 kPa surcharge

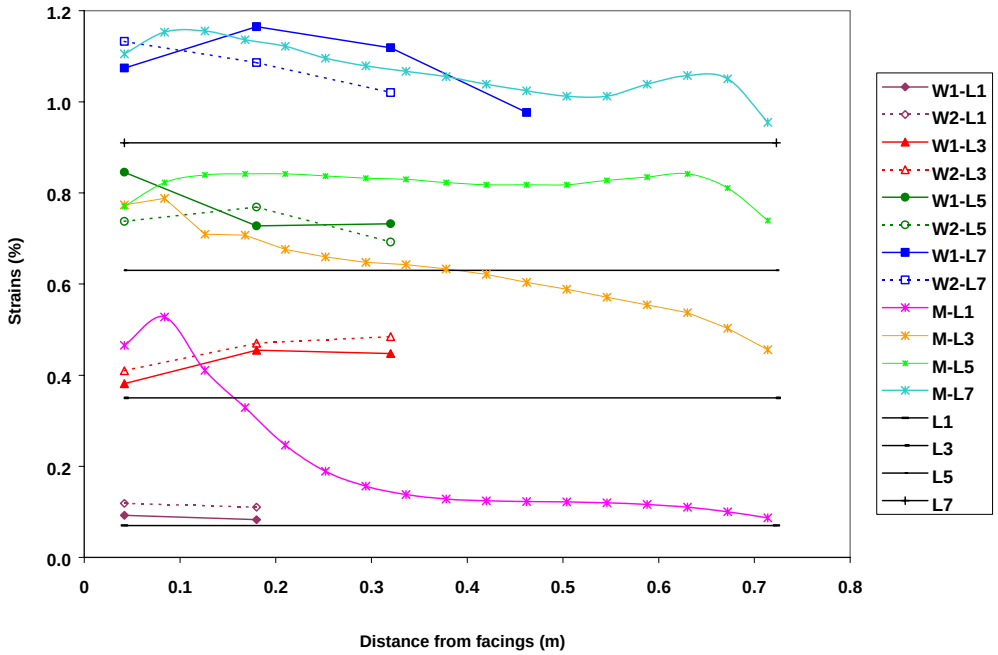

Figure 7.42. PET geogrid strains at 16.7 kPa surcharge

7.3.3 WALL SETTLEMENTS

Figures 7.43 to 7.54 show the comparison of the settlements obtained by the small scale MSE wall testing and the FLAC modeling. The results are presented for the wall after construction for the following surcharges 0.0, 0.8, 3.6, 6.4, 11.5, and 16.7 kPa. It can be observed from the figures that the HDPE small scale wall testing and the FLAC modeling results agree in terms of relative magnitudes of settlements at the different surcharge levels. However, similar to the strains and facing deformations, the values of the FLAC modeling are larger in almost all the cases.

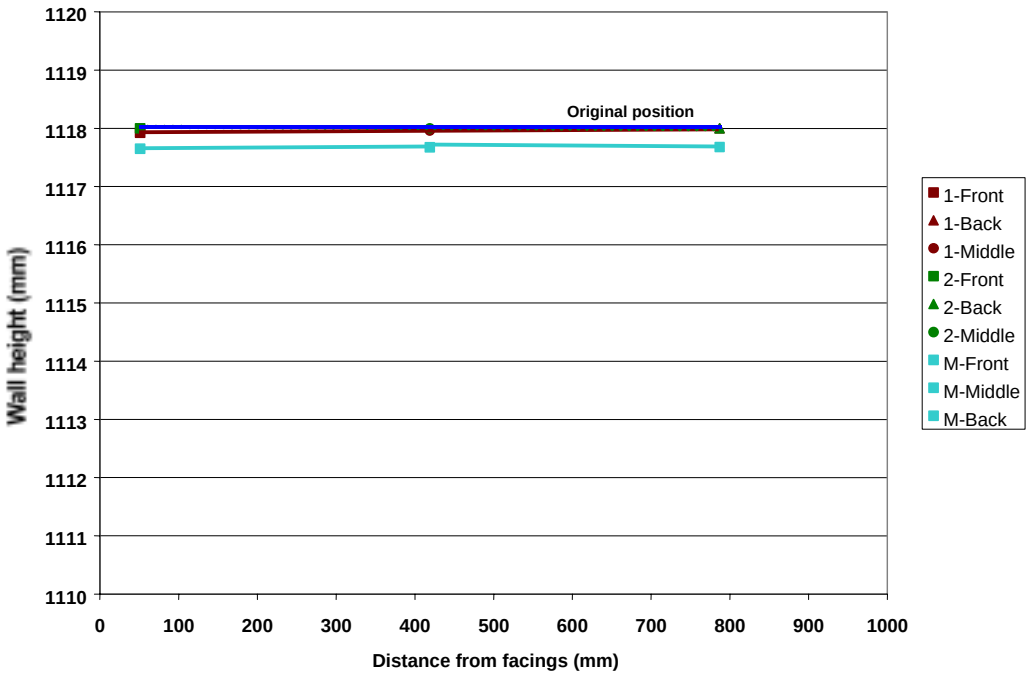

Figure 7.43. HDPE wall settlement at the end of construction

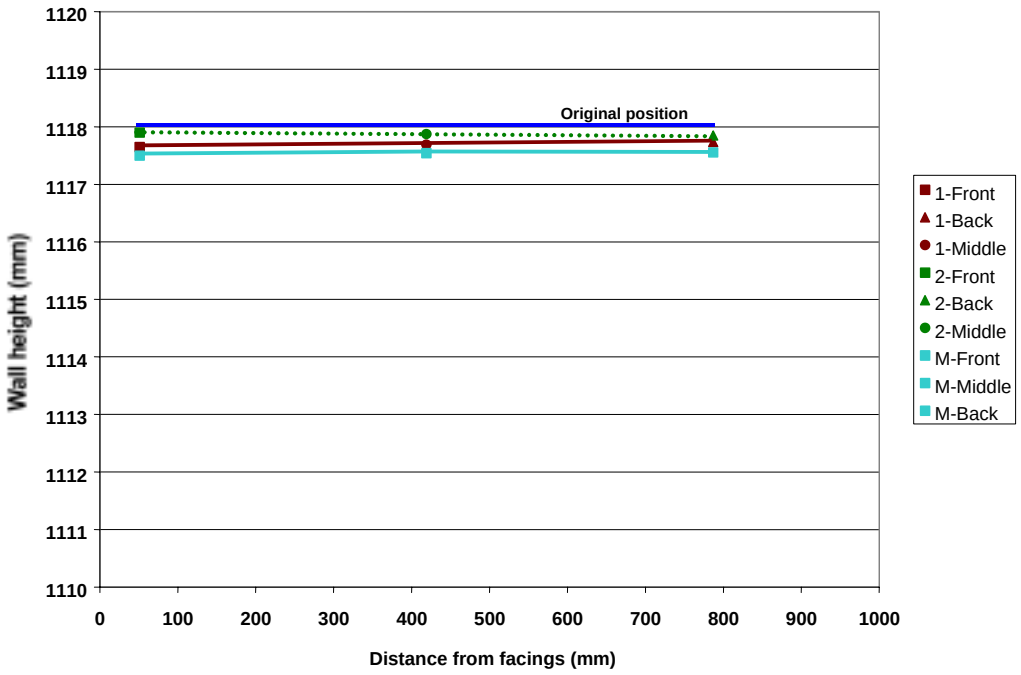

Figure 7.44. HDPE wall settlement at 0.8 kPa surcharge

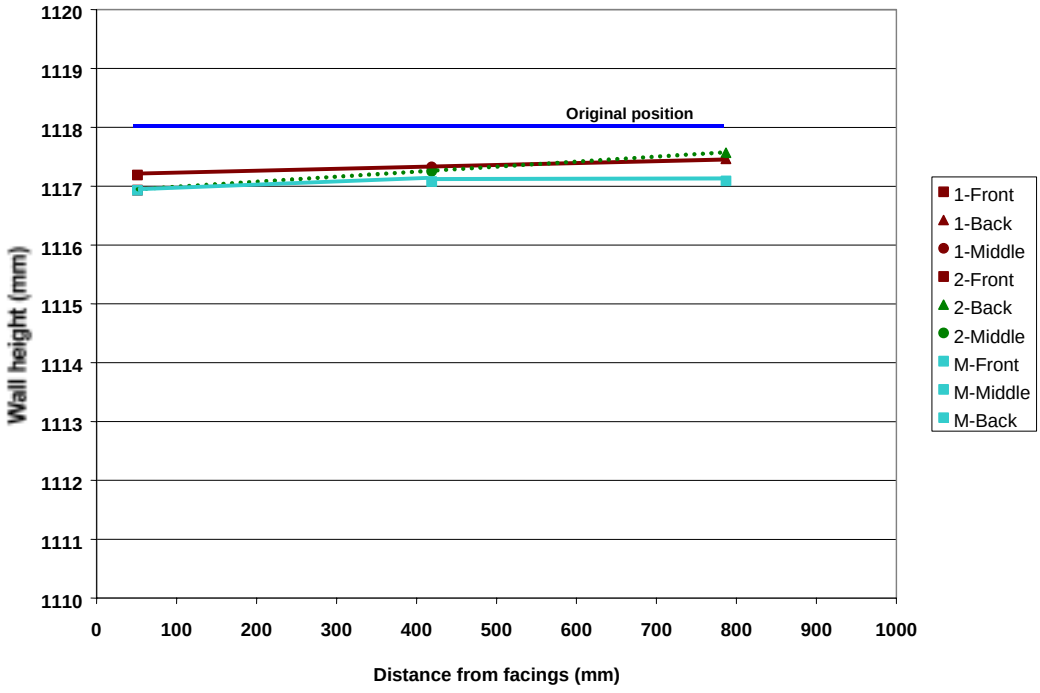

Figure 7.45. HDPE wall settlement at 3.6 kPa surcharge

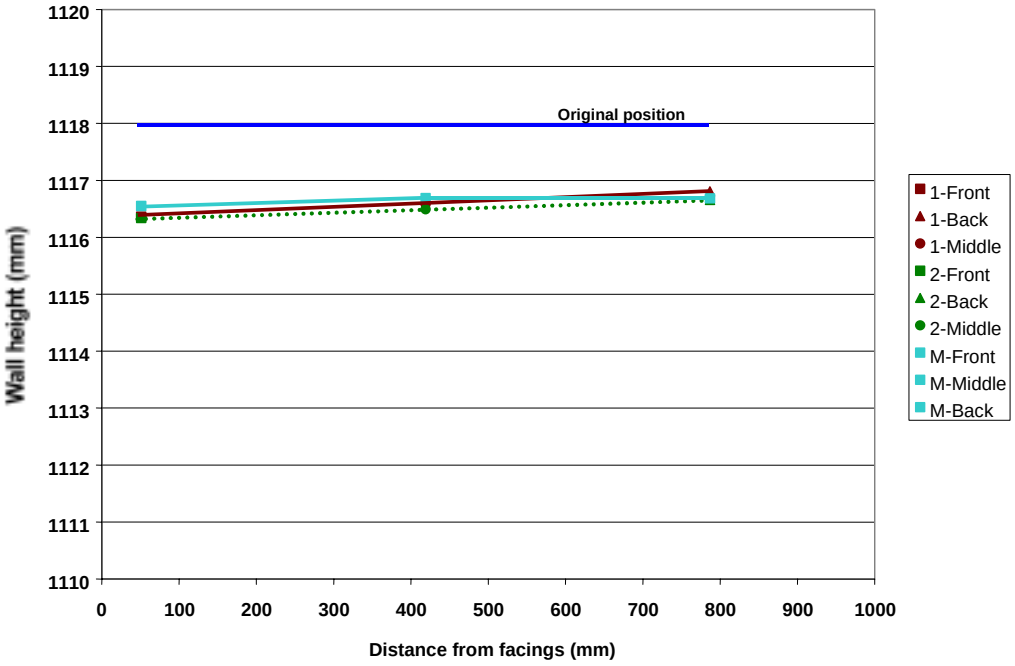

Figure 7.46. HDPE wall settlement at 6.4 kPa surcharge

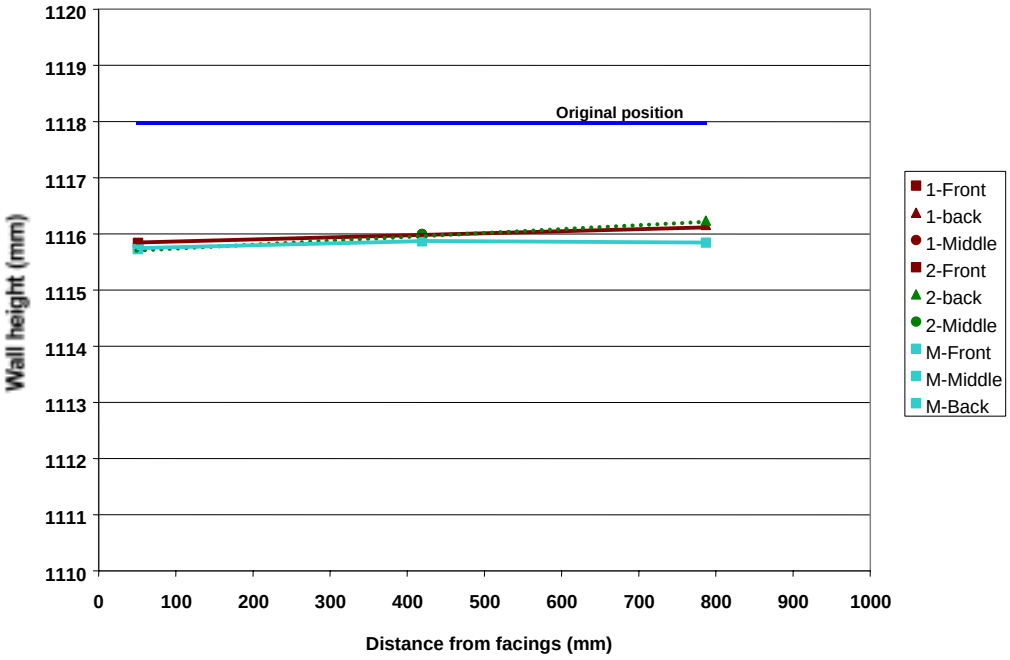

Figure 7.47. HDPE wall settlement at 11.5 kPa surcharge

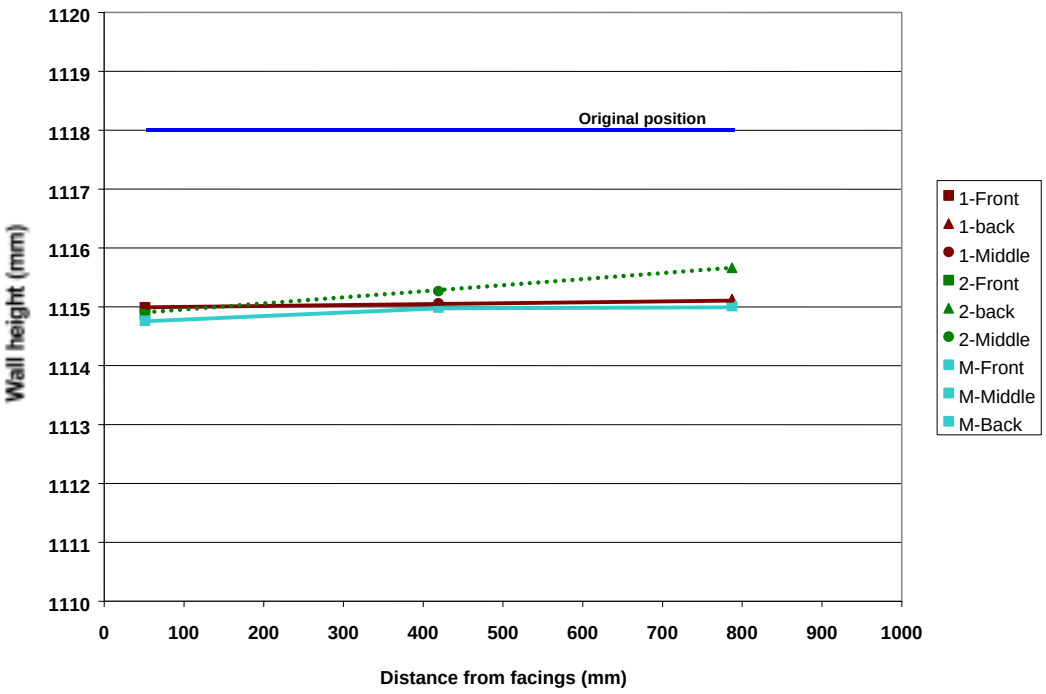

Figure 7.48. HDPE wall settlement at 16.7 kPa surcharge

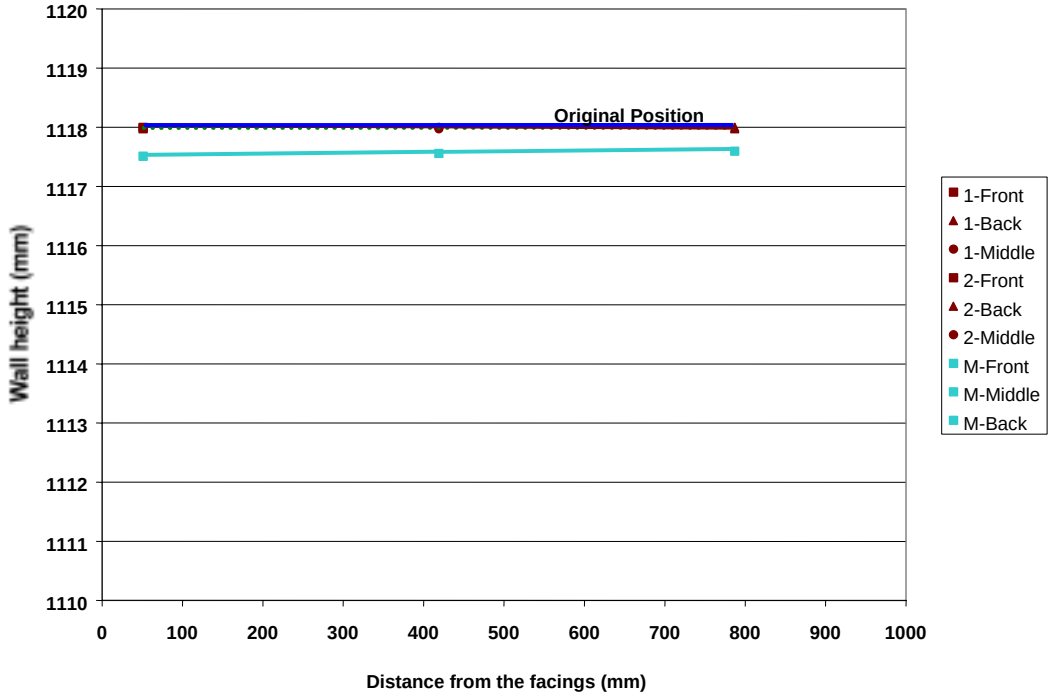

Figure 7.49. PET wall settlement at the end of construction

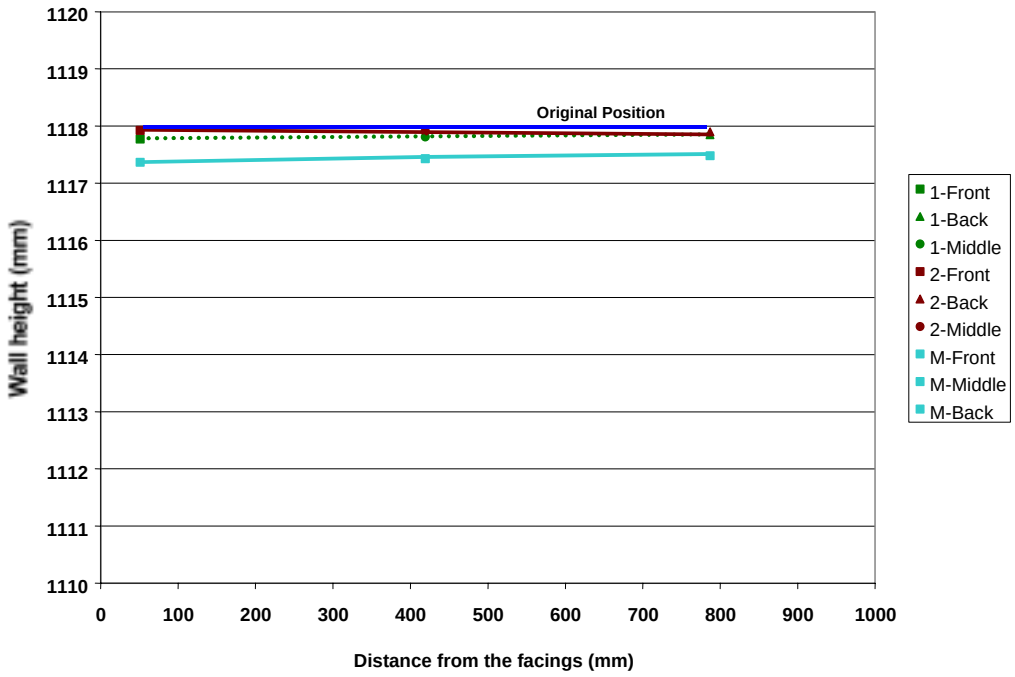

Figure 7.50. PET wall settlement at 0.8 kPa surcharge

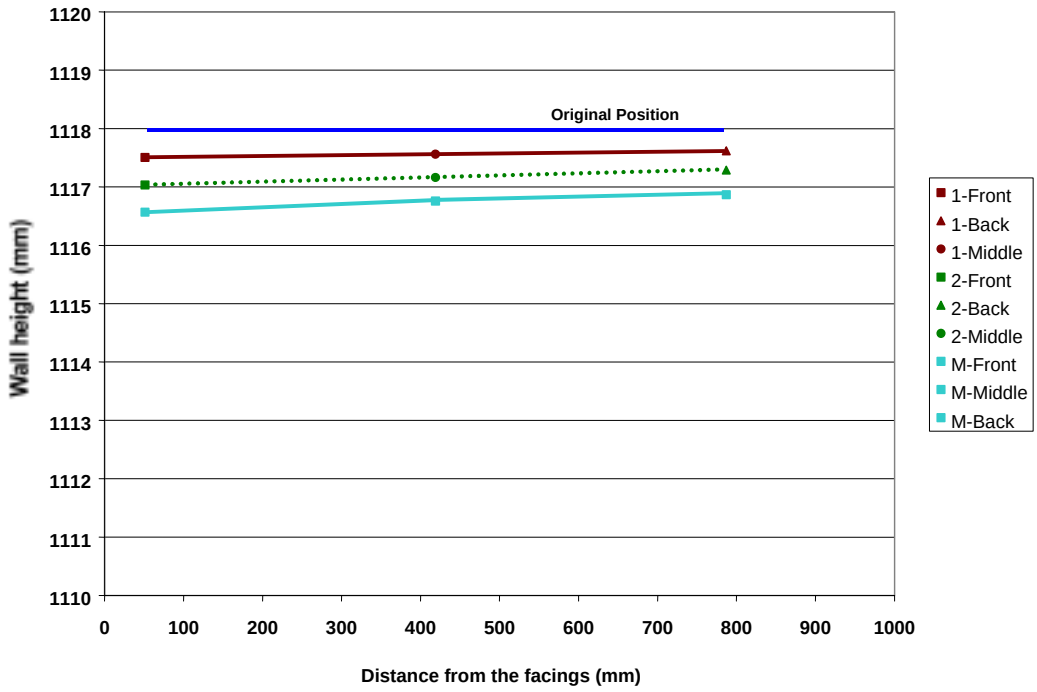

Figure 7.51. PET wall settlement at 3.6 kPa surcharge

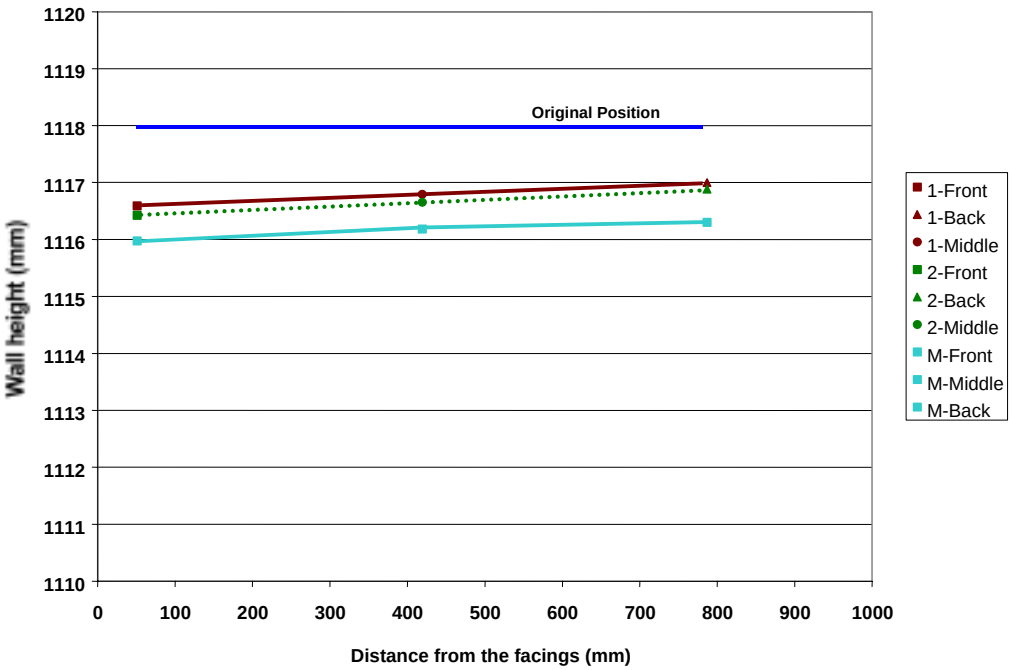

Figure 7.52. PET wall settlement at 6.4 kPa surcharge

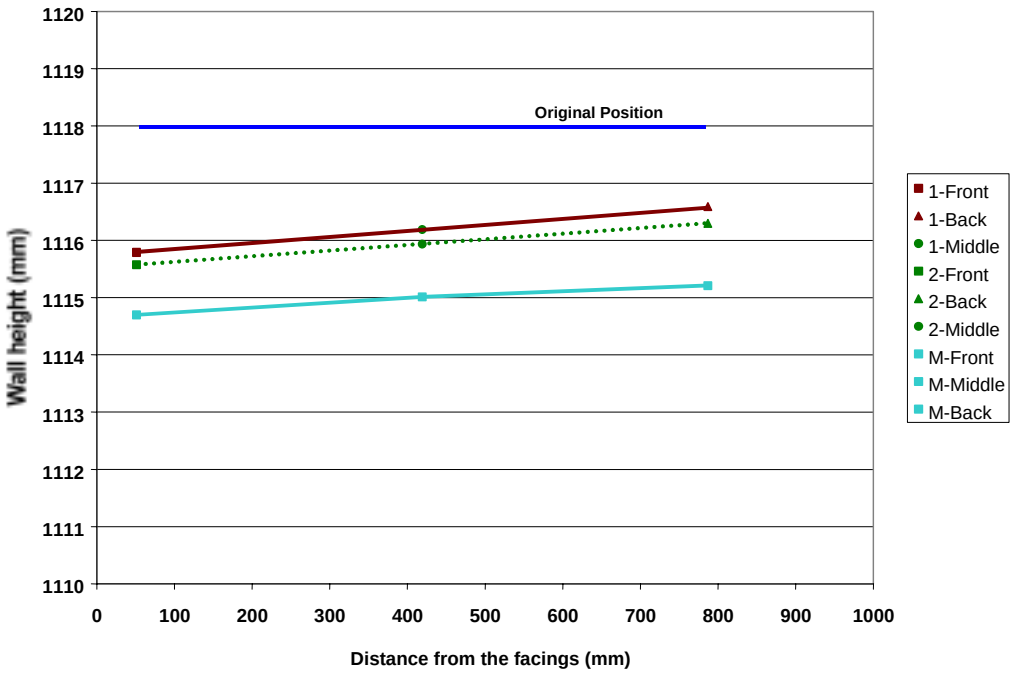

Figure 7.53. PET wall settlement at 11.5 kPa surcharge

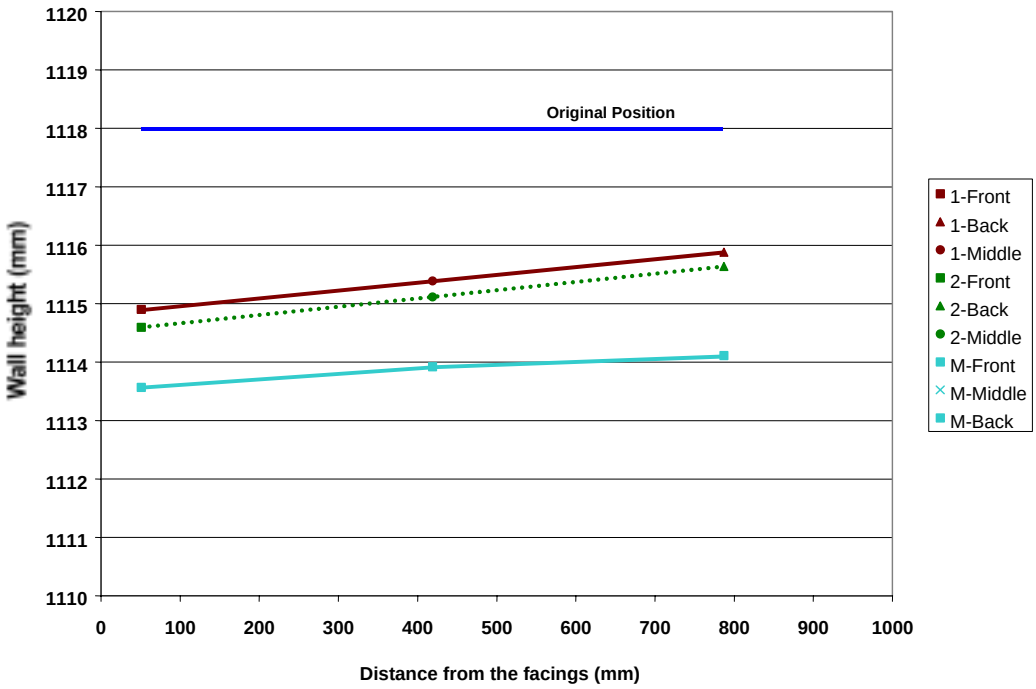

Figure 7.54. PET wall settlement at 16.7 kPa surcharge

7.4 CALIBRATION OF FLAC MODELING

In order to compare in a more reliable manner the small scale MSE wall testing and the FLAC modeling, two calibration factors, "a" and "b" were used to interpret the results obtain with the FLAC modeling. These factors account for differences due to material and geometric properties between the small scale walls and the FLAC model. For instance, the linear elastic-perfectly plastic Mohr-Coulomb model used to model the soil may not be accurate in defining the behavior of the backfill under scaled conditions due to the excessive dilation under low confinement. This is due to the fact that gravity could not be scaled in the physical model. In addition, simplifications are always made in numerical models with respect some of the geometric aspects of the system, such as boundary conditions. For example, the three-dimensional effects due to the limited width of the wall are not captured in

the numerical model. Instead, a plane strain condition is assumed. Therefore, parameters "a" and "b" are intended to capture the influence of such model irregularities. The theoretical formulation is described next.

Dancygier (1995) shows that when a centrifuge is not available, it is not possible to scale the gravitational effect. Therefore, for a variable X , there are two components X_g which is the gravitational component and X_{ng} which is the non-gravitational component. This gives the following general expression:

$$X = (X_g^{\alpha} + X_{ng}^{\alpha})^{1/\alpha} \tag{7.1}$$

where:

α = non-dimensional parameter that depends on the physical problem

X = variable representing a quantity measures in the small scale experiment

X_g = gravitational component of X

X_{ng} = non-gravitational component of X

The parameter α, a coupling factor for the non-gravitational and gravitational components, typically requires extensive testing of various scaled models, and is commonly assumed to be equal to 1. The distortion for $\alpha = 1$ has been defined by Dancygier (1995) as:

$$D' = 1/\left\{1 + \left[1/\left(n^{\beta} - 1\right)\right]\left(X^m / X_g^m\right)\right\} \tag{7.2}$$

where:

D' = distortion, relative to X'

n = scaling factor

β = non-dimensional parameter which depends on the system under investigation

m = small scale model

X^m = model value of X (usually measure in the small scale experiment)

X_g^m = gravitational component of X^m

The distortion relative to the extrapolated (distorted) value of X , D^{xpl} , is defined as follows:

$$D^{xpl} = \left(n^{\beta} - 1\right)\left(X_g^m / X^m\right) \tag{7.3}$$

The distortion in the extrapolation of the results from a small scale test, due to the lack of gravity scaling, can be significant when the gravitational component is large relative to the non-gravitational component (i.e., X^m / X_g^m is close to 1). On the other hand, if the gravitational component is small (i.e., X_g^m / X^m is relatively small), the distortion is small and can even vanish. Also, the larger the scaling factor, the larger is the distortion. From Figures 7.55 to 7.56, it can be further seen that the higher the scaling factor *n*, the lower the distortion.

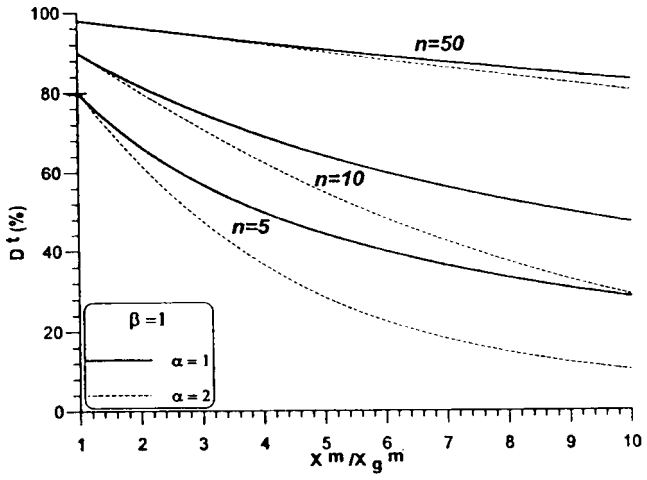

Figure 7.55. Distortion, relative to the undistorted variable, $1< X^m / X_g^m < 10$ (source: Dancygier, 1995)

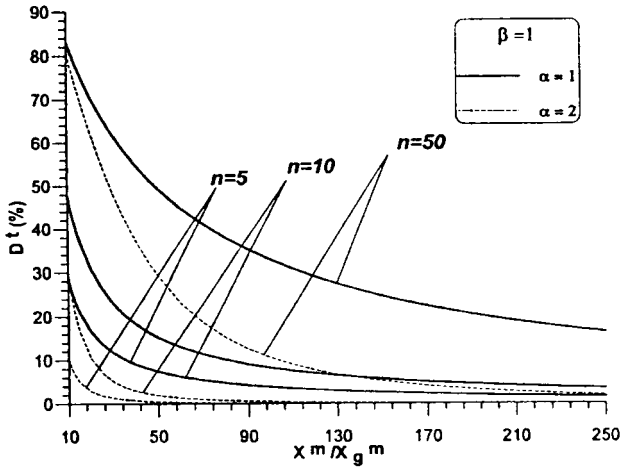

Figure 7.56. Distortion, relative to the undistorted variable, $10< X^m / X_g^m < 250$ (source: Dancygier, 1995)

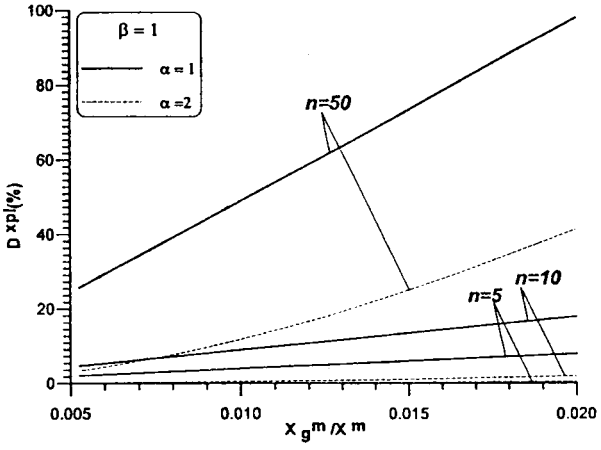

Figure 7.57. Distortion, relative to the extrapolated value, $0.005 < X_g^m / X^m < 0.02$ (source: Dancygier, 1995)

From these figures, it can be seen that the lower the surcharge on the MSE wall, the larger the distortion. This also explains why the higher layers of geogrid and panels have better agreement, since the gravity component is smaller near the top of the wall. To clarify this point, consider the stress, P_t, at a depth h from the top surface of the wall. If an external uniform surcharge, P_s, is applied at the top of the MSE wall, and soil arching is ignored, a first order estimate of the stress can be obtained as follows:

$$P_t = \rho g h + p_s \tag{7.4}$$

where:

P_t = total pressure over a specific depth in the MSE wall

ρ = mass density of the soil backfill

g = acceleration of gravity

h = depth to point of interest

P_s =surcharge on top of the MSE wall

For static loading conditions and first order approximation

$\alpha = \beta = 1;$ $\quad X^m = \rho g h^m + p_s^m;$ $\quad X_g^m = \rho g h^m$

Considering $n = 5.5$ and substituting into equation 7.2 and 7.3 gives the following:

$$D' = \frac{1}{1 + \left[\frac{1}{(5.5-1)}\right]\left(1 + \frac{p_s^m}{\rho g h^m}\right)}$$

$$D^{xpl} = (5.5-1)\left[\frac{1}{\left(1 + p_s^m / \rho g h^m\right)}\right]$$

Thus, the following values of D' *and* D^{xpl} are obtained:

For $P_s = 0$ $\quad D' = 82\%$ $\quad$ *and* $\quad D^{xpl} = 450\%$

For $P_s \approx \rho g h^m$ $\quad D' = 41\%$ $\quad$ *and* $\quad D^{xpl} = 225\%$

For $P_s = 16.7$ kPa $\quad$ and $\rho g h^m \approx 1$ $\quad D' = 5\%$ $\quad$ *and* $\quad D^{xpl} = 25\%$

It can be concluded that with no external load on top of the wall the distortion can be very significant. On the other hand, for surcharges of 11.5 and 16.7 kPa the distortion is reduced considerably and even more at the top, since just below the top $h^m \approx 0$ the values of D' *and* D^{xpl}. are close to 0%.

Following Dancygier (1995) methodology, the value of correction factor "a" was obtained by comparing the test curves and the model curves for all the different loads. Calibration factor "a" is then calculated by comparing the values with the least discrepancy between test and numerical model. It was found that for the HDPE geogrid reinforced walls the surcharge of 11.5 kPa showed the least discrepancy between the test and model curves. The corresponding value of factor "a" was 0.9, which means that the value of the numerical model must be multiplied by a calibration factor of 90% to match the test results. For the PET geogrid reinforced walls, this condition also occurred at a surcharge of 11.5 kPa, with a calibration factor "a" of 0.7.

The value of calibration factor "b" was obtained once "a" had been applied. Factor "b" accounts for the scale effects, therefore it varies depending on the surcharge, as mentioned earlier. Tables 7.1 and 7.2 show the factors used to correct the FLAC modeling curves for the HDPE and PET small scale MSE walls, respectively.

Table 7.1. Calibration Factors for the HDPE Small Scale MSE Wall

Surcharge level kPa	Correction factor "a"	Correction factor due to scaling "b"
0.0	0.9	0.25
0.8	0.9	0.4
3.6	0.9	0.3
6.4	0.9	0.85
11.5	0.9	1
16.7	0.9	0.95

Table 7.2. Calibration Factors for the PET Small Scale MSE Wall

Surcharge level kPa	Correction factor "a"	Correction factor due to scaling "b"
0.0	0.7	0.1
0.8	0.7	0.25
3.6	0.7	0.25
6.4	0.7	0.5
11.5	0.7	0.55
16.7	0.7	1

It can be seen from the tables that the surcharge levels affect the correction factor for scaling, which agrees with the findings of Dancygier, 1995. Also, the height of the wall has an impact on the agreement between the FLAC modeling and the small scale MSE wall testing,

with better agreement towards the top of the wall, where $\rho g h^m$ is closer to zero. There is better agreement for the HDPE MSE wall than the PET wall. This is attributed to the low modulus of the PET geogrid, which results in larger discrepancies between the test and the FLAC model.

A general equation can be derived for calibration factor "b" as a function of surcharge level. This is done through statistical regression analysis of the results presented in Tables 7.1 and 7.2. The resulting general equations for "a" and "b" are as follows:

For HDPE Walls:

$$a = 0.9 \tag{7.5}$$

$$b = 0.324 + 0.0463\, q \tag{7.6}$$

For PET Walls:

$$a = 0.7 \tag{7.7}$$

$$b = 0.132 + 0.0476\, q \tag{7.8}$$

where:

q = surcharge on top of the wall in kPa

Calibration coefficients "a" and "b", calculated from Eqs. 7.5 through 7.8, have been used to correct the FLAC model results for the small scale walls, to account for the discrepancies resulting from the scale effects. As mentioned earlier, when an MSE wall is constructed at a smaller scale and tested, such discrepancies arise from the soil excessive

dilatancy at small confining pressures, which adds an “apparent” stiffness to the wall. Coefficients “a” and “b” can also be used in the opposite sense, that is, to correct small scale test data to match the corresponding full scale behavior. For example, the results from a small model test may be divided by coefficients “a” and “b” before it is multiplied by the scale factor “n” in order to reproduce the large scale data. Within the scope of the present project, the use of coefficients “a” and “b” have been used to calibrate the FLAC model. The results from this procedure are outlined next.

Figures 7.58 to 7.60 show some examples of corrected curves for horizontal panel displacements for the HDPE small scale MSE wall, and Figs. 7.61 to 7.63 show similar examples of corrected curves for the PET small scale MSE wall. The full lines represent the values for the testing of the small scale MSE Wall 1, and the dotted lines for the testing of the small scale MSE Wall 2. The FLAC modeling results are represented with a teal color full lines. The lines for factor "a" are presented in lime color full lines and the ones for "a × b" in plum color full lines. It is noted that in Fig. 7.60, the calibration factor “b” has not been applied because its values is equal to 1. Therefore, the lines for factor “a” and “a × b” are identical.

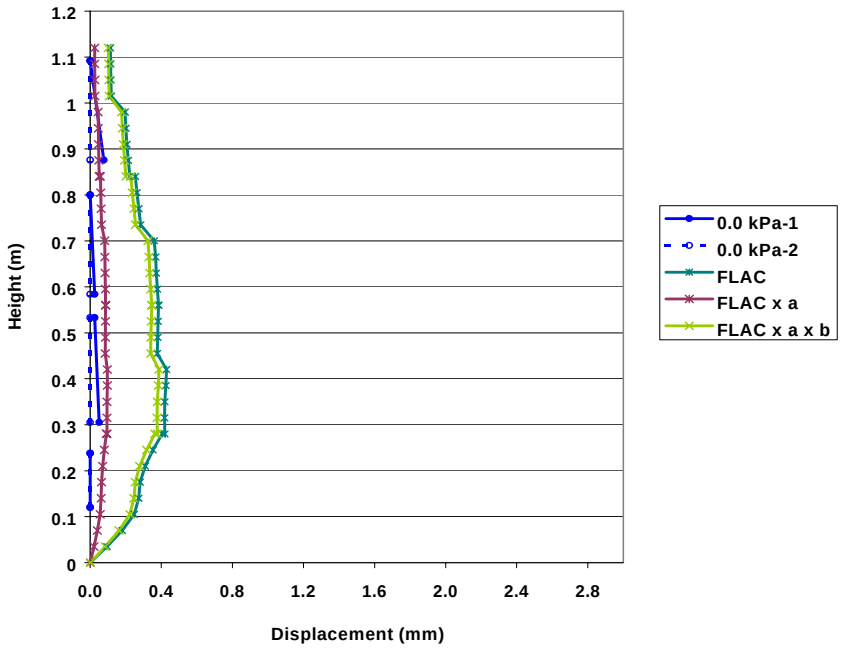

Figure 7.58. Test, FLAC, and FLAC corrected curves for 0.0 kPa surcharge, HDPE Wall

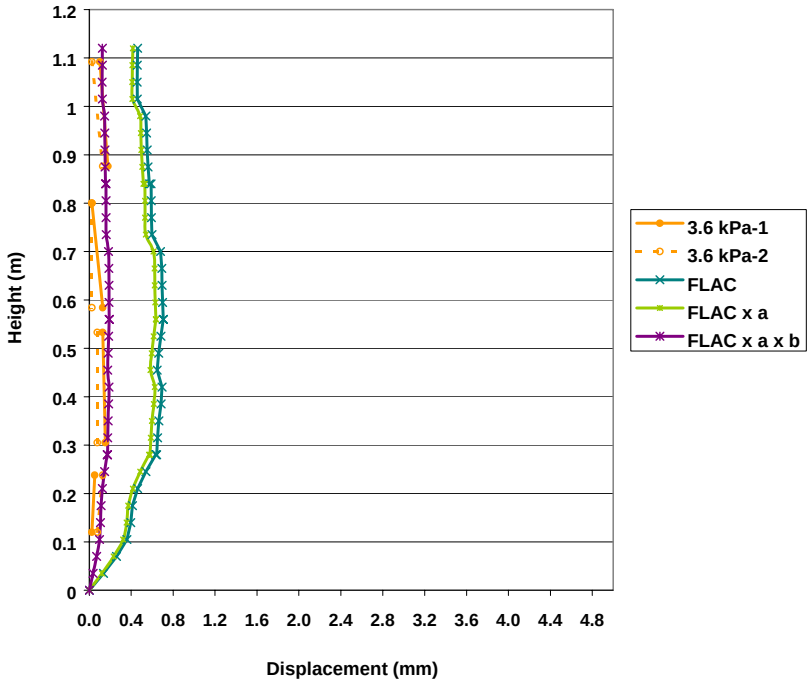

Figure 7.59. Test, FLAC, and FLAC corrected curves for 3.6 kPa surcharge, HDPE Wall

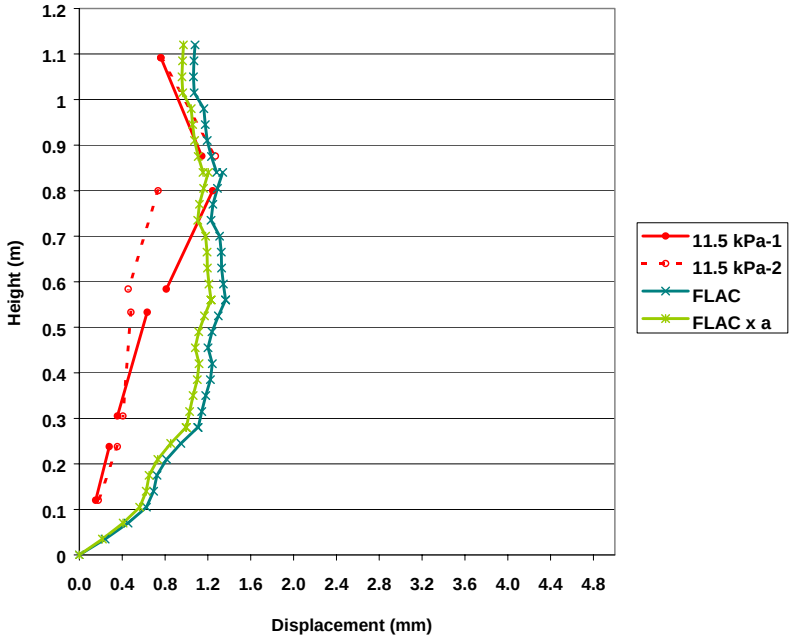

Figure7.60. Test, FLAC, and FLAC corrected curves for 11.5 kPa surcharge, HDPE Wall

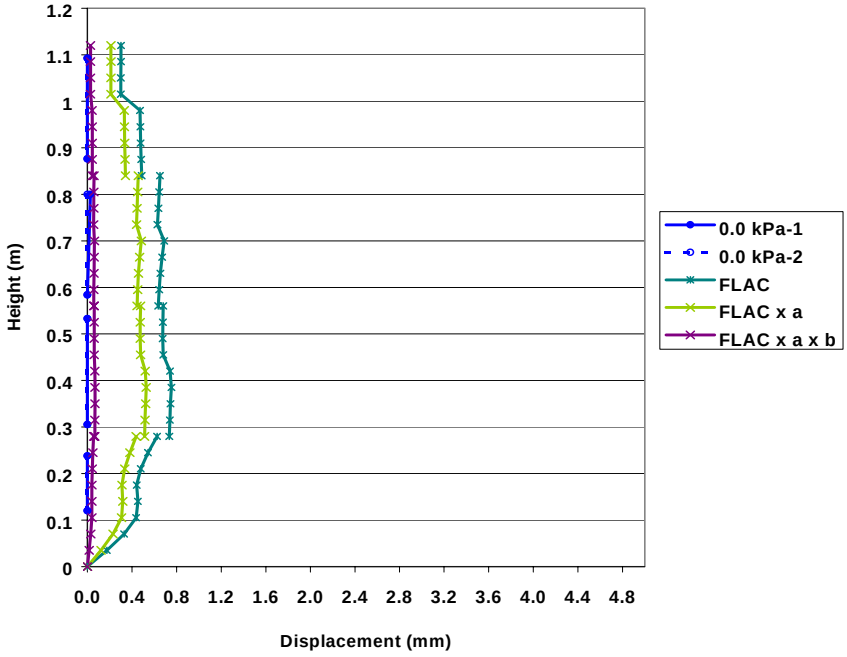

Figure 7.61. Test, FLAC, and FLAC corrected curves for 0.0 kPa surcharge, PET Wall

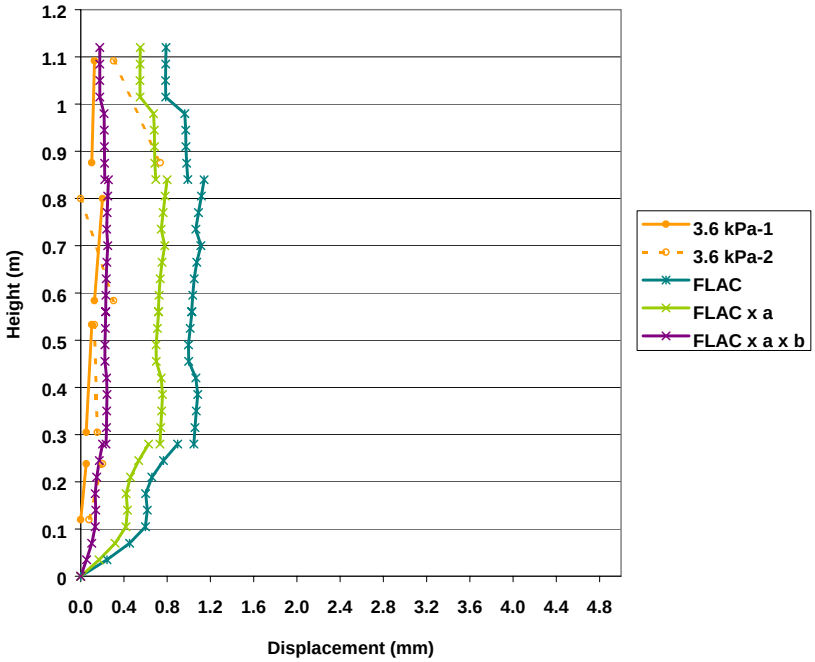

Figure 7.62. Test, FLAC, and FLAC corrected curves for 3.6 kPa surcharge, PET Wall

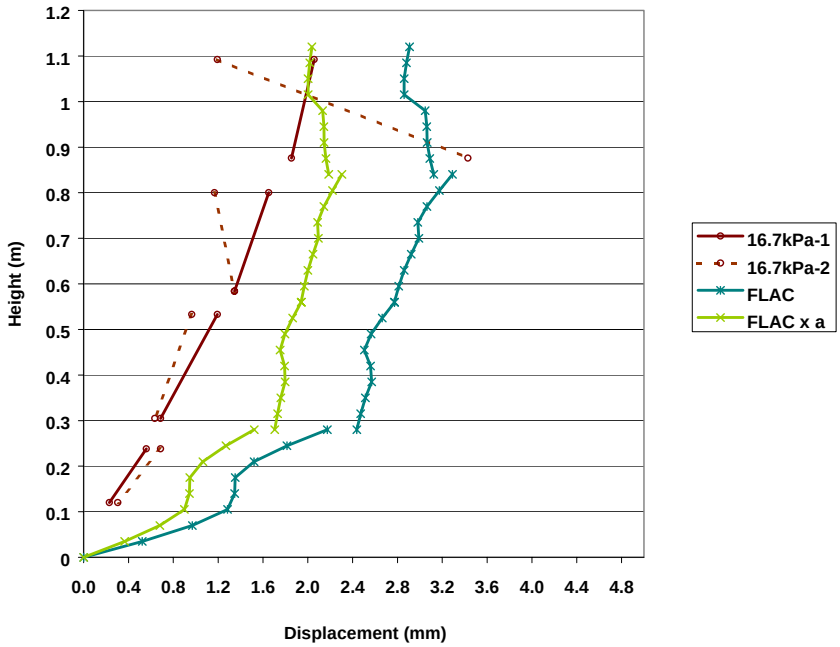

Figure 7.63. Test, FLAC, and FLAC corrected curves for 16.7 kPa surcharge, PET Wall

Figures 7.64 to 7.69 show the corrected curves for the strains in the first, third, fifth, and seventh layers of reinforcement obtained for the HDPE and PET small scale MSE wall testing, the corresponding FLAC modeling, and the corrected FLAC curves. Full lines represent the values for the testing of the small scale MSE Wall 1, and the dotted lines the testing of the small scale MSE Wall 2. The FLAC modeling results are represented with lighter tone of the corresponding color full line with seventeen points, while the test data has two points for the first layer, three for the third and fifth layer, and four for the seventh layer of wall 1, and three for wall 2. The curves for the correction factor "a" are presented in lime color full lines, and for "a × b" in plum color full lines. It is noted that in the cases where only the correction for “a” in included, the corresponding “b” values was equal to 1. Therefore, the corrected “a” and “a×b” values are identical.

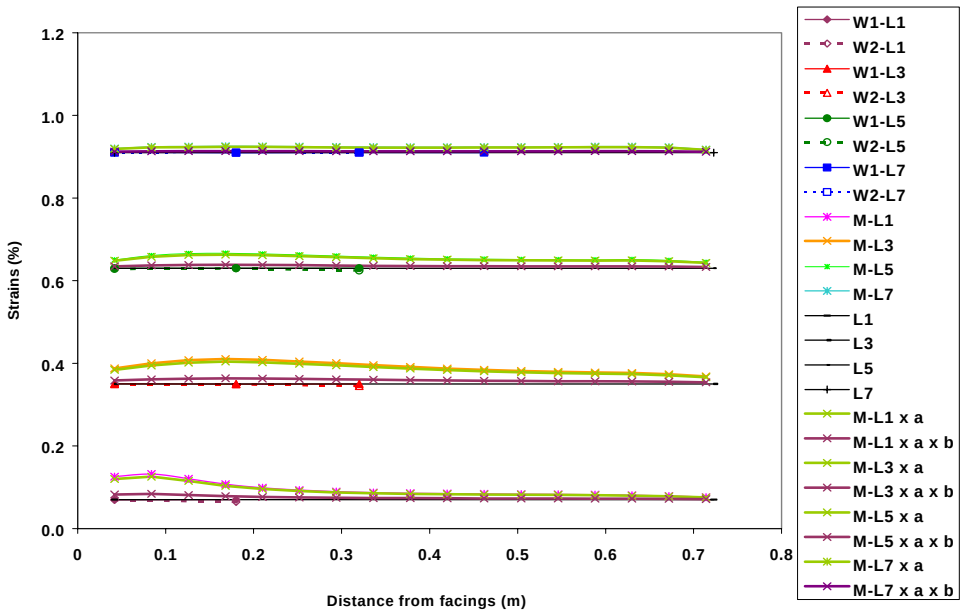

Figure 7.64. Test, FLAC, and FLAC corrected curves for strains for 0.0 kPa surcharge, HDPE Wall

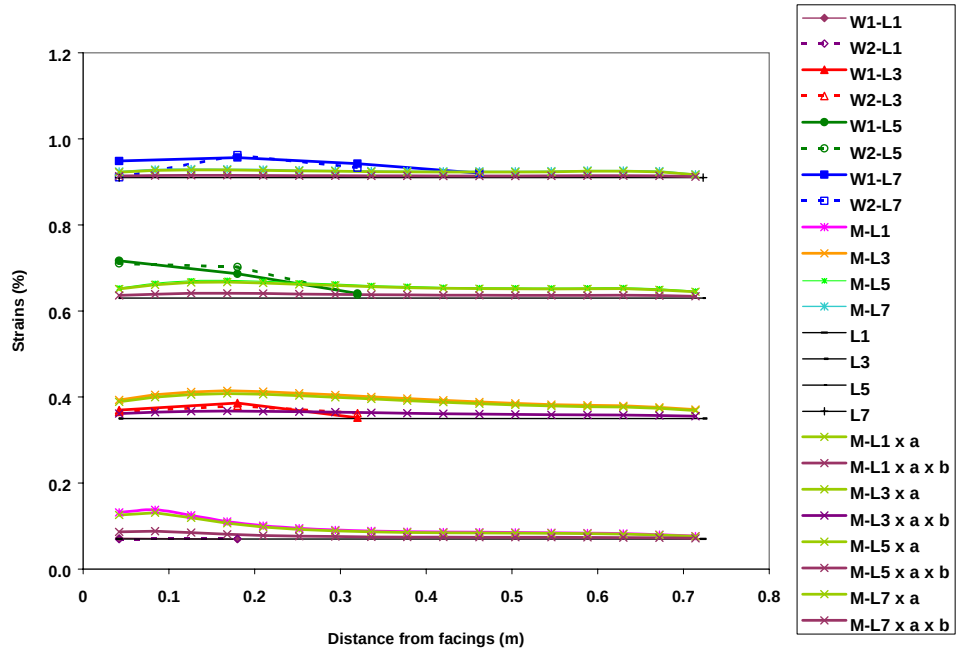

Figure 7.65. Test, FLAC, and FLAC corrected curves for strains for 3.6 kPa surcharge, HDPE Wall

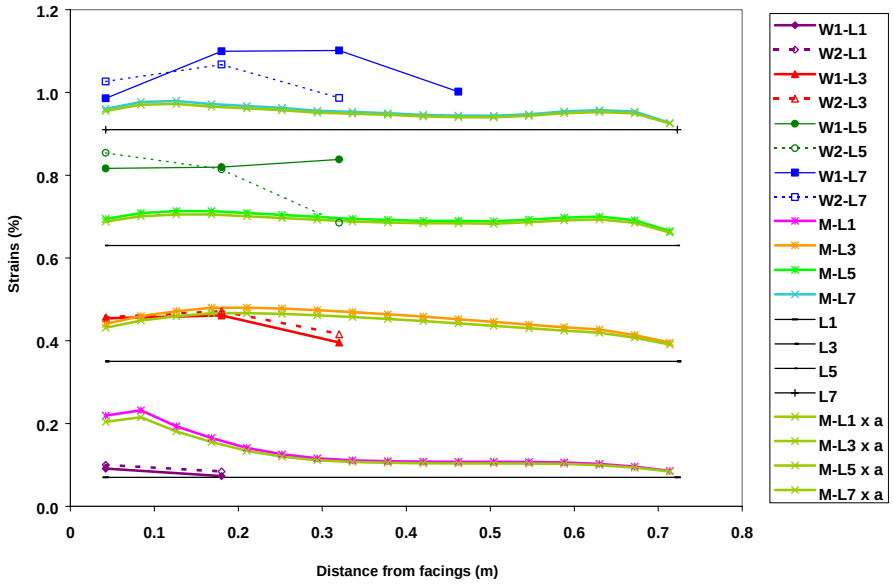

Figure 7.66. Test, FLAC, and FLAC corrected curves for strains for 11.5 kPa surcharge, HDPE Wall

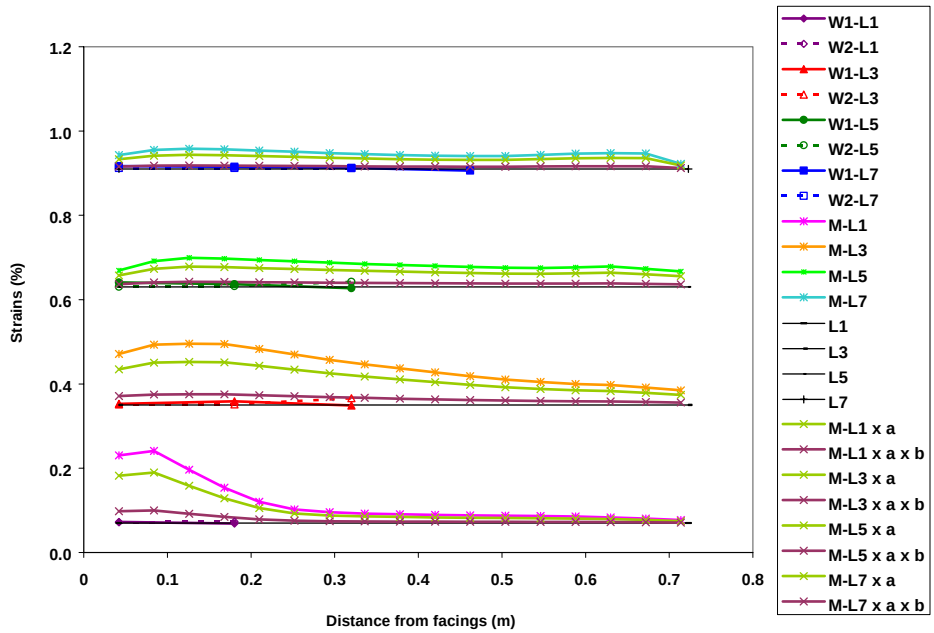

Figure 7.67. Test, FLAC, and FLAC corrected curves for strains for 0.8 kPa surcharge, PET Wall

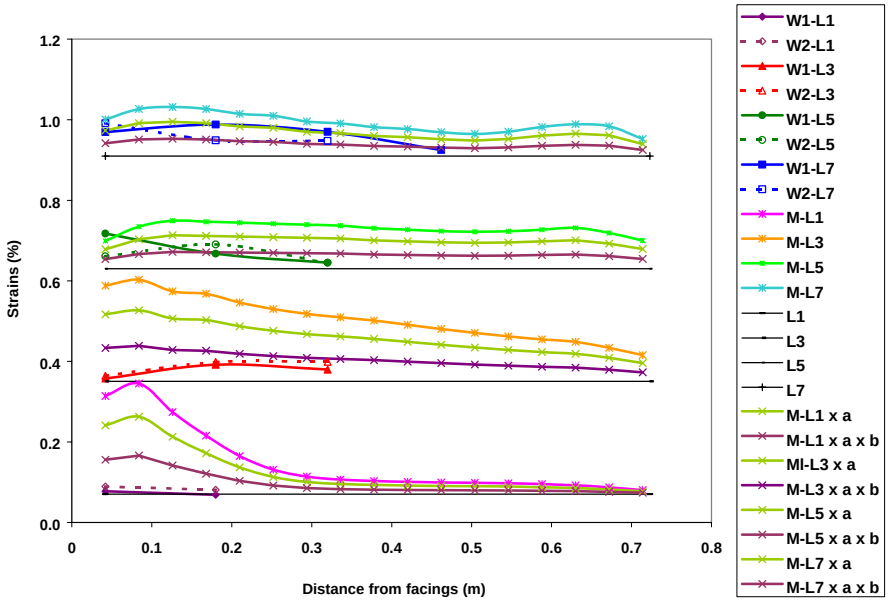

Figure7.68. Test, FLAC, and FLAC corrected curves for strains for 6.4 kPa surcharge, PET Wall

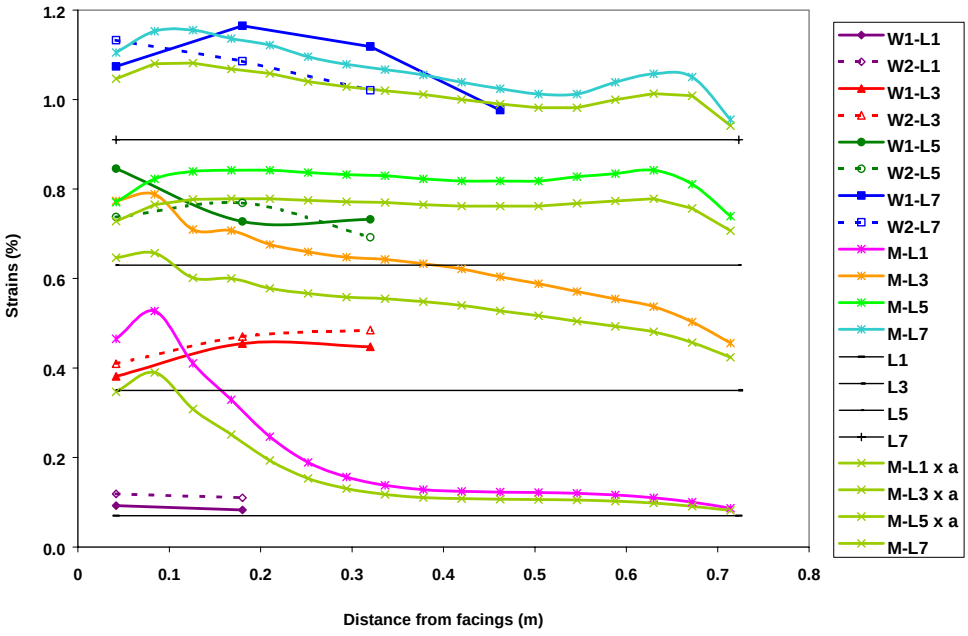

Figure 7.69. Test, FLAC, and FLAC corrected curves for strains for 16.7 kPa surcharge, PET Wall

Figures 7.70 to 7.75 show the comparison of the settlements obtained by the HDPE and PET small scale MSE wall testing, and the FLAC modeling. Full brown lines represent the values for the testing of the small scale MSE Wall 1, and the dotted green lines the testing of the small scale MSE Wall 2. The FLAC modeling results are represented in aqua color for all the surcharges. The curves for correction factor "a" are presented with lime color full lines, for the correction "a x b" in full red lines. A blue line indicates the level of the loading plate before removing the support after construction.

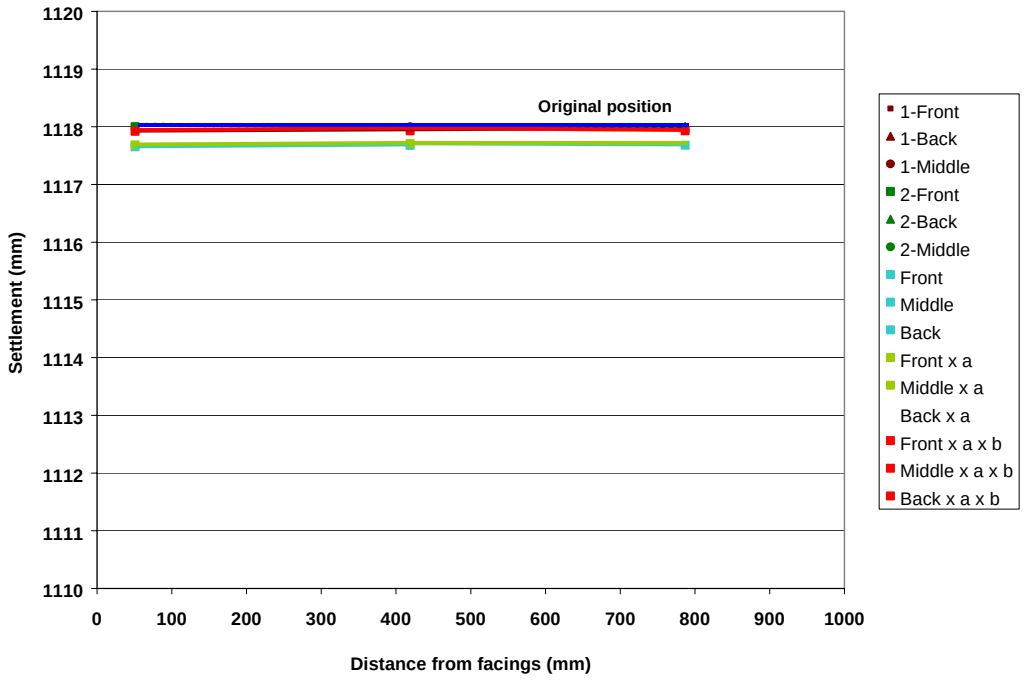

Figure 7.70. Test, FLAC, and FLAC corrected wall settlement for 0.0 kPa surcharge, HDPE Wall

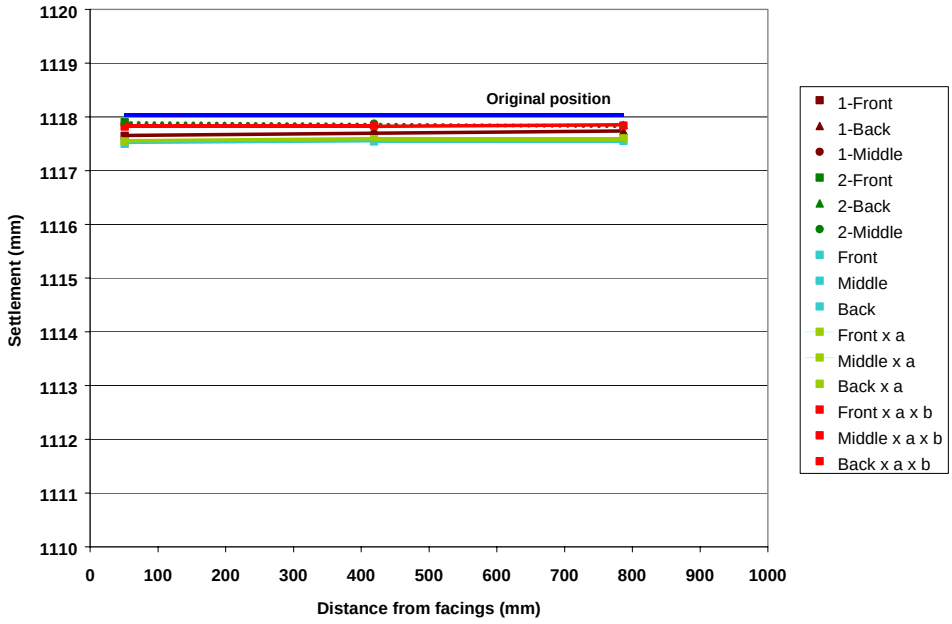

Figure 7.71. Test, FLAC, and FLAC corrected wall settlement for 0.8 kPa surcharge, HDPE Wall

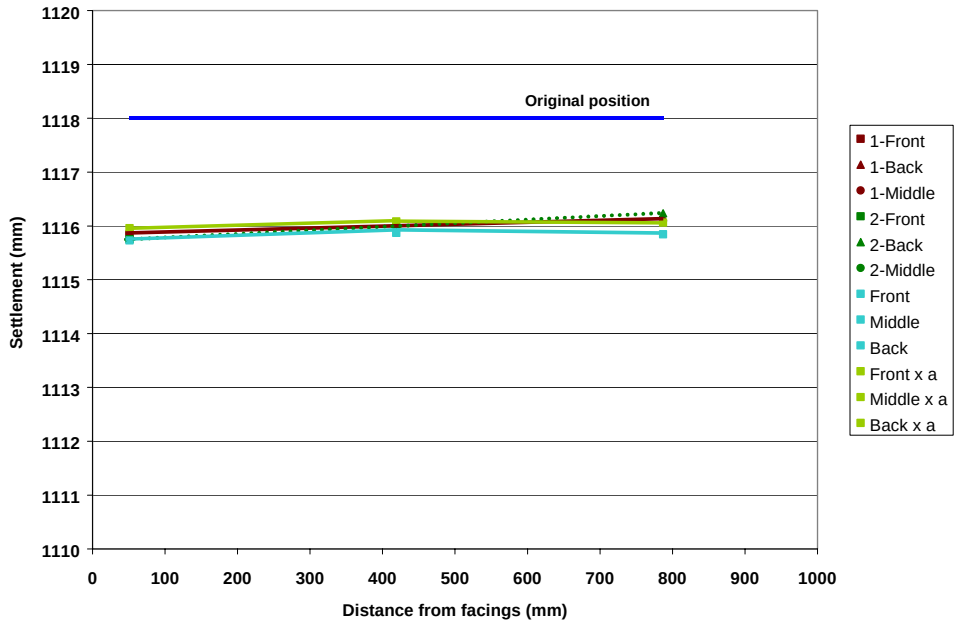

Figure 7.72. Test, FLAC, and FLAC corrected wall settlement for 11.5 kPa surcharge, HDPE Wall

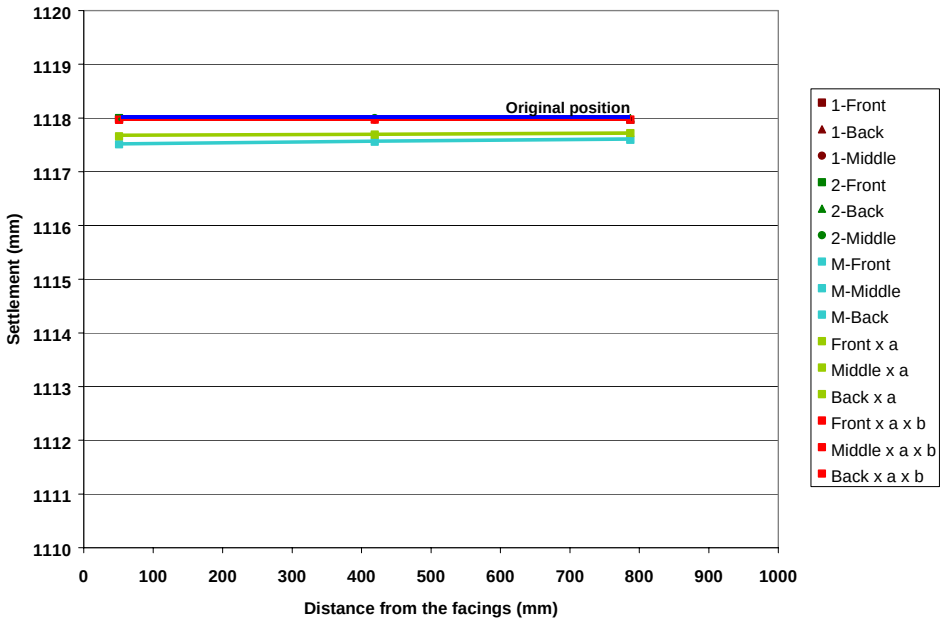

Figure 7.73. Test, FLAC, and FLAC corrected wall settlement for 0.0 kPa surcharge, PET Wall

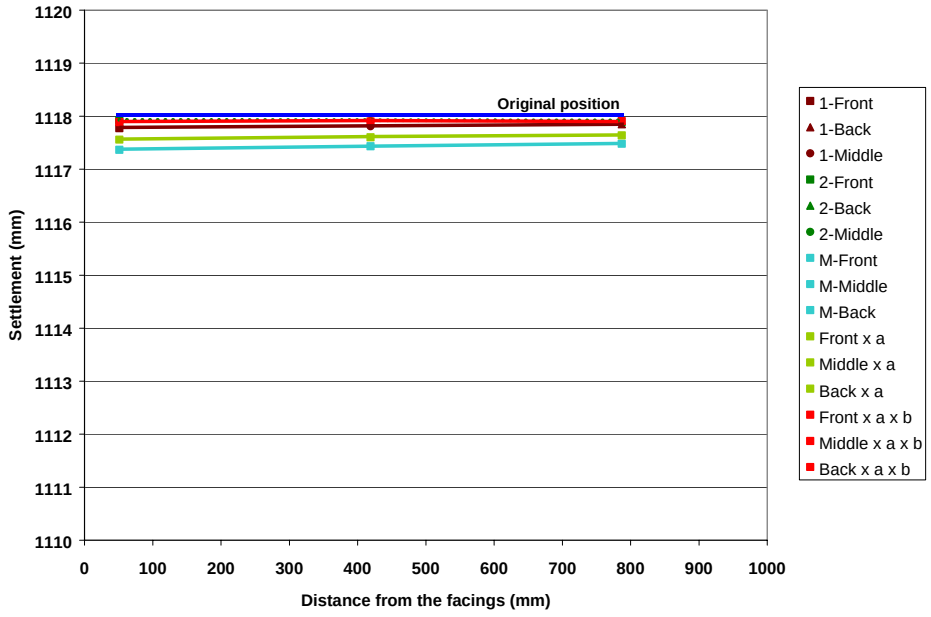

Figure 7.74. Test, FLAC, and FLAC corrected wall settlement for 0.8 kPa surcharge, PET Wall

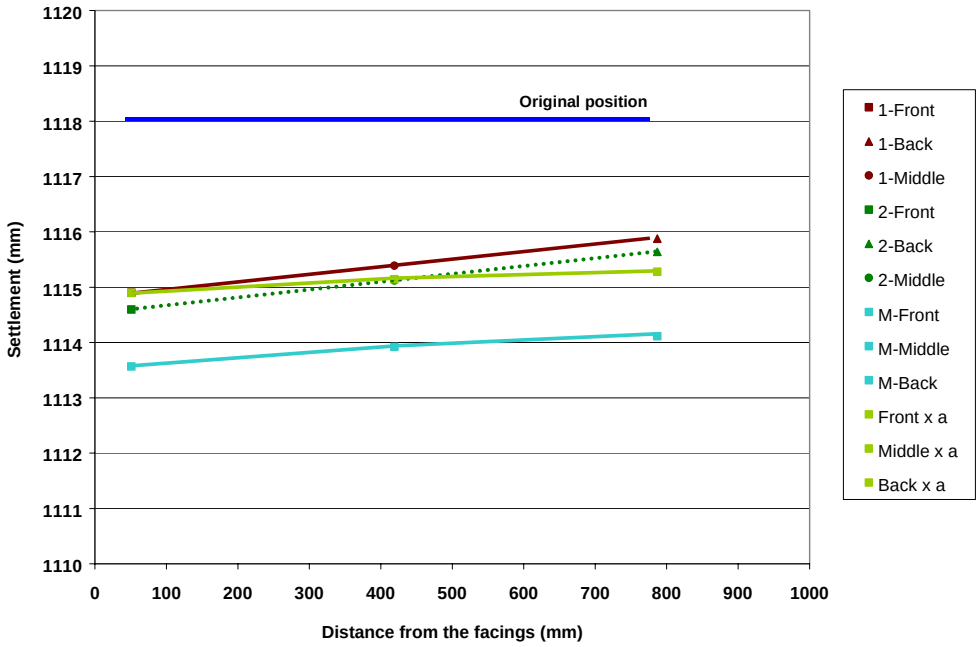

Figure 7.75. Test, FLAC, and FLAC corrected wall settlement for 16.7 kPa surcharge, PET Wall

7.5 ANALYSIS CONCLUSIONS

The small scale testing showed that both the HDPE and PET geogrids are effective for soil reinforcement since the deformations encountered and strains in the geogrid were very small, even at loads above normal working loads. While the HDPE small scale MSE wall exhibited smaller panel displacements, the PET small scale MSE wall showed smaller strains. This indicates that the reduction of the effective length may have affected the pullout capacity of the PET geogrid. This is attributed to the difference between the Rankine plane of failure which is currently used for the calculation of the effective length of geogrid and the observed curved surface of failure. The observed plane of failure requires larger effective lengths (see

Figs 7.3 and 7.4). This indicates that it would be more conservative to use the observed curved surface of failure in calculating the effective lengths beyond the active zone.

The comparison between the results from the small scale MSE wall testing and the FLAC modeling showed the same trend but the values of the model were larger than those obtained by the testing. The difference was greater for PET geogrids due to the low modulus of elasticity, which makes the FLAC model predict larger strains and deformations than occurred in the test. The difference between the testing and the FLAC modeling can be attributed to the distortion created by the limitation to scale the gravity and the corresponding distortions in soil properties, as well as the geometric differences between the three-dimensional test and the FLAC model. The effect is particularly significant at zero load. As the load on top of the wall increases the distortion is reduced. Further, the distortion was reduced as the depth in the wall decreases since the gravity component is reduced to zero at the top of the wall.

In order to compare in a more reliable manner the small scale MSE wall testing and the FLAC modeling, two calibration factors were used to correct the results obtained with FLAC. The first factor “a” accounts for parameter scaling and was equal to 0.9 for the HDPE wall and 0.7 for the PET. Factor "b" accounts for the scale effects, and is determined from Eqs. 7.6 and 7.8 for HDPE and PET walls, respectively.

8 CONSTRUCTION AND TESTING OF FULL SCALE WALL

A full scale wall was constructed on the Florida Atlantic University campus in Boca Raton with the purpose of long term testing, and a plan for loading to failure. More details on the design methodology and procedures of the wall were given in Chapter 5 and Appendix C. It is reiterated here that the wall was designed to a Factor of Safety of 1, according to the standard FHWA design methods, with the intent to expedite distress and fail the wall. The purpose behind this design was also to verify whether or not the current FHWA design method is overly conservative. As will be seen in Chapter 9, it was demonstrated through analysis and observation that indeed the current design is much more redundant than previously thought.

Figures 8.1 shows a schematic plan of the MSE wall. Figures 8.2 through 8.6 show the construction progress, and Figure 8.7 shows the finished MSE wall with the instrumentation setup. Because only one full scale wall was constructed, HDPE reinforcement was placed on one face while PET was used on the other face. It is important to note that, due to space restrictions and construction limitations, the wall does not simulate plane strain conditions. Instead, a sloped abutment was constructed on either side of the wall to allow equipment and machinery access (see Fig. 8.1). As a result, the sloped abutment wings, wrapped around the wall facing (Fig. 8.7), caused additional restrictions to the deformation of the wall, especially within the bottom layers. The analysis, done in plane strain conditions, cannot simulate this three-dimensional restrictive effect.

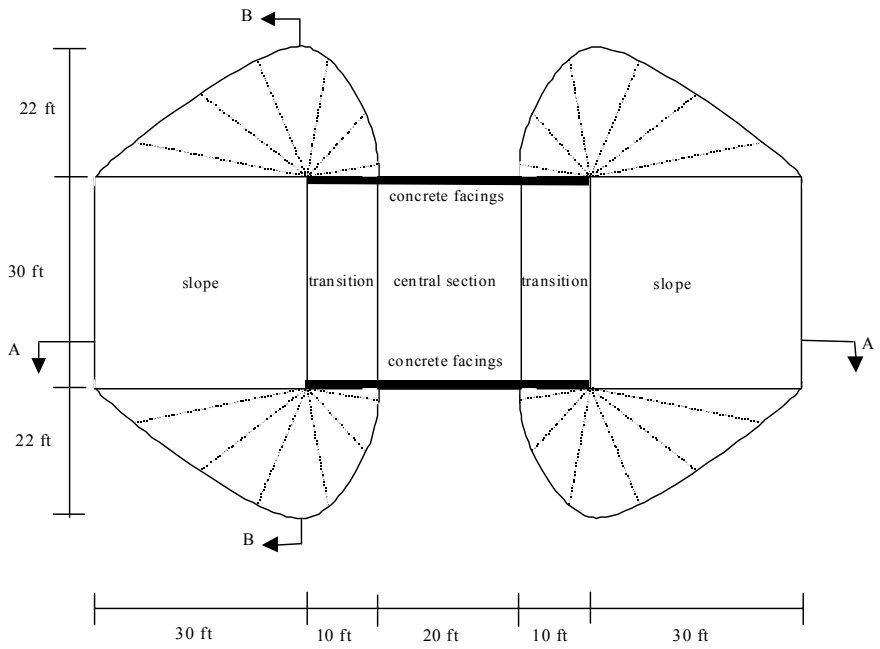

Figure 8.1. Schematic plan of the MSE wall.

Figure 8.2 Compaction of the MSE wall

Figure 8.3. Nuclear density gage measurements for compaction QC

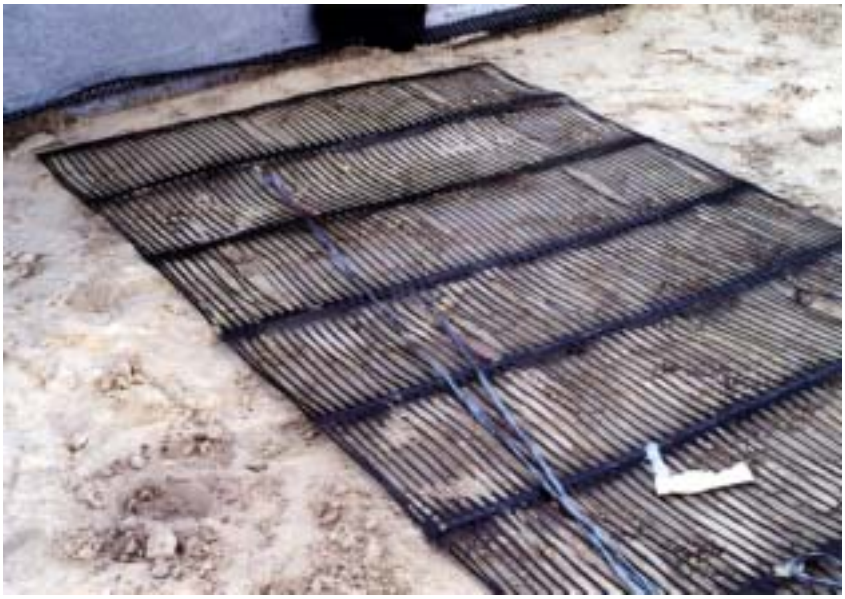

Figure 8.4. Geogrid instrumentation

Figure 8.5. Placing of geogrids

Figure 8.6. Vertical alignment of the facings

Figure 8.7. Full scale MSE wall built at FAU, at the end of construction

8.1 INSTRUMENTATION

The instrumentation for the large wall was similar to the small scale walls (Chapter 6) with the addition of six gas thermometers.

8.1.1 DATA ACQUISITION SYSTEM

A Vishay System 5000 from Measurements Group, Inc., with 40 channels was used to take readings from the strain gages. In addition, two Digital Strain Indicators, Model P-3500, and two Switch and Balance Unit, Model SB-10, were used.

8.1.2 STRAIN GAGES

Strain Gages-YFLA-2-3L from Tokyo Sokki Kenkyujo were used for strain measurement. The gage utilizes a special plastic carrier base that is able to withstand extreme elongation without creeping or cracking, and is capable of measuring approximately 10 to 20 % of strain with the needed accuracy. Extensive testing was carried out for the bonding and calibration of the strain gages.

8.1.2.1 Miscellaneous Agents for Strain Gages

Glue: Adhesive Type CN, Cyanoacrylate Base product from Yokyo Sokki Kenkyijo Co., Ltd, was used. The operating temperature range from –30°C to 100°C under curing pressure 980 kPa. It has a strain limit of 20 % and excellent electrical properties.

Degreaser: Type CSM-1A, a 1-1-1 Trichloro-ethylene solvent product of the Micro-Measurements Division of Measures Group, Inc, was used to degrease the surface of the test specimen because of its inertness to polyethylene. The degreaser prevents the embedding of contaminants on the surface of the geogrid specimen.

Neutralizer: Type MN5A-1, a mild ammonia solution was used, that leaves the test specimen with a slightly alkaline pH value.

ARON Polyprimer: Used only for the PET geogrid, this is a surface preparation agent which allows cyanoacrylate adhesives, such as TML type CN, to be used for strain gage bonding on polyethylene and polypropylene. It is a product of Yokyo Sokki Kenkyijo Co., Ltd..

Coating Material: A single-component microcrystaline wax was used to form a good moisture- and water-resistant coating.

Silicon cover: Marine glue 5200 was used to cover the coated strain gages for extra protection.

Plastic tubing: Clear plastic tubing (1/2") was used for final protection of the strain gages.

8.1.3 DIAL GAGES

Sixteen Dial Gages (MSC 76450071) with a measuring range of 2" and a precision of 0.001" were used to measure panel displacements.

8.1.4 SETTLEMENT PLATES

One settlement plate was placed for each half of the MSE Wall and readings were taken for the finished wall. A building adjacent to the site was marked as a reference for the readings.

8.1.5 GAS THERMOMETERS

Three gas thermometers were placed on each side of the wall for geogrid layers 3, 5 and 7. For the ambient temperature and the temperature in layer 1, an electronic thermometer was used. In addition, two gas thermometers were placed at the middle of the wall (Fig. 8.8).

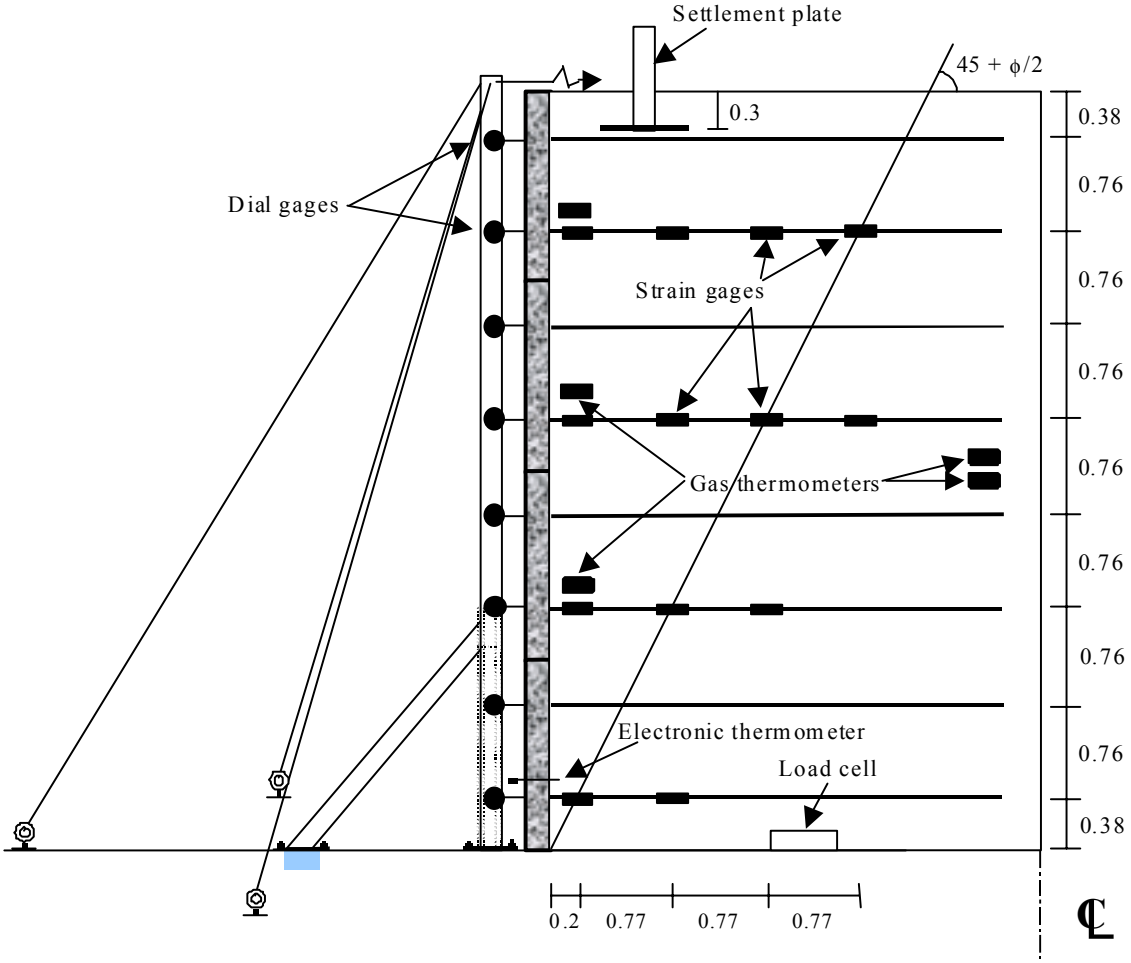

Figure 8.8. Full scale wall instrumentation

8.2 TEST PROCEDURE

During construction, the alignment of the panels was checked with a hand level, a plumbing bob, and a measuring tape, and the displacement values were recorded. Readings of the strain gages were taken with the Digital Strain Indicators before and after the placement of 2.5 ft for sand above each instrumented layer. All the layers gages were read at the end of construction.

Next the dial gages stands were mounted on each side of the MSE wall and readings taken to obtain the initial displacements of the panels with reference to the plumb line. The initial readings of the dial gages, strain gages, load cells, and thermometers were then recorded.

A surcharge of 40 tons (two times the HS-20 ASSHTO loading) was simulated on the top of the wall with an equivalent weight of sand. After the load was placed, readings were taken again. For the first three weeks, readings of all the gages, except the settlement plate movement, were taken twice a week.

Readings of the dial gages and strain gages were taken up to 5,000 hours every 168 hours (once a week) for long term testing. Readings for the settlement plates were taken after the surchage load was placed, at 2,500 hours, and 5,000 hours. The final loading of the MSE wall occurred in Spring 2002, when the load was gradually increased to induce failure. Upon final loading of the wall, the load at the top of the wall was subsequently increased by a factor of 2, yet the wall did not fail. In fact, little deformation occurred. Close examination and further analysis of the results, as outlined in the next Chapter, provided the explanation behind the resilience of the MSE wall.

9 ANALYSIS OF FULL SCALE WALL RESULTS

The full-scale MSE wall experimental results were compared with the values from the numerical solution. The types of geogrids used in the construction of the wall were HDPE-1400 Uniaxial SB, and PET Mirafi Miragrid 3XT. In order to compare the experimental values for the full scale wall with the numerical data, the MSE wall was modeled with the corresponding geogrid modulus used in the experimental wall. The horizontal displacement of the bottom part of the facing placed over the foundation was fixed in an attempt to best simulate the restrictions imposed by the sloped abutment wings.

9.1 INITIAL COMPARISON

Figure 9.1 shows the FLAC plot of horizontal displacements in the soil for the retaining wall. Figure 9.2 compares the horizontal displacements of the test wall at FAU with the numerical solution. The data for the displacements of the facing system was taken 72 hrs after construction of the wall for an initial comparison with the values from the computer analysis. The FLAC analysis results reported in Fig. 9.2 correspond to the calibrated materials properties, but do not account for time and temperature-dependent creep. Figure 9.2 shows maximum displacements of 3.5 cm in the full scale wall after construction and maximum displacements of 2.2 cm from FLAC. These displacements occurred at a height of 4 m in both experimental measurements and FLAC results.

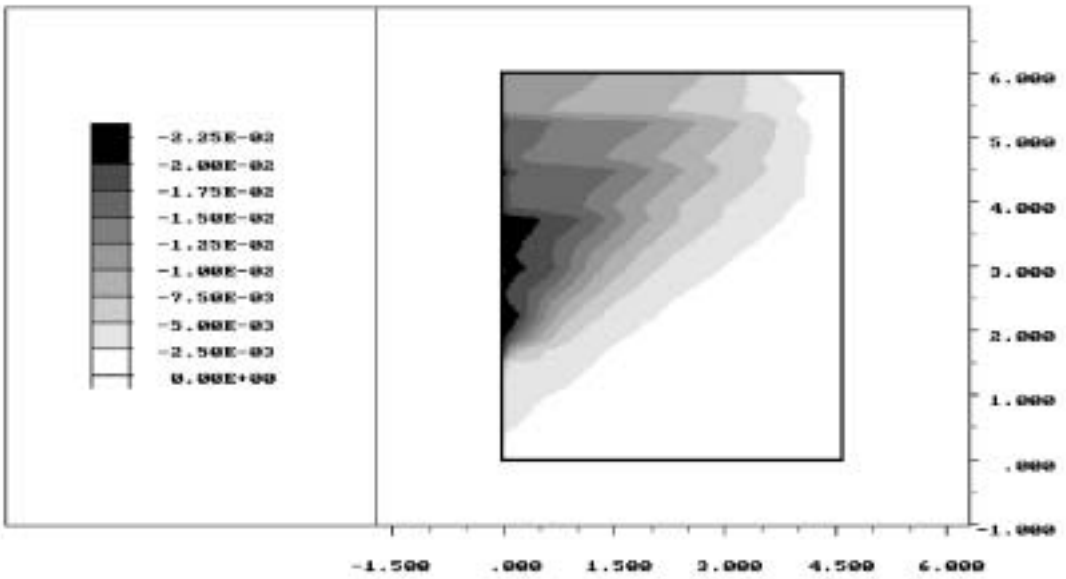

Figure 9.1. Horizontal displacements (in meters) in the full scale MSE wall reinforced with HDPE geogrid

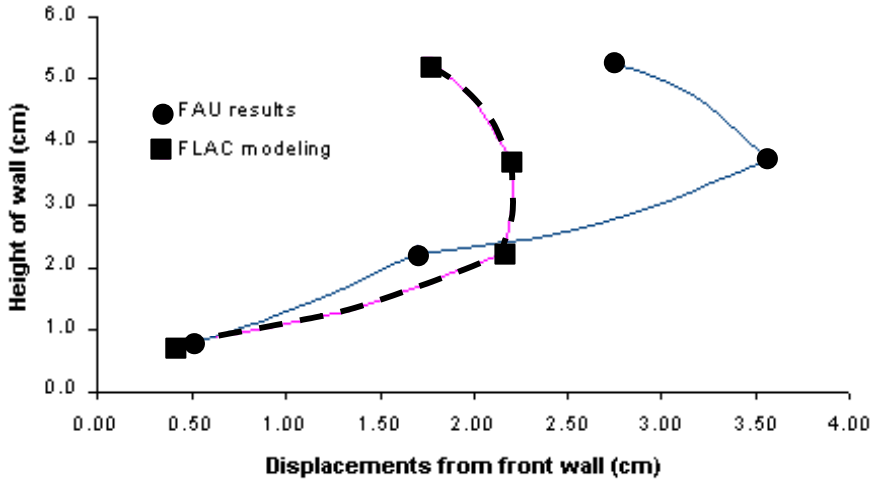

Figure 9.2. Comparison of horizontal displacements in the facing system using the original geogrid modulus (no creep correction)

It is evident that the displacement patterns are similar in trend, but different in magnitude, especially with respect to the maximum values of displacement (at a height of 4 m). The effect of additional restrictions imposed by the sloped abutment wings in the experimental full scale wall should have resulted in less deformation in the experimental wall than in the FLAC mode. However, it is noted that the original calibrated geogrid modulus represents the theoretical conditions immediately at the end of construction, before any creep occurs. In fact, the FLAC geogrid modulus in this analysis was obtained at a log time value of 1, corresponding to a time of 1 minute after the end of construction. In contrast, the experimental measurements were recorded 72 hours after the wall was constructed. Therefore, the deformations due to creep within that time period were not accounted for. In the following section, we describe the procedure taken to account for creep effects.

9.2 INCORPORATION OF CREEP IN THE NUMERICAL MODEL

The numerical modeling for the MSE walls presented in Section 9.1 did not account for the effect of time and temperature on the degradation of the geogrid. Numerical modeling solutions that consider the long-term behavior of any system have not been available in the past. However, with the development of the generalized time-temperature-stress level model for creep of geosynthetics in Chapter 4, it has become possible to incorporate the effect of creep in the analysis.

FLAC allows the modification of material properties while the solution is progressing, by accessing the program memory and changing the relevant parameters. Specifically, for the present situation, it was possible through additional programming to modify the modulus of the geogrid and the axial forces for every geogrid layer to account for geogrid modulus

degradation and the corresponding stress relaxation as a function of time, temperature, and stress level.

To illustrate the methodology of including creep in the modeling of the MSE wall, we considered the situation immediately at the end of construction. The model was first solved with the initial geogrid modulus, representative of the conditions at 1 minute after the end of construction. The program memory was then accessed, and the axial forces for every geogrid segment was changed to account for stress relaxation as a function of time. The new axial force was calculated from the following Equation:

$$\sigma_{axial,new} = \left(\frac{E_{new}}{E_{old}} \right) \sigma_{axial,old} \tag{5.11}$$

where:

$\sigma_{axial,new}$ = Newly assigned (relaxed) axial force (force per unit width)

$\sigma_{axial,old}$ = Original axial force at the end of construction

E_{new} = Newly assigned geogrid modulus

E_{old} = Original geogrid modulus at the end of construction

In the above Equation, the original axial force per unit width, $\sigma_{axial,old}$, is obtained from the analysis output at the end of construction. The geogrid modulus E_{old} is the material property assigned in the original input, and is also equal to the axial force per unit length in the geogrid, divided by the strain. For a specific time interval, say 72 hours, the new geogrid modulus, E_{new}, is obtained by dividing the axial force, $\sigma_{axial,old}$, by the creep strain at 72 hours, calculated from the generalized creep model (Eqs. 4.11 through 4.18), which is a function of

stress level, time, and temperature. The resulting value of $\sigma_{axial,new}$ is then obtained and the solution is iterated until a steady value of strain and stress is reached. This condition would then represent the strains and stresses at the end of 72 hours. Appendix D includes the input program used for this simulation.

At each step of the iteration, the deformations of the wall increase as a result of the creep effect included in the numerical model. The results presented in Fig. 9.3 illustrate the computed horizontal displacements of the facing, obtained from FLAC. By comparing these results to those shown in Fig. 9.2, the increase in deformations due to creep during the first 72 hours following construction is evident.

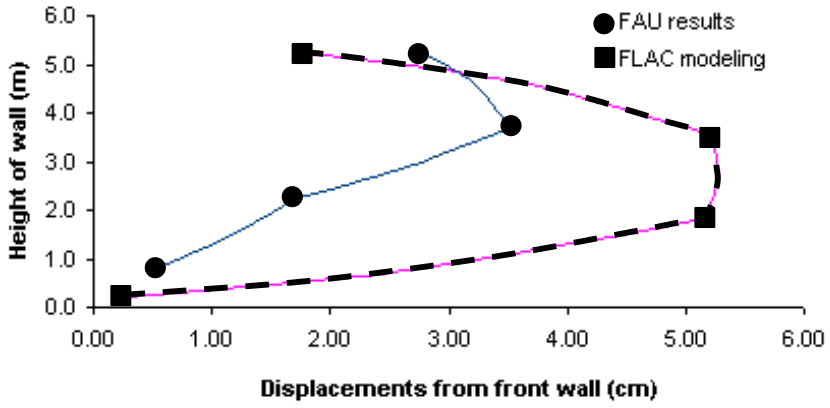

Figure 9.3. Comparison of horizontal displacements in the facing system, with geogrid creep taken into consideration, at 72 hours after construction

It should be noted that each geogrid segment assumes a different geogrid modulus due to the nonlinear distribution of axial loads generated along each geogrid. It is also noted that the deformation calculated from the FLAC model at 72 hours are higher than those measured in the full scale wall. This discrepancy is mainly due to the restrictions imposed by the sloped abutment wings, which prevent the full scale wall from deforming at the bottom.

From Fig. 9.3, it can be concluded that the prediction of the behavior of the MSE wall given by the numerical model could capture the deformation patterns from a qualitative standpoint. However, quantitatively, the magnitudes of the deformation could be further enhanced by much sophisticated modeling, such as three-dimensional FLAC analysis (FLAC3D), taking into account the three-dimensional effects of the wall geometry (abutment wings), as well as the nonlinearity in the soil behavior. A better match between results of the experimental tests with numerical solutions can be then achieved. However, the current analysis has identified the distress mechanisms in the wall, and have illustrated the importance of accounting for creep of the geogrid.

9.3 FINAL LOADING OF THE FULL SCALE WALL

The final loading of the MSE wall carried out in order to test the capability of the wall to react to extreme conditions. The load at the top of the wall was gradually increased up to a factor of 2 of the original design load, and the deformation was monitored. Upon loading, the wall did not fail, and little deformation was observed. Close examination of the conditions and further analysis of the results provided the explanation behind the resilience of the MSE wall.

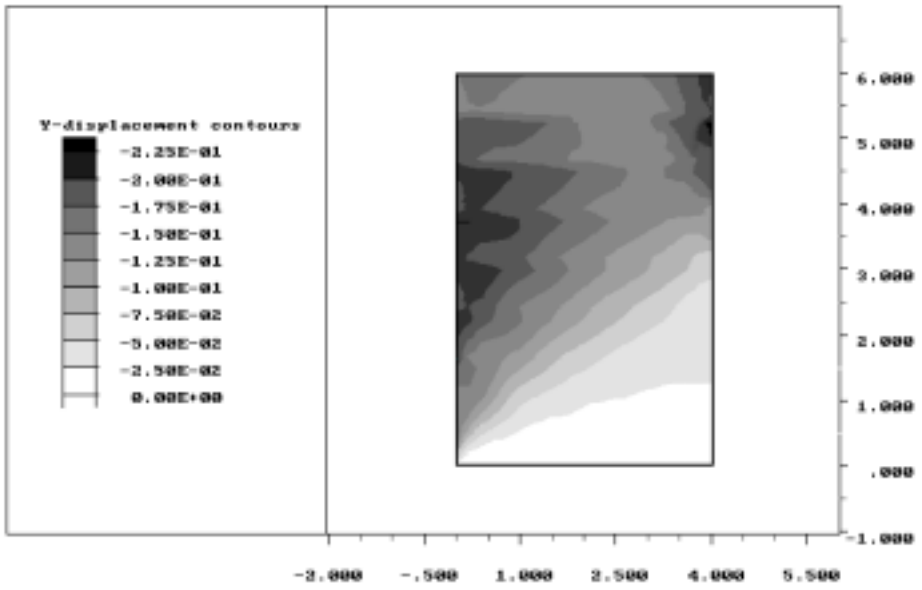

Figure 9.4. Vertical deformations (in meters) in the MSE wall upon loading with a load four times the AASHTO load

Figure 9.4 illustrates the vertical displacements incurred in the wall upon loading with a load four times the AASHTO standard load, with a design factor of safety of 1. Up to this level of loading, the maximum stresses within the geogrid layers had barely reached the ultimate strength. In other words, when the conventional design method is applied, and a factor of safety of 1 is used, the design is already overly conservative. This is due to the fact that, when calculating the anchorage length and required strength of the reinforcement in design, the values obtained for the most critical layer is used throughout the wall. For instance, the design may show that for a factor of safety of 1, the maximum stress occurs in layer 5, and is equal to 100 kN/m. The design may also show that the most critical layer for pullout purposes is layer 7, and that the required anchorage length for that layer is 5 meters. When specifying the wall dimensions and material, the engineer uses the stress of 100 kN/m and the embedment length of 5 meters for all layers. As a result, all other layers in the system

are over designed. Even layer 5 would be overly designed in terms of embedment length and layer 7 in terms of strength. Another important point to realize is that the stresses within each geogrid layer are at a maximum only at one point (along the postulated failure plane). Along the rest of the geogrid length, stresses are well below that maximum value.

A "true" design with a FS=1 requires that each layer of the wall be analyzed separately, and the required strength and embedment length specified for each layer independently of others. It would also require that the modulus of the geogrid be varied along the length of the geogrid in order to cause maximum stresses to be developed at all points. This would, obviously, be a futile exercise from a practical standpoint. The conclusion, however, is that a wall designed for a factor of safety of 1 is, in reality, at a higher safety factor.

The facts outlined above are evident in the strain measurements, which were taken in the small scale walls, which are reported in Figs. 7.31 through 7.42. Even at the very high loading levels, which exceed a theoretical factor of safety of 1, the strains within the geogrid layers are well below the ultimate strain, which is typically taken to be 10%. As a result of the low stress levels at various points within the geogrid length, the stresses within the system are redistributed, and the corresponding strains are well below the ultimate value.

In addition to the above factors, the influence of the three-dimensional abutment restrictions to movement cannot be overlooked. Such restrictions will reduce the stresses within the geogrid layer significantly, and further prevent failure and collapse of the wall. The full scale wall was also constructed on a rigid foundation, while the vast majority of MSE walls have failed or undergone excessive deformation mostly due to excessive settlement of

the foundation soil. The numerical analysis results of the case shown in Fig. 9.4 indicate that breakage of the geogrid layers will not occur, until the loads are increased to more than 4 times the AASHTO standard. Otherwise, only excessive displacement occurs, but no collapse is induced in the FLAC model either. It is therefore concluded that MSE walls are highly redundant systems, with a very low likelihood of internal stability failure due to breakage of the reinforcement.

9.4 COMPARISON WITH SMALL SCALE RESULTS

9.4.1 STRAINS IN THE GEOGRID REINFORCEMENT – HDPE WALLS

According to the scale effects (Section 5.1.1), we know that there is a relationship between the surcharge applied to the full-scale MSE wall and the one applied to the small scale MSE walls. Table 9.1 serves as a reminder of the basic correlation between the two surcharges. Using dimensional similitude, we will compare the small-scale and full-scale results to verify how the small-scale experiment predicts a full-scale event.

Table 9.1. Correlation between the surcharge applied to the full-scale and small-scale MSE walls.

Surcharge applied to the full-scale MSE wall	Surcharge applied to the small-scale MSE walls
4.4 kPa	0.8 kPa
20 kPa	3.64 kPa
40 kPa	6.4 kPa

Figure 9.5 shows strains in reinforcement for HDPE small-scale MSE walls. The expression "H-7-4 (1)" means strain HDPE value at layer number 7, position number 4 (the fourth strain gages far from the panel) and (1) means that it is regarding the first experiment (Wall 1). For both Walls 1 and 2, all the strain values are between 0 and 0.1 %. In both , the largest strains appear at layer number 5, and the lowest at layer number 1. Figure 9.6 shows the strains in reinforcement for HDPE full-scale MSE wall. All the strain values are between 0 and 5.5 % for the full-scale MSE wall experiment. The biggest strains appear at layer number 5 (as it was also observed on the small-scale MSE walls experiments) and the lowest at layer number 7.

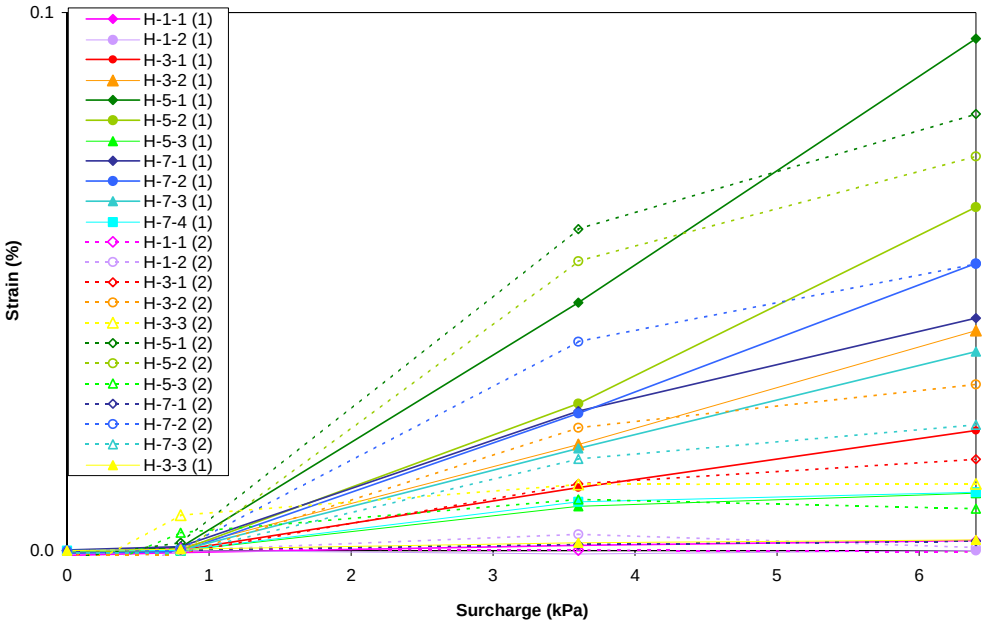

Figure 9.5. Strains in reinforcement for HDPE small scale MSE wall

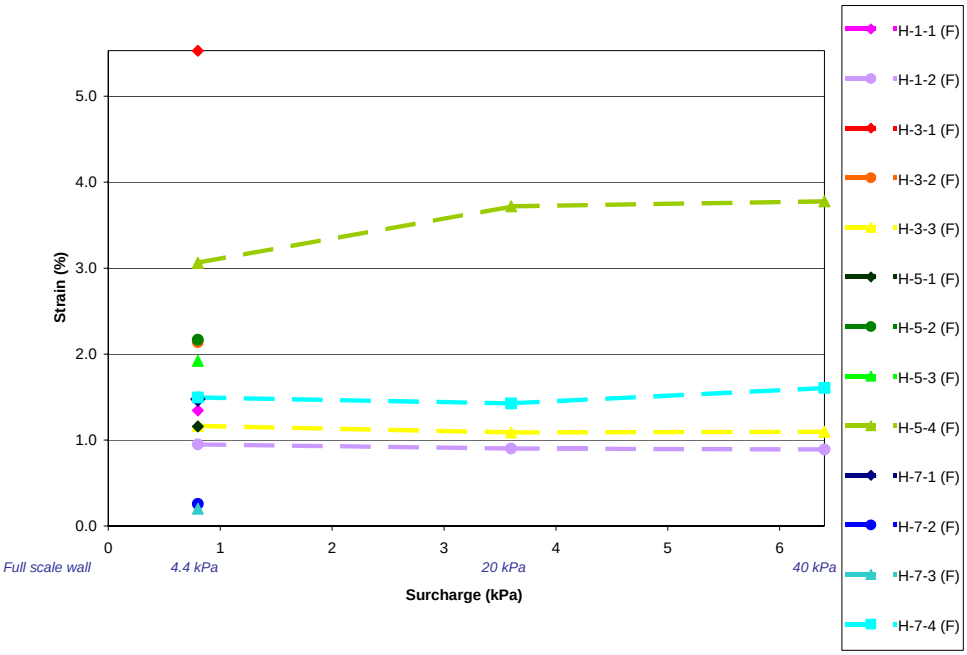

Figure 9.6. Strains in reinforcement for HDPE full scale MSE wall

Figure 9.7 shows the comparison of the strains in HDPE reinforcement for both small-scale and full-scale MSE walls values. The small-scale values are corrected with the values given in Table 9.2. The comparison between the results from the full-scale MSE wall testing and the small-scale MSE wall testing shows almost similar trends for the strains in HDPE reinforcement.

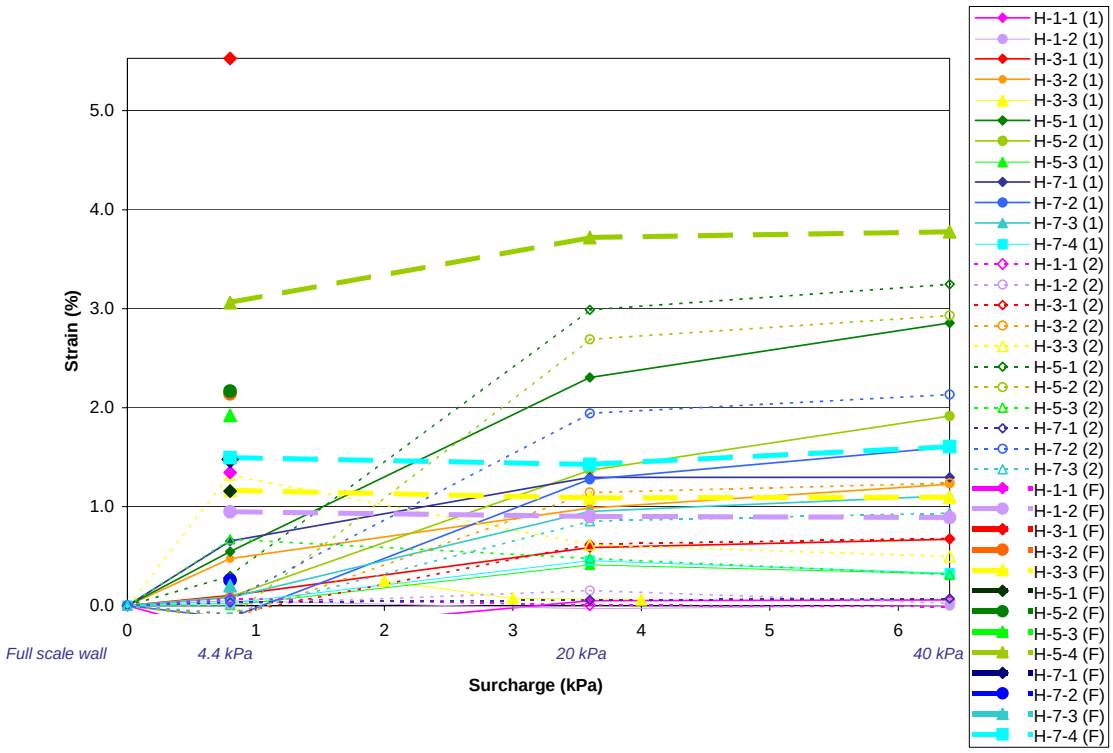

Figure 9.7. Comparison of strains in reinforcement for HDPE MSE walls

Table 9.2. Correction coefficient for small-scale MSE wall HDPE strain values

Surcharge in kPa	Small-scale wall # 1 correction coefficient	Small-scale wall # 2 correction coefficient
0	1	1
0.8	850	200
3.6	60	60
6.4	30	40

9.4.2 STRAINS IN THE GEOGRID REINFORCEMENT – PET WALLS

Figure 9.8 shows the strains in reinforcement for PET small-scale MSE walls. The expression "P-5-1 (2)" means the strain PET value at layer number 5, position number 1 (the closest strain gage from the panel), and (2) indicates the reference to the second experiment (Wall 2). For both tests 1 and 2, all the strain values were between 0 and 0.05 %. For experiment number 1, the biggest strains occurred at layer number 5 and the lowest at layer number 1. For experiment number 2, the biggest strains occurred at layer number 3 and the lowest at layer number 7.

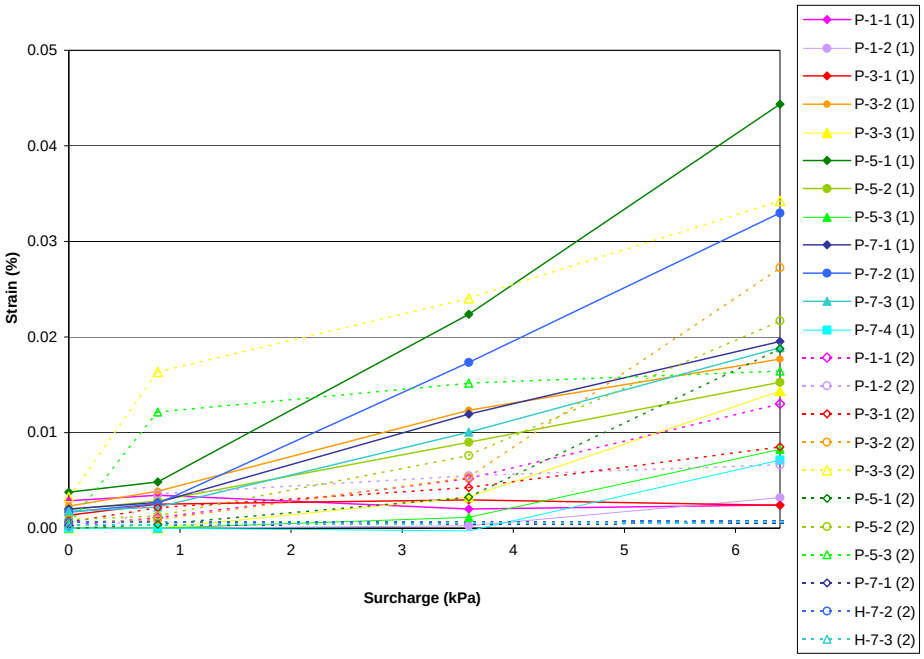

Figure 9.8 Strains in the "Small-Scale" PET wall, for various levels of surcharge.

Figure 9.9 shows the strains in reinforcement for the PET full-scale MSE wall. All the strain values were between 0 and 6.0 % for the full-scale MSE wall experiment. The biggest strains occurred at layer number 5 (as it was also observed on the small-scale MSE wall experiment number 1) and the lowest at layer number 7.

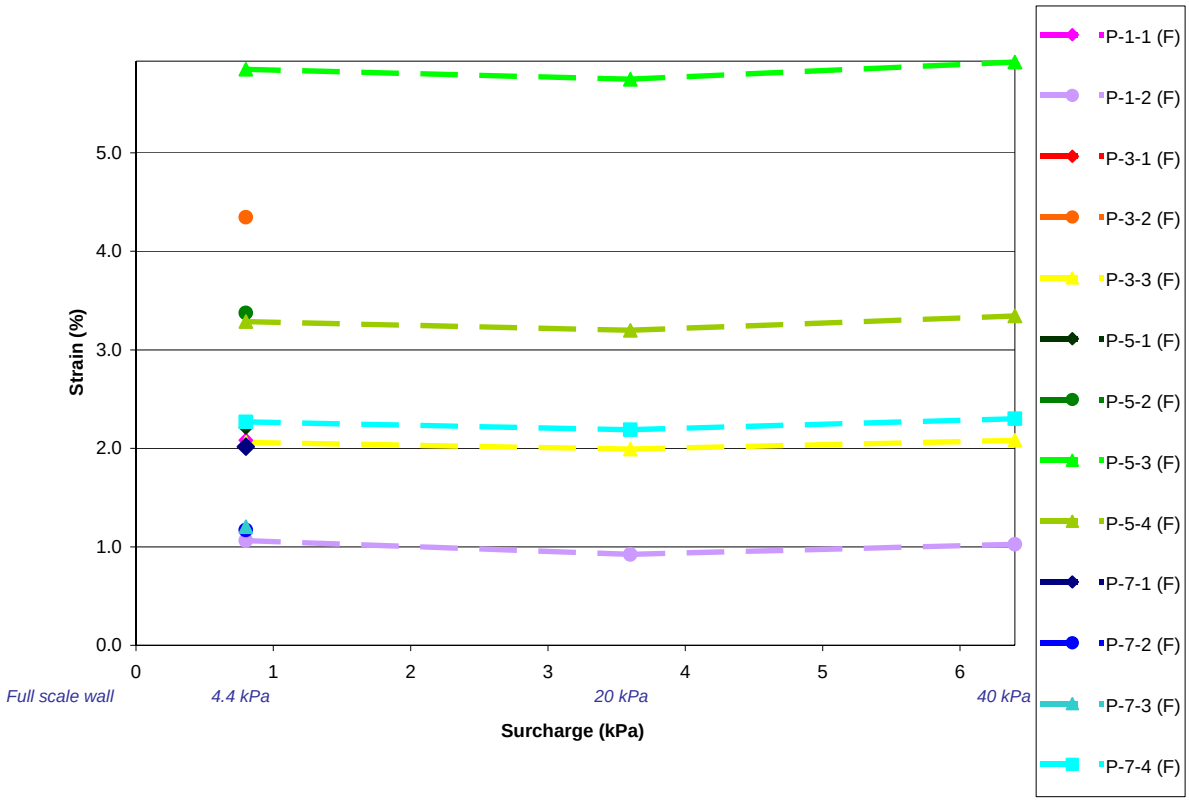

Figure 9.9. Strains in Full-Scale PET for various surcharge levels.

Figure 9.10 shows the comparison of the strains in PET reinforcement for both small-scale and full-scale MSE walls values. The small-scale values are corrected with the values given in Table 9.3.

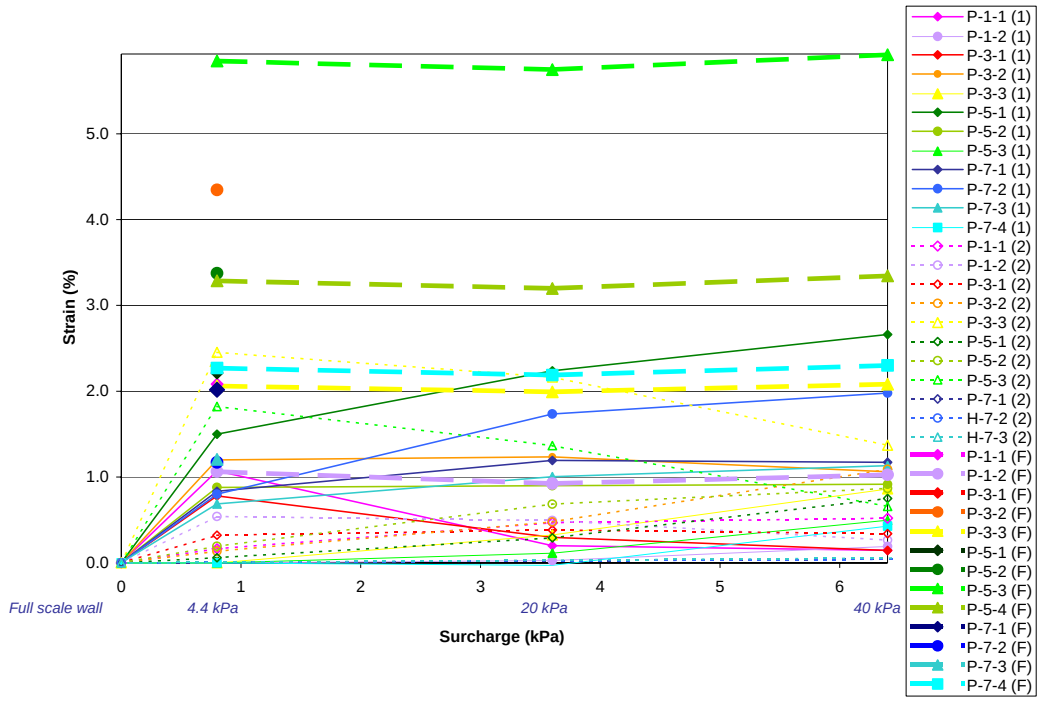

Figure 9.10 Comparison of strains in the PET reinforcement for increasing surcharge.

Table 9.3 Correction coefficients for small-scale MSE wall PET strain values

Surcharge in kPa	Small-scale wall # 1 correction coefficient	Small-scale wall # 2 correction coefficient
0	1	1
0.8	310	150
3.6	100	90
6.4	60	40

The comparison between the results from the full-scale MSE wall testing and the small-scale MSE wall testing shows almost similar trends for the strains in HDPE reinforcement. The small-scale PET MSE walls show less deviation compare to the full-scale PET MSE wall.

9.4.3 PANEL DISPLACEMENT – HDPE WALLS

The panel displacements for the MSE walls reinforced with HDPE and PET geogrids were shown in Figures 7.5 through 7.8. They were plotted for the entire time of the tests. The panel displacements were plotted for MSE walls reinforced with HDPE and PET geogrids function of the surcharge applied. Figure 9.11 shows the panel displacement for HDPE small-scale MSE wall function of the surcharge applied. The expression "H-1-top (1)" means HDPE MSE wall, top of the panel number 1, experiment number 1.

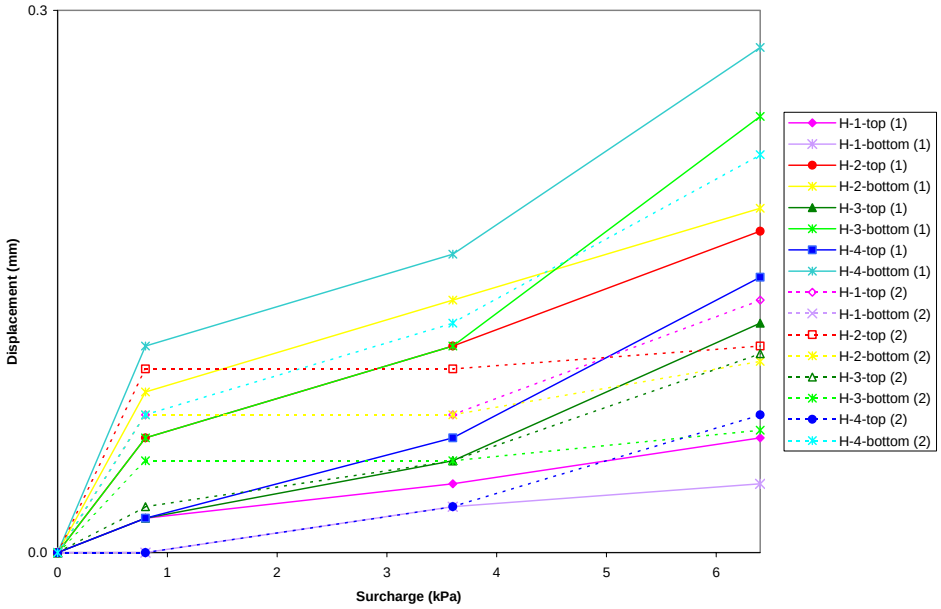

Figure 9.11. Panel displacements for the HDPE small scale MSE walls.

All the panels displacements were between 0 and 0.3 mm. For experiment number 1, the biggest displacement appears at the bottom of the panel number 4 and the lowest one at the bottom of the panel number 1. For experiment number 2, the biggest displacement also appears at the bottom of the panel number 4 and the lowest one at the top of the panel number 4.

Figure 9.12 shows the panel displacement for HDPE full-scale wall. For the full-scale MSE wall, the biggest displacements were at panels number 3, 6 and 7 and the lowest at panels number 1 and 5.

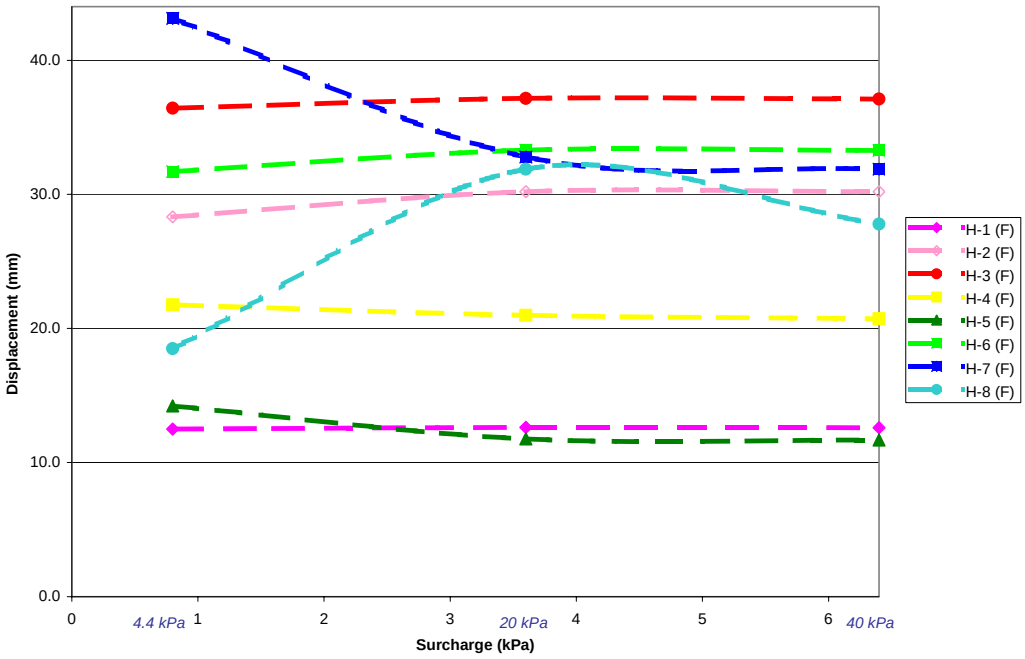

Figure 9.12. Panel displacements for HDPE full-scale MSE wall

Figure 9.13 shows the comparison between the panel displacements of HDPE full-scale and small-scale MSE walls values. The small-scale values have been corrected by a coefficient shows in Table 9.4.

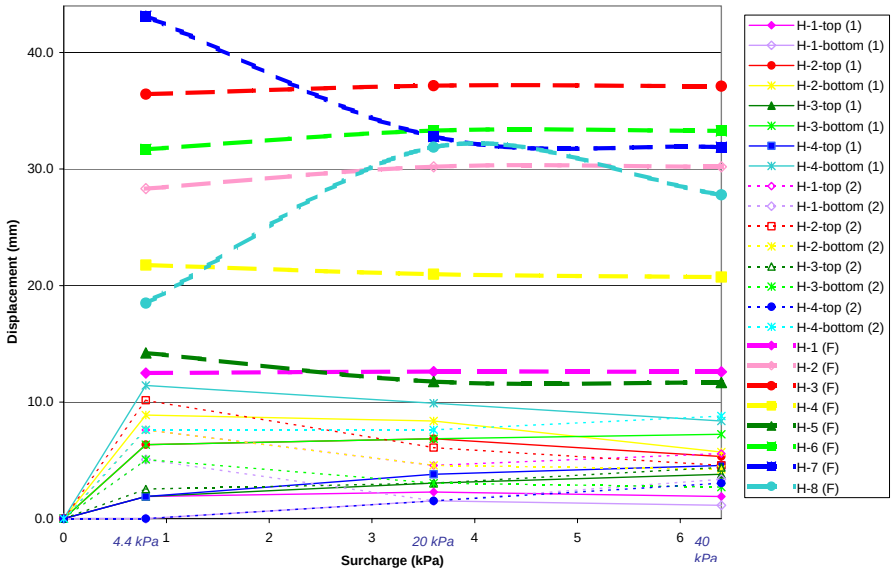

Figure 9.13. Comparison of the panel displacements for HDPE small-scale and full-scale MSE walls

Table 9.4. Correction Coefficient for the Panel Displacements for HDPE small-scale MSE Walls.

Surcharge in kPa	Small-scale wall # 1 correction coefficient	Small-scale wall # 2 correction coefficient
0	1	1
0.8	100	100
3.6	60	60
6.4	30	40

Figure 9.14 shows the panel displacements versus the height of the wall for the small-scale MSE walls. Figure 9.15 shows the panel displacements for HDPE full-scale MSE wall versus the height of the wall. The dimensional similitude is obtained from the values of Table 9.5.

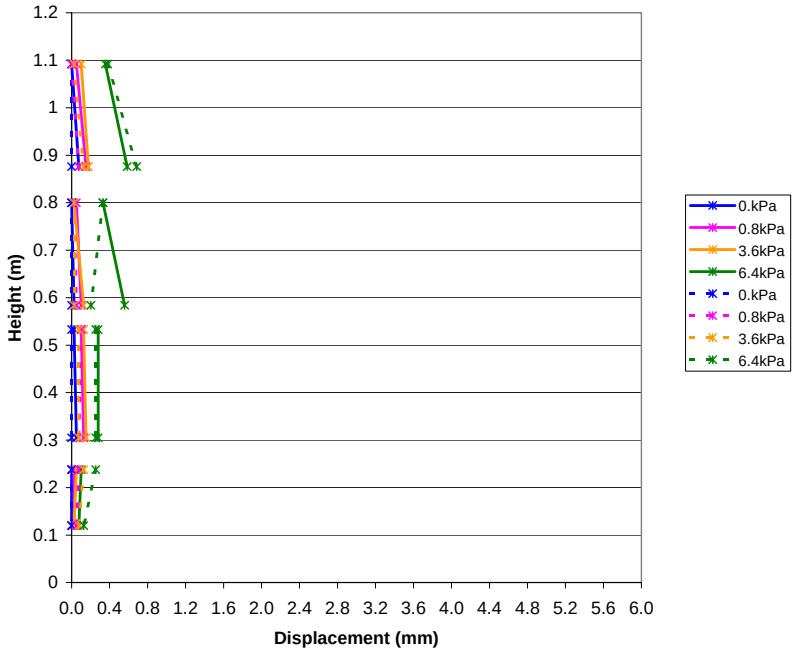

Figure 9.14. Panel displacements for HDPE small-scale MSE walls

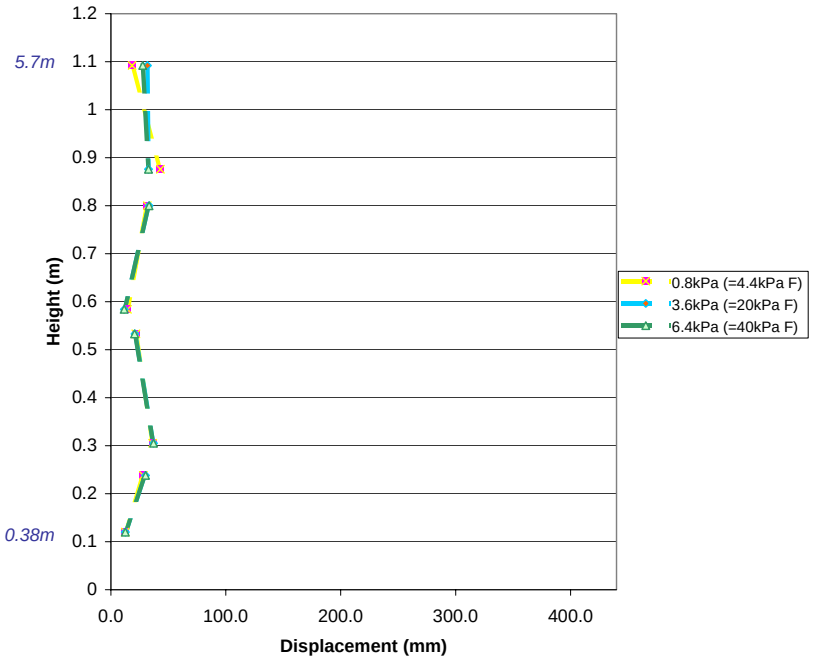

Figure 9.15. Panel displacements for HDPE full-scale MSE wall

Table 9.5. Corresponding heights between full-scale and small-scale MSE walls.

Height of the full-scale wall (in meters)	Corresponding height of the small-scale wall (in meters)
5.7	1.092
4.94	0.876
4.18	0.8
3.42	0.584
2.66	0.533
1.9	0.305
1.14	0.238
0.38	0.12

Figure 9.16 shows the comparison between the panel displacement for HDPE full-scale and small-scale MSE walls. The values from the small-scale MSE walls have been multiplied by a correction factor shown in Table 9.6.

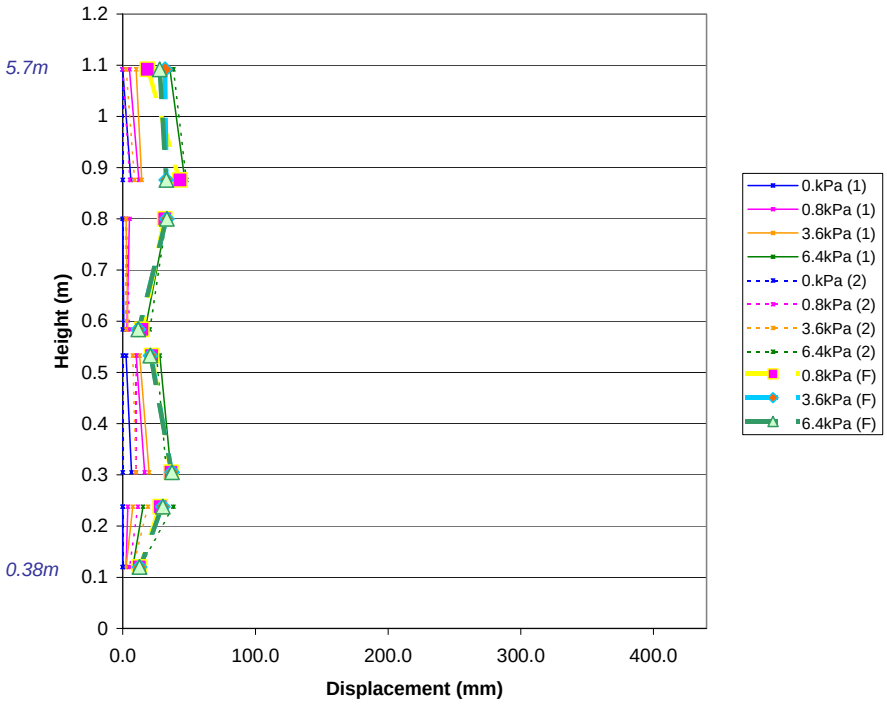

Figure 9.16 Comparison of panel displacements for HDPE full-scale and small-scale MSE walls

Table 9.6. Correction coefficient function of the height for the panel displacements for HDPE small-scale MSE walls.

Height of the wall (in meters)	Small-scale wall # 1 correction coefficient	Small-scale wall # 2 correction coefficient
1.092	100	100
0.876	80	70
0.8	100	100
0.584	30	100
0.533	100	100
0.305	130	130
0.238	150	150
0.12	100	100

We see that the first and the last panel movement show almost similar trends. For the other panels, bigger deviation appears.

9.4.4 PANEL DISPLACEMENTS – PET WALLS

Figure 9.17 shows the panel displacements for PET small-scale MSE wall as a function of the surcharge applied. The expression "P-1-top (1)" means PET MSE wall, top of the panel number 1, experiment number 1. All the panel displacements are between 0 and 1 mm. For experiment number 1, the biggest displacement appears at the top of the panel number 3 and the lowest one at the bottom of the panel number 1. For experiment number 2, the biggest displacement also appears at the bottom of the panel number 4 and the lowest one at the top of the panel number 3.

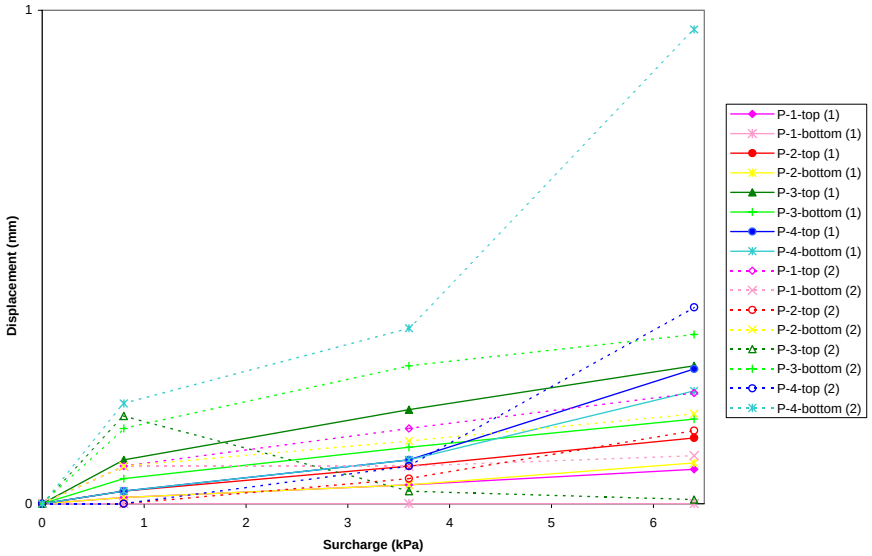

Figure 9.17. Panel displacements for PET small-scale MSE walls

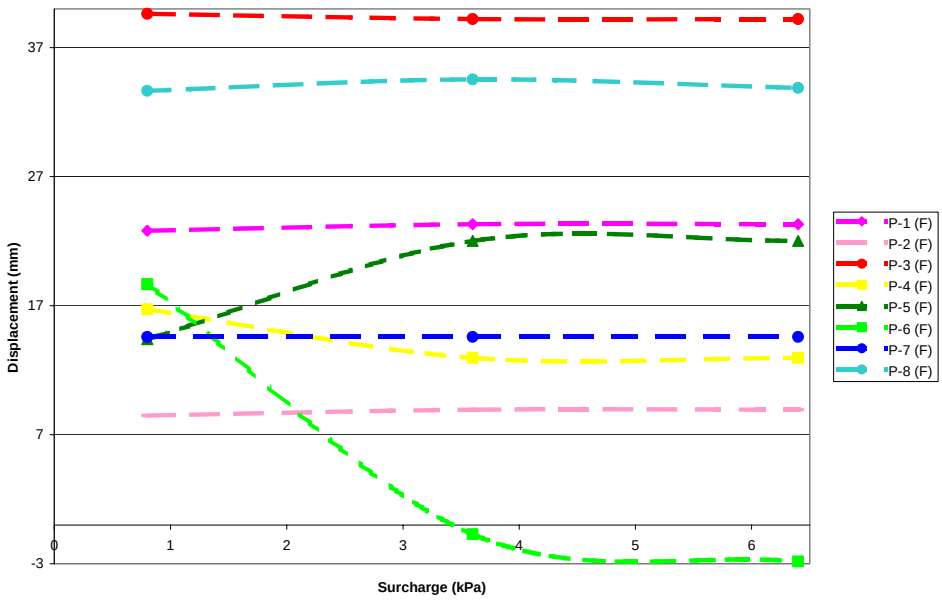

Figure 9.18. Panel displacements for the PET side of the full-scale MSE wall

Figure 9.18 shows the panel displacements for PET full-scale wall. For the full-scale MSE wall, the biggest displacements appear at panels number 1, 3 and 8 and the lowest at panels number 2 and 6.

Figure 9.19 shows the comparison between the panel displacements of PET full-scale and small-scale MSE walls values. The small-scale values have been corrected by a coefficient shows in Table 9.7.

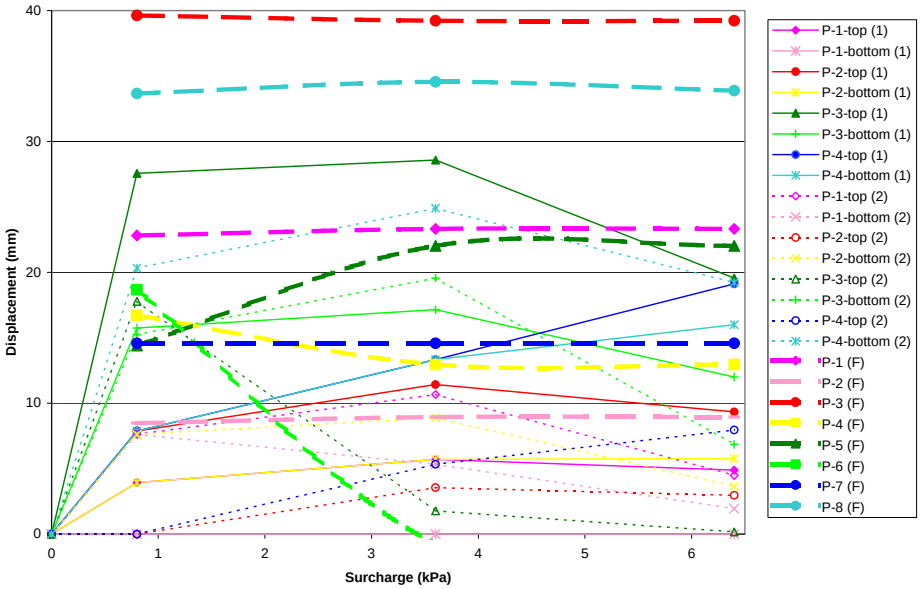

Figure 9.19. Comparison of panel displacements for the PET side of the MSE wall

Table 9.7. Correction coefficient for the panel displacements for PET small-scale MSE walls.

Surcharge in kPa	Small-scale wall # 1 correction coefficient	Small-scale wall # 2 correction coefficient
0	1	1
0.8	310	100
3.6	150	70
6.4	70	20

Figure 9.20 shows the panel displacement versus the height of the wall for the small-scale MSE walls. Figure 9.21 shows the panel displacements for the PET full-scale MSE wall versus the height of the wall. The dimensional similitude is based on the values presented earlier in Table 9.5.

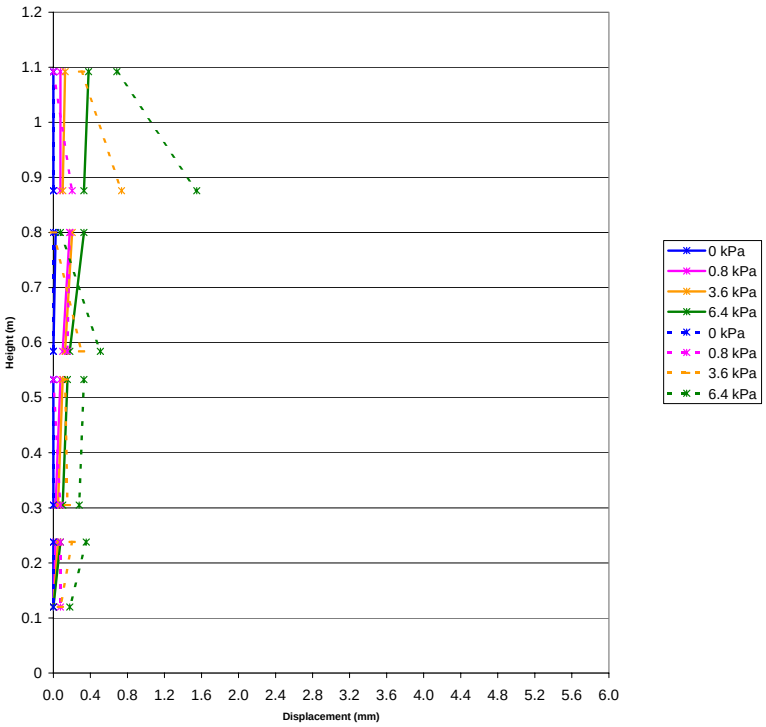

Figure 9.20. Panel displacements for PET small-scale MSE walls

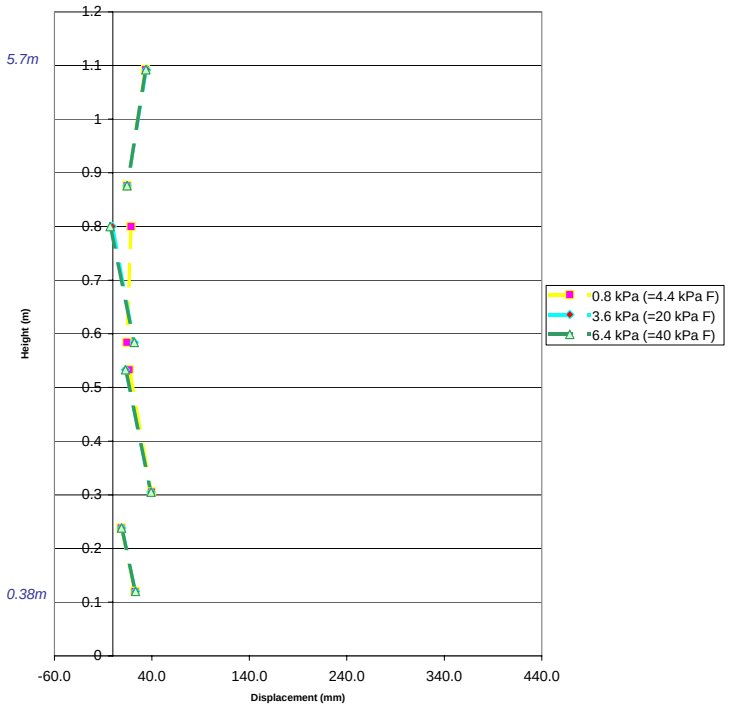

Figure 9.21 Panel displacements for PET full-scale MSE wall

Figure 9.22 shows the comparison between the panel displacement for PET full-scale and small-scale MSE walls. The values from the small-scale MSE walls have been multiplied by a correction factor shown in Table 9.8. The PET MSE walls show bigger deviations than HDPE MSE walls for panel displacements.

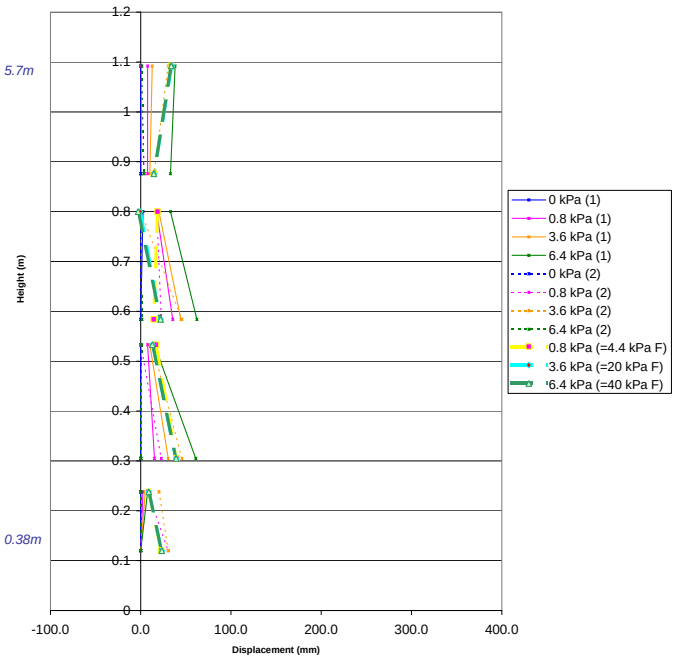

Figure 9.22 Comparison of panel displacements for the PET full-scale and small-scale MSE walls

Table 9.8. Correction coefficients as a function of the height for the panel displacements for PET small-scale MSE walls.

Height of the wall (in meters)	Small-scale wall # 1 correction coefficient	Small-scale wall # 2 correction coefficient
1.092	100	100
0.876	100	20
0.8	100	100
0.584	350	150
0.533	100	100
0.305	600	300
0.238	100	100
0.12	1	400

9.4.5 DISCUSSION

The comparison (using dimensional similitude) between the results from the full-scale MSE wall testing and the small-scale MSE walls testing showed almost similar trends, but the values for the prototype (strains and panel deformations) were greater than those obtained by the small-scale testing. This can be attributed to the distortion caused by scaling neglecting the gravity effect, and is in line with the analysis and conclusions described in Chapter 7. Correction factors were applied to correct the discrepancies between the prototype and the small-scale MSE walls.

10 MSE WALL DESIGN PROCEDURE AND SOFTWARE

10.1 INTRODUCTION

A design tool for MSE walls was developed as the last task of this research work. The Windows program is a stand-alone application programmed in Visual Basic™ and compiled to run on any Windows platform. There are two methods of design (ASD and LRFD) according to the requirements in the AASHTO ASD Specifications (1998a) and LRFD Specifications based on the most recent studies (FHWA, D'Appolonia, 2001). The current design program is focused on MSE walls reinforced with geosynthetics in cohesionless soil.

10.2 DESCRIPTION OF THE WINDOWS PROGRAM

Figure 10.1 shows the MSE wall design program with different menus in the toolbar for the following purposes:

1. File menu. This menu has the options: save (to save the input data), open (to open a specific file), print (to print input and output data) and exit (to exit the program). Figure 10.2 shows this menu.

2. Edit menu. This menu has the options for cutting, copying or pasting data information (Figure 10.3).

3. Input menu. This menu has two options to input the data of design either by a graphical interface (Figure 10.4) or by input each type of data individually (Figures 10.5 to 10.9).

4. Menu Settings. This menu gives the option to choose the unit system (British or SI) and the design method to use (ASD or LRFD). When the user clicks the design method, the

window with the resistance factors used in the program is shown. The user can modify these factors during the execution of the program. Figures 10.10 and 10.11 show the forms for this menu.

5. Help menu. The procedures of design can be consulted through this option.

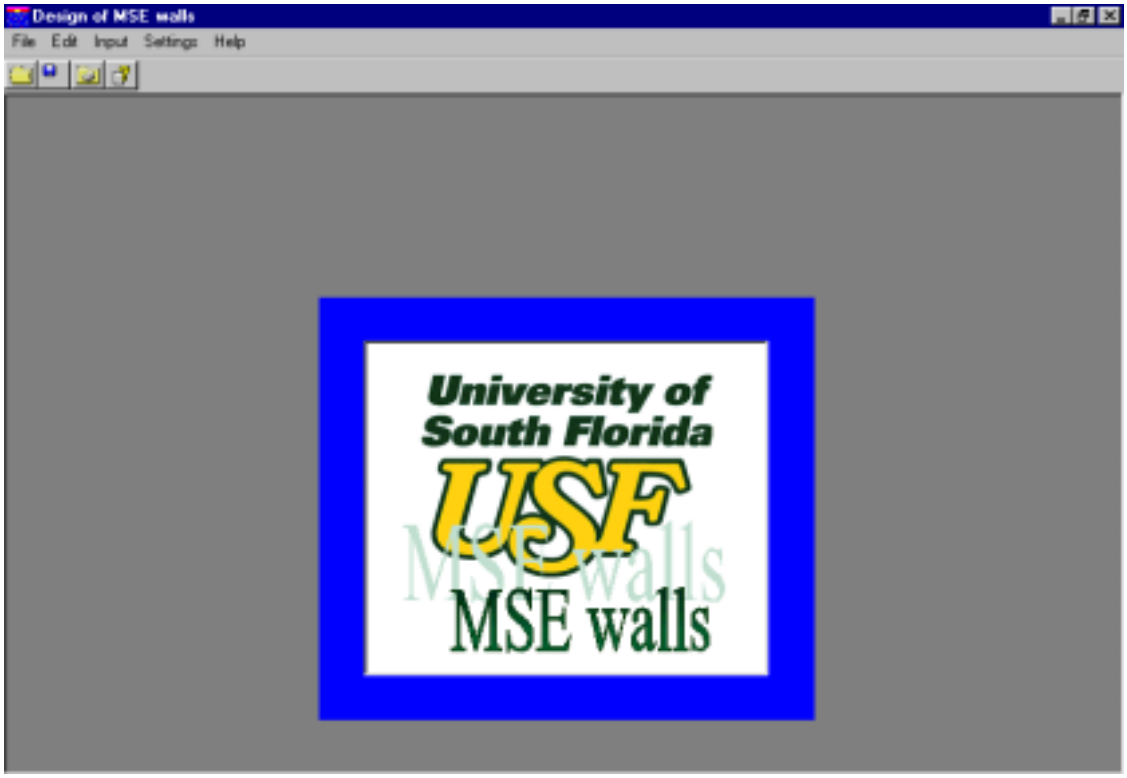

Figure 10.1 MSE wall design program

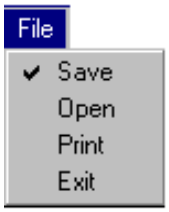

Figure 10.2 File menu

Figure 10.3 Edit menu

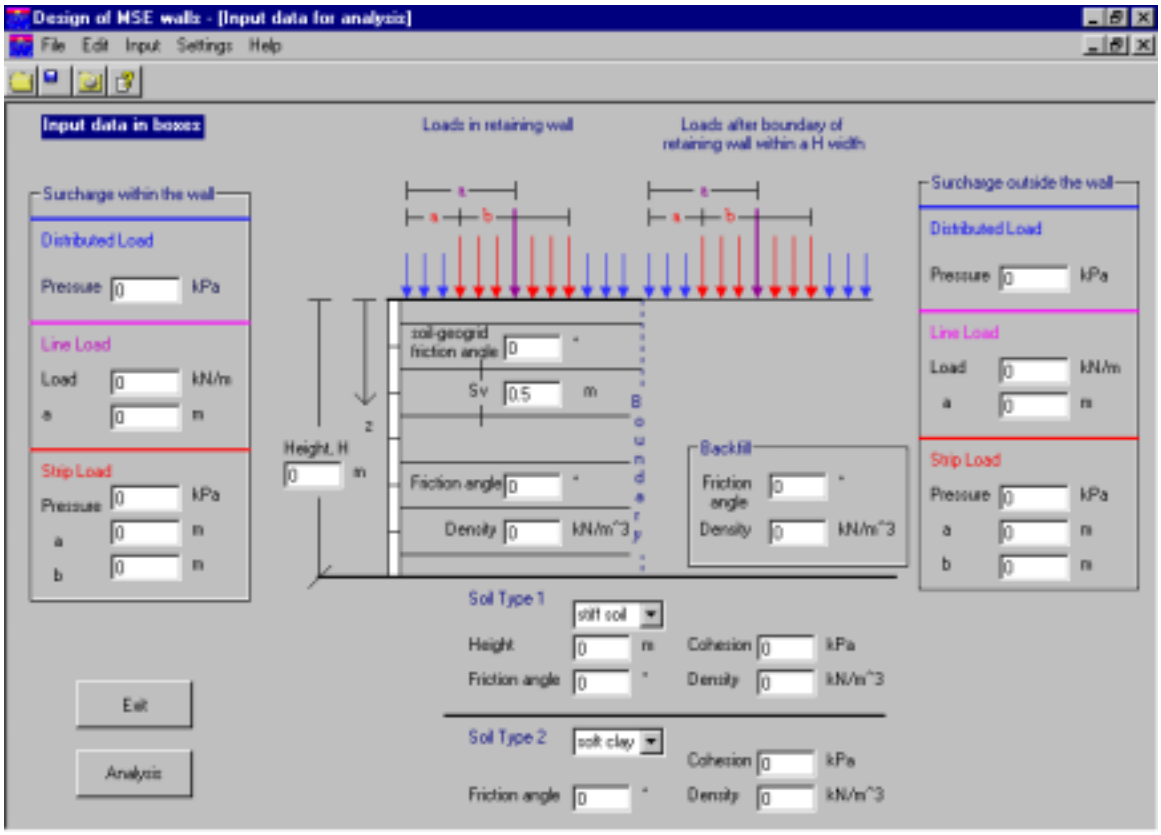

Figure 10.4 Graphical interface to input data

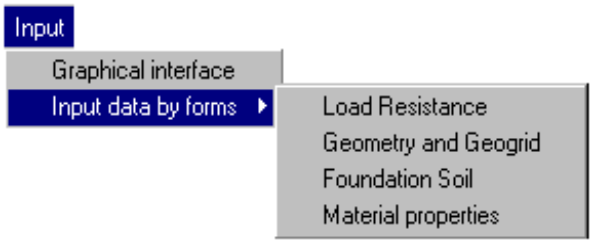

Figure 10.5 Input menu

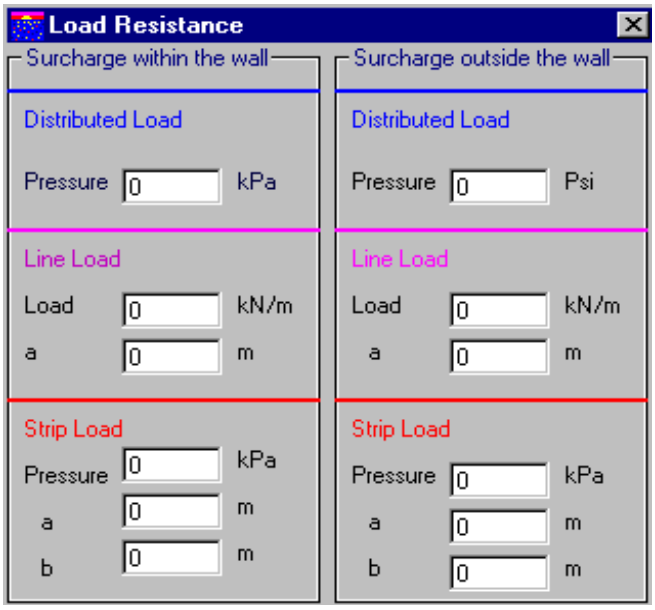

Figure 10.6 Load resistance input data form

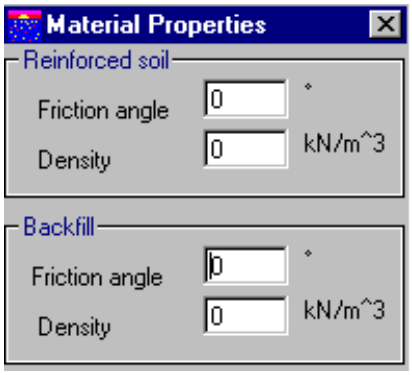

Figure 10.7 Material properties input data form

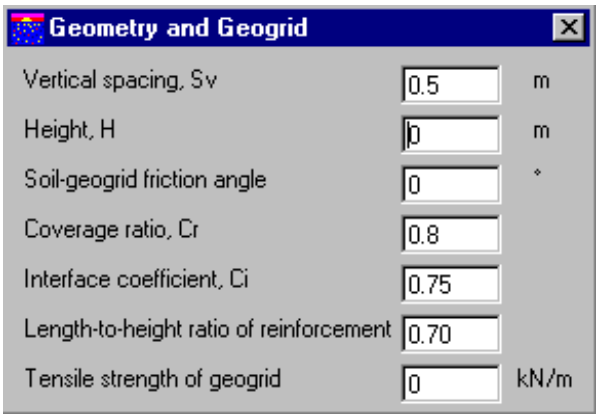

Figure 10.8 Geometry and geogrid input data form

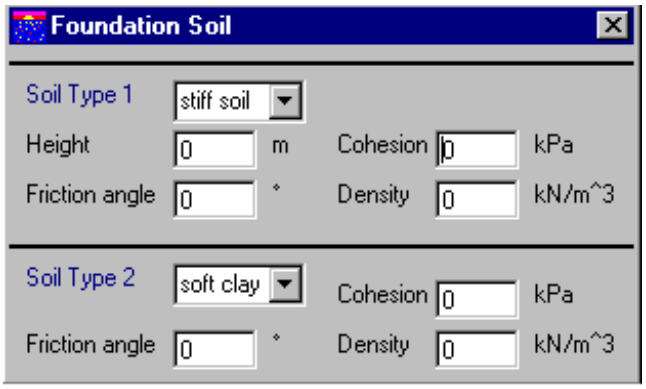

Figure 10.9 Foundation soil input data form

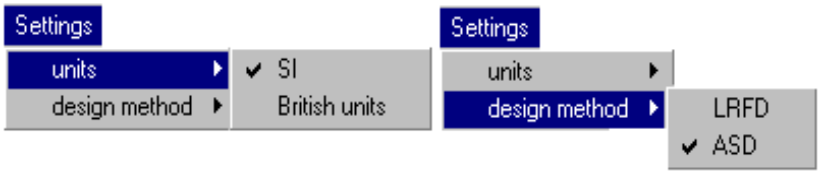

Figure 10.10 Settings menu

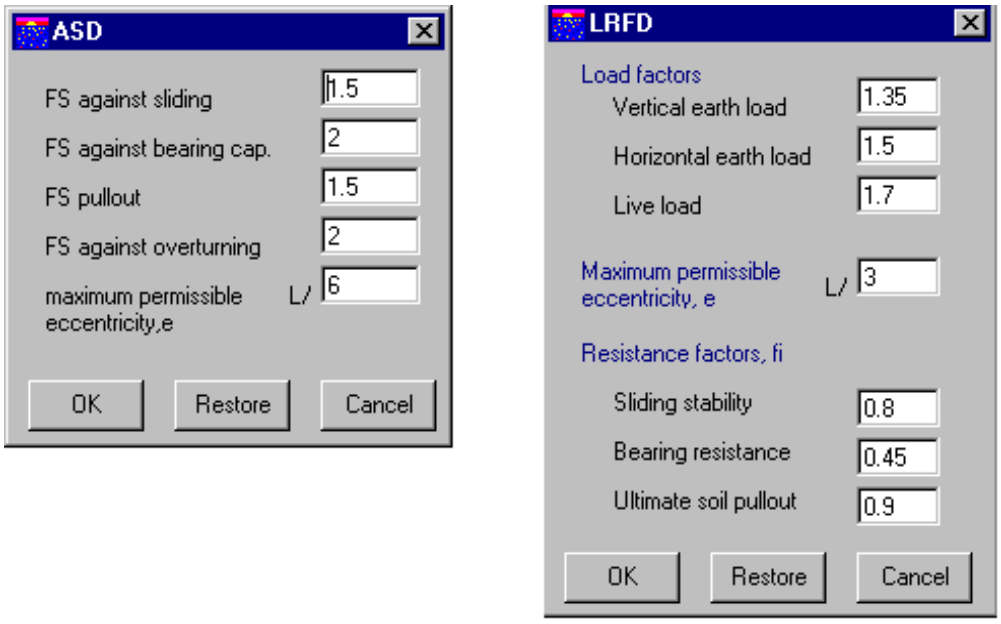

Figure 10.11 Input load resistance windows for LRFD and ASD methods

The graphical interface form will remain active through all the execution of the program once this form is opened from the input menu. The analysis form will be active only when the user clicks the button to perform the analysis of design. The user can open any time the menus of the toolbar to check data of design or any other information.

After the input data has been specified, the "Analysis" button shown in the graphical interface window (Figure 10.4) will perform the design steps in accordance with ASD or LRFD methods. Figure 10.12 shows this window. The procedures followed for the calculations are specified in section 10.3 of this chapter.

Error and warning messages are executed in the program when the user inputs data in the wrong format or values not within the acceptable ranges (for example the vertical spacing of geogrid layers).

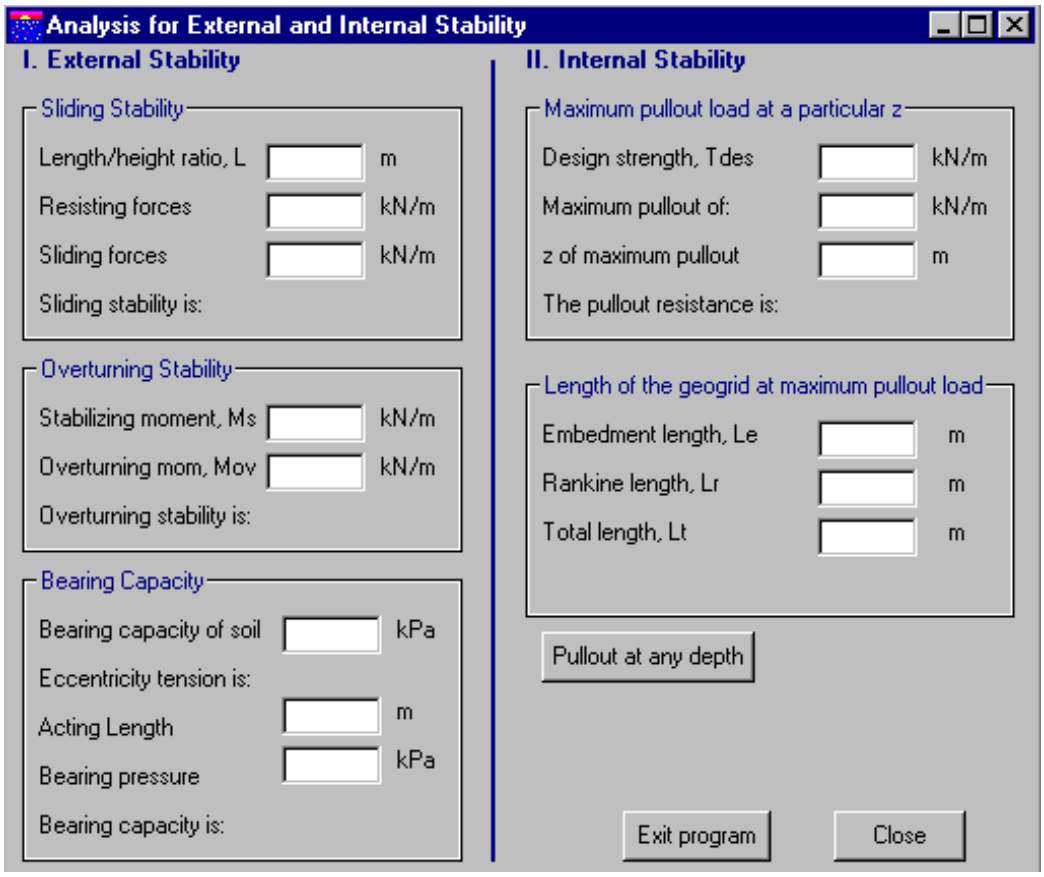

Figure 10.12 Analysis window

10.3 PROCEDURES FOR THE ANALYSIS

External and Internal stabilities are explained in sections 10.3.1 and 10.3.2 and follow design procedures cited in Koerner (1998) and Holtz et. al. (1997). These are in line with the FHWA design sequence.

10.3.1 EXTERNAL WALL STABILITY

External stability is evaluated assuming that the reinforced soil mass acts as a rigid body, although in reality the wall system is flexible. The external modes of failure to be considered are sliding of the wall, overturning of the wall and bearing capacity of the wall foundation.

Sliding stability is checked along the base by equating the external horizontal forces with the shear stress at the base of the wall (Figure 10.13). Sliding is evaluated with respect to the minimum frictional resistance provided by either the reinforced soil (φ_r), the foundation soil (φ_f), or the interaction between the geosynthetic and the reinforced soil (φ_{sg}).

Overturning is developed from the resultants of the horizontal earth pressure and surcharge diagrams for the retained backfill portion of the wall. This is checked by summing moments of external forces at the toe of the wall. The factor of safety against sliding and overturning is obtained from equation 10.1 and 10.2 respectively based on Figure 10.13:

$$FS_{sliding} = \frac{\sum Horizontal\,\mathrm{Re}sistingForces}{\sum HorizontalSlidingForces} = \frac{(V_q + W)\mu + cL}{P_b + P_q + P_Q} \qquad (10.1)$$

$$FS_{overturning} = \frac{\sum Resisting\ Moments}{\sum Overturning\ Moments} = \frac{(V_q + W)(L/2)}{P_b(H/3) + P_q(H/2) + P_Q R} \qquad (10.2)$$

where:

$V_q = \gamma_s h_s L$

$W = \gamma_r HL$

$P_b = 0.5 K_{a,b} \gamma_b H^2$

μ = Minimum of tan φ_r, tan φ_f, or tan φ_{sg}

$K_{a,b} = \tan^2 (45 - \varphi_b/2)$

$P_q = K_{a,b} \gamma_r h_s H$

c = Cohesion of foundation soil or adhesion between soil and reinforcement

P_Q = contribution of surcharge, determined from Eqs. 10.3 and 10.4)

It should be noticed that the design program allows the user to input external loads (loads applied in the backfill) not only for uniform surcharge but also for the cases of line and strip loads. These loads applied in the backfill are taken as horizontal sliding forces or overturning moments in the code program analysis. The vertical stress distribution due to a vertical line load and strip load is given by equation 10.3 and 10.4 respectively.

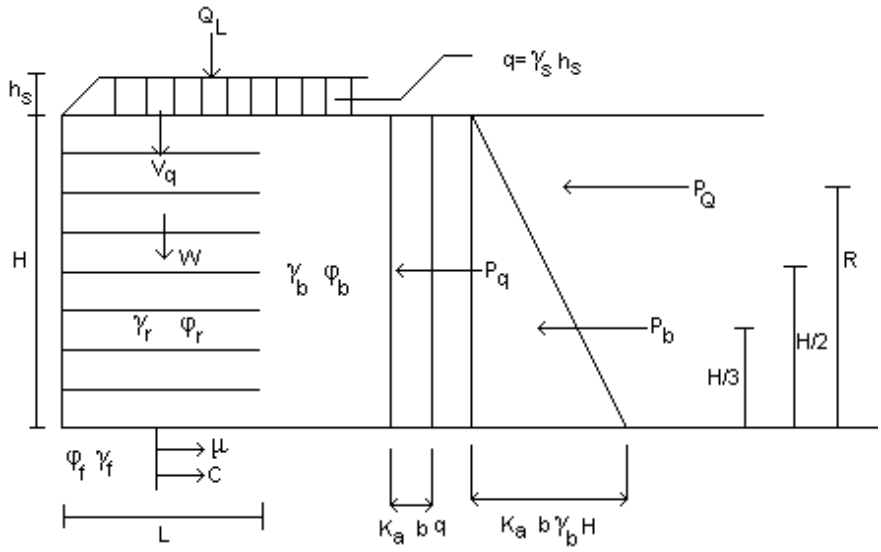

Figure 10.13 External sliding and overturning stability of a geosynthetic reinforced soil wall with uniform surcharge load (Christopher and Holtz 1985)

$$\sigma_z = \frac{2Qz^3}{\pi R^4} \tag{10.3}$$

$$\Delta\sigma_z = \frac{q}{\pi}\left[\alpha + \sin\alpha\cos(\alpha + 2\beta)\right] \tag{10.4}$$

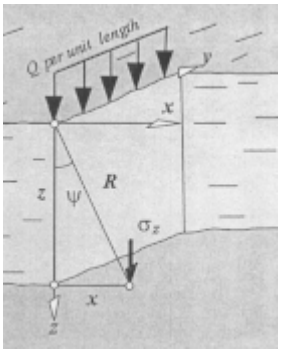

Figure 10.14 Stresses due to a vertical line load (Azizi, 2000)

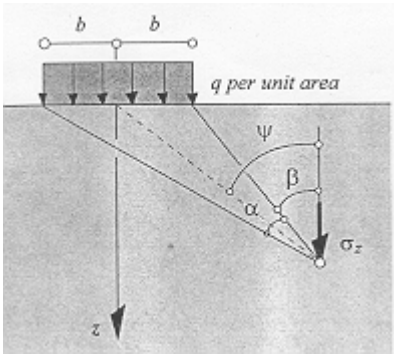

Figure 10.15 Stresses due a vertical strip load (Azizi, 2000)

The design for bearing capacity follows the same procedure as a shallow foundation. The entire reinforced soil mass is assumed to act as a footing. An incline resultant is obtained from the horizontal earth pressure component in addition to the vertical gravitational component. This resultant cannot be outside of the maximum permissible eccentricity (e ≤ maximum permissible eccentricity). The equations to calculate the bearing capacity follow (see Figure 10.14):

$$e = \frac{\sum DrivingMoments}{\sum VerticalForces} = \frac{P_b(H/3) + P_q(H/2) + P_q R}{W + V_q} \tag{10.5}$$

The magnitude of the maximum vertical stress, σ_{vmax}:

$$\sigma_{v\max} = \frac{V_q + W}{L - 2e} \leq \frac{q_{ult}}{FS_{Bearing}} \tag{10.6}$$

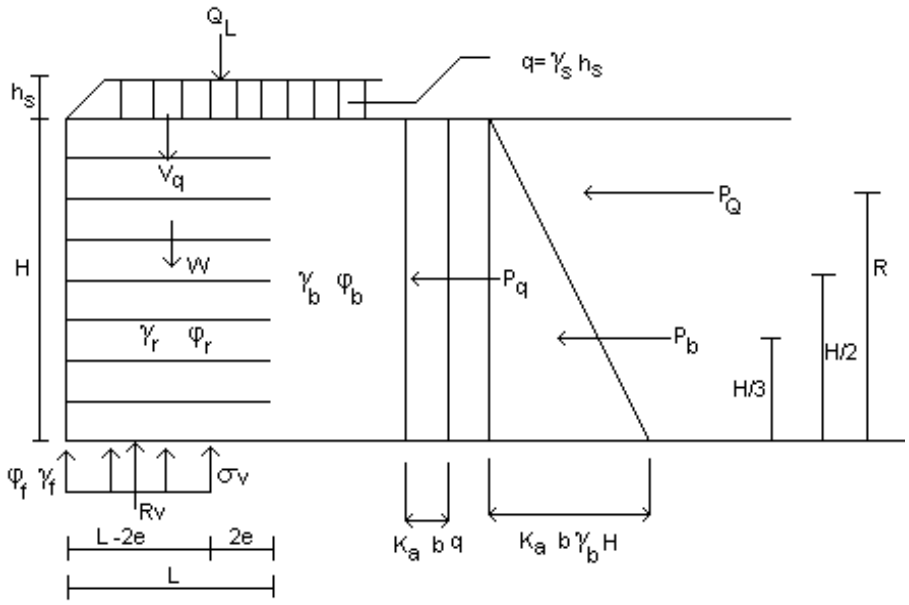

Figure 10.16 Bearing capacity for external stability of a geosynthetic reinforced soil wall with uniform surcharge load (Christopher and Holtz 1985)

The ultimate bearing capacity, q_{ult}, is determined using classical soil mechanics (Terzaghi, 1943). L' is equal to L-2e and it is call the acting length (Meyerhof's distribution).

$$q_{ult} = c_f N_c + 0.5\gamma_f L' N_\gamma \tag{10.7}$$

The program allows the user to input two types of soil for the foundation soil. The bearing capacity for the case of stiff soil overlying a soft clay stratum is determined by computing the bearing capacity of the soft clay stratum using equation 10.7 and considering an acting length increased by the depth between the base of the wall and the clay layer (Bowles, 1996).

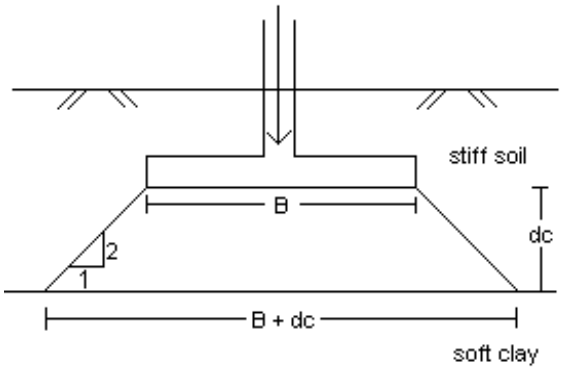

Figure 10.17 Foundation on stiff soil overlying a soft clay stratum, Bowles (1996)

The distributed stress of the soft clay is computed as:

$$\Delta p = q\left[\frac{B}{B+d_c}\right] \tag{10.8}$$

For the case of a thin surface stratum of clay overlying a relatively rigid stratum, the net ultimate bearing capacity of the clay is given by (Tomlinson, 1995):

For $B/d_c \geq 2$ (B is equal to the acting length):

$$q_{ult} = \left(\frac{B}{2d_c} + \pi + 1\right)c \tag{10.9}$$

For $B/d_c \geq 6$ (B is equal to the acting length):

$$q_{ult} = \left(\frac{B}{3d_c} + \pi + 1\right)c \tag{10.10}$$

The program allows the user to input soil data for two types of soil in order to obtain the bearing capacity. For stiff soils overlying soft clays, equations 10.7 and 10.8 are applied. For thin clay overlying stiff soil, equation 10.9 and 10.10 are applied. If two layers of stiff soil or clay layer are specified, equation 10.7 is applied for each layer and the smaller bearing capacity value is used. If one soil layer is specified, the bearing capacity of the first type of soil is calculated.

10.3.2 INTERNAL WALL STABILITY

The strength of the reinforcement, T_i, is computed at every geogrid layer, and the maximum tensile strength value is given as an output (Figure 10.12). The vertical spacing of the layers of the reinforcing controls the required tensile strength, and it is obtained from:

$$T_i = s_v \sigma_h \tag{10.11}$$

where:

S_v = Spacing between the reinforcement layers. This ranges from about 0.2 to 1.5 m (8 to 60 in) and is given by the user.

σ_h = Horizontal earth pressure at middle of the layer. The program allows to input loads for distributed, line and strip load applied in the reinforced soil wall.

After the maximum tensile strength, T_i, is obtained from the program, the embedment length, L_e, and the nonacting Rankine length, L_r, are obtained (equation 10.12 and 10.13). The program has a click-button (pullout at any depth) in the analysis window to calculate the tensile load at any depth of the wall:

$$L_e = \frac{T_i}{2C_i \gamma_r z \tan \varphi_r C_r} FS_{pullout} \quad (10.12)$$

$$L_R = (H - z)\tan\left(45 - \frac{\varphi_r}{2}\right) \quad (10.13)$$

where:

γ_r = Unit weight of backfill

φ_r = Friction angle of backfill

z = Depth of the layer being designed

T_i = Computed tensile load in the geosynthetic

$FS_{pullout}$ = Factor of safety against pullout

C_i = Interface coefficient

C_r = Coverage ratio

H = Height of the wall

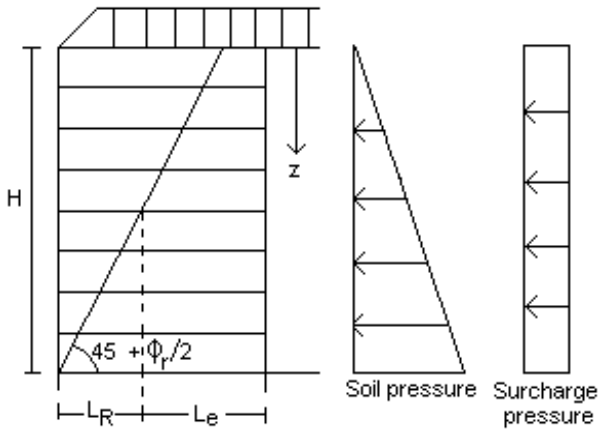

Figure 10.18 Embedment length for reinforcement required to resist pullout with distributed load, Koerner (1998)

10.4 CRITERION OF DESIGN WITH ASD AND LRFD METHODS.

The 1991 Interims to Division I of the AASHTO "Standard Specifications for Highway Bridges" (AASHTO Specifications) incorporated specifications and commentary for the allowable stress design (ASD) of foundations, retaining walls, piers and abutments. In ASD, all uncertainties of load, material resistance and the effects of construction control are assumed to be deterministic and embodied in a factor of safety, FS, or allowable stress. To overcome some of the limitations of ASD, Load and Resistance Factor Design (LRFD), accounts for variations in loads and material resistance by applying factors for uncertainty in load and resistance.

The design program developed in this report utilized the factors of safety (ASD method) as well as the load and resistance factors (LRFD method) based on the most recent studies (FHWA, D'Appolonia).

The ASD design method utilized the following factors of safety applied in the different equations cited in section 10.3.

1. Factor of safety against sliding equal to 1.5
2. Factor of safety against overturning equal to 2
3. Factor of safety for bearing capacity equal to 2 with a maximum permissible eccentricity of L/6
4. Factor of safety against pullout equal to 1.5

The loads and material resistance utilized in the LRFD method of design are listed as follow:

1. Load factor for vertical earth load as 1.35
2. Load factor for horizontal earth load equal to 1.5
3. Load factor for live load as 1.75
4. Recommended φ for sliding stability analysis of 0.8
5. Recommended φ for bearing capacity analysis of 0.45
6. Recommended φ for ultimate soil pullout of 0.45
7. The maximum permissible eccentricity for bearing resistance analysis of L/3.

For the LRFD method, the load factors were applied in the loads for external and internal analysis by multiplying the load by its corresponding factor. The material resistance factors were applied in both analyses by dividing the corresponding resisting force or property over the material factor. The equations corresponding to each analysis in section 10.3 consider a factor of safety equal to 1. The program has default values for the factors of safety, loads and material factors, as listed above; however the user can modify this data during the execution of this program.

The influence of creep and long term degradation has been incorporated through the generalized creep model described in Chapter 4, and verified against full scale testing in Chapter 9. Inclusion of the creep equations allows the user to input the time (required design life of the MSE wall) and temperature (average temperature throughout the design life). The equivalent modulus of the geogrid is then calculated accordingly and is used in further calculations. It is therefore possible to use the software to account for temperature and time-dependent creep of the geogrid, a main objective of the current study.

11 SUMMARY AND CONCLUSIONS

Analytical and experimental studies were performed to provide better design and analysis methods for geogrid reinforced MSE walls. Of particular importance is the incorporation of time and temperature dependent creep in the design and analysis methods. As part of the analytical study, a model was developed to predict creep for HDPE and PET geogrids. This model is considered an important contribution for creep of geosynthetics used in MSE wall applications, and especially for HDPE geogrids that display a nonlinear creep behavior. The analysis of results from this model fits well with the data obtained through an earlier study on creep. Additional creep tests at lower stress levels and lower temperatures could improve the model predictions by providing the necessary data to calibrate the general model to predict creep of geogrids under more typical conditions.

Two HDPE and two PET reinforcement small scale (1:5.5) MSE walls were tested, with different surcharges, each for 72 hour periods. Panel movements, strains in the reinforcement, and wall settlements were measured, indicating values smaller than the predicted, mostly for the smaller surcharges due to distortion caused by scaling neglecting the gravity effect.

The PET MSE small scale wall showed more deviations because the material has a high modulus of elasticity. It is noted that discrepancies were observed in certain parameters between duplicate walls that were identical in terms of materials and construction procedures especially at the higher load levels. Each pair of scaled walls, constructed using either PET or HDPE geogrid, exhibited differences in terms of displacements and strains along the geogrid layers. Rotation of the panels around the point of connection with the geogrid occurred in

certain cases. The panel displacements for HDPE geogrids were, in general, higher, although at higher stress levels, the PET geogrid walls exhibited slightly higher deformation, possibly due to slippage along the interface.

The model predictions were in agreement with the observed deformation in terms of deformation pattern, but not in magnitude. This is due, in part, to the differences in boundary conditions as well as model assumptions and approximations. The predicted strains in the geogrid layers were found to be in agreement with the experimental data.

One very important observation is that the experimental evidence and model predictions indicate that, even when the structure is loaded to very high stress levels, no catastrophic failure occurs, only excessive deformations. In fact, the experimental wall was loaded up to very high surcharge levels, beyond the design values with no signs of abrupt failure. The maximum amount of facing deformation in the scaled walls was approximately 160 mm, which corresponds to a full scale value of 880 mm. Although this level of distress would be unacceptable from a service standpoint, the lack of brittle response is certainly a desirable characteristic.

Close observation of the strains in the geogrid layers indicated that the strains developing in the geogrid layers are, in fact, much lower than the failure strains. For example, the strength of the geogrid, which was used in the original design, corresponded to a strain of 5%. However, the corresponding maximum strain from the numerical model using the same geogrid modulus, is 1.5%. The average value of strain in any layer did not exceed 1% in the analysis, and was often much lower. At first, this may seem inconsistent with the original design assumptions, where a factor of safety of 1.0 was considered. However, it is

necessary to emphasize that MSE wall design, even with low factors of safety, is highly conservative. Numerous redundancies exist at various design steps, including overly conservative assumptions regarding the failure mechanisms and material properties. A few such assumptions are outlined as follows:

1. It is assumed that an active failure wedge, similar to that used in Coulomb or Rankine's lateral earth pressure theory, will develop. This assumption results in a so-called lower bound solution, which is, by definition, safer than the actual failure condition. Experimental measurement as well as numerical modeling indicates that no such wedge develops within the anticipated failure load. Instead, the strains and stresses are distributed in a more uniform fashion within the wall.

2. Three dimensional restrictive effects are induced in shorter walls, and in walls that have wing abutments. The influence of these boundary conditions is to reduce the deformations and the stresses within the geogrid layers.

3. Although the strength of the geogrid corresponds to 5% axial strain, the actual value of design strength is reduced by the manufacturer (or designer) to account for creep and stress relaxation with time. The manufacturer's Minimum Average Roll Values (MARV) are within the 2.5 percentile of strength, and the actual strength is, in general, likely to be higher. Therefore the strains developing in the short term are much lower.

4. The role of the facing units is not considered in the design. Although the effect of deformation restrictions resulting from the facing is small, it may be significant when the wall is overloaded.

5. When designing the wall for a factor of safety of 1.0, the strength and pullout resistance of the most critical reinforcement layer controls the design. In other words, values of geogrid strength and length of embedment obtained for the most critical layer are repeated for all the layers. In an "ideal" borderline design, each layer should have a geogrid with a different strength and anchorage length. The use of stronger and longer reinforcement layers results in a redistribution of the stresses within the wall, which, in turn, yields a more conservative design.

6. Construction of the wall on a rigid foundation can mask the distress mechanisms which occur more commonly in practice.

12 REFERENCES

Ahn, W., "An Experimental and Analytical Investigation of Viscoelastic Pipe Soil Interaction", Ph.D. Dissertation, Florida Atlantic University, Boca Raton, Supervisor: Dr. D.V. Reddy, Florida DOT Research Contract Monitor: Powers, R. G, 1998.

Allen, T. M., J. R. Bell, and T. S. Vinson, "Properties of Geotextiles in Cold Regions Applications," Transportation Research Report No. 83-6, Oregon State University, 1983.

Allen, T. M., "Determination of Long-Term Strength of Geosynthetics: A State-of-the-Art Review", Proc., Geosynthetics '91 Conference, Atlanta, pp. 351-379, 1991.

Allen, T. M. and Elias V., " Overview and Status Report for FHWA HP & R National Pooled Fund Study", Durability Of geosynthetics For High way Applications", Earth Engineering and Sciences, Inc. , 1995

Arab R., Villard P., and Gourc J.P. " Large Deformation FEM Analysis of a Reinforced Earth Structure", Proc. Geosynthetics International, Vol. 2, Atlanta, GA, pp. 597-604, 1998.

ASTM D 2990-93a: "Standard Test Methods for Tensile, Compressive, and Flexural Creep and Creep-Rupture of Plastics", 1993.

ASTM D5265 Standard Test Method for Evaluating the Unconfined Tension Creep Behavior of Geosynthetics, Annual Book of ASTM Standards, Vol. 08 03., 1992.

Atmatzidis, D.K., Athanasopoulos, G.A., and Papantonopoulos, C.I. "Sand-Geotextile Interaction by Triaxial Compression Testing," Fifth International Conference on Geotextiles, Geomembranes and Related Products, Singapore, Vol. 1, pp. 377-380, 1994.

Bailey II, J. S., "New Jersey DOT Accepts Value Engineering Replacement of High-Strength Geotextile with Geogrid System for Embankment Stabilization", Proc., Symposium on Mechanically Stabilized Backfill Walls, Transportation Research Board, Washington, DC., 1995.

Barrows, R. And Machan, G., "Reinforcement of a Failed Embankment Over Slough Mud", Proc., Geosynthetics '91 Conference, Atlanta, GA, pp. 839-848, 1991.

Bathurst R.J. and Benjamin D. J., "Failure of a Geogrid-Reinforced Soil Wall", Transportation Research Record 1288, 1990.

Bathurst, R. J., "Instrumentation of Geogrid-Reinforced Soil Walls", Transportation Research Record 1277, Washington, DC., pp. 102-111, 1991.

Bathurst, R. J., and Simac R.," Review of Three Instumented Geogrid Reinforced Soil Retaining Walls ", Geosynthetics design and performance 6th Annual Symposium, Vancuver, B.C., 1991

Bathurst R.J., Crowe R.E. and Simac R.," Recent Innovations In Modular-Facing Retaining Wall Structures Using geosynthetic Reinforcement", 1991 Annual Conference Of The Canadian Society For Civil Engineering, May 29-31,1991, Vancouver

Bathurst R. J., Jarrett P.M. and Benjamin D.J.R.S. "A Data Base of Results From an Incrementally Constructed Geogrid-Reinforced Soil Wall Test" Symposium International, Paris, France, pp. 401-430, 1993.

Berg and Meyers "Analysis of the collapse of a 6.7 m High Geosynthetic-Reinforced Wall Structure", Proc., Geosynthetics '97 Conference, Long Beach, CA, pp. 85-105, 1997.

Billiard J. W. And Wu, J. T. H., "Load Test of a Large-Scale Geotextile-Reinforced Retaining Wall", Proc., Geosynthetics '91 Conference, Atlanta, GA, pp. 537-548, 1991.

Biondi G., Maugeri M. and Carrubba P., "Numerical Modeling of a Geogrid reinforced Wall" Proc. Second European Geosynthetic Conference, Bologna, Italy, pp 207-212, 2000.

Bolt A.F., and Duszynska A., "Pull-out testing of geogrid reinforcements", Proc. Second European Geosynthetic Conference, Bologna, Italy, pp 939-943, 2000

Brau G., and Floss R., "Geotextile Constructions Used at the Reconstruction of the Motorway BAB A8 Munich-Salzburg near the Lake Chiemsee", Proc. Second European Geosynthetic Conference, Bologna, Italy, pp 373-379, 2000

Bush, D.I., "Variation of Long-Term Design Strength of Geosynthetics in Temperature up to 40^{o}C", Proc. IV Int. Conf. on Geotextiles, Geomembranes and Related Products, pp. 673-676, The Hague, The Netherlands, 1992.

Cazzuffi D., Ghinelli A.: "European Experimental Approach to the Tensile Creep Behavior of High-Strength Geosynthetics", Geosynthetics '97 Conference Proceedings, Long Beach , pp.253-266, 1997.

CEN prEN ISO 13431, "Geotextiles and geotextile related products: determination of the tensile creep and creep rupture properties", Doc. CEN/TC 189/WG3/N31/Rev 1., 1995.

Christopher, B.R., Gill, S.A, Giroud, J.P., Juran, I., Mitchell, J.K., Schlosser, F., and Dunnicliff, J. "Reinforced Soil Structures. Volume I. Design and Construction Guidelines", *FHWA Report DTFH61-84-C-00073*, 1990.

Christopher, B.R., and Holtz, R.D., *Geotextile Engineering Manual*, Report No. FHWA-TS-86/203, Federal Highway Administration, 1985.

Chang, D. T., Chen, T. C., and Su, K. H., "Utilization of Geotextile-Reinforced Retaining Wall for Stabilizing Weathered Mudstone Slope", Proc., Geosynthetics '91 Conference, Atlanta, GA, pp. 739-753, 1991.

Chua, K. M., Aspar, W., and De La Rocha, A., "Simulating Failures of Geosynthetics-Reinforced Earth Structures Under Saturated Conditions", Geosynthetics '93, Vancouver, Canada, pp. 417-430, 1993.

Dancygier A. N. "Quantitative Evaluation of Effect of gravity on small-scale Modeling", Journal of Engineering Mechanics, Vol 121, No 7, pp 773-778, July 1995

Das, B.M. "Principles of Geotechnical Engineering", PWS, Third Edition, Boston MA, 1994.

Das B. M., "Principles of Foundation Engineering", PWS, Third Edition, Boston MA, 1995.

Den Hoedt: "Creep Relaxation of Geotextile Fabrics", Geotextiles and Geomembranes, No 4, pp. 83-92, 1986.

Desai, C. S. and Lightner, J. G., "Improved Numerical Procedures for Soil-Structure Interaction Including Simulation of Construction", Report # VPI-E-7932, Virginia Polytech, Blacksberg, VA 1979.

Desai, C. S., Somasundaram, S., Frantziskonis, G.N., "A Hierarchical Approach to Constitutive Modelling of Geological Materials" In. Jl. Num. Anal. Methods in Goemechanics 10(3): pp. 225-257, 1986.

Elias, V., "Durability/Corrosion of Soil Reinforcement Structures", FHWA/RD-89/186. Federal Highway Administration, Washington, DC. 1990

Elias, V., Barry R. and Christopher B.R., "Mechanically Stabilized Earth Walls and Reinforced Soil Slopes, Design and Construction Guidelines", FHWA Report # FHWA-SA-96-071, August 97.

Environment Protection Agency: "How to Meet Requirements for Hazardous Waste Landfill Design, Construction and Closure", Pollution Technology Review, No. 185, pp. 113, 1990.

Fadzilah S., Race R. J. and Holtz R. D., "Strees Distribution and Deformations in Modular Block Faced GRS Walls Subjected to Increasing Surcharge", Proc. Geosynthetics Conf. 2001, Portland, Oregon, February 12-14, 2001.

Fannin, R. J., and Raju, D. M. "Pullout Resistance of Goesynthetics," Proceedings of the 44th Canadian Geotechnical Conference, Calgary, Vol. 2, October, 1991.

Fannin, R. J., and Raju, D. M. "Large Scale Pullout Test Results on Goesynthetics," Proceedings of the '93 Geosynthetics Conference, Vancouver, Canada, Industrial Fabrics Association International, Vol. 2, pp. 633~643. 1993.

Fannin, R.J., and Raju, D.M. "On the Pullout Resistance of Geosynthetics," *Canadian Geotechnical Journal*, Vol. 30, pp. 409-417, 1993.

Farrag, K., Acar, Y. B., and Juran, I., "Pull-Out Resistance of Geogrid Reinforcements" Geotextiles and Geomembranes, Vol. 12, 1993, pp. 133-159.

Farrag, K., "Evaluation of the Effect of Moisture Content on the Interface Properties of Geosynthetics", Proc., Geosynthetics '95 Conference, Nashville, TN, 1995.

Fishman, K. L. And Desai, C. S., "Response of a Geogrid Earth Reinforced Retaining Wall With Full Height Precast Concrete Facing", Proc., Geosynthetics '91 Conference, Atlanta, GA, pp. 691-700, 1991.

US Department of Transportation Report: FHWA-RD-89-186, "Durability/Corrosion of Soil Reinforced Structures", December 1990.

Floss R. And Thamm B.R. " Field measurements of a Reinforced Earth Retaining Wall Under Static and Dynamic Loading", Proc. International Conf. on Soil Reinforcements Paris, Vol. 3, pp.183-188, 1995.

Floss R., Brau G., and Bauer A., "In-soil-testing of Geogrids with Low Construction Deformations", Proc. Second European Geosynthetic Conference, Bologna, Italy, pp 945-950, 2000.

Gao, S "Long-Term Pullout Resistance of Geogrid Reinforcement for Retaining Walls", Master Thesis, Florida Atlantic University, Boca Raton, Supervisor: Dr. Reddy, D.V., Florida DOT Research Contract Monitor: Lai P., 1999.

Giroud, J.P., Darrasse, J., and Bachus, R.C. "Hyperbolic Expression for Soil-Geosynthetic or Geosynthetic-Geosynthetic Interface Shear Strength," *Geotextiles and Geomembranes*, Vol. 12, pp. 275-286, 1993.

Gourc, Gotteland, Haza, Perrier, and Baraize "Geotextile Reinforced Structures as Bridge Abutments: Full Scale Experimentation, Geosynthetics 95, Nashville, TN, pp 79-93. 1995.

Haza E., Gourc J.P., Gotteland P., "Locally Loaded Geosynthetic Reinforced Soil Structures: Calculation Method", Proc. Geosynthetics International, Vol. 2, Atlanta, GA, pp. 511-516, 1998.

Hatami K., Bathurst R. J., Di Pietro P. and Bianco P. M., "Numerical Study of Retaining Walls With Non-Uniform Reinforcement", Proc. Second European Geosynthetic Conference, Bologna, Italy, pp 219-224, 2000.

Ho S.K., Rowe R.K., "Finite Element Analysis of Geosynthetics- Reinforced Soil Walls", Proc. Geosynthetics '93 - VAncounver, Canada- 203, 1993

Holtz, R.D., Christopher, B.R., and Berg, R.R., *Geosynthetic Engineering*, BiTech Publishers, 1997.

ICI: "Durability of Polyester, Polyaramid and Polyethylene Materials in Soil Reinforcement Applications", Report to British Standart Technical Committee CBS/56, 1986.

Jailloux, J. M. and Segrestin, “Present State of Knowledge of Long-Term Behavior of Materials Used as Soil Reinforcements”, International Geotechnical Symposium on Theory and Practice of Earth reinforcement, Japan, pp. 105-110, 1988.

Juran I., and Chen, C.L. “Soil-Geotextile Pull-Out Interaction Properties: Testing and Interpretation,” *Transportation Research Record 1188*, pp. 37-47, 1988.

Kharchafi, M. And Dysli, M., “ The Mechanical Performances of Two Experimental Full-Scale Embankments Reinforced by Geotextiles”, Proc. Geotextile Conference, Singapore, pp.1-4, 1994.

Karpurapu, R., and Bathurst, R.J. “Behavior of Geosynthetic Reinforced Soil Retaining Walls Using the Finite Element Method,” *Computers and Geotechnics*, Vol. 17, No. 3, pp. 279-299, 1995.

Keller, R. G., "Experiences with Mechanically Stabilized Structures and Native Soil Backfill", Proc., Symposium on Mechanically Stabilized Backfill Walls, Preprint No. 950752, Transportation Research Board, Washington, DC., 1995.

Kemp, S., Martin, J. S., and Stadler, A. T., "The Design and Construction of Geogrid-Reinforced Retaining Walls at the South Carolina Port Authority's Wando Terminal", Proc., Geosynthetics '93 Conference, Vancouver, Canada, pp. 153-166, 1993.

Koerner, R.M., Wayne, M.H., and Carroll, R.G., Jr., "Analytic Behavior of Geogrid Anchorage," Proc. Geosynthetics, St Paul, MN: IFAI, pp 525-536,1989.

Koerner, R.M., Lord, A.E., Jr., and Hsuan, Y.H. “Arrhenius Modeling to Predict Geosynthetic Degradation,” *Geotextiles and Geomembranes*, Vol. 11, No. 2, pp. 151-182, 1992.

Koerner, R.M. “*Designing with Geosynthetics”*, Fourth Edition. Prentice Hall, Inc., Upper Saddle River, N.J., 1998.

Kundu P. K. and Cohen I. M., " Fluids Mechanics", Academic Press, Philadelphia, Pensilvania, 1990.

Leonards, Frost, and Bray, "Collapse of Geogrid-Reinforced Retaining Structure", Journal of Performance of Constructed Facilities, ASCE, Vol. 8, No. 4, pp. 274-292, November 1994.

Leshchinsky, D., Dechasakulsom, M., Kaliakin, V.N., and Ling, H.I. “Creep and Stress Relaxation of Geogrids,” *Geosynthetics International*, Vol. 4, No. 5, pp. 463-479, 1997.

Ling, H.I., and Tatsuoka, F. “Simulating Performance of GRS-RW by Finite-Element Procedure,” Journal of Geotechnical Engineering, Vol. 121, No. 4, pp. 330-340, 1995.

Long R.P., “Mechanically Stabilized Earth Walls”, Transportation Research Board, Washington, D.C., 17p, 1995.

McGown A., Andrawes K.Z., Pradham S., and Khan A.J. “Limit State Design of Geosynthetic Reinforced Soil Structures“, Proc. Geosynthetics International, Vol. 1,Atlanta, GA, pp. 143-176, 1998.

Merry, S.M., and Bray, J.D., “Temperature-Dependent Multi-Axial Creep Response of HDPE Geomembranes,” Geosynthetics ‘97 Conference Proceedings, pp. 163-176, 1997

Moreno, O. A., King, J. L., and MacDonald, R. A., "From a Contractor's Viewpoint: Construction Technicalities of a Tiered Modular Block Wall -- The Fiesta, Texas Case", Proc., Geosynthetics '93 Conference, Vancouver, Canada, pp. 167-187, 1993.

Munfakh, G.A., "Contracting for Mechanically Stabilized Backfill Walls", Transportation Research Board 74th Annual Meeting, Washington, D.C., 1995

Navarrete F, Reddy D.V, and Lai P, "Creep of Geogrid Reinforcement for Retaining Wall Backfills", Proc. Geosynthetics Conf. 2001, Portland, Oregon, February 12-14, 2001.

Peggs, I. D. And Kanninen, M. F., "HDPE Geosynthetics: Premature Failures and Their Prediction", Proc. Geosynthetics International, Vol. 2, No. 1, pp. 327-339, 1995.

Poh, K. W. “General Creep-Time Equation,” Journal of Materials in Civil Engineering, May 1998.

Popelar C.H., "A Comparison of the Rate Process Method and the Bidirectional Shifting Method" Polymer Engineering and Science, Vol 30 pp 151-160, 1990

Raju, D. M. and Fannin R. J., "Large Scale Pullout Testing of Geosynthetics", A thesis submitted in partial fulfillment of the M. A. Sc. Degree at the University of British Columbia, 1991.

Ramos, H. R., McDaniel, G. T., and Maher, S. A., "Geogrids Strengthen Foundation for Mechanically Stabilized Earth Retaining Wall -- A Case Study", Proc., Geosynthetics '93 Conference, Vancouver, Canada, pp. 365-377, 1993.

Reddy D.V., Navarrete F., and Lai P.,"Strength and Durability of Backfill Geogrid Reinforcement for Retaining Walls", proc. EuroGeo 2000, Second European Geosynthetics Conference and Exhibition, Bologna, Italy, October 15-19, 2000.

Reddy D.V., Gao S., Navarrete F., and Lai P., "Pull-out of Backfill Geogrid Reinforcement for Retaining Walls", proc. EuroGeo 2000, Second European Geosynthetics Conference and Exhibition, Bologna, Italy, October 15-19, 2000.

Reddy D.V., Navarrete F., and Lai P., "Creep of Backfill Geogrid Reinforcement for Retaining Walls", proc. EuroGeo 2000, Second European Geosynthetics conference and Exhibition, Bologna, Italy, October 15-19, 2000.

Reddy D. V., Navarrete F. and Lai P., "Durability, Creep, and Creep-Rupture of Backfill Geogrid Reinforcement for Retaining Walls", Proc. Geossinteticos '99, Rio de Janeiro, Brazil, October 19-22, 1999, pp.107-114.

Reddy, D. V., Strength and Durability of Backfill Geogrid Reinforcement for Retaining Walls, Report to FDOT, Florida Atlantic University, BocaRaton, FL USA, 2000.

Sandri, D., Martin, J. S., Vann, C. W., Ferrer, M., and Zeppenfeldt, I., "Installation Damage Testing of Four Polyester Geogrids in Three Soil Types", Proc., , Vancouver, Canada, pp. 743-455, 1993.

Sawicki, A. "A basis for Modeling Creep and Stress Relaxation Behaviour of Geogrids," Geosynthetics International, Vol 5, No. 6, pp. 637-645, 1998.

Simac, Bathurst, and Fennessey., "Design of Gabion-geosynthetic Retaining Walls on the Tellico Plains to Robbinsville highway", Geosynthetics '97, Conference, Long Beach, California, pp. 105-118, 1997.

Simac R., Bathurst R.J., Goodrum A., " Design and Analysis of Three Reinforced Soil Retaining Walls" , Proc. Geosynthetics '91 Conference Atlanta, USA, 1991

Simonini P., Schiavo M., Gottardi L. and Tonni L., "Numerical Analysis of a Model Wall Reinforced With Polypropylene Geogrids", Proc. Second European Geosynthetic Conference, Bologna, Italy, pp 231-236, 2000

Schneider, H. and Groh M. " An Analysis of Durability Problems of Geotextiles", Proceedings Geosynthetics 87 Conference, New Orleans, pp 434-441, 1987.

Soni, K.M., Varadarajan, A., and Sharma, K.G., "Constitutive Modeling of a Geosynthetic Reinforced Soil", Proc. Environmental Geotechnology with Geosynthetics, new Delhi, India, 1996.

Tatsuoka F., Koseki, J. And Tateyama, M., "Performance of Reinforced Soil Structures during the 1995 Hyogo-ken Nanbu Earthquake", Earth Reinforcement, (Ochiai *et al.*, eds.), Balkema (in print)., 1998,

Tsukada Y., Ochiai Y., and H. Miyatake, " Filed Performance Test of a Geosynthetic-Reinforced Soil Wall with Rigid Facing" , Proc. Geosynthetics International, Vol. 1,Atlanta, GA, pp. 577-586, 1998.

Van Zanten, R. V., "Designing with Geosynthetics in Civil Engineering", John Wiley and Sons, 1986.

Vitton S.J., Harris W.W., Whitman M.F., and Liang R.Y., "Analysis of Anchored Geosynthetic Systems for In Situ Slope Stabilization of Fine-Grained Soils", Transportation Research Board 77th Annual Meeting, Washington, D.C., 28p, 1998.

Wharton, G., Harper, W. J., and Witt, C. M., "Geogrid and Geotextile Reinforced Foundation for Major Refinery Processing Unit", Proc., Geosynthetics '93 Conference, Vancouver, Canada, pp. 339-353, 1993.

Williams M. L., Landel R. F., and Ferry J. D. Journal of American Chemistry Society, 77, 3701, 1995

Withiam, J.L., Voytko, E.P., Barker, R.M., Duncan, J.M., Kelly, B.C., Musser, S.C. and Elias V. "Load and Resistance Factor Design (LRFD) for Highway Bridge Substructures", FHWA Publication No. FHWA HI-98-032, 1998.

Wrigley, N. E., "Durability and Long Term Performance of Tensar Polymer Grids for Soil Reinforcement", Materials Science and Technology, Vol. 3, 1987.

Wu, J.T.H., and Helwany, S.M.B. "A Performance Test for Assessment of Long-Term Creep Behavior of Soil-Geosynthetic Composites," *Geosynthetics International*, Vol. 3, No. 1, pp. 107-124, 1996.

Yarger, T. L. and Barnes, R. S., "Montana Department of Transportation's Introduction to Geogrid Use for Steepened Embankment Design", *Proc., Geosynthetics '91 Conference*, Atlanta, GA, pp. 311-326, 1991.

Appendix A. Pullout Calculations

Following are the detailed calculation of the preliminary analysis on the HDPE-1600 geogrid. The following tables show the properties used in FLAC modeling for this case.

SOIL

DATA	STATUS	VALUE	UNITS
1.Density=	Given	1560.00	kg/m^3
2. Modulus of elasticity=	Assumed	4.00E+07	N/m^2
.----->between 25-50 MPa			
3. Poisson's ratio=	Assumed	0.30	-
4.Friction angle=	Given	36.00	degree
CALCULATIONS			
1. Shear modulus (G)=	Calculated	1.54E+07	Pa
2. Bulk modulus (K)=	Calculated	3.33E+07	Pa

GEOGRID

DATA	STATUS	VALUE	UNITS
1. Tensile modulus=	Given	1896000	N/m
2. Thickness=	Given	0.0018	m^2
3.Area (A=Thickness*Unit length)=	Given	0.0018	m^2
CALCULATIONS			
1. Modulus of elasticity (E)=	Calculated	1.05E+09	Pa
2. Moment of inertia (I)=	Calculated	4.86E-10	m^4

INTERFACE PROPERTIES

DATA	**STATUS**	**VALUE**	**UNITS**
1. Depth of the box=	Given	0.6	m
2. Number of effective y-zones=	FLAC input file	16	grids
CALCULATIONS			
1. Kn=10*max[(K+ (4/3)G)/Dz]=		1.43E+10	N/m
2. Ks=		1.43E+10	N/m

CALCULATION OF FRICTION ANGLE

Tmax=	Max. load applied in the geogrid-------> Load applied in geogrid			
	Expected load for this geogrid			
tmax=	Max. shear stress applied in the geogrid			
< Delta=	Angle of friction between soil-geogrid			
DATA		**STATUS**	**VALUE**	**UNITS**
1. Tmax=	load --->	Given	54000	N/m
2. Length of geogrid/unit =		Wide of box	1.22	m
CALCULUS				
1. Area geogrid/unit length=			1.22	m^2
2. tmax=		Calculated	2.21E+04	Pa
3. < Delta=		Calculated	28.4	degrees

INCREMENTS IN PULLOUT LOAD

DATA GIVEN IN THE TEST (FAU)	Time of application	VALUE	UNITS
1.Confining pressure=	Always	41000	Pa
2. Pullout load			
Stage I	9800 hrs	5693	N/m
Stage II	25 hrs	15660	N/m
	26 hrs	31310	N/m
	27 hrs	45550	N/m
	28 hrs	54090	N/m

Appendix B. Creep Data

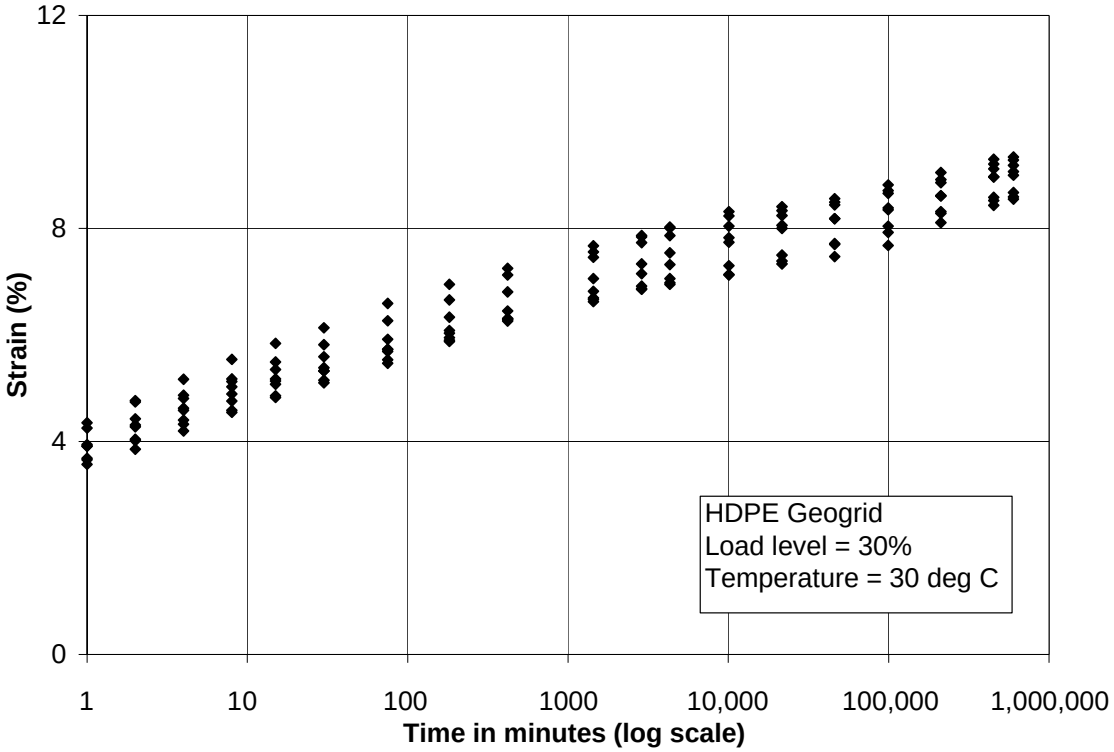

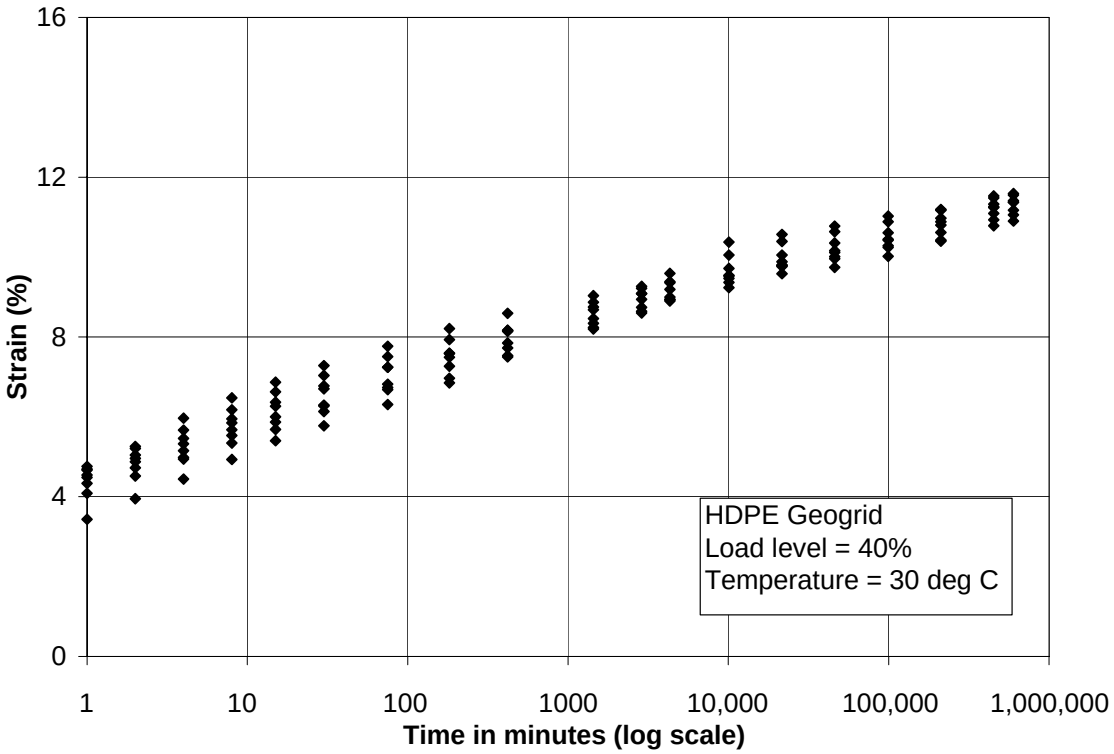

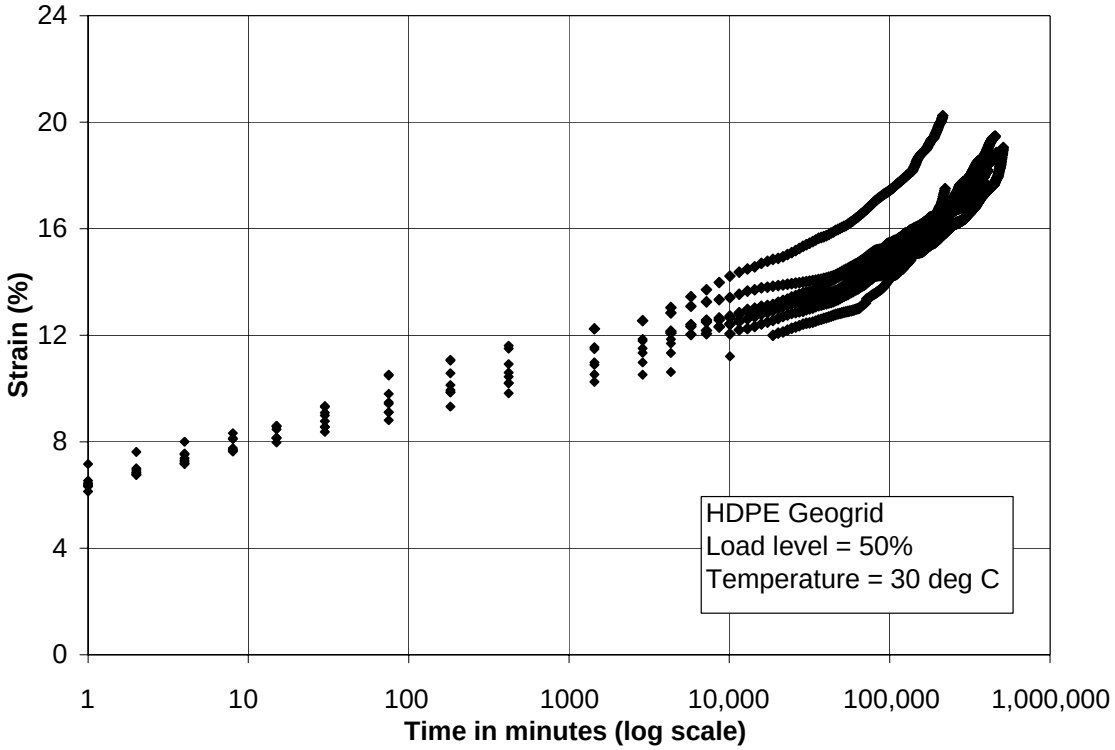
24
20
16
12
8
4
0
Strain (%)
1
10
100
1000
10,000
100,000
1,000,000
Time in minutes (log scale)
HDPE Geogrid
Load level = 50%
Temperature = 30 deg C

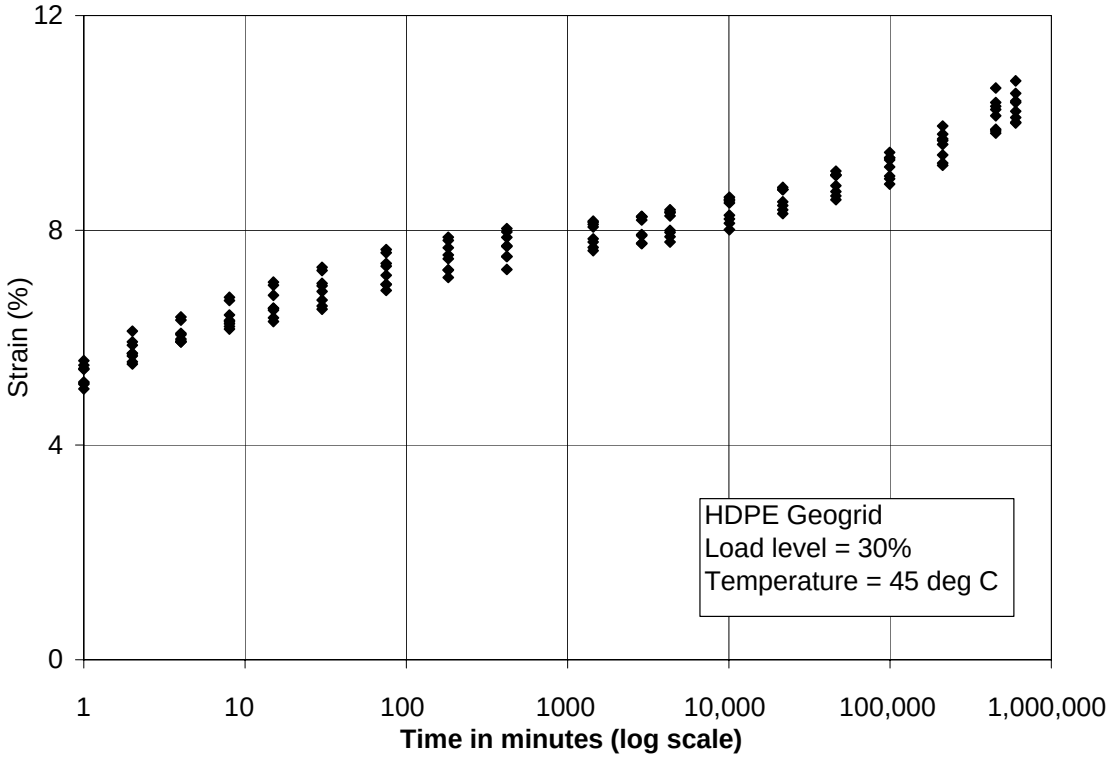
12
8
4
0
Strain (%)
1
10
100
1000
10,000
100,000
1,000,000
Time in minutes (log scale)
HDPE Geogrid
Load level = 30%
Temperature = 45 deg C

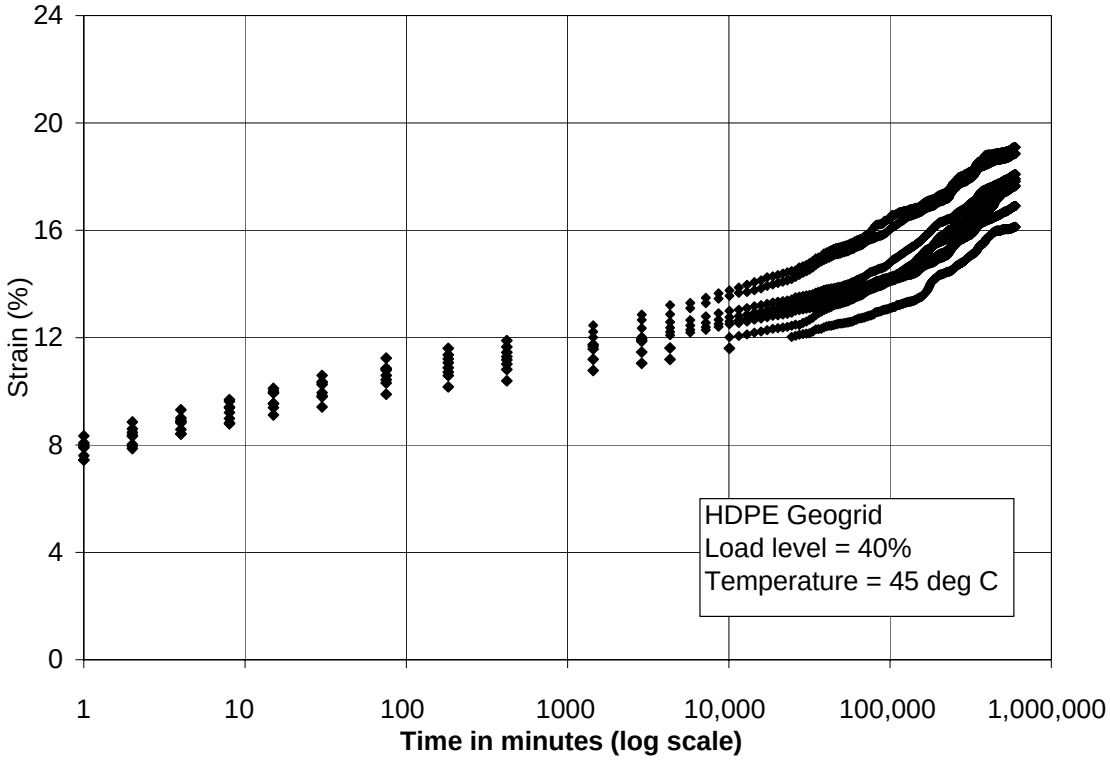
24
20
16
12
8
4
0
Strain (%)
HDPE Geogrid
Load level = 40%
Temperature = 45 deg C
1
10
100
1000
10,000
100,000
1,000,000
Time in minutes (log scale)

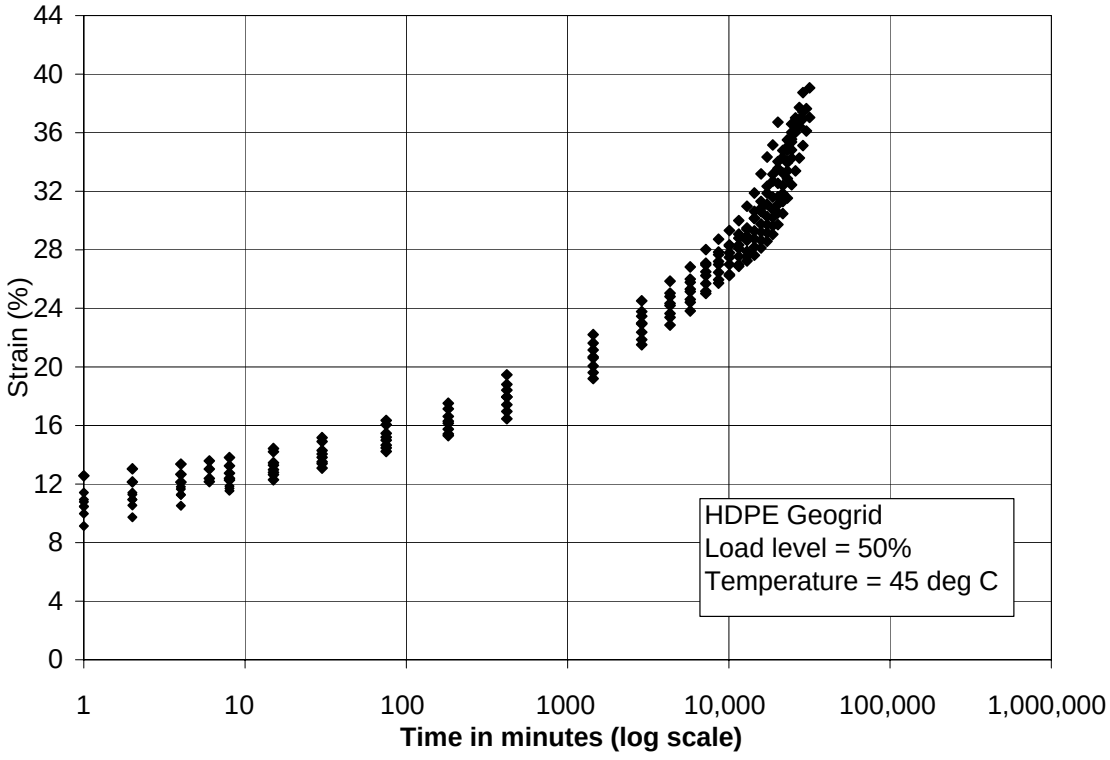
44
40
36
32
28
24
20
16
12
8
4
0
Strain (%)
HDPE Geogrid
Load level = 50%
Temperature = 45 deg C
1
10
100
1000
10,000
100,000
1,000,000
Time in minutes (log scale)

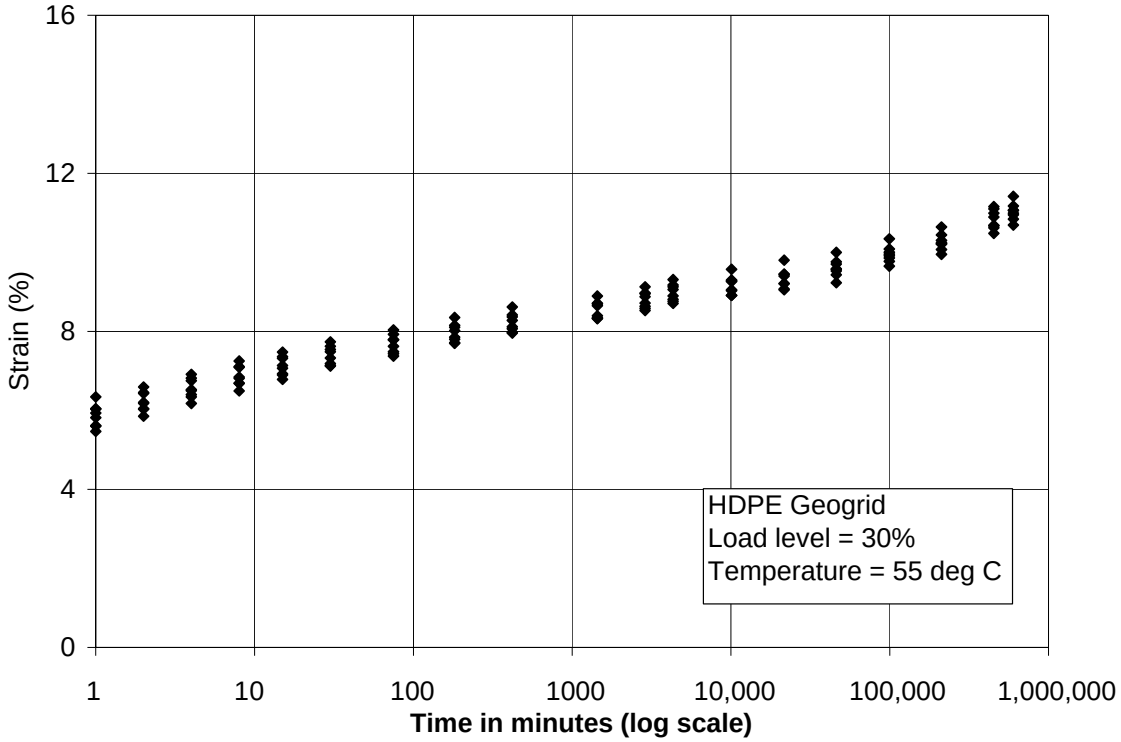
16
12
8
4
0
Strain (%)
HDPE Geogrid
Load level = 30%
Temperature = 55 deg C
1
10
100
1000
10,000
100,000
1,000,000
Time in minutes (log scale)

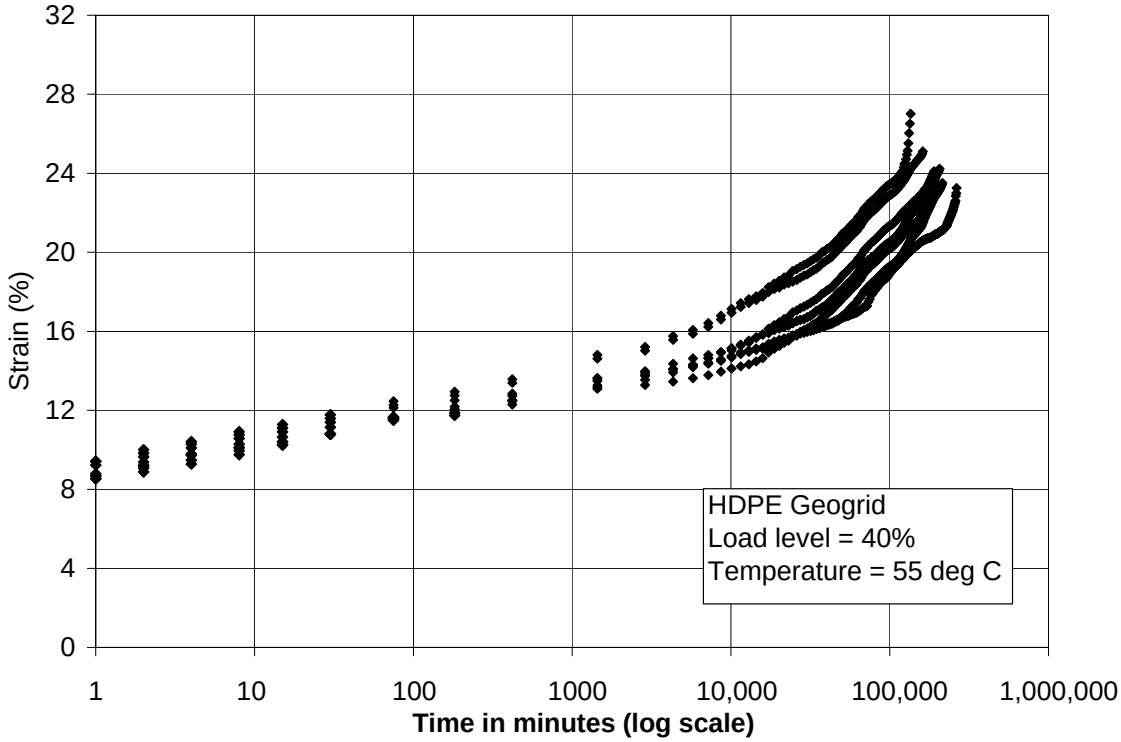
32
28
24
20
16
12
8
4
0
Strain (%)
HDPE Geogrid
Load level = 40%
Temperature = 55 deg C
1
10
100
1000
10,000
100,000
1,000,000
Time in minutes (log scale)

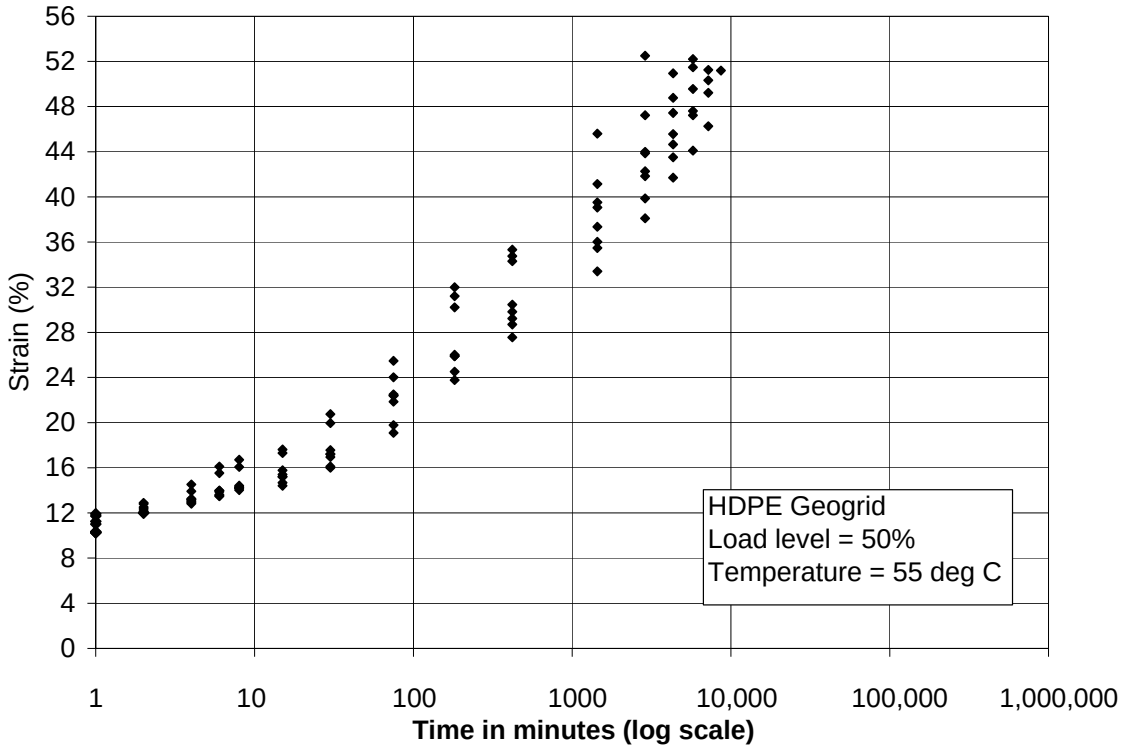
56
52
48
44
40
36
32
28
24
20
16
12
8
4
0
Strain (%)
1
10
100
1000
10,000
100,000
1,000,000
Time in minutes (log scale)
HDPE Geogrid
Load level = 50%
Temperature = 55 deg C

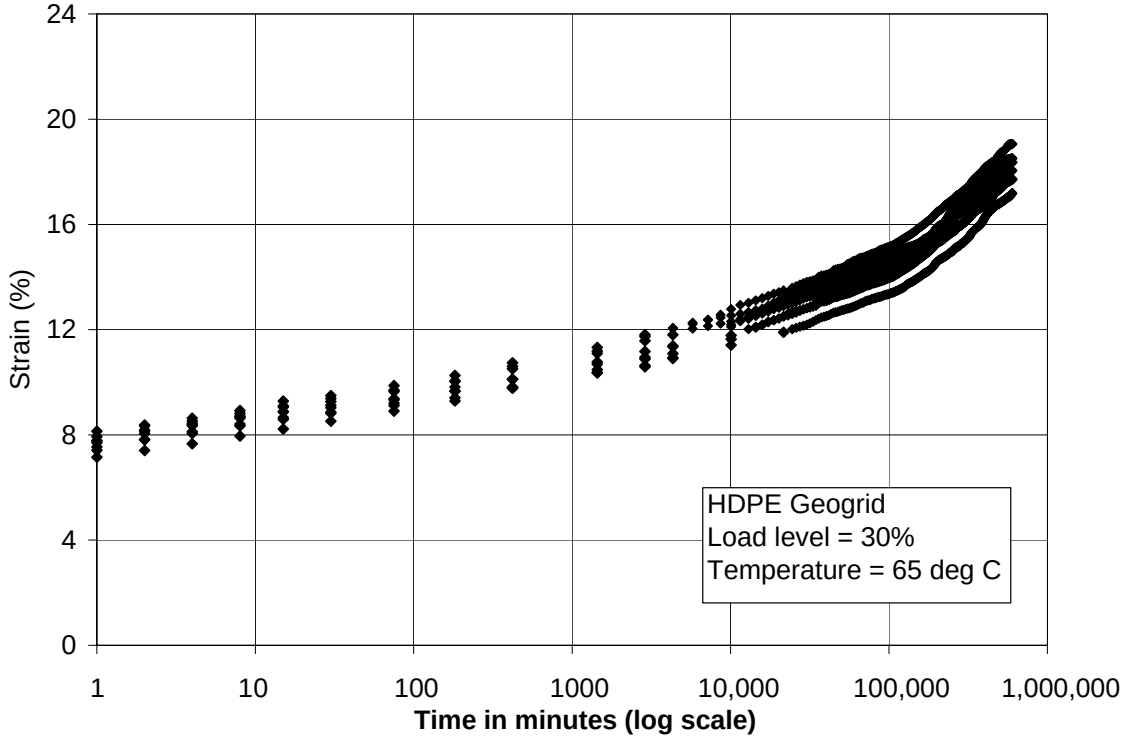
24
20
16
12
8
4
0
Strain (%)
1
10
100
1000
10,000
100,000
1,000,000
Time in minutes (log scale)
HDPE Geogrid
Load level = 30%
Temperature = 65 deg C

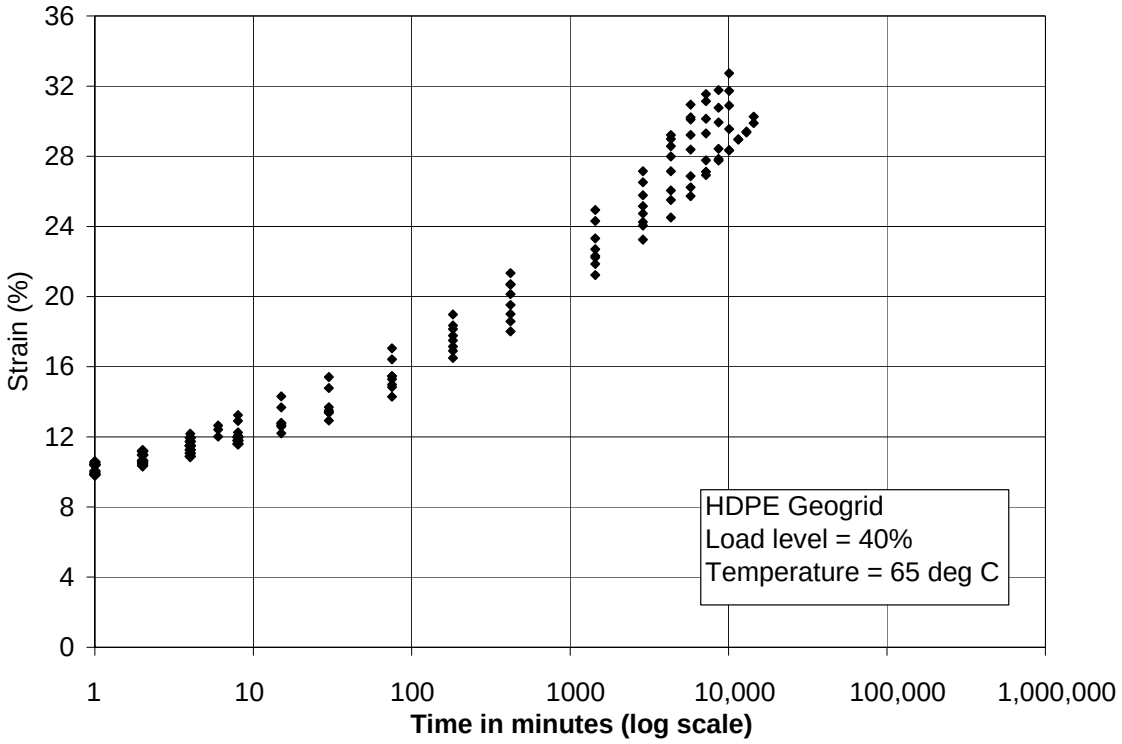
36
32
28
24
20
16
12
8
4
0
Strain (%)
1
10
100
1000
10,000
100,000
1,000,000
Time in minutes (log scale)
HDPE Geogrid
Load level = 40%
Temperature = 65 deg C

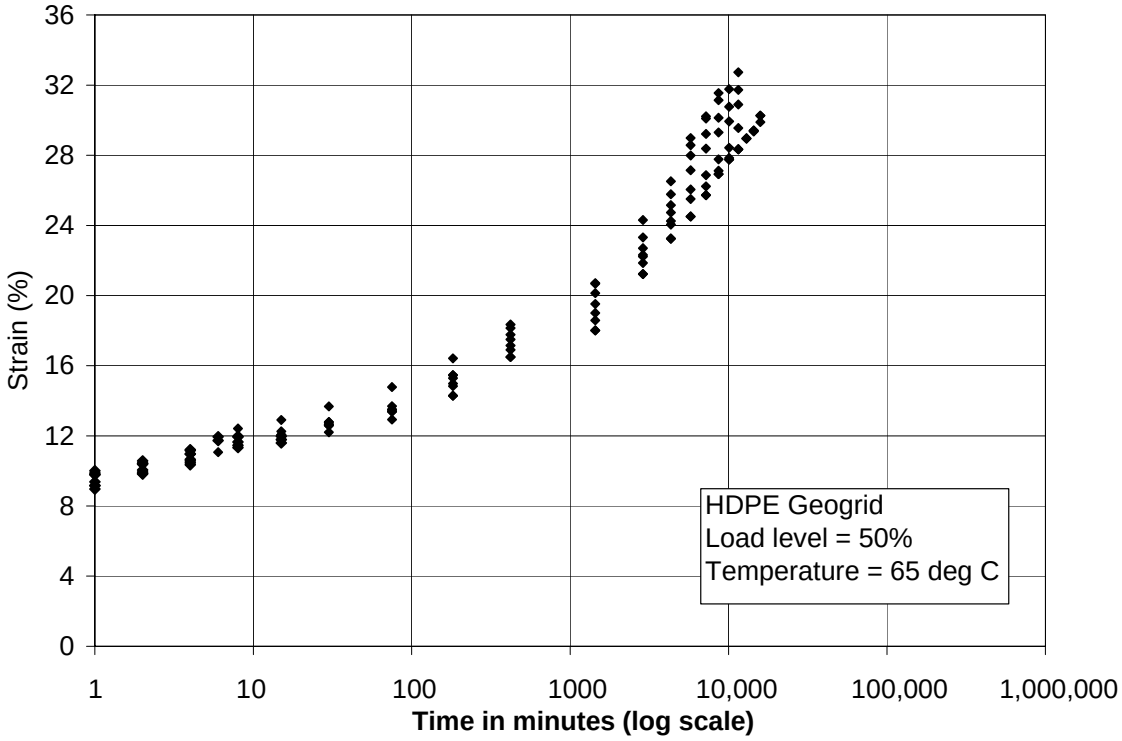
36
32
28
24
20
16
12
8
4
0
Strain (%)
1
10
100
1000
10,000
100,000
1,000,000
Time in minutes (log scale)
HDPE Geogrid
Load level = 50%
Temperature = 65 deg C

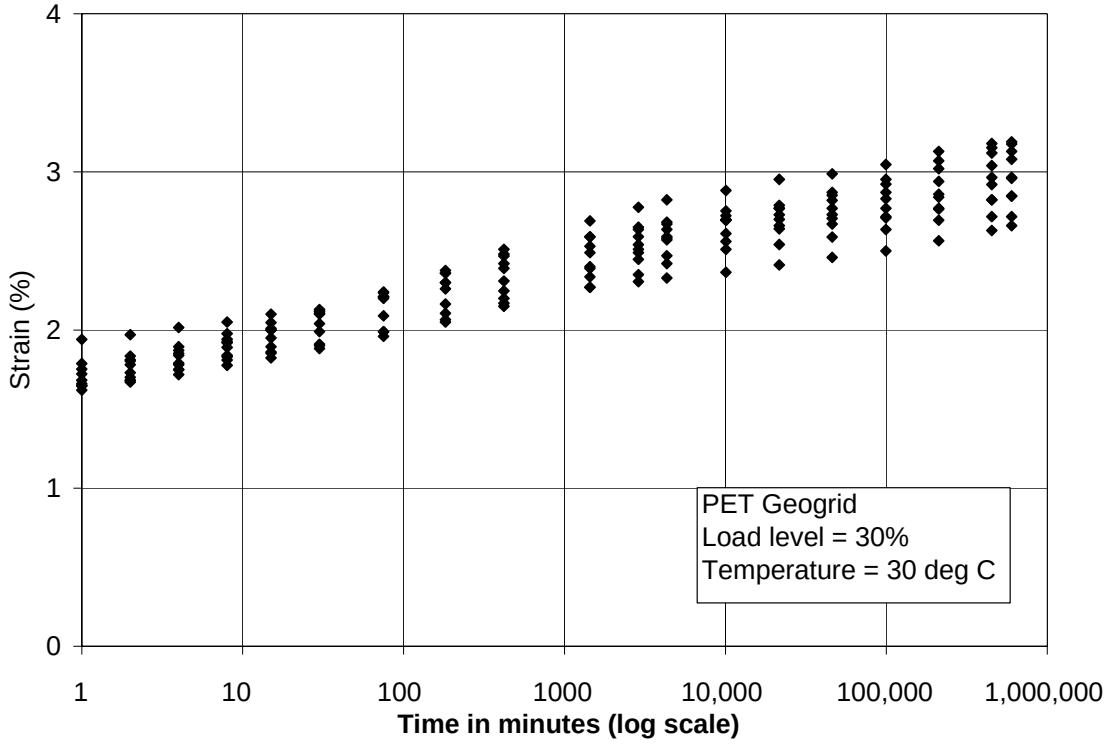
Strain (%)
0
1
2
3
4
1
10
100
1000
10,000
100,000
1,000,000
Time in minutes (log scale)
PET Geogrid
Load level = 30%
Temperature = 30 deg C

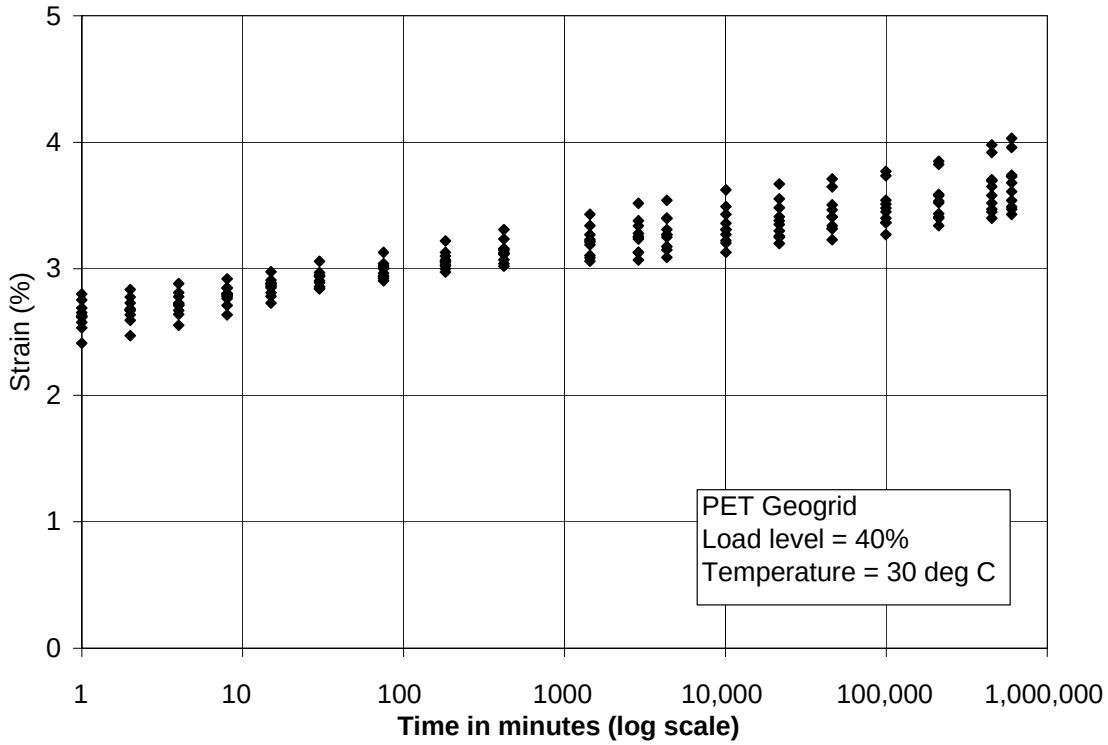
Strain (%)
0
1
2
3
4
5
1
10
100
1000
10,000
100,000
1,000,000
Time in minutes (log scale)
PET Geogrid
Load level = 40%
Temperature = 30 deg C

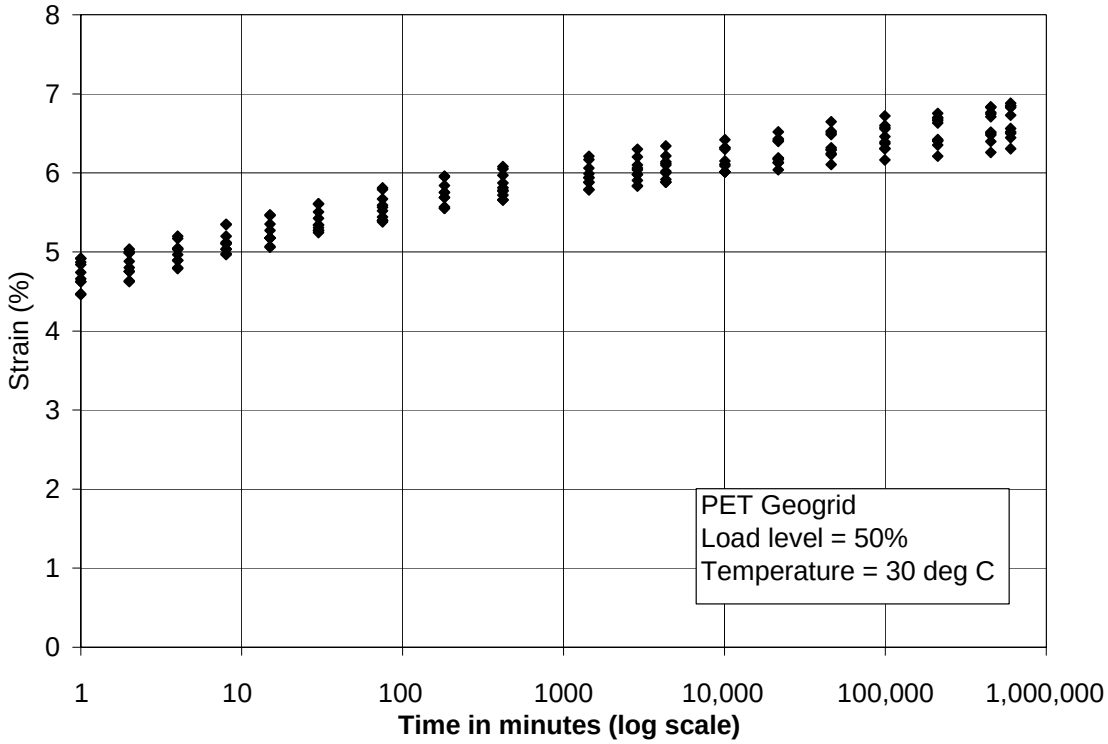
Strain (%)
0
1
2
3
4
5
6
7
8
1
10
100
1000
10,000
100,000
1,000,000
Time in minutes (log scale)
PET Geogrid
Load level = 50%
Temperature = 30 deg C

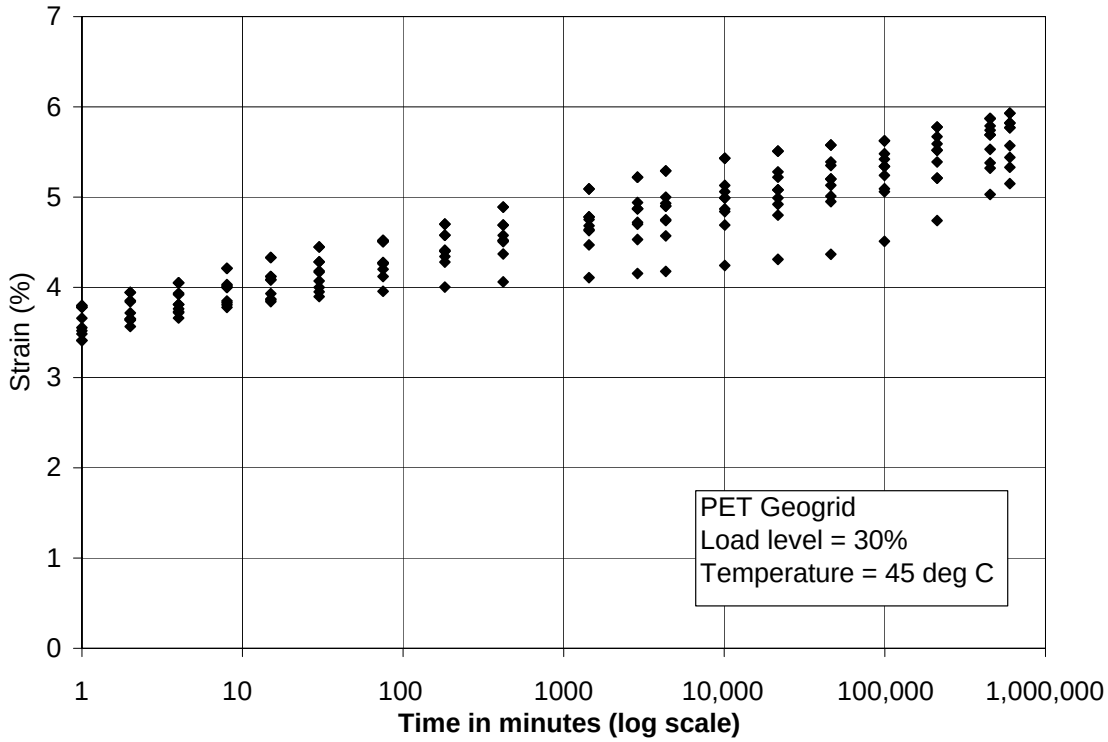
Strain (%)
0
1
2
3
4
5
6
7
1
10
100
1000
10,000
100,000
1,000,000
Time in minutes (log scale)
PET Geogrid
Load level = 30%
Temperature = 45 deg C

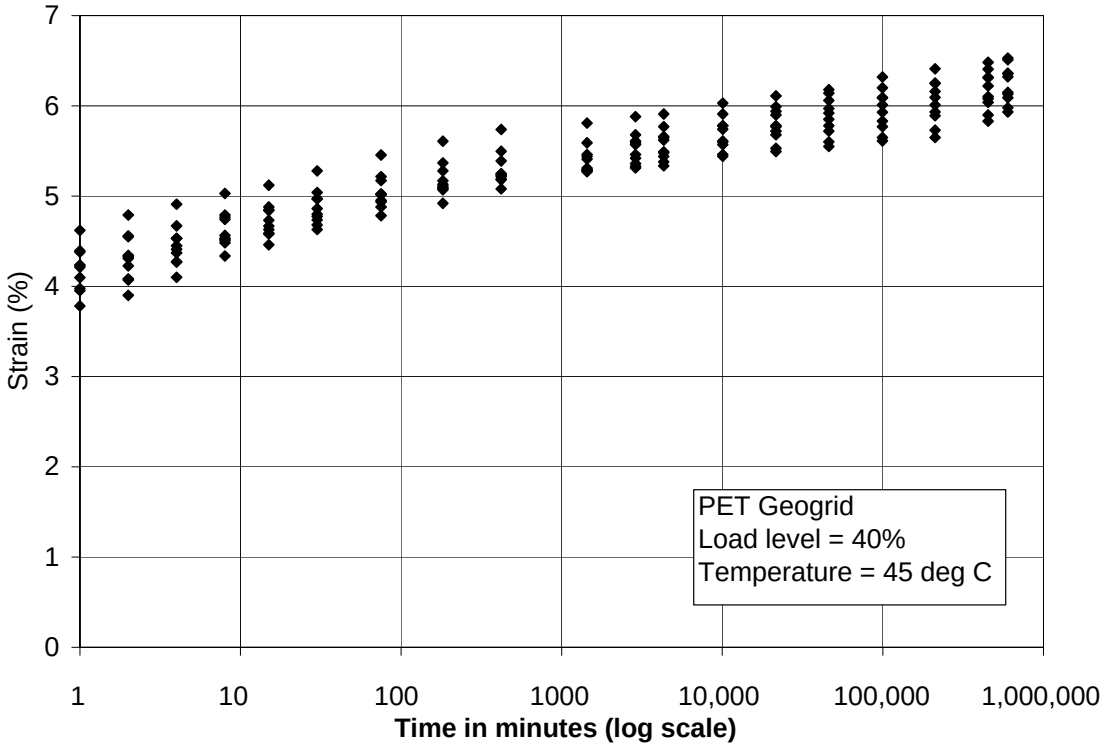
Strain (%)
0
1
2
3
4
5
6
7
1
10
100
1000
10,000
100,000
1,000,000
Time in minutes (log scale)
PET Geogrid
Load level = 40%
Temperature = 45 deg C

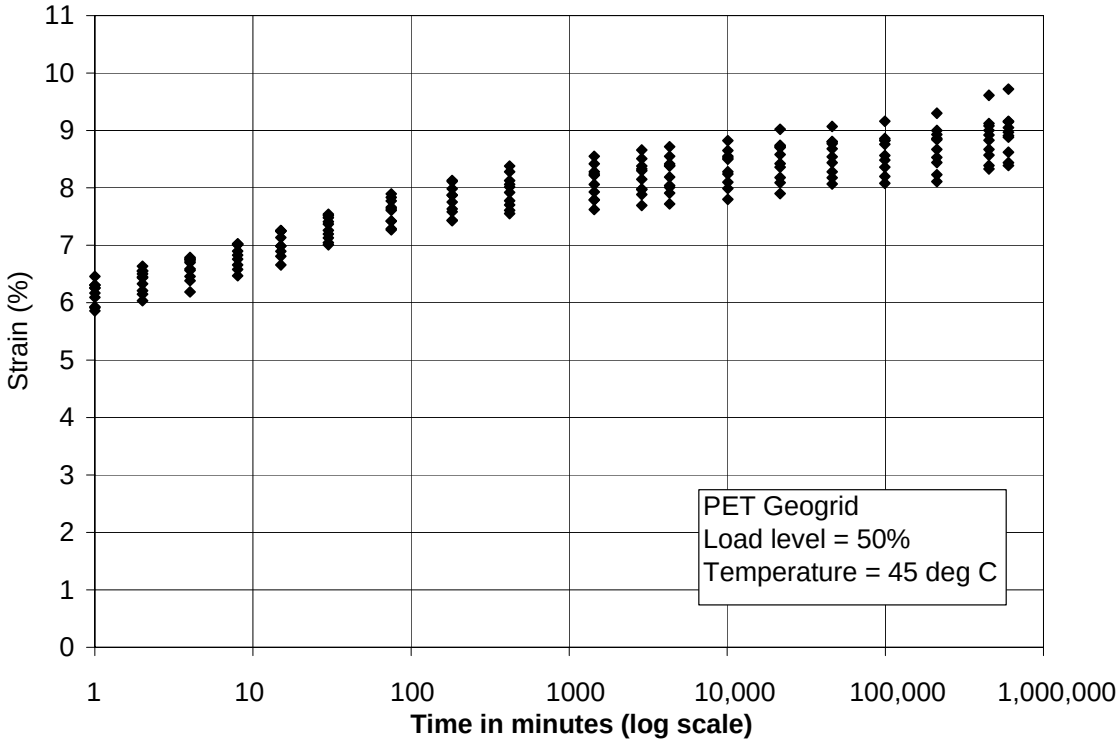
Strain (%)
0
1
2
3
4
5
6
7
8
9
10
11
1
10
100
1000
10,000
100,000
1,000,000
Time in minutes (log scale)
PET Geogrid
Load level = 50%
Temperature = 45 deg C

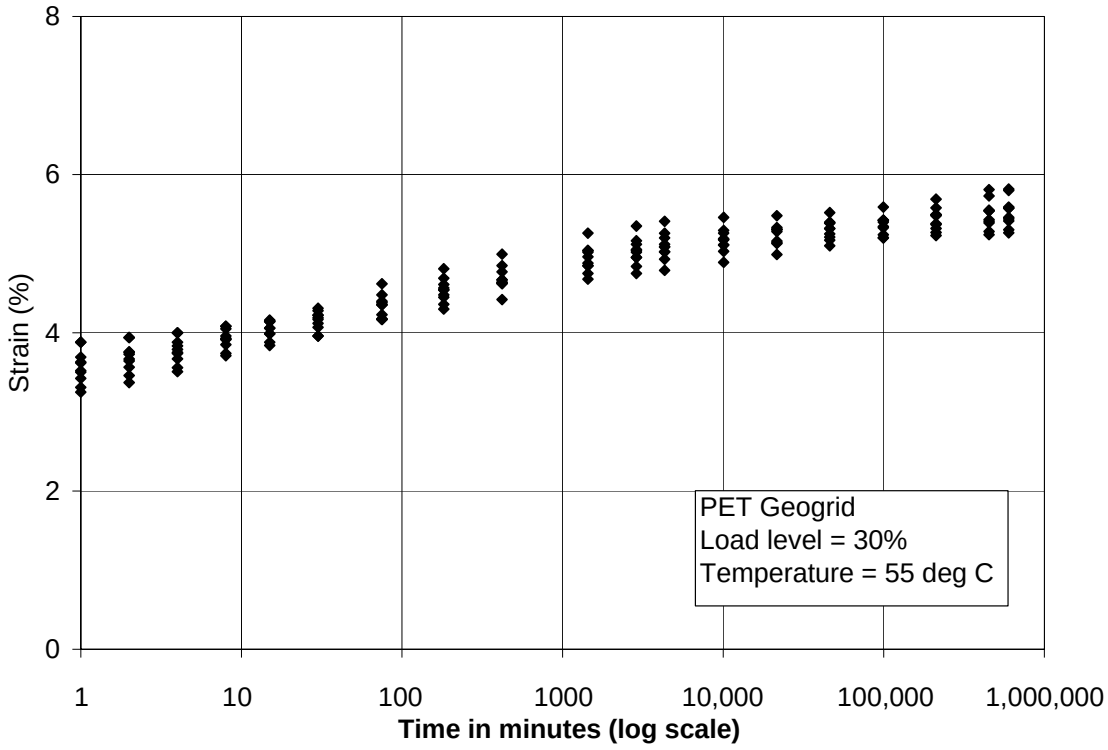
8
6
4
2
0
Strain (%)
PET Geogrid
Load level = 30%
Temperature = 55 deg C
1
10
100
1000
10,000
100,000
1,000,000
Time in minutes (log scale)

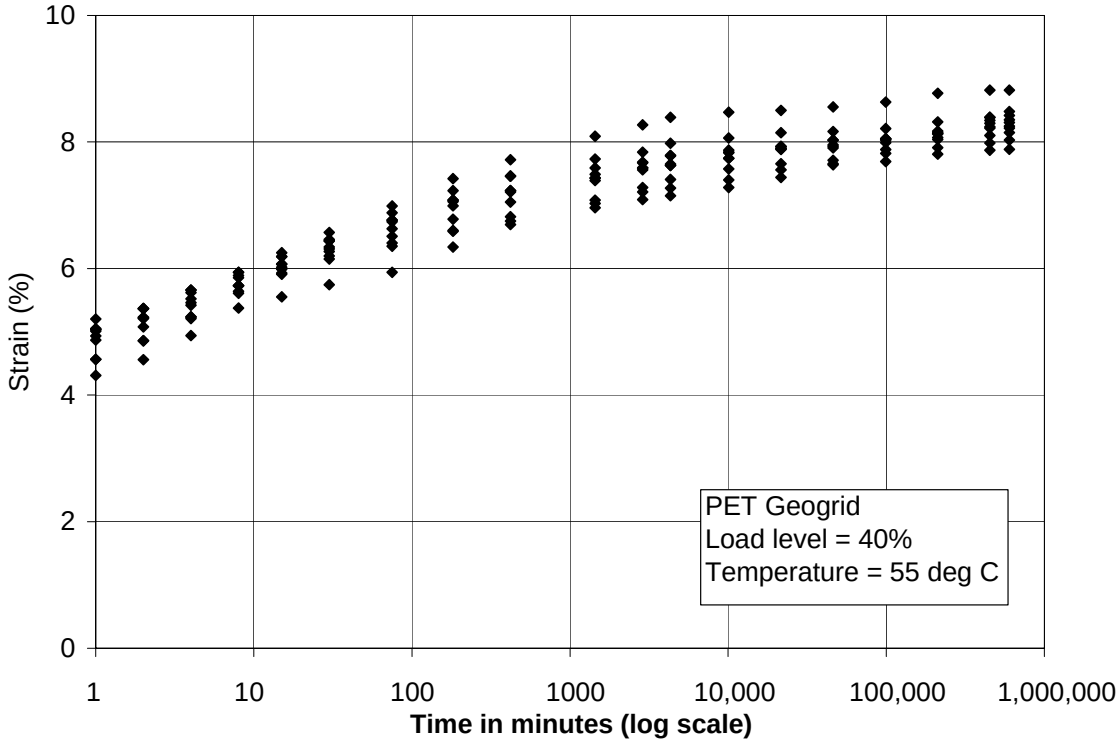
10
8
6
4
2
0
Strain (%)
PET Geogrid
Load level = 40%
Temperature = 55 deg C
1
10
100
1000
10,000
100,000
1,000,000
Time in minutes (log scale)

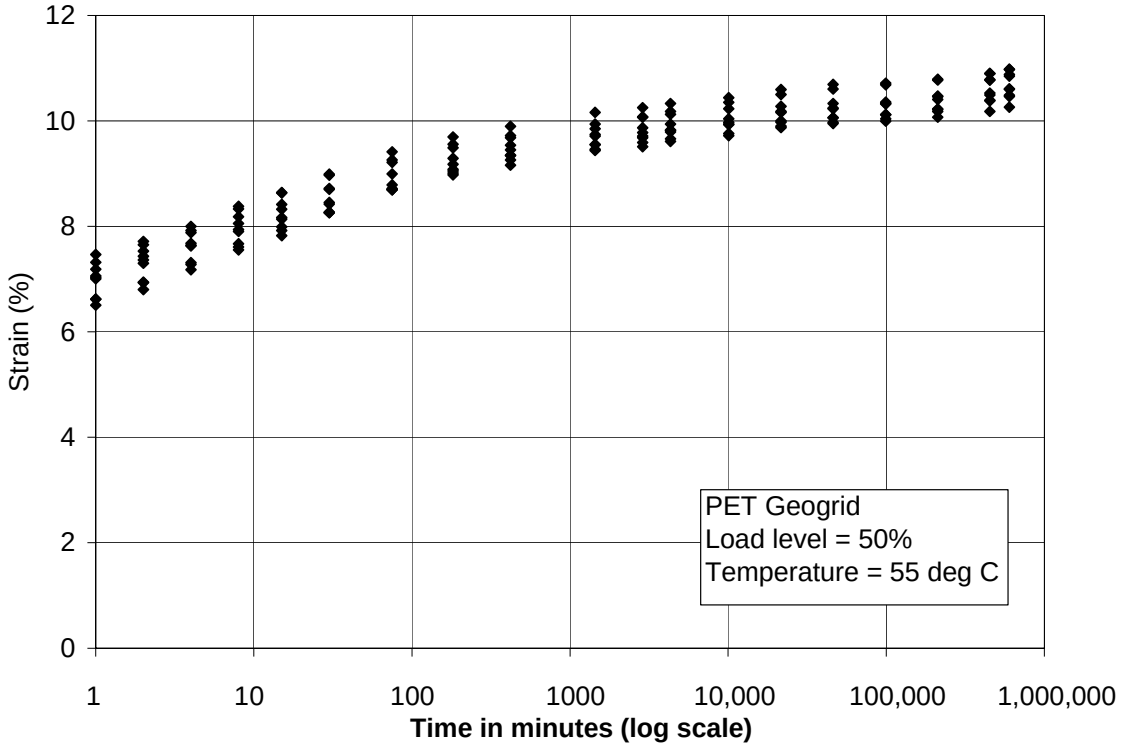
12
10
8
6
4
2
0
Strain (%)
PET Geogrid
Load level = 50%
Temperature = 55 deg C
1
10
100
1000
10,000
100,000
1,000,000
Time in minutes (log scale)

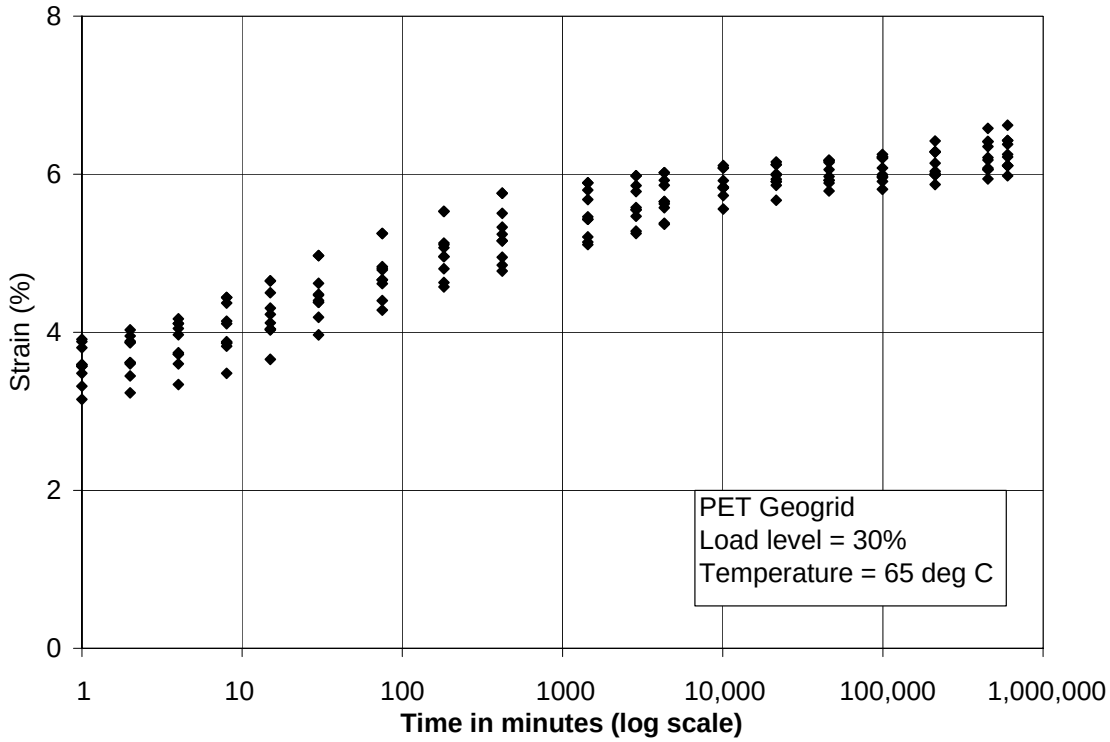
8
6
4
2
0
Strain (%)
PET Geogrid
Load level = 30%
Temperature = 65 deg C
1
10
100
1000
10,000
100,000
1,000,000
Time in minutes (log scale)

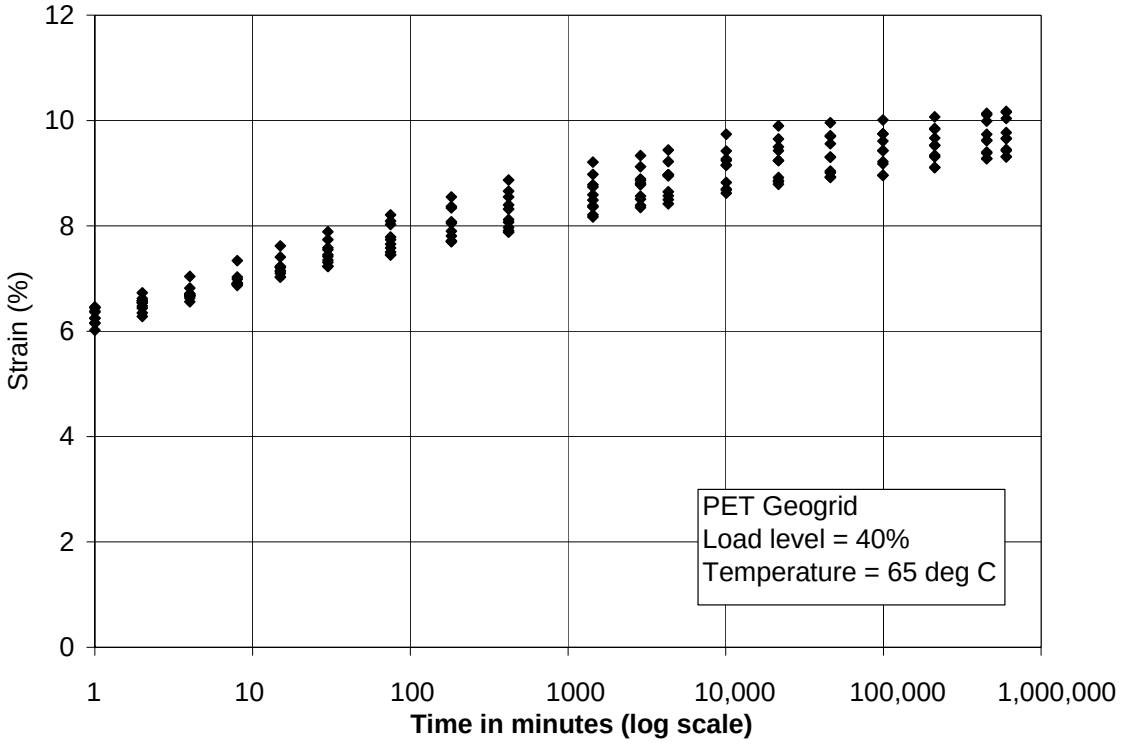
12
10
8
6
4
2
0
Strain (%)
PET Geogrid
Load level = 40%
Temperature = 65 deg C
1
10
100
1000
10,000
100,000
1,000,000
Time in minutes (log scale)

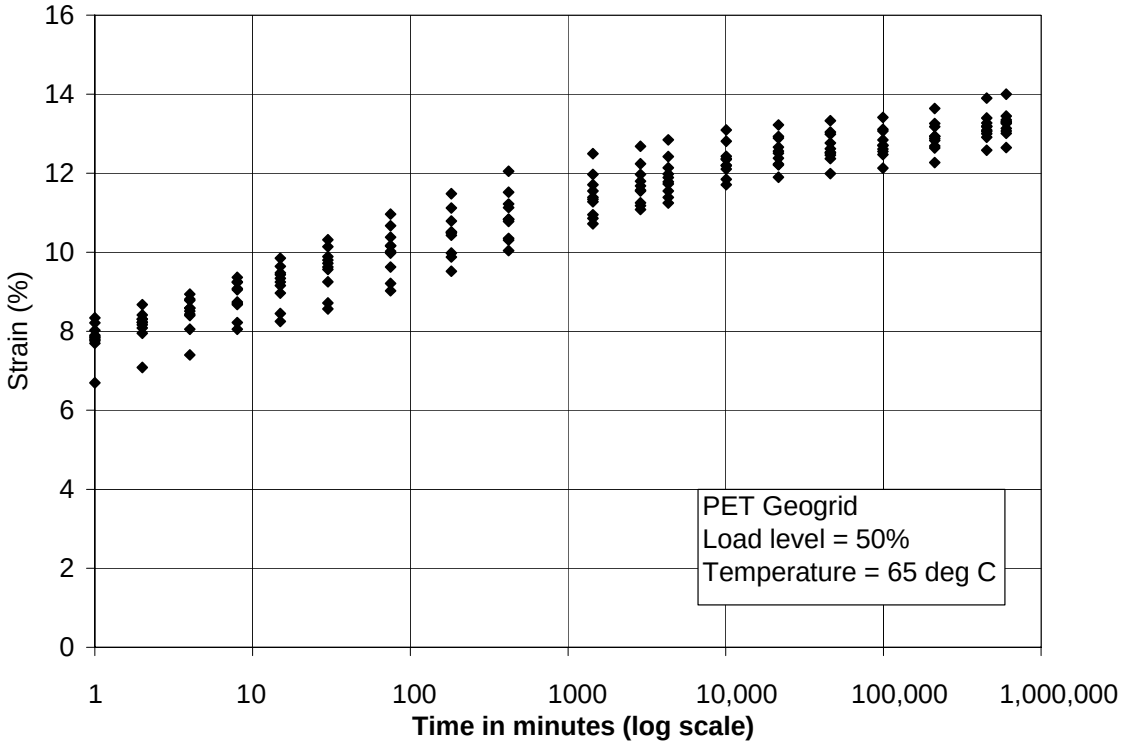
16
14
12
10
8
6
4
2
0
Strain (%)
PET Geogrid
Load level = 50%
Temperature = 65 deg C
1
10
100
1000
10,000
100,000
1,000,000
Time in minutes (log scale)

Appendix C. MSE Wall Design

1. Design Limits

a) Wall height H = 6m

b) Wall length L= no restriction (double-face wall)

c) Face angle = 90^o

d) External Loads: Dead load = 10 kPa

Live load = 10 kPa

Dead Load: Equivalent to a concrete pavement slab, 0.3 m thick.

Live load: Equivalent height of soil according to AASHTO LRFD specs (FHWA H1-98-032)

Seismic load: None.

e) Facing: segmental facing will be used

f) Construction requirements: none, but the spacing between the reinforced

layers will be increased to accentuate wall distress. The soil layers shall be subjected to 95% AASHTO T-99 Standard Proctor Compactor.

g) Environmental conditions: No aggressive chemicals

h) Design / service life: short (<10 years)

2. Foundation soil

The foundation must have good drainage characteristics. Dense sand and gravel or rock are recommended. The groundwater table must be 1 meter or deeper from the ground surface.

3. Backfill soil

The backfill soil must be free-draining. Sand with 35^0 friction angle is recommended.

4. Safety factors

Factor of safety of 1.0 will be used for internal stability to increase distress, for the purposes of the FDOT research project. This is done to increase the wall distress.

5. Preliminary dimensions

$L = 0.7\ H = 4.2$ m

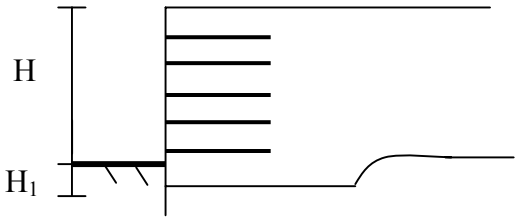

Embedment depth:

$H_1 = 0.6$ m

6. Internal Earth Pressure distribution

$$K_A = \tan^2 (45 - \phi/2) = 0.27$$

Active earth pressure is considered so that the design is not too conservative, and distress can be observed.

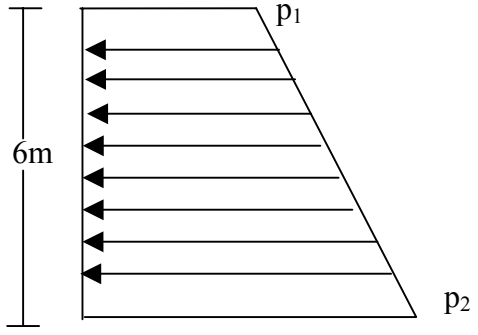

$$p_1 = q\ K_A = (20)\ (0.27) = 5.4\ \text{kPa}$$

$$p_2 = p_1 + \gamma z\ K_A = 5.4 + (17)\ (6)\ (0.27) = 33\ \text{kPa}$$

7. External Stability

a) The wall is safe against bearing capacity failure and slope failures if a strong foundation (e.g. BC = 300 kPa) is used.

b) Sliding is not an issue since a double-face wall is used.

c) Overturning is not an issue in a double face wall.

8. Settlement

Settlement is negligible since the wall will be constructed on a rigid foundation.

9. Overburden and Lateral Pressures

The normal and lateral pressures for $\gamma = 17\ \text{kN/m}^3$ are given in the following Table.

Normal and Lateral pressures

z(m)	σ_v (kPa)	σ_k (kPa)
0.3	5.1	1.4
0.6	10.2	2.8
0.9	15.3	4.1
1.2	20.4	5.5
1.5	25.5	6.9
1.8	30.6	8.3
2.1	35.7	9.6
2.4	40.8	11.0
2.7	45.9	12.4
3.0	51.0	13.8
3.3	56.1	15.1
3.6	61.2	16.5
3.9	66.3	17.9
4.2	71.4	19.3
4.5	76.5	20.7
4.8	81.6	22
5.1	86.7	23.4
5.4	91.8	24.8
5.7	96.9	26.2

10) Internal stability

Assuming 0.8 m spacing of the geogrids

$$T_i = S_i \ \sigma_h$$

$$T_{max\ req} = (0.8)\ (26.2) = 20.96\ kN/m$$

Since the design uses creep-limited strength,

UX 1400 HS $\longrightarrow$ $S_{creep\ 5\%} = 20.4$ kN/m

TC Mirafi 3XT $\longrightarrow$ $S_{creep\ 5\%} = 20$ kN/m

Using a stronger material such as UX 1600 or Matrex 60 will mask the distress mechanisms.

11) <u>Length of the Geogrids</u>

$$L_e = \frac{T}{2\,\gamma\, z\,\alpha\, F^*} = \frac{s\,K_A\,(1+ q/\gamma\, z)}{2\,F^*}$$

where:

α = 1 (no scale correction)

F^* = $0.8 \tan\phi = 0.58$

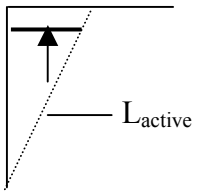

$$L_{e\,max} = \frac{(0.8)(0.27)}{2(0.56)} \quad (1+\frac{20}{(17)(0.3)}) = 0.95 \text{ m}$$

$$L_{max} = 0.95 + L_{acitve} = 0.95 + 6 \tan (45 - \frac{35}{2}) = 4.0 \text{ m}$$

Therefore, the wall must be at least 8 m (26.24ft) in length. A longer wall will be needed for constructability.

Final wall parameters

a) Wall height H = 20ft

b) Wall length L = 74 ft at maximum location

c) Wall width B = 100 ft

d) Face angle = 90^{o}

e) Facing: 5ft x 4.8ft and 6 inches thick segmental concrete panels. Facing dimensions are approximate depending on the provider

f) Backfill soil: **SP** (poorly-graded sands and gravely sands, little or no fines),

Class II (coarse-grained one, clean) [ASTM D2321 and D2487]

g) Geogrids:

i) PET: TC Mirafi 3XT

ii) HDPE: Tensar UX 1400

Appendix D. Input Program for Full Scale Wall with Creep Effect

```
;*****FULL MSE WALL
;Fixing the rotation in the middle of the facings

grid 21 40
model mohr
set large
set gravity 9.8


;Properties of the soil
prop  s=1.54e7 b=3.33e7 d=1560 coh=1e3 fric=36



;************************Define null zones*********************
def delzones
  loop  num(0,7)
  jjj= 3+num*5
  command
    model null  j=jjj
  end_command
  end_loop
end
delzones
model null i=1

;************************Define coordenates********************
;define coordenates of the middle layers
def coormiddle
   xc= 4.6
   yc= 6
   loop c(0,6)
          c1a=0
          c1b=.375+.75*c
          c2a=xc
          c2b=.375+.75*c
          c3a=0
          c3b=.375+.75*(c+1)
          c4a=xc
          c4b=.375+.75*(c+1)
          ja=4*(c+1)+c
          jb=ja+4
```

```
  command
        generate c1a c1b c3a c3b c4a c4b c2a c2b i=2,22 j=ja,jb
  end_command
  end_loop
 end
coormiddle


;define coordenates of the boundaries
generate 0 0 0 .375 xc .375 xc 0 i=2,22 j=1,3
generate 0 5.625 0 yc xc yc xc 5.625 i=2,22 j=39,41

;**************************Define geogrid***************
def geogrid
  dimc=4.6/20           ;dimension of every grid in x direction (every square)
  nele=17               ;number of beams
  nnele=17+1


   loop j(1,8)
    loop i(1,nnele)
      xc=(i-1)*dimc
      yc= .375+.75*(j-1)
      num=600+ (i+(j-1)*nnele)
    command
       struc node num xc yc pin
    end_command
    if i>1 then
     num1=num-1
     command
       struc beam begin node num end node num1 prop 2
     end_command
    endif
  end_loop
  end_loop
end
geogrid

;Properties of the geogrid
struc prop 2 e=4.4e8 area=.0018 i=4.86e-10



;***************Define interfaces for geogrid*************
def intHorizontalMiddle
```

```
;"""""give this values
  nele=17                  ;number of beams
  nnele=17+1
  nx=nele+2
;"""""""""

  loop  inta(1,8)
    int1=inta+(inta-1)
    int2=int1+1
   ;int3=1000+int2
         c1x=2
         c1y=3+(inta-1)*5
         c1yp=c1y+1
         c2x=nx
         c2y=3+(inta-1)*5
         c2yp=c2y+1
         n1=601+nnele*(inta-1)
         n2=n1+nele


         c2yy=c2y+1
       c2xx=nx

  command
    int int1 aside from c1x c1y to c2x c2y bside from node n2 to node n1
    int int1 fric 35 kn 2.87e8 ks 2.87e8

    int int2 aside from node n1 to node n2 bside from c2x c2yp to c1x c1yp
    int int2 fric 35 kn 2.87e8 ks 2.87e8


;************************INTERFACES JUST IN SOIL

    int 1111 aside from c2xx 3 to 22 3 bside from 22 4 to c2xx 4
    int 1111 fric 36 kn 2.87e8 ks 2.87e8

    int 1112 aside from c2xx 8 to 22 8 bside from 22 9 to c2xx 9
    int 1112 fric 36 kn 2.87e8 ks 2.87e8

    int 1113 aside from c2xx 13 to 22 13 bside from 22 14 to c2xx 14
    int 1113 fric 36 kn 2.87e8 ks 2.87e8

    int 1114 aside from c2xx 18 to 22 18 bside from 22 19 to c2xx 19
    int 1114 fric 36 kn 2.87e8 ks 2.87e8

    int 1115 aside from c2xx 23 to 22 23 bside from 22 24 to c2xx 24
```

```
    int 1115 fric 36 kn 2.87e8 ks 2.87e8

    int 1116 aside from c2xx 28 to 22 28 bside from 22 29 to c2xx 29
    int 1116 fric 36 kn 2.87e8 ks 2.87e8

    int 1117 aside from c2xx 33 to 22 33 bside from 22 34 to c2xx 34
    int 1117 fric 36 kn 2.87e8 ks 2.87e8

    int 1118 aside from c2xx 38 to 22 38 bside from 22 39 to c2xx 39
    int 1118 fric 36 kn 2.87e8 ks 2.87e8
;*********************************************


  end_command
  end_loop
end
intHorizontalMiddle

;********************Define facing system*********************
def facing
loop jj(0,3)
  loop j (0,1)
  if j=0 then
    num1=100+jj*8+1
    num2=num1-99
    y11= 1.5*jj
    y22= y11 + .1875
      command
       struc node num1 -.001  y11
       struc node num2 -.001  y22
       struc beam begin node num1 end node num2 prop 1
     end_command
   endif
  if j=1 then
   n1=jj*8+3
   n2=n1+1
   n3=n2+1
   n4=n3+1
   n5=n4+1
   n6=n5+1
   n7=n6+1
   n8=n1-1
   y1=y22+.1875
   y2=y1+.1875
   y3=y2+.1875
   y4=y3+.1875
```

```
  y5=y4+.1875
  y6=y5+.1875
  y7=y6+.1875

  command
    struc node n1 -.001 y1
    struc node n2 -.001 y2
    struc node n3 -.001 y3
    struc node n4 -.001 y4
    struc node n5 -.001 y5
    struc node n6 -.001 y6
    struc node n7 -.001 y7

    struc beam begin node n8 end node n1 prop 1
    struc beam begin node n1 end node n2 prop 1
    struc beam begin node n2 end node n3 prop 1
    struc beam begin node n3 end node n4 prop 1
    struc beam begin node n4 end node n5 prop 1
    struc beam begin node n5 end node n6 prop 1
    struc beam begin node n6 end node n7 prop 1

  end_command
  endif
end_loop
end_loop
end
facing
;Properties of the facing system
struc prop 1  e=5e9 area=.17 i=4.2e-4


;****************Define interface between facing and soil*********
def intVerticals
loop jv(0,3)

;Iface for the bottom of the facing
  num1=101+jv
  c1x=2
  c1y=1+10*jv
  c1xx=2
  c1yy=3+10*jv
  n1=3+8*jv
  n11=101+8*jv

;Iface for the middle of the facing
  num2=201+jv
```

```
  d1x=2
  d1y=4+10*jv
  d1xx=2
  d1yy=8+10*jv
  dn1=7+8*jv
  dn11=3+8*jv

;Iface for the top of the facing
  num3=301+jv
  e1x=2
  e1y=9+10*jv
  e1xx=2
  e1yy=11+10*jv
  en1=9+8*jv
  en11=7+8*jv
  command
    int num1 aside from c1x c1y to c1xx c1yy bside from node n1 to node n11
    int num1 glue kn 2.69e9 ks 2.69e9
    int num2 aside from d1x d1y to d1xx d1yy bside from node dn1 to node dn11
    int num2 glue kn 2.69e9 ks 2.69e9
    int num3 aside from e1x e1y to e1xx e1yy bside from node en1 to node en11
    int num3 glue kn 2.69e9 ks 2.69e9
  end_command
 end_loop
end
intVerticals


;*********************Conexion facing and geogrid*********************
def conslave
;"""""value to give
  nele=17                  ;number of beams
  nnele=17+1
  nx=nele+2
;""""""""""


 loop con(0,7)
  num1=3+4*con
  num2=601+nnele*con
  command
    struc node num2 slave num1
  end_command
  end_loop
 end
conslave
```

```
set force 10
fix y x j=1
fix x i=22

;***********Fix rotation boundary at the middle of facings**********
def fixfacing
  loop inc(0,3)
  n1=5+8*inc
  command
   struc node  n1 fix r
   end_command
  end_loop
end
fixfacing


;**Define boundary conditions for last node of each geogrid layer******

def BoundaryGeogrid
;"""""value to give
  nele=17                   ;number of beams
  nnele=17+1
  nx=nele+2
;""""""""""

  loop gen(0,7)
   lastnodet=gen
    jnt=600+nnele+nnele*lastnodet
    command
      struc node  jnt fix r
    end_command
  end_loop
end
BoundaryGeogrid


;**********************apply normal pressure of 20 kN/m2*********

apply p=15000 i=2,22 j=41
solve
save WcreepA1.save


;************************************************************
```

```
;-------------
set echo off
def $str_fin
;Structural Elements:  include-file for FISH program
;--------------------
;Global pointer to structural list:  STR_PNT
;Block sizes
;-----------
  $nvstr  = 7     ;Control Block
  $nvels  = 20    ;Element Block
  $nvnod  = 69    ;Node Block
  $nvtyp  = 25    ;Property Block
  $nvsupp = 18    ;Support Block
;Control
;-------
  $ksnode = 0     ;Pointer to Node List
  $ksels  = 1     ;Pointer to Element List
  $ksnseq = 2     ;ID Number of last node created
  $kseseq = 3     ;ID Number of last element created
  $kstyp  = 4     ;Pointer to Property List
  $kssupp = 5     ;Pointer to Support List
  $kssext = 6     ;Spare Extension (can be used by FISH function)
;Element
;-------
;          0     ;Link to next block
  $kelext = 1     ;Spare extension (can be used by FISH function)
  $kelid  = 2     ;ID number of element
  $keln1  = 3     ;Pointer to Node 1
  $keln2  = 4     ;Pointer to Node 2
  $kelcod = 5     ;Type flag:  1 = beam;  2 = cable  3 = pile
  $keltyp = 6     ;Property number
  $keltad = 7     ;Pointer to property block
  $kell   = 8     ;Length
  $kelfsh = 9     ;Shear force
  $kelfax = 10    ;Axial force
  $kelm1  = 11    ;Moment around end 1
  $kelm2  = 12    ;Moment around end 2
  $kelut1 = 13    ;X component of tangential unit vector
  $kelut2 = 14    ;Y component of tangential unit vector
  $kelhin = 15    ;hinge indicator: 0 no hinge, 1 el. has a hinge
  $kelhm1 = 16    ;offset kndfr or kndhfr for unbalanced moment around node 1
;                 if it is a hinge node, 0 otherwise
  $kelhm2 = 17    ;offset kndfr or kndhfr for unbalanced moment around node 2
;                 if it is a hinge node, 0 otherwise
  $keleax = 18    ;Unused
  $keluti = 19    ;Utility field - currently used in plotting.
```

```
;Node
;----
;         0     Link to next block
  $kndext = 1     ;Spare extension (can be used by FISH function)
  $kndid  = 2     ;ID number
  $kndx   = 3     ;X position
  $kndy   = 4     ;Y position
  $kndud1 = 5     ;X velocity
  $kndud2 = 6     ;Y velocity
  $kndu1  = 7     ;X displacement
  $kndu2  = 8     ;Y displacement
  $kndthd = 9     ;Angular velocity
;               hinge node: angular velocity of hinge node a
  $kndth  = 10    ;Angular displacement
;               hinge node: angular displacement of hinge node a
  $kndmx  = 11    ;X effective mass
  $kndmy  = 12    ;Y effective mass
  $kndmr  = 13    ;Rotational effective mass
  $kndi   = 14    ;I index of connecting gridpoint (or mapped zone)
  $kndj   = 15    ;J index of connecting gridpoint (or mapped zone)
  $kndadd = 16    ;Address of connecting gridpoint (or mapped zone)
  $kndf1  = 17    ;X unbalanced force .. reset to zero in motion loop
  $kndf2  = 18    ;Y unbalanced force .. reset to zero in motion loop
  $kndfr  = 19    ;Rotational unbalanced force
;               hinge node: unbalanced moment around hinge node a
;               reset to zero
  $kndf1c = 20    ;X unbalanced force .. copy, not set to zero
  $kndf2c = 21    ;Y unbalanced force .. copy, not set to zero
  $kndfrc = 22    ;Rotational unbalanced force copy
  $kndcod = 23    ;Type of attachment flag:  1 = not linked to grid
;                                            2 = direct link to gridpoint
;                                            3 = cable-type connection in zone
  $kndpin = 24    ;Pin flag:  0 = free; 1 = fix
  $kndap1 = 25    ;X applied force
  $kndap2 = 26    ;Y applied force
  $kndapr = 27    ;Rotational applied force
  $kndxfx = 28    ;X direction Fix flag:  0 = free; 1 = fixed
  $kndyfx = 29    ;Y direction Fix flag:  0 = free; 1 = fixed
  $kndrfx = 30    ;Rotational Fix flag:  0 = free; 1 = fixed
  $kndefl = 31    ;Effective length
  $kndt1  = 32    ;X component of Tangential Unit vector
  $kndt2  = 33    ;Y component of tangential unit vector
  $kndbfl = 34    ;Bond flag:  0 = yielded; 1 = intact
;               Pile: shear spring status
;               1 = elastic, 2 = plastic now or in the past
  $kndw1  = 35    ;Grid zone weighting factor 1
```

```
 $kndw2  = 36    ;                   2
 $kndw3  = 37    ;                   3
 $kndw4  = 38    ;                   4
 $kndfs  = 39    ;Shear force
;               Pile: force in shear spring
 $kndtad = 40    ;Pointer to property block
 $kndmxd = 41    ;Dynamic X effective mass
 $kndmyd = 42    ;Dynamic Y effective mass
 $kndmrd = 43    ;Dynamic Rotational effective mass
 $kndmsf = 44    ;Master/Slave Flag Bit 1 = Master
;                           Bit 2 = Slave in X
;                           Bit 3 = Slave in Y
 $kndma1 = 45    ;If Master thet address of slave triple list
;               if Slave then address of master node in Y
;               else zero
 $kndma2 = 46    ;if Slave then address of master node in Y
;               else zero
 $kndnfl = 47    ;Pile: normal spring status
;               1 = elastic, 2 = plastic now or in the past
 $kndfn  = 48    ;Pile: force in normal spring
 $kndup  = 49    ;Pile normal spring hysteresis: permanent (plastic)
;               relative normal displacement on positive side of pile
 $kndum  = 50    ;Pile normal spring hysteresis: permanent (plastic)
;               relative normal displacement on negative side of pile
 $kndua  = 51    ;Pile relative normal displacement
 $kndunr = 52    ;Pile relative normal displacement increment
 $kndhfr = 53    ;Hinge node: unbalanced moment around node b, reset to zero
 $kndhtd = 54    ;Hinge node: angular velocity of node b
 $kndhth = 55    ;Hinge node: angular displacement of node b
 $kndhin = 56    ;Hinge indicator:
;               0 no hinge, >0 hinge node
;               1 a-b are attached (elastic loading/unloading)
;               2 a-b are separate (hinge at yield)
 $kndhmi = 57    ;Hinge node: moment transmitted between a and b
 $kndhtr = 58    ;Hinge node: sign of relative a-b angular velocity
;               (+1 or -1 to detect unloading)
 $kndep  = 59    ;Pile: effective pressure in plane normal to pile
 $kndnc  = 60    ;Node counter used in hinge logic
 $kndnc1 = 61    ;Node counter used in hinge logic
 $kndlo1 = 62    ;X-applied force (does not include gravity)
 $kndlo2 = 63    ;Y-applied force (does not include gravity)
 $kndfor1= 64    ;X-unbalanced force for combined damping
 $kndfor2= 65    ;Y-unbalanced force for combined damping
 $kndus  = 66    ;Accumulated shear diplacement
 $kndcstr = 67   ;Node's characteristic stress (used for mech ratio)
 $kndcarea = 68  ;Node's characteristic area (used for mech ratio)
```

```
;Hinge Node
;----------
;composed of an a-b doublet
;in elastic range moment and rotation are continuous
;in plastic range moment is continuous, rotation is discontinuous
;Master/Slave Triple List
;------------------------
;          0     ;Pointer to next triple
;          1     ;Flag, Bit 1 = Slave in X
;                      Bit 2 = Slave in Y
;          2     ;Pointer to Slave node
;Property
;--------
;         0      Link to next block
  $ktypex = 1     ;Spare extension (can be used by FISH function)
  $ktype  = 2     ;Elastic Modulus
  $ktypi  = 3     ;Moment of Inertia
  $ktypar = 4     ;Area
  $ktypid = 5     ;Property number
  $ktypei = 6     ;Elastic Modulus * Moment of Inertia
  $ktypkb = 7     ;Bond stiffness
;                 Pile: shear spring stiffness
  $ktypsb = 8     ;Bond strength
;                 Pile: shear spring strength
  $ktypyi = 9     ;Yield
  $ktyppm = 10    ;Plastic Moment
  $ktyden = 11    ;Density
  $ktypkn = 12    ;Normal Stiffness
;                 Pile: normal spring stiffness
  $ktypks = 13    ;Shear Stiffness
  $ktypfb = 14    ;Pile: shear spring friction coefficient
  $ktypyc = 15    ;Cable compressive yield
  $ktypsn = 16    ;Pile: normal spring 'compressive' strength
  $ktyppe = 17    ;Pile: length along perimeter in contact with soil
  $ktypfn = 18    ;Pile: normal spring friction coefficient
  $ktypcg = 19    ;Pile gap closing coefficient
;                 (0: no-, 1: full-gap closing)
  $ktyppy = 20    ;Pile normal spring: pointer to fish function
;                 (p-y curve)
  $ktypte = 21    ;Pile: normal spring 'tensile' strength
  $ktyphe = 22    ;Height of rectangular cross-section
  $ktypwi = 23    ;Width  of rectangular cross-section
  $ktypra = 24    ;Radius of circular    cross-section
;Support
```

```
;-------
;          0     Link to next block
  $ksuext = 1     ;Spare extention
  $ksut1  = 2     ;X component unit vector
  $ksut2  = 3     ;Y component unit vector
  $ksupro = 4     ;Property number
  $ksupad = 5     ;Pointer to property block
  $ksufn  = 6     ;Normal force
  $ksufs  = 7     ;Shear force
  $ksuun  = 8     ;Normal displacement
  $ksuus  = 9     ;Shear displacement
  $ksutad = 10    ;Pointer to top zone
  $ksubad = 11    ;Pointer to bottom zone
  $ksutra = 12    ;Ratio of Top intersection
  $ksubra = 13    ;Ratio of bottom intersection
  $ksutij = 14    ;Top 0 = East, 1 = North (other adjacent gridpoint)
  $ksubij = 15    ;Bottom 0 = East , 1 = North
  $ksusub = 16    ;Pointer to Sub-elements
  $ksunsm = 17    ;Number of Elements
end

$str_fin
set echo on
;-------------
;

def relax_force
oldmod=4.4e8
newmod=3e8

          ip=imem(str_pnt + $ksels)
          loop while ip # 0
                    axial_force=fmem(ip+$kelfax)
                    element_addr=ip
                    relaxed_force=axial_force*newmod/oldmod
                    ;fmem(ip + $kelfax)=relaxed_force
                    fmem(element_addr + $kelfax)=relaxed_force
                    ip=imem(ip)
          end_loop
end

relax_force
struc prop 2 e=3e8 area=.0018 i=4.9e-10
solve
save wcreepA2.save
```